



The University of
Nottingham

UNITED KINGDOM • CHINA • MALAYSIA

**Dynamic response of high-performance honeycomb
cores and hybrid fibre composite laminates for
lightweight sandwich structures**

By

Yuwu Zhang

Submitted to the University of Nottingham for the degree
of Doctor of Philosophy

June, 2018

Acknowledgements

I would like to express my sincere gratitude to the people mentioned below. My PHD would not have been completed without their support.

I would like to offer my gratitude to my supervisor, Dr. Tao Liu, for his wonderful guidance, support and motivation throughout my PhD. I would like to thank a number of academics and collaborators, in particular Dr. Ian Maskery, Professor Ian Ashcroft, Dr. Walid Tizani and Professor Arthur Jones of the University of Nottingham, for extensive discussions and suggestions. I also offer my thanks to all the members of my research group, the Centre for Structural Engineering and Informatics (CSEI), of the University of Nottingham.

I am grateful for the technical support provided by technicians and staff, including Nigel Rook, Gary Davies, Tom Buss, Steve Lawton, Jason Greaves, Graham Malkinson, Paul Johns, Paul Turner and Ben Jennison. Thanks to the great help and advice of my colleagues, Paul Turner and Huan Ren. I would further like to thank my flatmates as well as friends, Jack Tomlin, Shunze Cao and Nan Ma, for sharing a lot of happiness with me.

I would also like to acknowledge the financial support of the China Scholarship Council (CSC) during my PHD study.

Lastly, I express my thanks to my family for their love and understanding. They support and encourage me to pursue my dream.

Abstract

Lightweight sandwich structures that are composed of high-performance core and face sheets, have been attracting attention in both civilian and military applications due to their outstanding mechanical properties. Honeycomb cores and fibre reinforced composite face sheets have specific advantages for resisting dynamic impact. For example, honeycomb cores possess higher specific-strength (ratio of strength to relative density) than the other sandwich cores under compression, and carbon fibre composites possess high tensile strength and low density. This thesis focuses on the understanding of the dynamic compressive response of high-performance honeycombs and the ballistic impact resistance of stiff/soft hybrid fibre composite laminate beams.

For honeycomb cores, the out-of-plane compressive behaviour of the AlSi10Mg alloy hierarchical honeycombs and commercially available Nomex honeycombs have been experimentally and numerically investigated. Owing to the complex in-plane topology, hierarchical honeycombs were fabricated using the Selective Laser Melting (SLM) technique. The experimental measurement and finite element (FE) calculation indicate that the two hierarchical honeycombs, specifically two-scale and three-scale honeycombs, both offer higher wall compressive strengths than the single-scale honeycombs. With an increase in relative density, the single-scale honeycomb experiences a transition in terms of failure mechanism from local plastic buckling of walls to local damage of the parent material. Alternately, the two-scale and three-scale hierarchical honeycombs all fail with solely parent material damage. The dynamic

compressive strength enhancement of the hierarchical honeycombs is dominated by the strain rate sensitivity of the parent material. For Nomex honeycombs, the dynamic failure mode under out-of-plane compression is different from the quasi-static failure mode, i.e. the honeycombs fail due to stubbing of cell walls at the end of specimens under dynamic compression, whereas fail due to local phenolic resin fracture after elastic buckling of the honeycomb wall under quasi-static compression. The dynamic compressive strength of Nomex honeycombs increases linearly, and the strength enhancement is governed by two mechanisms: the strain rate effect of the phenolic resin and inertial stabilization of honeycomb unit cell walls. The inertial stabilization of unit cell walls plays a more significant role in strength enhancement than the strain rate effect of the phenolic resin. In addition, the effect of key parameters such as impact method and initial geometrical imperfections on the compressive responses of honeycombs has also been numerically investigated.

For face sheets, the ballistic resistance of the beams hybridizing stiff and soft carbon fibre composites has also been experimentally studied, and these results were compared with those of stiff and soft composite beams with identical areal mass. The failure modes of composite beams under different velocity impacts have been identified to be different. For monolithic beams, the hybrid and soft monolithic beams exhibited similar energy absorption capacity. As for the sandwich beams, the hybrid sandwich beams behaved better in terms of energy absorption than soft sandwich beams at high projectile velocities. Both the hybrid and soft composite beams absorbed more kinetic energy from projectiles

than stiff composite beams. The advantages of the stiff/soft hybrid composites can be summarized as follows: (i) the soft composite part survives at low velocity impact; (ii) the stiff composite part of the hybrid monolithic/sandwich beams has a more uniform stress distribution than the stiff monolithic/sandwich beams owing to the buffer effect of the soft composite part.

This work identifies the advantages of high performance honeycomb cores as well as fibre composite face sheets. These findings can be used to develop high strength, low weight and multi-functional sandwich structures, thereby widening their applicability to a wider array of fields.

List of Notations

Roman symbols

T^*	homologous temperature
T_0	room temperature
T_M	melting temperature of metallic materials
A	metallic materials constant in Johnson-Cook model
B	metallic materials constant in Johnson-Cook model
e	metallic materials constant in Johnson-Cook model
C	metallic materials constant in Johnson-Cook model
m	metallic materials constant in Johnson-Cook model
E_f	elastic modulus of fibre
c_f	longitudinal wave speed in fibre
u_f	transverse wave speed in fibre
c_{fc}	longitudinal wave speed in fibre composites ply
M_0	mass of fibre composites ply per unit length
F_T	tensile force of fibre ply

c^*	Cunniff velocity of fibre
H	out-of-plane thickness of honeycombs
D	in-plane maximum diameter of AlSi10Mg alloy honeycombs
E_{SLM}	elastic modulus of AlSi10Mg alloy material
c_{SLM}	elastic wave speed of AlSi10Mg alloy material
F	compressive force of honeycombs
A_0	original cross-sectional area of honeycomb specimens
v_0	initial impact velocity of projectile
D_s	diameter of maraging steel striker and Kolsky bar
E_s	elastic modulus of maraging steel
A_s	cross sectional area of maraging steel striker
D_m	diameter of magnesium alloy Kolsky bar
E_m	elastic modulus of magnesium alloy
c_m	elastic wave speed in magnesium alloy Kolsky bar
A_m	cross sectional area of magnesium alloy Kolsky bar
l	length of striker

M	mass of striker
d	damage variable of element
C_{SLM}	material constant for selective laser melting manufactured AlSi10Mg alloy
k_1	strength enhancement ratio of AlSi10Mg alloy material
G_f	fracture energy of element
L_e	characteristic element size
t	time instant during dynamic impact
L_W	the width of Nomex honeycombs along 1-axis direction
L_L	the width of Nomex honeycombs along 2 direction
t_f	thickness of single aramid paper layer
t_r	thickness of single phenolic resin layer
t_N	single-wall thickness of Nomex honeycomb unit cell
L_C	characteristic cell size of Nomex honeycombs
l_c	edge length of Nomex honeycomb unit cell
$v_{s-\text{max}}$	the maximum velocity of steel striker for impacting magnesium alloy bar
E_{ap}	elastic modulus of aramid paper layer

c_{ap}	elastic wave speed in aramid paper layer
E_r	elastic modulus of phenolic resin
c_r	elastic wave speed in phenolic resin
k_2	ratio of yield stress of phenolic resin
C_N	material constant of phenolic resin
P_{ST}	percentage of strain rate effect of phenolic resin
P_{IN}	percentages of inertial effect of honeycomb walls
L	length of fibre composite beam
w	width of fibre composite beam
t_{CFRP}	thickness of fibre composite panel
D_{ssp}	diameter of steel spherical projectile
E_{k_0}	initial kinetic energy of steel spherical projectile
E_{k_r}	residual kinetic energy of steel spherical projectile
v_r	residual velocity of steel spherical projectile

Greek symbols

$\bar{\rho}_f$	relative density of cellular foams
----------------	------------------------------------

σ_{fY}	compressive yield strength of cellular foams
σ_Y	compressive yield strength of solid materials
σ_{eq}	von Mises equivalent flow stress of metallic materials
$\dot{\varepsilon}^*$	dimensionless plastic strain rate
$\dot{\varepsilon}_p$	von Mises equivalent plastic strain rate
$\dot{\varepsilon}_o$	reference strain rate
ε_p	von Mises equivalent plastic strain
ρ_f	density of fibre
ε_f	tensile strain of fibre ply
σ_f	tensile strength of fibre
$\bar{\rho}$	relative density of honeycombs
ρ	density of honeycombs
ρ_0	density of AlSi10Mg alloy material
ν_{SLM}	Poisson's ratio of AlSi10Mg alloy material
σ_y^{SLM}	tension yield strength of AlSi10Mg alloy material
σ_T	tensile strength of AlSi10Mg alloy material

δ	vertical displacement of honeycombs
ε	nominal compressive strain of honeycombs
σ	nominal compressive stress of honeycombs
$\bar{\sigma}$	average wall stress of honeycombs
$\dot{\varepsilon}$	strain rate imposed on the honeycombs
σ_s	yield strength of maraging steel striker
ρ_s	density of maraging steel
c_s	elastic wave speed in maraging steel
σ_m	yield strength of magnesium alloy
ρ_m	density of magnesium alloy
σ_c	Theoretical axial stress of maraging steel Kolsky bar in calibration test
ε_c	critical equivalent plastic strain for the damage initiation
ε_{frac}	equivalent plastic fracture strain
σ_{y0}	yield stress at the initiation of damage
σ_o	yield stress of parent material
σ_{S-max}	quasi-static out-of-plane compressive strength of honeycombs

$\sigma_{D-\max}$	dynamic out-of-plane compressive strength of honeycombs
$\bar{\sigma}_{\max}$	peak wall stress of honeycombs
ρ_w	density of Nomex honeycomb cell walls
ρ_{ap}	density of aramid paper layer
ν_{ap}	poisson's ratio of aramid paper layer
ρ_r	density of phenolic resin
ν_r	poisson's ratio of phenolic resin
σ_{r0}	compressive yield stress of phenolic resin under quasi-static compression
σ_{rp}	compressive yield stress of phenolic resin under dynamic compression
$\Delta\sigma_{EN}$	enhanced compressive strength of Nomex honeycombs under impact
σ_{ST}	enhanced compressive strengths caused by strain rate effect of phenolic resin
σ_{IN}	enhanced compressive strengths caused by inertial effect of honeycomb walls
ρ_{CFRP}	density of fibre composites
ΔE_{abs}	kinetic energy absorbed by fibre composite beam

Acronyms

UHMWPE	Ultra High Molecular-weight Polyethylene
PBO	Poly- <i>p</i> -phenylene benzobisoxazole
2D	Two-dimensional
3D	Three-dimensional
SLM	Selective Laser Melting
SHPB	Split Hopkinson Pressure Bar
AM	Additive manufacturing
SLS	Selective laser sintering
FDM	Fused deposition modelling
SHTB	Split Hopkinson Tensile Bar
DIC	Digital image correlation
PPS	Polyphenylene sulphide
FE	Finite element
cp-Ti	Commercially pure titanium
SEM	Scanning electron microscopic
LVDT	Linear Variable Differential Transformers
VA-RTM	Vacuum assisted resin transfer moulding

Table of Contents

Acknowledgements	ii
Abstract	iii
List of Notations.....	vi
Chapter 1	1
1.1 Sandwich cores.....	2
1.2 Fibre composite face sheets.....	3
1.3 Thesis objectives	6
1.4 Thesis outline	8
Chapter 2.....	11
2.1 Introduction	11
2.2 Honeycomb cores	12
2.2.1 Comparison between honeycombs and other cellular topologies .	14
2.2.2 In-plane compressive response of honeycombs.....	17
2.2.3 Quasi-static out-of-plane compressive response of honeycombs .	20
2.2.4 The dynamic out-of-plane compressive response of honeycombs and strength enhancement mechanisms	24
2.2.5 Strain rate sensitivity and thermal properties of aluminium alloy	27
2.2.6 Hierarchical honeycombs.....	28
2.2.7 Nomex honeycombs.....	31
2.2.8 Manufacturing methodology of honeycombs	35
2.3 Ballistic impact on laminated fibre composites	39
2.3.1 Strain rate dependency of fibre/yarn/composites.....	41
2.3.2 Ballistic performance of yarn/single fibre ply	43
2.3.3 Effect of fibres	46
2.3.4 Effect of matrix	48
2.3.5 Ballistic resistance of hybrid fibre composite laminates	51
2.3.6 Effect of ply-stacking orientation	55
2.3.7 Effect of ply-stacking sequence and laminate-stacking sequence	56
Chapter 3.....	60
3.1 Introduction	61
3.2 Material and manufacturing	63
3.2.1 The honeycomb specimens	63
3.2.2 Manufacturing	66

3.2.3 Quasi-static tensile coupon tests of parent material.....	67
3.3 Experimental protocols for honeycombs under compression	70
3.3.1 Quasi-static compression testing.....	70
3.3.2 Dynamic compressive testing	71
3.4 Finite element simulation	76
3.4.1 The finite element model	76
3.4.2 The constitutive model and material parameters	78
3.5 Quasi-static compressive response of honeycombs	81
3.5.1 Experimental measurement and numerical prediction.....	81
3.5.2 Effect of relative density on quasi-static compression.....	84
3.6 Dynamic compressive response of the honeycombs.....	88
3.6.1 Back face impact.....	88
3.6.2 Effect of strain rate sensitivity of the parent material.....	98
3.7 Effect of key parameters on the compressive response of honeycombs	99
3.7.1 Effect of experimental method.....	99
3.7.2 Effect of mass of striker	100
3.7.3 Effect of initial geometrical imperfections	102
3.7.4 Quasi-static compressive responses of the honeycombs based on the 3-axis or 1-axis (2-axis) uniaxial tension test data.....	104
3.8 Concluding Remarks	105
Chapter 4	108
4.1 Introduction	109
4.2 Nomex honeycomb specimen	110
4.3 Experimental protocols.....	112
4.3.1 Quasi-static compression testing.....	112
4.3.2 Dynamic compression testing	114
4.4 Finite element simulation	119
4.4.1 Finite element model.....	119
4.4.2 Constitutive model for aramid paper layer	121
4.4.3 Constitutive model for phenolic resin.....	123
4.5 Quasi-static compressive response of Nomex honeycombs.....	124
4.6 Dynamic compressive response of Nomex honeycombs	128
4.6.1. Back face impact.....	128
4.6.2 Effect of the experimental method.....	135
4.6.3 Effect of strain rate sensitivity	136

4.6.4 Effect of initial geometrical imperfections	137
4.6.5 Effect of strain rate independency of aramid paper layer	138
4.7 Conclusion remarks	139
Chapter 5	141
5.1 Introduction	142
5.2 Materials and manufacturing	144
5.2.1 Materials	144
5.2.2 Manufacturing	146
5.3 Mechanical properties of constituent materials	151
5.4 Ballistic impact test protocol	153
5.5 Ballistic impact responses of beams	156
5.5.1 Impact responses of monolithic beams	157
5.5.2 Impact responses of sandwich beams	170
5.5.3 Ballistic resistance of beams characterised by the initial-residual velocity relation of the projectile	176
5.5.4 Energy absorption capacity of beams	177
5.5.5 The effect of epoxy adhesive	180
5.6 Concluding remarks	181
Chapter 6	183
6.1 Conclusions	183
6.1.1 Compressive response of additively manufactured AlSi10Mg alloy hierarchical honeycomb structures	183
6.1.2 Dynamic compressive response of Nomex honeycombs	185
6.1.3 Dynamic response of hybrid carbon fibre laminate beams under ballistic impact	186
6.2 Future work	188
6.2.1 Compressive response of additively manufactured hierarchical honeycombs	188
6.2.2 Dynamic compressive response of Nomex honeycombs	189
6.2.3 Ballistic impact on hybrid fibre composites	190
Published work	192
References	193
Appendix	215

List of Figures

Fig. 1.1 The time line of the development of engineering materials from prehistoric times to the present day [17]. BC and AD in this figure represent before Christ and anno Domini, respectively.	4
Fig. 1.2 (a) damage of an airplane nose caused by the collision with a flock of birds (Image reproduced from https://newsavia.com/tag/badr-airlines), (b) ballistic damage of a vehicle caused by an ISIS (Islamic State of Iraq and Syria)-inspired mass shooting (Image reproduced from https://www.independent.co.uk/news/world/americas/san-bernardino-surge-gun-violence-since-2015-mass-shooting-a7235091.html).	5
Fig. 2.1 A route map of the literature review.	12
Fig. 2.2 Cellular solids used as the cores of sandwich structures.....	15
Fig. 2.3 Typical in-plane configurations of honeycombs for bending-dominated and stretching-dominated deformation modes under in-plane compression. ‘F’ represents ‘force’.	19
Fig. 2.4 Deformation modes of hexagonal honeycombs under (a) & (b) quasi-static compressions in two different directions [56], and (c) under dynamic compression [58]. ‘F’ represents force.	19
Fig. 2.5 In-plane sketch of starcell honeycombs [68].....	22
Fig. 2.6 Experimentally measured and numerically predicted deformation modes of stainless steel square honeycombs subject to impulsive loading [77].....	25
Fig. 2.7 In-plane sketch of (a) hierarchical honeycomb unit cells with first and second order hierarchy [70] and of (b) honeycombs with hierarchical walls [102], (c) macroscopic and microscopic structures of vertebra and femora [104], and (d) hierarchical structural Eiffel Tower (Image reproduced from http://www.5857.com/wall/39264.html).	30
Fig. 2.8 A compressive strength versus density map for engineering materials [117], including the measured properties of Nomex honeycombs in the current study (see Chapter 4) as well as investigated by several authors [72, 112-116], these are denoted by a solid hexagon and hollow hexagons. The measured compressive strengths of the additively manufactured AlSi10Mg alloy hierarchical honeycombs investigated in Chapter 3 are also included, denoted by stars. The solid line represents the maximum theoretical strength of fibre composite square honeycombs [31], which falls into a high specific strength gap at low densities.	33

Fig. 2.9 The different methodologies and processes for manufacturing honeycomb structures [41]. (a) Expanded manufacturing process and (b) corrugated manufacturing process for fabricating hexagonal honeycombs, and (c) trip slotting methodology for fabricating triangular and square honeycombs.	36
Fig. 2.10 Cone formation at the back face of fibre composites during ballistic impact [146].	40
Fig. 2.11 Strain rate effect on the ultimate tensile stress of fibre bundles, including M40 J carbon fibre, T300 carbon fibre, E-glass fibre and Kevlar 49 fibre [162].	42
Fig. 2.12 Improved experimental setup for measuring the high strain-rate tensile response of ultra high molecular-weight polyethylene (UHMWPE) yarn [156].	43
Fig. 2.13 Two distinct failure modes observed in polymeric fibres under projectile ballistic impact [173].	45
Fig. 2.14 A map showing specific energy absorption as a function of longitudinal wave speed of fibres and other high-performance materials [178]. The contours of Cunniff velocity c^* are also included in the map. ‘PBO’ and ‘PIPD’ in this figure represent Poly-p-phenylene benzobisoxazole and polyhydroquinone-diimidazopyridine, respectively.	48
Fig. 2.15 The penetration mechanism of the edge clamped ultra high molecular-weight polyethylene (UHMWPE) fibre composite laminate [189].	51
Fig. 2.16 The possible outcomes of hybridization based on two component materials [117]. M1 and M2 represent the original materials, A, B, C and D represent the possible outcomes after the hybridization of A and B.	52
Fig. 2.17 A schematic of helicoidal quasi-isotropic stacking architecture with an angle mismatch of 11.25° [197].	56
Fig. 2.18 Two types of ply-stacking sequence in Kevlar/basalt hybrid composite armors [202].	57
Fig. 2.19 Summary of the measured critical velocity v_c to initiate failure and ballistic limit v_p of the UHMWPE fibre composites for back supported and free standing cases [207].	59
Fig. 3.1 (a) Sketch and (b) photograph of the Selective Laser Melting (SLM) manufactured single-scale, two-scale and three-scale honeycombs. All dimensions are in mm.	65

Fig. 3.2 (a) The Renishaw AM250 SLM machine used for manufacturing AlSi10Mg alloy dog-bone coupons and honeycombs, (b) the microstructure of the SLM manufactured AlSi10Mg alloy material [214].	67
Fig. 3.3 The uniaxial tensile stress - strain relation of AlSi10Mg alloy at selected strain rates. The insert shows the geometry of the dog-bone coupon employed in the quasi-static test.....	69
Fig. 3.4 (a) Quasi-static and (b) dynamic experimental setups for determining the compressive response of additively manufactured AlSi10Mg alloy honeycombs.	71
Fig. 3.5 Sketches of Kolsky bar setup employed in the experiment, (a) back face and (b) front face impact. All dimensions are in mm.	73
Fig. 3.6 Time history of stress measured by the Kolsky pressure bar setup during a calibration test.	76
Fig. 3.7 Honeycombs under quasi-static compression. (a)-(c) Compressive stress-strain relations of the three types of honeycombs, and (d)-(f) experimentally measured (left) and FE predicted (right) damage mechanisms at Point A in (a), Point B in (b), and Point C in (c), respectively. The white dash lines in (e) and (f) show the damage locations of the single-scale and two-scale honeycombs, respectively.	83
Fig. 3.8 The effect of mesh size on the compressive response of two-scale honeycomb.....	84
Fig. 3.9 The cross-sectional views of the single-scale, two-scale and three-scale honeycombs for finite element prediction. All dimensions are in mm.....	86
Fig. 3.10 Finite element predictions for honeycombs under quasi-static compression, including the compressive stress-strain relations and the damage mechanisms of the three types of honeycombs at relative density of (a) $\bar{\rho} = 0.19$, (b) $\bar{\rho} = 0.26$, (c) $\bar{\rho} = 0.35$. The damage mechanisms of honeycombs which have been shown in Fig. 3.7 are not included in this figure.	87
Fig. 3.11 Compressive stress as a function of normalised time $v_0 t/H$ obtained by the back face impact test at low ($v_0 = 20 \text{ ms}^{-1}$), medium ($v_0 = 80 \text{ ms}^{-1}$) and high velocities ($v_0 = 120 \text{ ms}^{-1}$). The hollow circle “○” marks the stresses at the selected time instants in Fig. 3.12 – Fig. 3.15.	90
Fig. 3.12 Montage of the single-scale honeycomb under back face impact at the velocity of 20 ms^{-1} obtained from experiment and numerical simulations. Time $t=0$ corresponds to the time instant when the steel striker impacted on the honeycomb. The images were taken at (a) $t=50 \text{ us}$, (b) $t=100 \text{ us}$, (c) $t=200 \text{ us}$, (d) $t=350 \text{ us}$, respectively.	91

Fig. 3.13 Montage of the single-scale honeycomb under back face impact at the velocity of 80ms^{-1} obtained from experiment and numerical simulations. Time $t=0$ corresponds to the time instant when the steel striker impacted on the honeycomb. The images were taken at (a) $t=20\text{ us}$, (b) $t=40\text{ us}$, (c) $t=60\text{ us}$, (d) $t=80\text{ us}$, respectively.	92
Fig. 3.14 Montage of the two-scale honeycomb under back face impact at the velocity of 120ms^{-1} obtained from experiment and numerical simulations. Time $t=0$ corresponds to the time instant when the steel striker impacted on the honeycomb. The images were taken at (a) $t=13.3\text{ us}$, (b) $t=26.7\text{ us}$, (c) $t=39.9\text{ us}$, (d) $t=66.5\text{ us}$, respectively.	94
Fig. 3.15 Montage of the three-scale honeycomb under back face impact at the velocity of 80ms^{-1} obtained from experiment and numerical simulations. Time $t=0$ corresponds to the time instant when the steel striker impacted on the honeycomb. The images were taken at (a) $t=20\text{ us}$, (b) $t=40\text{ us}$, (c) $t=60\text{ us}$, (d) $t=80\text{ us}$, respectively.	95
Fig. 3.16 The peak nominal wall stresses $\bar{\sigma}_{\max}$ of the honeycombs normalized by the quasi-static 1(2)-axis tensile strength σ_T of the AlSi10Mg alloy parent material as a function of v_0/H . The (a) experimental measurements and numerical predictions of the honeycombs at the relative density of (b) $\bar{\rho} = 0.19$, (c) $\bar{\rho} = 0.26$, (d) $\bar{\rho} = 0.35$ are presented.	97
Fig. 3.17 Finite element predicted dynamic compressive responses of the three types of honeycombs at three different relative densities.	98
Fig. 3.18 Numerical study on the effect of strain rate sensitivity of the parent material. (a) The single-scale honeycomb impacted at the velocity 20 ms^{-1} and (b) the two-scale honeycomb impacted at the velocity 80 ms^{-1}	99
Fig. 3.19 Nominal compressive stress as a function of $v_0 t/H$ for selected honeycombs at selected striker velocities obtained by both back face and front face experimental measurements as well as FE simulations.	100
Fig. 3.20 FE predictions of the normalized striker velocity as a function of $v_0 t/H$ for the back face impact on honeycombs.	101
Fig. 3.21 Nominal compressive stress as a function of $v_0 t/H$ for the three-scale honeycomb under back face impact with striker velocity 80 ms^{-1} and striker mass $M = 0.0927\text{ kg}$ and $M = 0.463\text{ kg}$	102
Fig. 3.22 FE predictions of the honeycombs with initial imperfections, the single-scale honeycomb for (a) quasi-static and (b) back face dynamic compression at the velocity 80 ms^{-1} , the two-scale honeycomb for (c) quasi-static and (d) back face dynamic compression at the velocity 80 ms^{-1}	103

Fig. 3.23 Predicted quasi-static compressive responses of the honeycombs based on the 3-axis or 1-axis (2-axis) uniaxial tension test data of the AlSi10Mg alloy parent material.	105
Fig. 4.1 (a) Three-dimensional sketch of the Nomex honeycombs and (b) the in-plane sketch of a unit cell. (c) The scanning electron microscopic (SEM) photograph at the wall joint.	112
Fig. 4.2 Quasi-static experimental setup for determining the compressive response of Nomex honeycomb.....	114
Fig. 4.3 Sketch of the Magnesium alloy Kolsky bar setup in (a) back face and (b) front face impact tests, and (c) the three-dimensional sketch at the impact point. All dimensions are in mm.	118
Fig. 4.4 Finite element (FE) model of (a) Nomex honeycombs sandwiched by two rigid plates, (b) a honeycomb unit cell and (c) wall joint.	120
Fig. 4.5 (a) The stress-strain relations of aramid paper layer [121] and compressive response of phenolic resin layer [228]. (b) The yield ratio rate-dependent model of phenolic resin layer.	123
Fig. 4.6 Experimental measured and FE predicted stress-strain relationships of the Nomex honeycombs of density $\rho = 54 \text{ kg} \cdot \text{m}^{-3}$ and out-of-plane thickness $H=10 \text{ mm}$ under quasi-static compression.	125
Fig. 4.7 (a) Montage of the Nomex honeycombs under quasi-static compression obtained from experimental measurements and numerical simulations, and (b) three-dimensional view of the unit cell taken from the middle of the FE honeycomb model at strain level B. The strain levels A-D refer to the Points A-D in Fig. 4.6.	127
Fig. 4.8 Scanning electron microscopic (SEM) photographs of (a) the Nomex honeycomb wall at strain level B, and (b) top view of the honeycomb unit cell after quasi-static compression at strain level D, respectively. It is noted that the left image in (a) was taken by normal camera. The strain levels B and D refer to the Points B and D in Fig. 4.6, respectively.	128
Fig. 4.9 Nominal compressive stress of Nomex honeycombs as a function of normalised time $v_0 t / H$ obtained from the back face impact tests at different strain rates of (a) 450 s^{-1} , (b) 900 s^{-1} , (c) 1050 s^{-1} and (d) 1500 s^{-1} , respectively.	130
Fig. 4.10 Montage of high speed photographs showing the deformation patterns of the Nomex honeycombs under back face impact at strain rate of 450 s^{-1} obtained from experiment and numerical simulations. The time instants A-D refer to the Points A-D in Fig. 4.9 (a).	131
Fig. 4.11 Montage of high speed photographs showing the deformation patterns of the Nomex honeycombs under back face impact strain rate of 1500 s^{-1} obtained from experiment and numerical simulations. The time instants A-D refer to the Points A-D in Fig. 4.9 (d).	132
Fig. 4.12 (a) The dynamic peak compressive stress of the Nomex honeycombs under back face impact normalised by the experimentally measured quasi-static peak compressive stress as a function of strain rate $\dot{\epsilon}$, and (b) the contributions of two key factors, strain rate effect of phenolic resin and inertial stabilization of	

unit cell walls, to the compressive strength enhancement of the Nomex honeycombs under dynamic compression.	134
Fig. 4.13 Nominal compressive stress of the Nomex honeycombs as a function of $v_0 t / H$ at selected impact velocities obtained from back face and front face experimental measurements as well as FE simulations.	135
Fig. 4.14 FE study on the effect of strain rate sensitivity of the phenolic resin material at strain rates (a) 450 s^{-1} and (b) 1500 s^{-1}	136
Fig. 4.15 FE predictions of the Nomex honeycombs with initial imperfections under (a) quasi-static compression and (b) back face impact at strain rate 1500 s^{-1}	138

Fig. 5.1 (a) The in-plane sketch of the honeycomb core unit cell in sandwich beams, (b) the layer-up orientation of the laminated fibre composites and the types of face sheets. The sketch of the assembled sandwich beam is shown in (c). The co-ordinate systems associated with the beam and core are included in the figure. All dimensions are in mm. 146

Fig. 5.2 The vacuum assisted resin transfer moulding system (VA-RTM) (a) before and (b) after assembly. The sketch in (a) shows the unidirectional carbon fibre layers with orthogonal stacking. 148

Fig. 5.3 Quasi-static stress-strain relationships of the stiff and soft fibre composites under uniaxial compression and tension tests for (a) $0^\circ/90^\circ$ and (b) $\pm 45^\circ$ lay-up architecture. The measured quasi-static out-of-plane compressive response of the Nomex honeycomb core of density $\rho = 54 \text{ kg} \cdot \text{m}^{-3}$ is shown in (c). 153

Fig. 5.4 Sketch of the experimental setup for ballistic impact on monolithic and sandwich beams. All dimensions are in mm. 155

Fig. 5.5 The initial projectile velocity as a function of applied gas pressure. 155

Fig. 5.6 The history of back face deflection of the stiff monolithic beams at selected impact velocities. Time $t=0$ corresponds to the time instant when the projectile impacted on the beams. The photographic image shows the part fracture of clamped end when the impact velocity was 67 ms^{-1} 160

Fig. 5.7 Montage of the high speed photographs of the stiff monolithic beams under ballistic impact. Three different failure modes of the beams are shown in the figure. The back face view of the beam failed with perforation at the impact point is also shown in (c). 161

Fig. 5.8 The history of back face deflection of the soft monolithic beams at (a) impact velocities of 72 ms^{-1} and (b) higher impact velocities. Time $t=0$ corresponds to the time instant when the projectile impacts on the beams. 163

Fig. 5.9 Montage of the high speed photographs of the soft monolithic beams under ballistic impact. Three different failure modes of the beams are shown in the figure. 164

Fig. 5.10 The back face deflection history of the stiff part and soft part in hybrid monolithic beams at selected impact velocities. Time $t=0$ corresponds to the time instant when the projectile impacted on the beams. 166

Fig. 5.11 Montage of the high speed photographs of the hybrid monolithic beams under ballistic impact. Three different damage modes of the beams are shown in

the figure. (a) also shows the micro damage of the stiff composites and soft composites after impact, and (c) also shows the back face view of the beam failed with perforation at the impact point.....	167
Fig. 5.12 The different ranges of impact velocity regarding to the different damage modes of the stiff, soft and hybrid monolithic beams.	168
Fig. 5.13 Montage of the high speed photographs of the (a) stiff-face, (b) soft-face and (c) hybrid-face sandwich beams impacted by the spherical projectile at velocity around 73 ms^{-1} . The two red curves in (c) represent the edges of back face sheet and honeycomb core, and the front face view of hybrid-face sandwich beam at impact point are also shown in (c).	172
Fig. 5.14 Back-face deflection history of monolithic and sandwich beams at impact velocity of around 73 ms^{-1} . It should be noted that the stiff monolithic beam and hybrid-face sandwich beam are impacted at the velocity of 67 ms^{-1} and 75 ms^{-1} , respectively.	173
Fig. 5.15 Montage of the high speed photographs of the (a) stiff-face, (b) soft-face and (c) hybrid-face sandwich beams impacted by the projectile at velocity around 105 ms^{-1}	174
Fig. 5.16 Montage of the high speed photographs of the (a) stiff-face, (b) soft-face and (c) hybrid-face sandwich beams impacted by the projectile at velocity around 144 ms^{-1}	175
Fig. 5.17 Initial projectile velocity v_0 as a function of residual projectile velocity v_r . The projectile embedded in the hybrid-face sandwich beam has been highlighted in Fig. 5.13 (c). The straight dash lines are reference lines. The impact direction of projectile is along 3-axis of the coordinate system.	177
Fig. 5.18 Kinetic energy of projectile absorbed by the beams as a function of initial kinetic energy of projectile.....	180

List of Tables

Table 2.1 Typical out-of-plane compressive strengths of Nomex honeycombs under quasi-static loading.	32
Table 2.2 A summary of additive manufacturing methodologies [145].....	38
Table 3.1 Tensile properties of the SLM manufactured AlSi10Mg alloy material in different loading directions.....	69
Table 3.2 Summary of the pressurised gas used in the tests.....	75
Table 3.3 Material properties for the SLM manufactured AlSi10Mg alloy.....	81
Table 4.1 The mechanical properties of magnesium AZ61A alloy.....	116
Table 5.1 Constituent details of the monolithic and sandwich beams.....	150
Table 5.2 A summary of the experimental measurements for six types of composite beams.....	156

Chapter 1

Introduction

Background

Over the past 100 years, the manner of war has changed from large-scale conflicts (e.g. World War I and World War II) to regional conflicts (e.g. Israel-Palestine conflict) and civil wars (e.g. Iraqi Civil War). In large-scale wars, the front line of army opponents is in the way of most harm. Hence, heavy armaments such as battle planes, tanks and missiles are normally used to destroy enemy military bases, bridges, airports, railways and other important installations. These armaments cause severe damage to military targets. However, contemporary wars and attacks mainly arise from internal conflicts of a country or boundary issues between adjacent countries. The armed forces from different organizations are intertwined and dispersed in a specific area, thereby leading to both personnel armour and vehicle armour being potentially under attack. Such threats can be classified into two categories, i.e. blast impact and ballistic impact. For blast impact which is also termed as soft impact, there is a fluid-structure interaction between a shock wave and armour structures due to bombs, landmines or accidental explosions. The impulse transfers from explosives to structures through the medium of air [1, 2], water [3, 4] or sand [5, 6]. For ballistic impact which is also termed as hard impact, structures are penetrated by bullets or fragments at high velocity. Normally, effective

protection systems should meet the requirements against hard and soft impacts simultaneously. As the threats are varied and unpredictable, it is important to improve the passive protection capacity of armour types. This will require not only high-performance impact resistance, but also lightweight capabilities to ensure excellent mobility of personnel and vehicles.

Based on these requirements, the sandwich structure which consists of face sheets and a low-density thick core is a promising multi-functional design to resist high strain-rate multiple loads. This weight-saving structure has been recorded to possess better bending resistance and energy absorption capacity than the monolithic plate in dynamic impact events [7-10]. Consequently, the performance of the sandwich structure is strongly dependent on the properties of the core components and face sheets.

1.1 Sandwich cores

By separating two face sheets, the sandwich core significantly enhances the moment of inertia and stiffness of a plate. Also, the core improves the capacity of thermal and sound insulation [11, 12], and vibration dampening of the plate [13]. As the impact energy can be transformed into the compressive strain energy of the core during impact, the sandwich plate enables a reduction in potentially harmful momentum transfer in comparison to a monolithic plate [14]. Hence, it can be concluded that the sandwich core plays a far more effective role in resisting distributed-force impact (e.g. blast impact) than concentrated-force

impact (e.g. ballistic impact), with the compressive response of the core being crucial.

The design of a sandwich core needs to balance mechanical properties, weight and the overall manufacturing cost. The desired sandwich core should have high strength and low density. This can be achieved by optimizing the structure of the core or using lightweight constituent materials. In addition, the manufacturing methods employed are different for sandwich cores with different structures and materials [15]. As traditional techniques such as sheet folding/drawing, laser welding and investment casting are difficult to conduct and cost more for manufacturing cores with complex geometries, a more convenient and achievable manufacturing method needs to be developed.

In the present study, the dynamic compressive response of optimized core structures manufactured by a novel method will be addressed.

1.2 Fibre composite face sheets

The face sheets of a sandwich structure play a far more significant role in resisting impact than the core [16]. The material selection of the face sheet is a key point for improving the impact resistance of sandwich structures. Figure 1.1 shows the time line of the development of engineering materials from prehistoric times to the present day. Obviously, materials have made considerable progress over the last several thousand years from natural to synthetic types. In recent decades, polymer composites reinforced by high-performance fibres have been extensively applied in protection engineering. Examples of this include Ultra

High Molecular-weight Polyethylene (UHMWPE) fibre (Dyneema[®], Spectra[®]), aramid fibre (Kevlar[®], Twaron[®]), Poly-*p*-phenylene benzobisoxazole (PBO) fibre (Zylon[®]) and carbon fibre. Among the composites reinforced by these fibres, carbon fibre composites are the most widely used materials owing to their low cost and various fabric architectures e.g. unidirectional laminated, 2D and 3D woven.

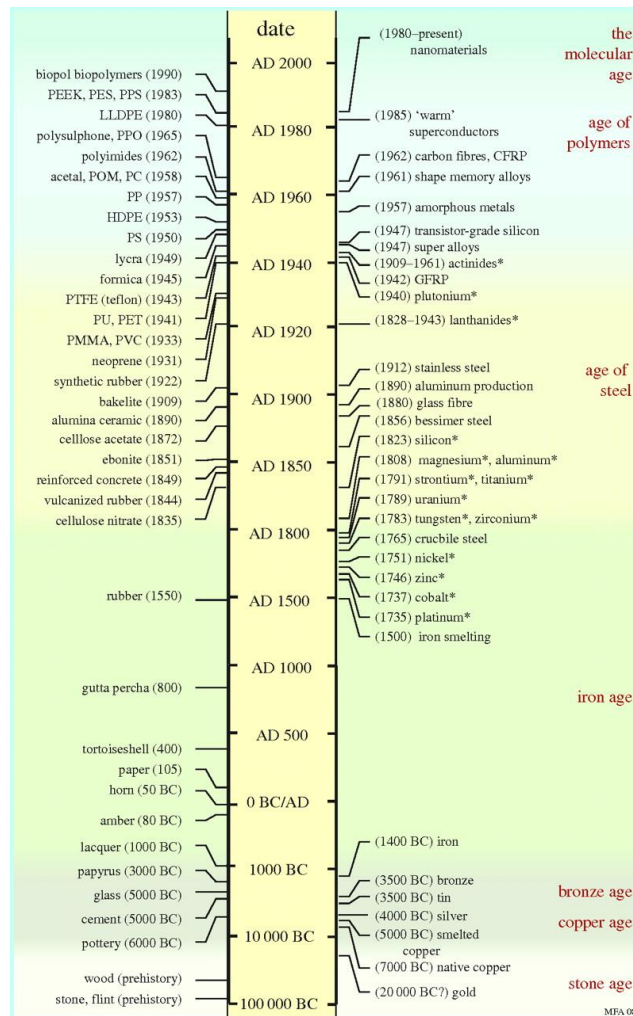


Fig. 1.1 The time line of the development of engineering materials from prehistoric times to the present day [17]. BC and AD in this figure represent before Christ and anno Domini, respectively.

Stiff fibre composites are normally used to meet the stiffness requirement of structures. However, with regards to certain structures, the requirements for stiffness and ballistic resistance are equally important, e.g. the shell of an airplane nose subject to bird collision (Fig. 1.2 (a)) and the hood of an automobile subject to bullets as well as debris impact (Fig. 1.2 (b)). These parts are not only required to sustain quasi-static loads, but they must also possess high ballistic resistance for protecting personnel and important internal components (e.g. the engine). Hence, it is imperative to develop hybrid composites which can not only guarantee structural stiffness but also resist high-velocity ballistic impact. The present work will address this issue to fill this gap.

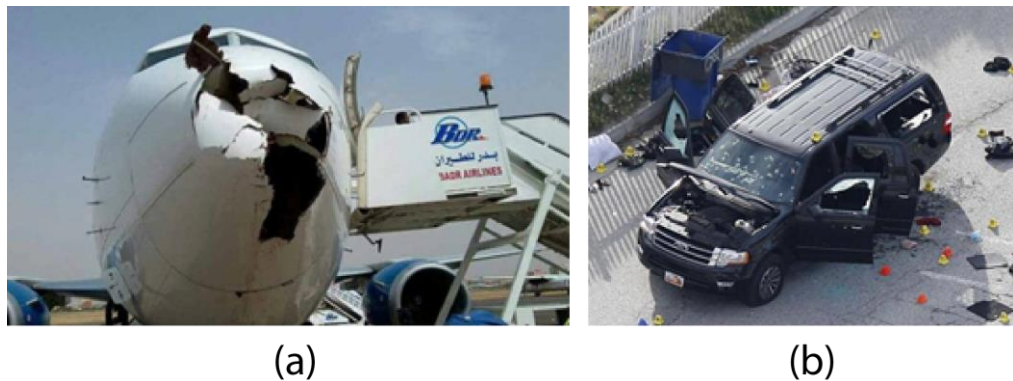


Fig. 1.2 (a) damage of an airplane nose caused by the collision with a flock of birds (Image reproduced from <https://newsavia.com/tag/badr-airlines>), (b) ballistic damage of a vehicle caused by an ISIS (Islamic State of Iraq and Syria)-inspired mass shooting (Image reproduced from <https://www.independent.co.uk/news/world/americas/san-bernardino-surge-gun-violence-since-2015-mass-shooting-a7235091.html>).

1.3 Thesis objectives

Based on the above statement, the impact resistance of a sandwich structure is dependent on the properties of both core and face sheet, and the research gaps can be summarized as follow:

- The efficient cost-saving and time-saving manufacturing methodology should be developed for fabricating the hierarchical honeycombs with complicated topologies.
- The compressive response of hierarchical honeycombs under dynamic impact has not been investigated, and the finite element modelling on the dynamic compressive response of hierarchical honeycombs has not been reported.
- The compressive response of Nomex honeycombs under high strain rate (higher than 300 s^{-1}) impact has not been investigated, and the validated finite element modelling on the dynamic compressive response of Nomex honeycombs has not been developed.
- The hybridization of fibre composites with different matrixes of different stiffness is expected to possess excellent ballistic resistance. However, the ballistic impact response of this type of hybrid composites has not been understood well.

There is an urgent need to understand damage modes and improve the impact performance of each component of sandwich structure for expanding its applicability. Both metallic hierarchical honeycombs and Nomex fibre

composite honeycombs will be investigated due to their distinct out-of-plane specific strengths and application fields.

The objectives of this thesis are presented as follows:

- To characterise the out-of-plane compressive responses of aluminium alloy hierarchical honeycombs under dynamic impact, and identify the advantages of hierarchical honeycombs relative to normal honeycombs.
- To examine the dynamic compressive response of Nomex fibre composite honeycombs at high strain rates.
- To develop novel hybrid fibre composite beams and understand the dynamic response of the beams under ballistic impact.

In order to achieve the above objectives, the following original investigations have been conducted. The first objective is achieved through the additive manufacturing of high-performance AlSi10Mg alloy honeycombs (one normal hexagonal honeycomb and two hierarchical honeycombs), and then conducting a series of dynamic compression tests on honeycombs using a steel Kolsky bar setup. A validated elastic-plastic finite element model was created for predicting the experimental response. The failure mechanisms of the honeycombs with different in-plane structures under quasi-static and dynamic compressions have been identified, providing guidance for future high-performance honeycomb design. The second objective has been achieved by experimentally and numerically investigating the compressive response of Nomex honeycombs at strain rates from quasi-static values up to 1500 s^{-1} . In the experimental

measurements, a Kolsky bar made from magnesium alloy was used to detect the low compressive force of Nomex honeycombs while improving the responsive sensitivity of the measurement setup. To characterise the failure mechanism of Nomex honeycombs accurately in the finite element simulation, the constituent materials (i.e. aramid paper and phenolic resin) were modelled separately. The novelty of this study lies in the investigation of the compressive response of Nomex honeycombs at high strain rates ranging from 300^{-1} to 1500 s^{-1} . The effects of key parameters, e.g. impact configuration, strain rate sensitivity and initial geometrical imperfections, on both the metallic hierarchical honeycombs and Nomex honeycombs have also been studied. The third objective has been achieved by hybridizing stiff and soft fibre composites to improve the integrated performance of beams under ballistic impact. The hybrid composites are motivated by the shortage of Cunniff velocity [18] and the growing demand for structures of high impact resistance. The manufacturing process, damage modes and energy absorption capacity of the hybrid composite beams have also been discussed.

1.4 Thesis outline

Chapter 2 reviews the present developments in understanding the dynamic responses of honeycomb cores and fibre composite face sheets. Based on the two components in a sandwich structure, this review is divided into two sections. The first section addresses the advantages of honeycomb core relative to other cellular cores, and the quasi-static as well as dynamic compressive responses of honeycombs. In the second section, the response of the laminated fibre

composites under ballistic impact is reviewed, including the effects of fibre reinforcements, matrix and layer-up sequence.

Chapter 3 gives an insight into the dynamic compressive response of AlSi10Mg alloy hierarchical honeycomb structures. The Selective Laser Melting (SLM) manufacturing method is detailed and the uniaxial tensile responses of the parent material in two orthogonal directions are discussed initially. Subsequently, the dynamic compressive response of hierarchical honeycombs measured by a steel Kolsky bar setup is compared with that of normal honeycombs. In order to facilitate interpreting experimental measurements and the effects of key parameters (e.g. impact method, strain rate dependency and initial geometrical imperfections), a finite element simulation is also undertaken.

Chapter 4 examines the dynamic compressive response of the other high-performance honeycombs, namely Nomex honeycombs, using a sensitive magnesium alloy Kolsky bar setup. The failure mechanisms and strength enhancement mechanisms of the honeycombs are determined via observation through SEM and validated finite element calculation, respectively. In addition, the modelling strategy and key parameter effects are also discussed in this Chapter.

Chapter 5 investigates the dynamic response of hybrid fibre reinforced composite beams subject to non-deformable spherical projectile impact. For the aim of a comprehensive comparison, six types of beams including monolithic, hybrid and sandwich beams are addressed. The Nomex honeycombs investigated in Chapter 4 are used as the core of sandwich beams. The different damage

modes, ballistic limits, energy absorption capacities of these beams are presented to explore the benefits provided by hybrid beams.

Chapter 6 summarizes the conclusions and contributions of this work, and also proposes potential topics for future work.

Chapter 2

Literature Review

2.1 Introduction

As stated in Chapter 1, the sandwich core and fibre reinforced composite face sheets play different roles in resisting dynamic impact. Hence, this review focuses on the dynamic impact responses of honeycomb cores and fibre composites, and aims to determine the research gap in this field. Based on this, the review is classified into two parts. The first part gives an overview of the compressive responses of honeycomb cores. The advantages of honeycomb structures compared to other cellular solids are identified initially, followed by the effects of topology on the quasi-static in-plane and out-of-plane compressive behaviour of honeycombs. Finally, the dynamic out-of-plane compressive response of honeycombs is also elucidated. The compressive response of high-performance honeycombs (i.e. hierarchical honeycombs and Nomex honeycombs) and the fabrication methodology are also reviewed. The second part provides an overview of the ballistic resistance of fibre composites, including the strain rate sensitivity of fibre/yarn/composites, the effect of fibre and matrix on the ballistic performance of composites, and ballistic impact resistance of hybrid fibre composites. Fig. 2.1 shows the route map that summarizes the logical sequence of this literature review.

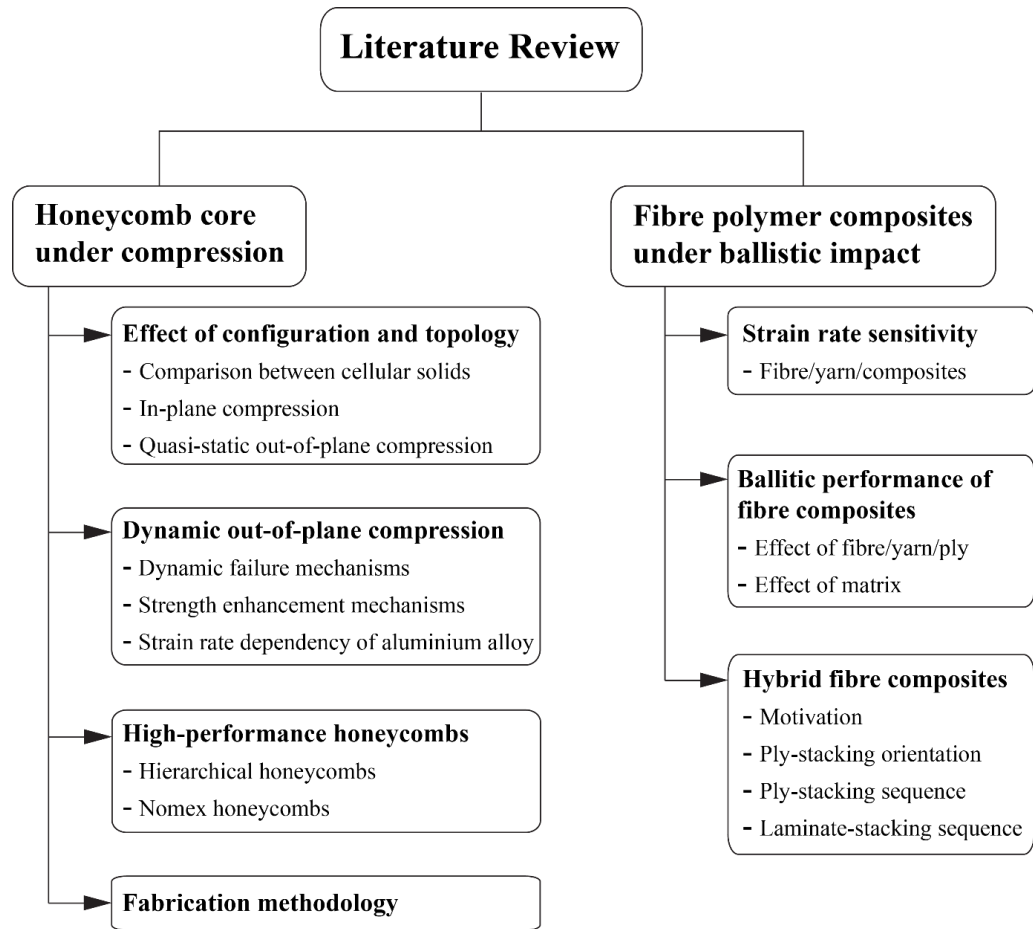


Fig. 2.1 A route map of the literature review.

2.2 Honeycomb cores

A vast majority of man-made items are motivated by prototypes in nature [8, 19, 20]. A most typical example of this is the honeycomb structure which is inspired by macro honeybee combs. With the help of an advanced electron microscopy technique, honeycomb structures can be replicated within micro and nano natural materials, like biological tissues [21] and cells [22, 23]. Since the first use of honeycomb structures by Höfler and Renyi in 1914, this type of structure has been applied in large-scale engineering designs, e.g. aerospace,

transportation, construction. In the past two decades, further applications have expanded to the fields of micro and nano fabrications as well as biomedicine [24].

Periodic honeycombs have been used to create the core of lightweight sandwich structures with high stiffness/strength-to-density ratios [8]. Compared to a monolithic plate, the honeycomb core sandwich structure has superior structural efficiency per unit area mass in terms of mitigating damage. Liu et al. [25] investigated the multifunctional performance of honeycomb core sandwich cylinders under simultaneous internal pressure and active cooling. They demonstrated that sandwich construction was more weight efficient than a monolithic structure while providing the additional benefit of an active cooling function. Hutchinson and Xue [4] demonstrated that a well-designed square honeycomb core sandwich plate could sustain significantly larger blast impulses than a solid plate of the same mass.

Honeycomb cores are composed of sheets which form the edges of unit cells, with the unit cells being repeated in two dimensions to create a cellular topology. These kinds of structures are normally subject to compressive loading along the out-of-plane direction (or height direction) of unit cells. In some conditions, honeycombs also need to resist in-plane compression and shear, out-of-plane shear, heat conduction and sound transfer. In order to meet specific requirements, the in-plane configurations of honeycomb unit cells are various, typically being triangular, square, hexagonal and circular in nature. Except for the honeycomb geometry, the constituent material is another key factor in determining the

mechanical properties of honeycombs. With the development of materials, the candidate materials used for manufacturing honeycombs have developed from original beeswax and propolis (a type of plant resin) in bee honeycombs to paper [26, 27], metal [10, 28], ceramics [29, 30] and composites [31, 32].

This section reviews the mechanical properties of honeycomb structures under quasi-static and dynamic compression. A review regarding the comparison between mechanical properties of a honeycomb topology and other cellular topologies is presented initially, followed by in-plane and out-of-plane compressive responses of normal honeycombs. The review moves on to out-of-plane compressive responses of promising hierarchical honeycombs and Nomex honeycombs, and lastly focuses on the fabrication methodologies of honeycombs.

2.2.1 Comparison between honeycombs and other cellular topologies

The structures widely used as the cores of lightweight sandwich structures can be classified into foam core and periodic cellular topology types, as shown in Fig. 2.2. Foam core (Fig. 2.2 (a)) is a kind of random cellular solid normally made from polymer [33], metal [34, 35] or ceramic materials [36, 37]. As the distribution of highly imperfect micro structures within the foams is close to uniform, the stress state of foams can be regarded as isotropic. The elastic modulus of the foams is mainly governed by the bending stiffness of cell walls, and the elastic and plastic collapses are activated by elastic buckling and plastic hinges of cell walls, respectively [38, 39]. However, in the case of distinct parent materials, the mechanical properties of foams are different. Take metal foams as

an example, the elastic modulus scales with $\bar{\rho}_f^2$, with $\bar{\rho}_f$ being the relative density of foams [35]. The compressive yield strength of foams has the following relationship with $\bar{\rho}_f$

$$\frac{\sigma_{fY}}{\sigma_Y} = \bar{\rho}_f^{2/3} \quad (2.1)$$

where σ_{fY} and σ_Y are the compressive yield strengths of cellular foams and solid materials, respectively.

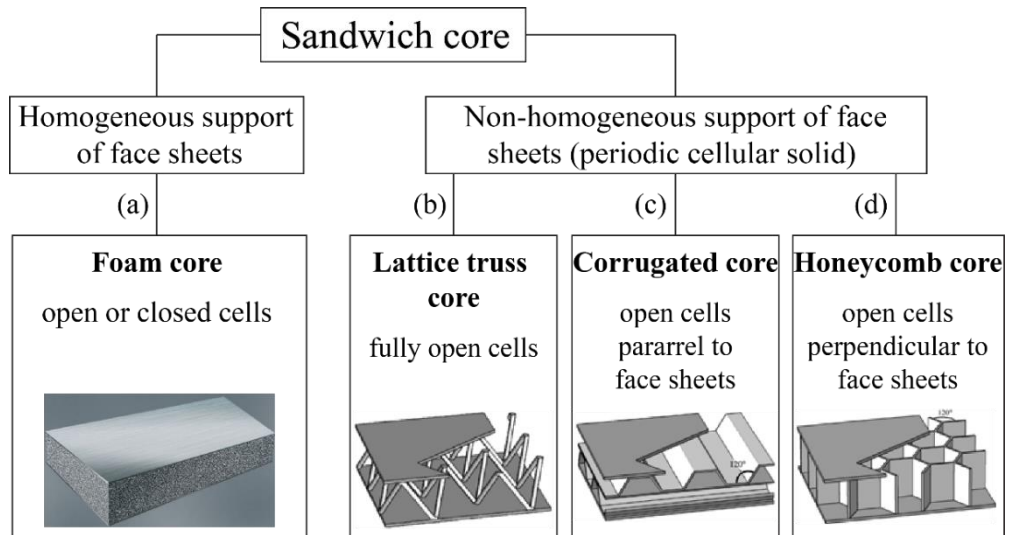


Fig. 2.2 Cellular solids used as the cores of sandwich structures.

Unlike foams, periodic cellular topologies, i.e. lattice truss topology (Fig. 2.2 (b)), corrugated topology (Fig. 2.2 (c)) and honeycomb topology (Fig. 2.2 (d)), exhibit regular configurations. However, they exhibit superior performance than foams under out-of-plane compression [40]. This is due to the fact that the cell wall stretching of periodic cellular structures along an in-plane direction plays a

significant role in resisting loading, especially for honeycombs. Alternately, the deformation of foams is mainly governed by the bending of cell walls [41].

Lattice truss structures are composed of inclined trusses with three or more trusses meeting at a common point. Hence, they can be fabricated into a variety of geometries using different topologies and angles [42, 43]. Wicks and Hutchinson [44] investigated the structural efficiency of sandwich plates with truss lattice cores and honeycomb cores under 3-point bending. They demonstrated that the minimum weight of a hexagonal honeycomb core sandwich plate was less than that of truss lattice core sandwich plates. However, as a fully open cell topology, the lattice cores exhibit better heat exchange and ventilation capacities [45, 46] than honeycombs. The corrugated structures, which are obtained by rotating honeycomb structures 90° about the horizontal axis, also exhibit these advantages as the open cells are parallel to face sheets. In addition, the corrugated structures show high shear strength that is comparable with honeycomb structures [47].

Among the three competitive cellular topologies, the honeycomb structure has the highest out-of-plane compressive strength, elastic modulus and energy absorption capacity under quasi-static loading, followed in succession by corrugated and lattice truss structures [41, 47]. This is because stress concentration at the attachment points in a lattice truss and attachment edges in corrugated structures, leads to a decrease in mechanical properties. On the other hand, both load-bearing trusses as well as walls in truss and corrugated structures are inclined. This results in the inability to provide sufficient support along the

loading direction. However, honeycombs with cells parallel to the loading direction avoid these disadvantages.

In air and water blast impact events, the sandwich structures with honeycomb or corrugated cores outperform those with lattice truss cores [10, 48-50]. This is contributed by the superior in-plane mechanical properties and stretching resistance offered by honeycomb and corrugated cores. It is interesting that the corrugated core sandwich structure is able to withstand higher blast impulses than the honeycomb core sandwich structure, although the mechanical properties of a corrugated core are inferior to those of a honeycomb core. This can be explained by the fact that the corrugated core gives rise to larger deformations and absorbs more energy under impact.

2.2.2 In-plane compressive response of honeycombs

The typical in-plane compressive stress-strain relation of honeycombs includes the following three regimes [51, 52]: a linear elastic response followed by an almost plateau stress stage, and finally a densification regime at high compressive strain. Hence, the first two regimes are close to an elastic-perfectly plastic response. Due to different in-plane configurations, loading directions and loading rates, the honeycombs exhibit different in-plane compressive behaviours. Wang et al. [53] presented a systematic comparison of in-plane compressive responses between periodic honeycombs with different unit cell types. For the in-plane configuration of honeycombs, cell walls can be regarded as truss or beam elements. Based on the distinct in-plane topologies, the honeycombs can be designed to have either a ‘bending-dominated’ deformation mode under

macroscopic in-plane stresses, such as hexagonal and square honeycombs, or a ‘stretching-dominated’ deformation mode, such as triangular, Kagome and diamond honeycombs. For bending dominated honeycombs (Fig. 2.3 (a)), hexagonal honeycombs are the most commonly used in terms of structural applications. Hexagonal honeycombs have an in-plane connectivity of three trusses meeting at each cell wall joint, with the applied load giving rise to bending moments at joints. The in-plane stiffness and strength of hexagonal honeycombs scale with $\bar{\rho}^3$ and $\bar{\rho}^2$ [17, 54], respectively, with $\bar{\rho}$ being the relative density of the honeycombs. As a result of the orthogonal in-plane configuration, hexagonal honeycombs exhibit distinct deformation modes in two orthogonal loading directions: one is cell wall crushing deformation in the centre induced by the initial biases (Fig. 2.4 (a)) [55, 56] and the other is shear crushing deformation along two main bands (X-shape) (Fig. 2.4 (b)) [56]. In addition, the deformation modes are also different under quasi-static and dynamic compressions (Fig. 2.4 (c)) [56-58]. For the stretching-dominated honeycombs (Fig. 2.3 (b)), they have higher in-plane connectivity than bending-dominated honeycombs, e.g. triangular honeycombs have a connectivity of 6 trusses meeting at each joint. The collapse load is dominated by the axial strength of cell walls due to the stretching deformation of cell walls [59], and both the in-plane stiffness and strength scale linearly with $\bar{\rho}$ [17, 54]. Hence, the stretching-dominated honeycomb structures possess greater in-plane elastic modulus and yield strength than bending-dominated honeycomb structures. However, the

stretching-dominated honeycombs suffer the disadvantage of post-yield softening behaviour owing to structural buckling [60].

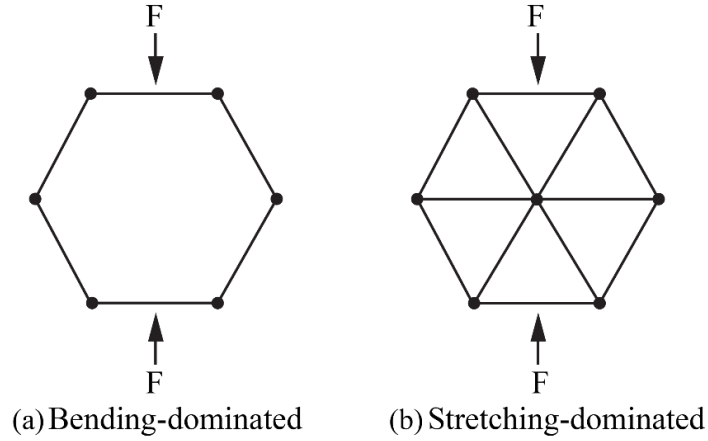


Fig. 2.3 Typical in-plane configurations of honeycombs for bending-dominated and stretching-dominated deformation modes under in-plane compression. 'F' represents 'force'.

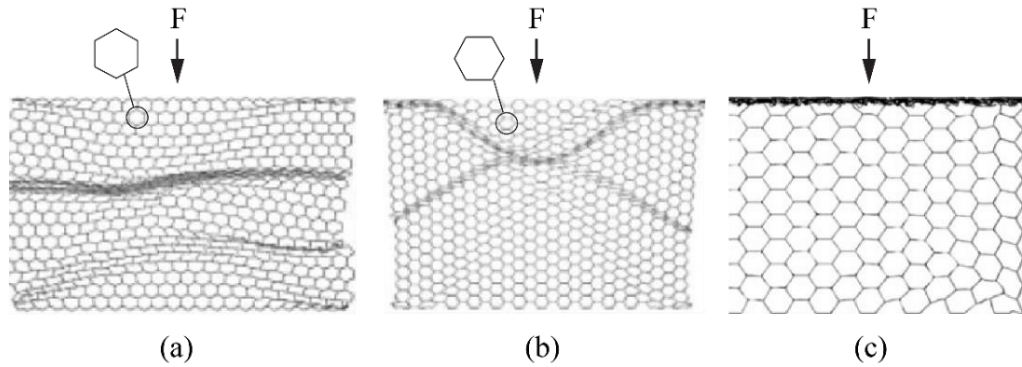


Fig. 2.4 Deformation modes of hexagonal honeycombs under (a) & (b) quasi-static compressions in two different directions [56], and (c) under dynamic compression [58]. 'F' represents force.

In addition, the deformation modes of honeycombs under in-plane tension are identical to those under in-plane compression [61].

2.2.3 Quasi-static out-of-plane compressive response of honeycombs

Compared to the in-plane compressive performance, the out-of-plane stiffness and strength of the periodic honeycombs are much greater [17, 62, 63]. For example, the out-of-plane compressive strength of aluminium hexagonal honeycombs is 2 times greater than the in-plane compressive strength [63]. This is because that the cell walls normally fail with bending under in-plane compression, whereas the cell walls are more likely to fail with parent material damage under out-of-plane compression.

The out-of-plane compressive stress-strain relation of honeycombs is a key indicator for evaluating compression resistance and energy absorption capacity. Typically, the stress versus strain response of honeycombs can be described as follows: an elastic [64] or elastic-plastic [65] response with a sharp increasing stress before achieving peak load, followed by the softening response and plateau crushing stress after peak load. The key factors that influence the out-of-plane compressive response of honeycombs include parent material, cell geometry, relative density, out-of-plane thickness and entrapped air. All of these factors will be reviewed in the following section.

Effect of parent material

Honeycombs can be made from different parent materials, e.g. metal, polymer, aramid paper, fibre composite and ceramics, exhibiting different specific out-of-plane compressive strengths. However, literature is sparse on the comparison between honeycombs with different types of materials. As for the case of

stainless steel square honeycombs [65] and fibre reinforced composite square honeycombs [31] which have the same relative density and similar heights, the out-of-plane compressive strength of stainless steel honeycombs is higher than that of fibre composite honeycombs. Moreover, the specific strength (the ratio of out-of-plane compressive strength to relative density of honeycombs) of stainless-steel honeycombs is higher than that of aluminium alloy square honeycombs [64]. The honeycombs made from brittle materials, e.g. ceramic [30], have lower failure strain than the honeycombs made from ductile materials. Progressive folding is thus observed in aluminium alloy honeycombs due to low strain hardening but not in stainless steel honeycombs due to high strain hardening.

Effect of cell geometry

Under out-of-plane compression, the lesser the amount of solid materials used in honeycombs to enclose the same pore volume, the more weight efficient the structures that can be obtained. As reviewed in Section 2.2.2, the joint connectivity of hexagonal cells is 3, whereas the joint connectivity of square and triangular cells is 4 and 6, respectively. Hence, hexagonal honeycombs are the most weight saving and stable structures for providing maximum internal space by using a minimum amount of materials, as demonstrated by Hales [66]. Square honeycombs have higher compressive strength and superior energy absorption capacity than triangular honeycombs [67]. Kim and Christensen [68] investigated the out-of-plane compressive characteristics of starcell honeycombs (Fig. 2.5) including the joint connectivity of 2 and 4 cell types. They reported

that starcell honeycombs have an almost equal out-of-plane compressive strength and shear buckling strength to hexagonal honeycomb ratio, far higher than even triangular honeycombs.

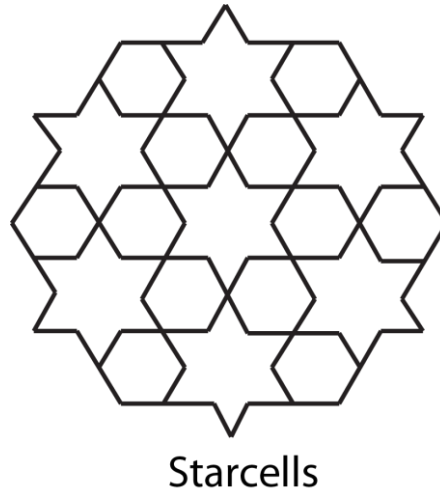


Fig. 2.5 In-plane sketch of starcell honeycombs [68].

For hexagonal honeycombs, the unit cells with a branch angle of 120° can resist the highest amount of out-of-plane compressive loading in comparison to unit cells with other branch angles [69]. In addition, the aluminium alloy honeycombs with too large or too small cell sizes may lead to the decrease of out-of-plane compressive strength [70], whereas the out-of-plane compressive strength of stainless steel honeycombs is insensitive to cell size [71].

Effect of relative density

With the increase in relative density, honeycombs exhibit higher compressive strength and experience distinct failure modes [71], such as elastic buckling to plastic buckling and finally parent material damage. For example, there is a

failure mode transition for the stainless steel honeycombs from elastic buckling to plastic buckling when the relative density of honeycombs is 0.03 [71]. However, rarely have honeycombs investigated in literature failed due to parent material damage that is an expected failure mode under out-of-plane compression.

Specifically, honeycombs made from fibre composite fail by macro-buckling at low relative density, whereas failing by micro-buckling at high relative density occurs due to the axial compression of fibres. This micro-buckling failure mode does not occur in honeycombs that are made from homogeneous metallic and ceramic materials [65].

Effect of out-of-plane thickness

Sometimes, the compressive strength of honeycombs only changes slightly even though the out-of-plane thickness has changed. This is because honeycombs with different out-of-plane thicknesses, still maintain the same failure mode. For example in the case of two Nomex honeycombs with thicknesses 14 mm and 20 mm, both have the same failure mode and similar out-of-plane compressive strengths [72]. However, the high strain-hardening stainless steel honeycombs of thickness 30 mm have higher compressive strength and more abrupt softening than those of thickness 6 mm [65]. Hence, though the out-of-plane thickness of honeycombs plays an important role in influencing the out-of-plane compressive strength of honeycombs, it is also dependent on other parameters as discussed above.

Entrapped air within cells

The entrapped air within a closed honeycomb cell is also a non-negligible factor that influences the compressive response of honeycombs. Hu et al. [73] numerically and theoretically demonstrated that honeycomb cells with and without internal pressure exhibited different deformation modes, and the plateau stress of honeycombs with internal pressure was higher than that without internal pressure. Feng et al. [74] reported that the improvement in energy absorption capacity of honeycombs was mainly due to the effect of entrapped air within the cells.

2.2.4 The dynamic out-of-plane compressive response of honeycombs and strength enhancement mechanisms

Honeycomb cores play a significant role in dissipating impulse and preventing impulse from transferring to the back face of sandwich structures. Under dynamic out-of-plane compression, the collapse behaviour of honeycomb cores is more complex than under quasi-static compression owing to shock wave propagation and the strain rate effect. The axial stress equilibrium of honeycombs from the impact end to the distal end is hard to achieve at a high velocity impact [75], and the failure modes of honeycombs observed under quasi-static compression may even change due to dynamic loading. Wadley et al. [50] argued that the hardening of stainless steel honeycombs, caused by the initial stabilization of cell walls under dynamic impulse loading, postpones the onset of wall buckling. Wall buckling and folding, activated by a plastic wave propagated from the stationary end of honeycombs, is shown in Fig. 2.6.

However, alternate findings from literature state that stainless steel honeycombs fail with torsional plastic buckling in the mid height of walls under quasi-static out-of-plane compression [71]. Tao et al. [76] investigated the out-of-plane dynamic behaviour of hexagonal thin-wall aluminium honeycombs using a Split Hopkinson Pressure Bar (SHPB) at strain rates up to 1350 s^{-1} . They found that the failure mode is plastic buckling with significant compressive strength enhancement owing to strain rate effect, and that the buckling location and sequence depends on the applied strain rate and size of honeycomb cells.

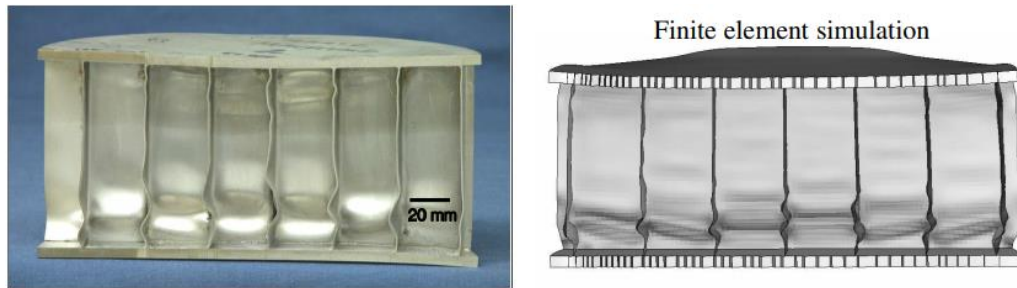


Fig. 2.6 Experimentally measured and numerically predicted deformation modes of stainless steel square honeycombs subject to impulsive loading [77].

It has been widely demonstrated that dynamic compressive strength as well as plateau crushing stress [78, 79] of honeycombs is higher than the value under quasi-static compression, respectively. Extensive studies on the strength enhancement mechanisms have been reported in the literature. Although the strain rate effect of the parent material contributes largely to the macroscopic strain rate sensitivity of honeycombs, it cannot explain the strength enhancement of honeycombs alone [80]. Harrigan et al. [81] experimentally investigated the compressive behaviour of aluminium hexagonal honeycombs with an initial

impact velocity up to 300 ms^{-1} using a Split Hopkinson Pressure Bar. They reported that the honeycombs failed with local instabilities and dynamic micro-buckling of unit cell walls, and the inertial effect of the unit cell walls contributed to the enhancement of the collapse strength as well as the crushing stress. As proposed by Su et al. [82, 83], the parent material strain-rate effect and structural inertial effect play an equally important role in the dynamic enhancement behaviour of an energy-absorbing structure. However, Tao et al. [84] concluded that the strain rate effect of the parent material plays a more significant role than the inertial effect in enhancing the plateau stress of metallic honeycombs. Xue and Hutchinson [85], using the finite element simulation method, identified that the dynamic compressive response of stainless-steel square honeycombs was governed by three distinct mechanisms: material rate sensitivity, inertial stabilization of the webs against buckling, and plastic wave propagation. This conclusion was then experimentally verified by Radford et al. [65]. Park et al. [86] investigated the compressive behaviour of carbon fibre-epoxy composite square honeycombs at strain rates up to 10^4 s^{-1} . By using a Kolsky pressure bar setup, they found that the failure mode of the honeycombs was governed by plastic buckling, and the strain rate sensitivity of the composites was due to the matrix. Unlike quasi-static compression, the strength enhancement of honeycombs caused by entrapped air under dynamic compression is negligible [80].

Although a large amount of investigations have been conducted to understand the quasi-static and dynamic mechanical properties of honeycombs, some

aspects are still unknown in terms of the development of high-performance honeycombs.

2.2.5 Strain rate sensitivity and thermal properties of aluminium alloy

Aluminium alloy has been broadly used in a variety of fields benefiting from its excellent physical and mechanical properties, e.g. corrosion resistance, high ratio of strength to density and high energy absorption capacity. Except for the quasi-static mechanical response of aluminium alloys at room temperatures, the mechanical response of aluminium alloy subject to high strain rate and high temperature is an equally important field of study in terms of widening the sphere of potential applications. The Johnson-Cook model [87], which takes high strain rate as well as high temperature into account, can explain the mechanical response of metallic materials. The model is expressed as follows:

$$\sigma = (A + B\varepsilon^n)(1 + C\ln\dot{\varepsilon}^*)(1 - T^{*m}) \quad (2.2)$$

where σ is the flow stress of material, ε is the equivalent plastic strain, $\dot{\varepsilon}^* = \dot{\varepsilon}/\dot{\varepsilon}_0$ is the dimensionless plastic strain rate with $\dot{\varepsilon}_0 = 1 \text{ s}^{-1}$ with $\dot{\varepsilon}$ and $\dot{\varepsilon}_0$ as the accumulated strain rate and reference strain rate. $T^* = (T - T_0)/(T_M - T_0)$ is the homologous temperature with T_0 and T_M as the room temperature and melting temperature of metallic material, respectively. A , B , n , C , m are the material constants in this regard. This model indicates that the flow stress of the material is enhanced by the applied high strain rate, whereas it is decreased by

thermal softening arising from high temperatures. A great number of experimental measurements [88-92] have demonstrated that the behaviour of most aluminium alloy materials can be predicted reasonably using the Johnson-Cook model. However, several types of aluminium alloys like aluminium alloy AA5083-H116 [93] and 5059-H131 [94] exhibit negative strain rate sensitivity that has not been understood well. These disagreements need to be further investigated.

2.2.6 Hierarchical honeycombs

As reviewed in Section 2.2.2, hexagonal honeycombs have a bending-dominated deformation mode under in-plane compression, with the maximum bending moment occurring at the cell wall joints. The hierarchical honeycombs are obtained by replacing the material close to wall joints with smaller-scale hexagonal honeycombs. Thus, the hierarchical honeycombs, as a new class of weight efficient structure, are expected to possess superior mechanical properties than traditional honeycombs. Periodically, hierarchical honeycombs have emerged by combining in-plane geometrical elements at different length scales, see [17, 62, 95-97] and Fig. 2.7 (a). Oftadeh et al. [98] investigated the in-plane mechanical behaviour of hierarchical honeycombs with various hierarchical levels. They found that increasing the hierarchical level can significantly increase the in-plane effective elastic modulus of the honeycomb. For example, two-scale and three-scale (the in-plane structure is the combination of hexagons at two scales and three scales, respectively) hierarchical honeycombs were 2.0 and 3.5 times respectively, stiffer than the standard hexagonal honeycomb with

identical relative density [95]. Hierarchical honeycombs also have higher in-plane collapse strength [62] and energy absorption capacity [99] than standard hexagonal honeycombs with identical relative density. With increasing hierarchical level, there is a transition of in-plane deformation mode from bending dominated to stretching dominated [100], and a transition of the in-plane failure mode from elastic buckling to plastic buckling [101]. However, increases in the in-plane collapse strength were only seen to be significant for the first, second and third levels of hierarchy; higher hierarchical level did not significantly increase performance [62]. The concept of hierarchy is also employed in the cellular solid walls as a substitute for monolithic walls, see Fig. 2.7 (b), contributing to the improvement of elastic modulus, collapse strength, fracture toughness and stability of structures [102, 103].

Based on the in-plane advantages, hierarchical honeycombs have also been seen in nature and engineering applications. Typical examples of this are the microscopic structures of bones in a body (Fig. 2.7 (c)) [104] and the Eiffel Tower (Fig. 2.7 (d)), respectively.

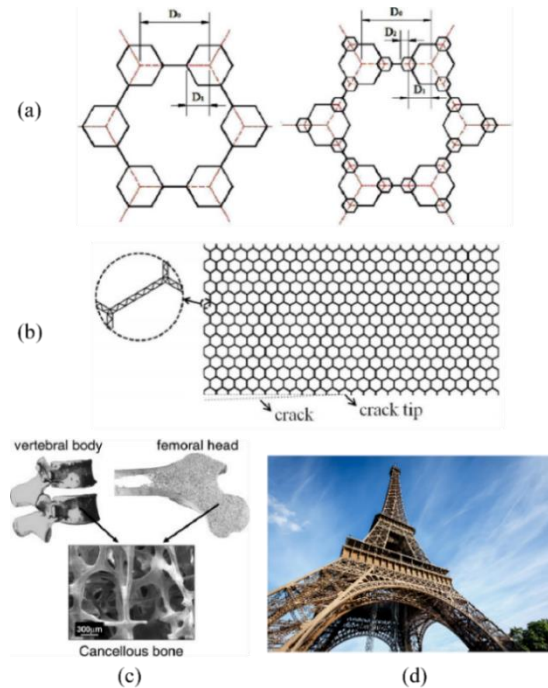


Fig. 2.7 In-plane sketch of (a) hierarchical honeycomb unit cells with first and second order hierarchy [70] and of (b) honeycombs with hierarchical walls [102], (c) macroscopic and microscopic structures of vertebra and femora [104], and (d) hierarchical structural Eiffel Tower (Image reproduced from <http://www.5857.com/wall/39264.html>).

It has been reported that the severe plastic deformation of honeycombs under out-of-plane compression is mainly concentrated on cell wall joints [67]. Hence, the energy absorption capacity of honeycombs can be expected to improve by distributing greater material and more optimized structures around the wall joints. Understanding the out-of-plane compressive behaviour of metallic hierarchical honeycombs, however, is still not well established. As the hierarchical honeycombs with complicated topologies are difficult to be manufactured, most investigations are conducted using finite element simulation methods.

Numerical investigations have suggested that hierarchical honeycombs may possess improved energy absorption capability and greater resistance to out-of-plane crushing compared to regular honeycombs [70, 105, 106]. However, the manufacturing issue of hierarchical honeycombs was not considered in the aforementioned cases. **The dynamic out-of-plane compressive responses of additively manufactured hierarchical honeycombs, by means of experimental measurement and finite element simulation, will be investigated in Chapter 3.**

2.2.7 Nomex honeycombs

Phenolic resin-impregnated aramid paper honeycombs, commercially known as Nomex[®] honeycombs, are promising cores of stiffness-dominated sandwich structures. They are largely used in aerospace applications due to their high ratios of stiffness and strength against density, respectively. The typical applications of Nomex honeycomb core sandwich structures are the doors, floors, overhead bins and wing flaps of the airplane. Commercial Nomex honeycombs are composed of aramid paper layer [107] and phenolic resin coating [108-110]. Both components have excellent performance in terms of heat, flame and corrosion resistance. These honeycombs have weak in-plane strength but excellent out-of-plane strength under compression [111], which means the out-of-plane compressive behaviour of the honeycombs plays a dominate role in obtaining specific benefits. Table 2.1 shows the quasi-static out-of-plane compressive strengths of Nomex honeycombs at different relative densities, investigated by several authors [72, 112-116]. The out-of-plane compressive

properties of the Nomex honeycombs in the present study and Table 2.1, have been compared with those of other materials in the Ashby material strength versus density map [117], see Fig. 2.8. In this figure, the solid line marked ‘Analytical’ represents the maximum theoretical strength of the carbon fibre composite square honeycombs [31]. It indicates that the ratios of compressive strength to density of Nomex honeycombs are higher than many of the existing materials and structures as well as the carbon fibre composite square honeycombs [31, 118]. Marasco et al. [119] also reported that Nomex honeycombs had higher specific strength per unit mass than composite truss cores.

Table 2.1 Typical out-of-plane compressive strengths of Nomex honeycombs under quasi-static loading.

References	Density ($\text{kg} \cdot \text{m}^{-3}$)	compressive strength (MPa)
[72]	48	1.72
[112]	48	2.92
[113]	48	2.1
	48	1.8
[114]	64	4.0
[115]	48	2.08
[116]	26	0.16
	34	0.98
	34	0.91
	46	1.90
	50	2.64
	70	5.07
	83	4.12

132

13

141

16

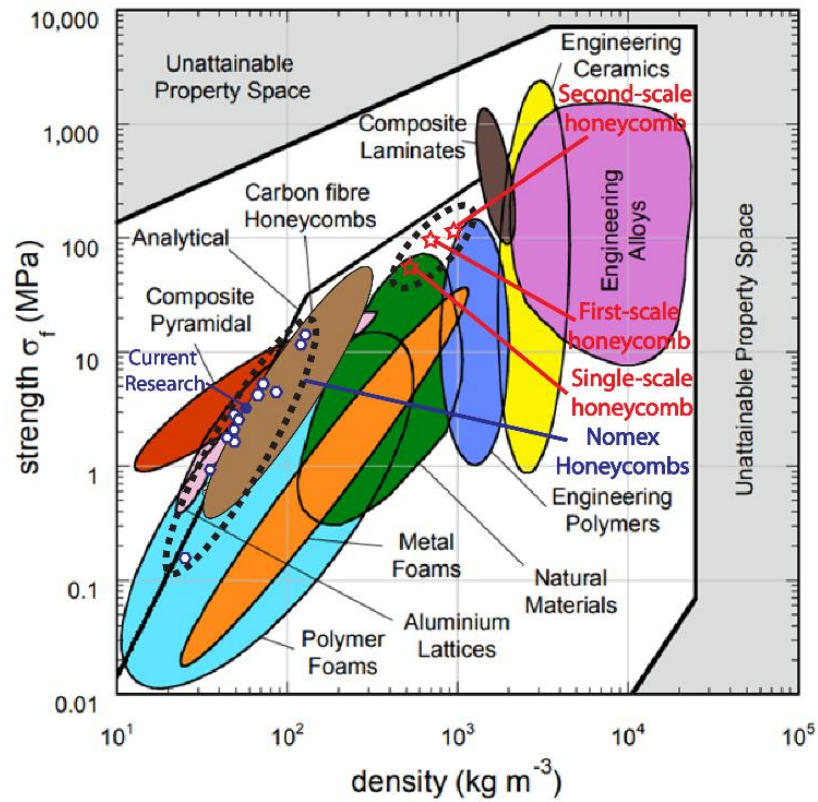


Fig. 2.8 A compressive strength versus density map for engineering materials [117], including the measured properties of Nomex honeycombs in the current study (see Chapter 4) as well as investigated by several authors [72, 112-116], these are denoted by a solid hexagon and hollow hexagons. The measured compressive strengths of the additively manufactured AlSi10Mg alloy hierarchical honeycombs investigated in Chapter 3 are also included, denoted by stars. The solid line represents the maximum theoretical strength of fibre composite square honeycombs [31], which falls into a high specific strength gap at low densities.

The quasi-static out-of-plane compressive behaviour of Nomex honeycombs has been extensively investigated. As reported in the literature [72, 116, 120-123], Nomex honeycombs behave linearly in an elastic manner prior to achieving their peak compressive strength and fail with a local fracture of the coated phenolic resin. Liu et al. [72] evaluated the effects of key material parameters on the compressive strength of Nomex honeycombs using finite element simulations. They reported that the thickness, elastic modulus as well as the compressive strength of the phenolic resin coating had positive effects on the compressive strength of the honeycombs. Liu et al. [122] also numerically demonstrated that the debonding imperfections of adhesive in the double cell walls affect the out-of-plane compressive response of the honeycombs significantly, and that debonding occurs when the strength of the adhesive decreases. Keshavanarayan and Thotakuri [123] reported that the off-axis angle decreases the out-of-plane compressive collapse strength as well as the crush stress due to structural instability.

Limited studies have been carried out on the dynamic out-of-plane compressive behaviour of Nomex honeycombs at low strain rates. Anagnostopoulos and Kim [114] experimentally investigated this behaviour using a Pendulum impactor system at strain rates up to 65 s^{-1} . They found that the mechanical performance of the Nomex honeycombs did not significantly improve with increasing strain rate. Heimbs et al. [111] studied the effect of loading rate on the out-of-plane compressive response of Nomex honeycombs with a drop weight tester. They reported that the compressive strength of the honeycombs had a 30%

enhancement for the strain rates increasing from quasi-static value to 300 s^{-1} . However, no investigation thus far has been able to provide insight into the high strain rate (more than 300 s^{-1}) compressive response of Nomex honeycombs.

This issue will be addressed in Chapter 4.

As the mechanical properties of the constituent materials are different, i.e. low-strength aramid paper is ductile but coated high-strength phenolic resin is stiff; Nomex honeycombs exhibit more complex failure modes than homogeneous metallic honeycomb structures. It is difficult to capture the failure modes of Nomex honeycombs using exclusively either experimental or numerical methods.

2.2.8 Manufacturing methodology of honeycombs

Periodic honeycombs with simple topologies can be obtained using conventional fabrication methodologies [15, 41, 124]. Hexagonal honeycombs of low relative density ($\bar{\rho} \leq 0.1$) are normally fabricated via the expanded manufacturing process, see Fig. 2.9 (a) for details. In this process, thin metal sheets or aramid paper sheets are cut into panels initially, then are bonded by adhesive at intervals and finally stretched perpendicular to the adhesive strips to create a hexagonal structure. When the relative density of the honeycombs increases, the adhesion provided by adhesive strips is insufficient to resist thick sheet stretching. Hence, alternate methodologies are required to fabricate honeycombs of high relative density. The corrugated fabrication methodology technique (Fig. 2.9 (b)), which first corrugates the sheets and then stacks them together, is suitable for

manufacturing high relative-density honeycomb structures. The stacked corrugated sheets are finally adhered to each other by strips or any welding technique. In this way, the sheet stretching process is avoided, which prevents the premature damage of honeycombs at the bonded location. For honeycombs fabricated by expanded and corrugated manufacturing processes respectively, the wall thickness along the sheet stacking direction is twice as thick as the thickness in the other direction. Alternately in comparison to hexagonal honeycombs, triangular and square honeycombs [65, 71, 125] are fabricated using the strip slotting method, as shown in Fig. 2.9 (c). As there is no bending moment that occurs during manufacturing, both honeycombs made from ductile and brittle materials [31, 126] can be produced by this approach.

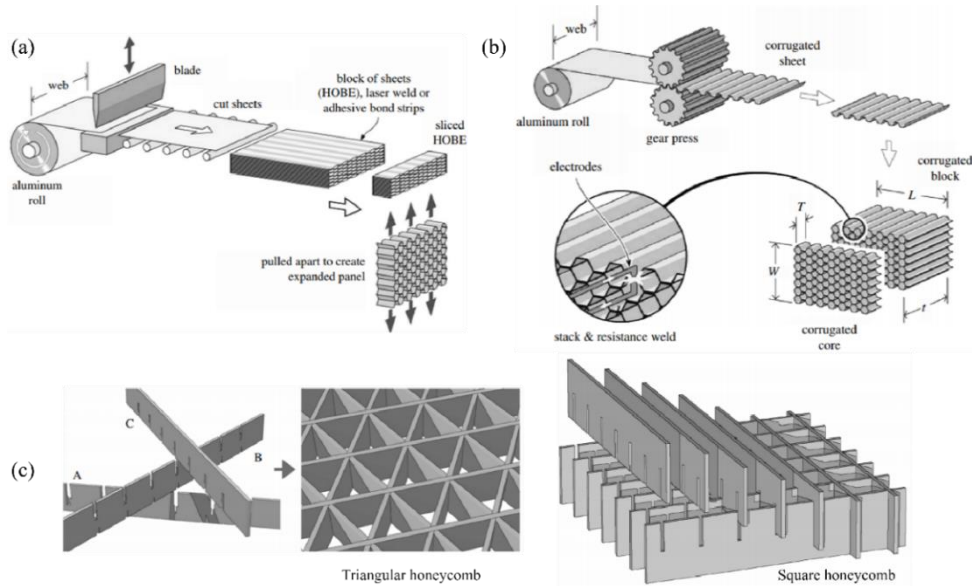


Fig. 2.9 The different methodologies and processes for manufacturing honeycomb structures [41]. (a) Expanded manufacturing process and (b) corrugated manufacturing process for fabricating hexagonal honeycombs, and (c) trip slotting methodology for fabricating triangular and square honeycombs.

However, complicated topologies such as hierarchical honeycombs, lattice structures as well as irregular topologies, are difficult to obtain by means of conventional manufacturing approaches mentioned above. This difficulty can be overcome by the additive manufacturing (AM) technique that is also commonly known as 3D printing. This technique was initially developed by Hull [127] in 1986 to be known as stereo lithography, subsequently followed by powder bed fusion [128-130] (selective laser melting (SLM) and selective laser sintering (SLS)), fused deposition modelling (FDM) [131, 132], inkjet printing [133, 134], contour crafting [135] and direct energy deposition [136]. Table 2.2 summarizes the main manufacturing methods and the corresponding parent materials, applications, advantages, disadvantages and resolution range. Additive manufacturing enables the fabrication of complex structures continuously from the microscale to the macroscale level, through stacking parent materials layer by layer. Meanwhile, it has many other advantages including freedom of design, flexibility of parent materials, parent material saving, automation and high precision. Based on these advantages, the additive manufacturing technique has promising applications in the fields of aerospace, automotive, architecture, biomedicine and art.

Depending on the parent materials used, honeycomb structures can be produced by different additive manufacturing techniques. For example, selective laser melting (SLM) and selective laser sintering (SLS) techniques, which use high-intensity laser to melt or sinter powders, are suitable for manufacturing metallic [137-139] and ceramic [140, 141] honeycombs whose parent materials have high

melting points. It should be noted that SLM manufactured structures have superior mechanical properties than SLS manufactured structures as powders can be fused fully by SLM but not by SLS [142]. Due to the low melting point, fibre reinforced polymers and pure thermoplastic polymer honeycombs can be obtained by means of fused deposition modelling or inkjet printing [96, 143]. Hence, it is possible to manufacture the desired, complex honeycombs using various parent materials. However, some disadvantages limit additive manufacturing to a wider range of applications. The distinct microstructures inside and between printed layers lead to anisotropic behaviour of structures, and the void formation between printed layers leads to poorer mechanical properties [144]. Moreover, additive manufacturing takes more time and consumes more energy than conventional manufacturing methods. Thus, it is hard to produce large-scale structures efficiently.

Table 2.2 A summary of additive manufacturing methodologies [145].

Methods	Materials	Applications	Benefits	Drawbacks	Resolution range (μm)
Fused deposition modelling	Continues filaments of thermoplastic polymers Continuous fibre-reinforced polymers	Rapid prototyping Toys advanced composite parts	Low cost High speed Simplicity	Weak mechanical properties Limited materials (only thermoplastics) Layer-by-layer finish	50-200 μm [13]
Powder bed fusion (SLS, SLM, 3DP)	Compacted fine powders Metals, alloys and limited polymers (SLS or SLM) ceramic and polymers (3DP)	Biomedical Electronics Aerospace Lightweight structures (lattices) Heat exchangers	Fine resolution High quality	Slow printing Expensive High porosity in the binder method (3DP)	80-250 μm [13]
Inkjet printing and contour crafting	A concentrated dispersion of particles in a liquid (ink or paste) Ceramic, concrete and soil	Biomedical Large structures Buildings	Ability to print large structures Quick printing	Maintaining workability Coarse resolution Lack of adhesion between layers Layer-by-layer finish	Inkjet: 5-200 μm Contour crafting: 25-40 mm [32]
Stereolithography	A resin with photo-active monomers Hybrid polymer-ceramics	Biomedical Prototyping	Fine resolution High quality	Very limited materials Slow printing Expensive	10 μm [13]
Direct energy deposition	Metals and alloys in the form of powder or wire Ceramics and polymers	Aerospace Retrofitting Repair Cladding Biomedical	Reduced manufacturing time and cost Excellent mechanical properties Controlled microstructure Accurate composition control Excellent for repair and retrofitting	Low accuracy Low surface quality Need for a dense support structure Limitation in printing complex shapes with fine details	250 μm [23]
Laminated object manufacturing	Polymer composites Ceramics Paper Metal-filled tapes Metal rolls	Paper manufacturing Foundry industries Electronics Smart structures	Reduced tooling and manufacturing time A vast range of materials Low cost Excellent for manufacturing of larger structures	Inferior surface quality and dimensional accuracy Limitation in manufacturing of complex shapes	Depends on the thickness of the laminates

2.3 Ballistic impact on laminated fibre composites

High performance fibre reinforced composite is a promising material as a face sheet for the sandwich structure in terms of resisting ballistic impact. The ballistic performance of fibre composites is influenced by the properties of fibre, matrix and fibre-matrix interface. Possible damage mechanisms and energy absorbing mechanisms for fibre composites are tensile failure of primary yarns, deformation of secondary yarns, formation of cone at the back face, interlaminar delamination, matrix cracking and friction between projectile and composites during penetration [146, 147]. Among these mechanisms, more energy is absorbed by the deformation of secondary yarns than absorbed by the tensile failure of primary yarns [146]. This is because the volume fraction of the secondary yarns is considerably higher than primary yarns. Figure 2.10 shows the cone formation at the back face of fibre composites in the ballistic impact event.

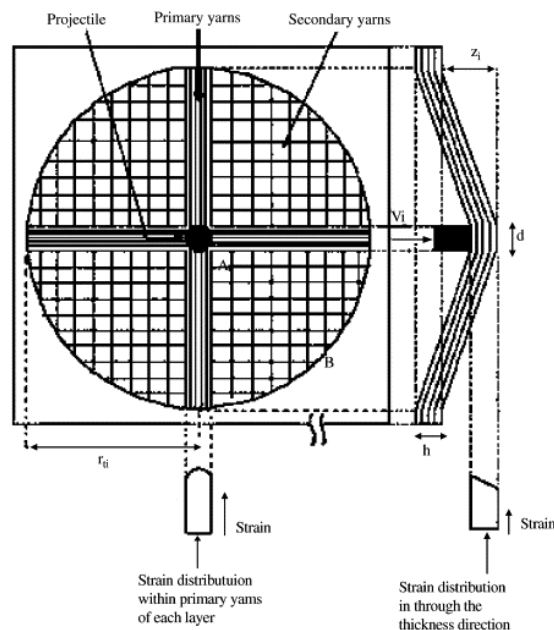


Fig. 2.10 Cone formation at the back face of fibre composites during ballistic impact [146].

Composites can be divided into cross-ply laminate and woven fabric based on the architecture of the fibre layer. Although woven fabric reduces the propensity of fibre splitting in the event of impact, it has the following adverse effects as a result of wavy fibre tows [148]:

- (1) The volume fraction of fibres is lower than that for unidirectional fibre laminates;
- (2) Due to the existence of crimps in woven fibre fabric, the velocity of longitudinal waves propagating along the fibres is reduced, thus preventing the dissipation of shock waves and leading to a smaller range of composite deformation during impact;
- (3) The strain of fibres near the impact site is amplified by shock wave reflection at the crossovers [149, 150];
- (4) The woven architecture is locked up under significant shear strain, resisting further scissoring in the fabric.

Some studies have reported that unidirectional cross-ply fibre laminates exhibit more excellent ballistic resistance than woven fabrics [151, 152]. Moreover, cross-ply fibre laminates cost less than 2D and 3D woven fabrics [153-155] due to a simpler manufacturing process.

The focus of the review in this section is on the ballistic impact response of non-woven laminated composites. The effects of fibre, matrix, hybrid composites, lay-up orientation and sequence on the ballistic resistance of composites will be discussed.

2.3.1 Strain rate dependency of fibre/yarn/composites

Generally, the quasi-static tensile response of single fibre/yarn and fibre composites is linear elastic up to failure, dominated by the elastic modulus, failure strength and failure strain [156-160]. Under ballistic impact, fibre composites undergo dynamic tension with the movement of projectiles, and the deformation rate is in the order of 10^3 s^{-1} . Hence tensile strength, failure strain and Young's modulus of the constituent materials in composites might be influenced by the strain rate.

The axial tensile responses of fibres/yarns/composites at high strain rates are normally measured by the modified Split Hopkinson Tensile Bar (SHTB). It is reported that the mechanical properties of carbon fibre composites are strain rate sensitive [157, 161]. Carbon fibre reinforcements are insensitive to the strain rate [157, 162, 163], whereas the polymer matrix showcases behaviour that is dependent upon the strain rate [164]. As the composites in $\pm 45^\circ$ layer-up are matrix shearing governed [161, 165], the tensile response of composite laminate in this orientation under dynamic tension is identical to the shear response of the matrix, which is strain rate dependent [166]. This strain rate effect on carbon fibre is different from other high performance fibres, e.g. E-glass fibre [167], aramid fibre [168] and UHMWPE fibre [169], which exhibit strain rate

sensitivity. The strain rate effects on the dynamic tensile strength of selected fibre bundles have been shown in Fig. 2.11.

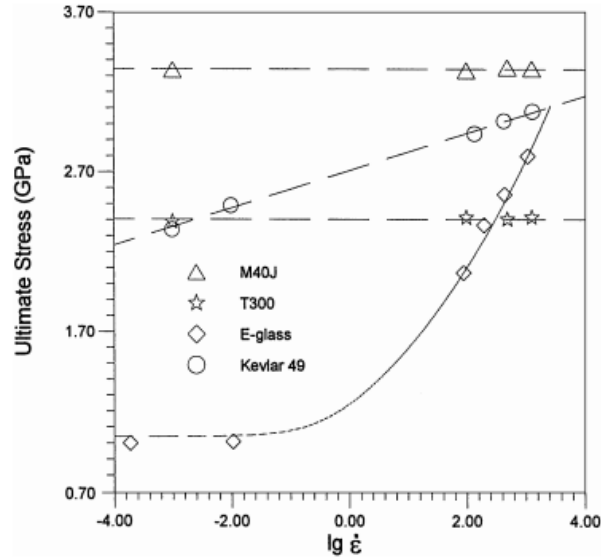


Fig. 2.11 Strain rate effect on the ultimate tensile stress of fibre bundles, including M40 J carbon fibre, T300 carbon fibre, E-glass fibre and Kevlar 49 fibre [162].

Koh et al. [170] argued that external grips in the SHTB setup used for clamping fibres introduced an impedance mismatch between grips and bars (input and output bars). This resulted in the change of the stress wave profile when the wave propagated to the interfaces of bars and grips. The error with respect to the strain obtained from the experimental measurement is therefore produced and affects the veracity of the measured Young's modulus for the fibres. Also, the fibres are prone to slip from the grips during dynamic tension. Based on these disadvantages, Russell et al. [156] developed an improved setup to investigate the dynamic tensile behaviour of UHMWPE yarn, as shown in Fig. 2.12. The

force of the yarn was detected by the force sensors, and strain of the yarn was obtained via post processing high speed photographic images using digital image correlation (DIC). This test methodology gave rise to an error only within 0.1% regarding the strain of the yarn. The proposed setup can be used for correcting the published data for other fibres.

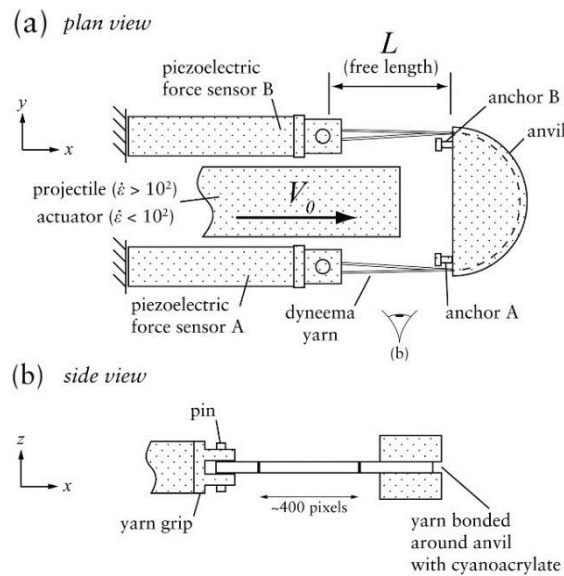


Fig. 2.12 Improved experimental setup for measuring the high strain-rate tensile response of ultra high molecular-weight polyethylene (UHMWPE) yarn [156].

2.3.2 Ballistic performance of yarn/single fibre ply

The performance of individual fibre/yarn against ballistic impact plays an important role in the global performance of fibre composites. When the two-end clamped fibre/yarn is transversely impacted at the centre by a projectile, two types of stress wave can be obtained, i.e. longitudinal wave and transverse wave [171]. The longitudinal wave propagates symmetrically outward along the fibre

axis from the impact point, and the tensile strain is zero before the propagation of this wave. The longitudinal wave speed c_f can be calculated as follows:

$$c_f = \sqrt{\frac{E_f}{\rho_f}} \quad (2.3)$$

where E_f and ρ_f are the elastic modulus and density of the fibre, respectively.

With the propagation of the longitudinal wave, the fibre material flows to the impact point giving rise to a tensile strain in the fibre.

The transverse wave is behind the longitudinal wave, propagating at approximately one order of magnitude lower speed than the longitudinal wave.

The velocity of the transverse wave u is calculated based on the following relation

$$u = c_f \sqrt{\varepsilon_f \sqrt{\varepsilon_f (1 + \varepsilon_f)} - \varepsilon_f} \quad (2.4)$$

where ε_f is the failure strain of fibres. It can be concluded that a higher longitudinal wave speed of the fibre contributes to higher transverse wave speed; this has also been confirmed by Song et al. [172]. Hence, a fibre of high elastic modulus and low density can benefit the ballistic resistance of fibre yarn.

Two different types of failure mode are identified in polymeric yarns, i.e. a transverse stress wave mode at low impact velocity and a shear mode at high impact velocity [173], as shown in Fig. 2.13. There is a critical impact energy

for the transition between the two failure modes, and the value for UHMWPE yarn (higher elastic modulus and lower density) is higher than that for aramid yarn, verifying the conclusion from Eq. (2.4).

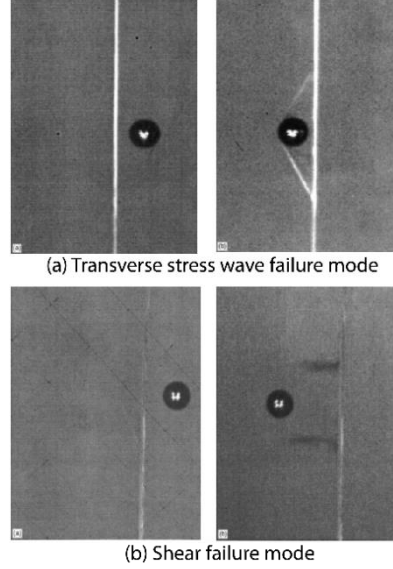


Fig. 2.13 Two distinct failure modes observed in polymeric fibres under projectile ballistic impact [173].

For the single fibre ply, the theoretical speed of the longitudinal wave calculated by Eq. (2.3) only considers the role of fibre, and is higher than the experimental value [174, 175]. This is due to the fact that the matrix applied in the ply decreases the wave speed. The matrix influence can be taken into account using the following equation

$$c_{fc} = \sqrt{\frac{1}{M_0} \frac{dF_T}{d\varepsilon_f}} \quad (2.5)$$

where c_{fc} is the longitudinal wave speed in the fibre composites ply, M_0 is the mass per unit length (in kg/m), F_T and ε_f are the tensile force (in N) and strain of fibre ply, respectively. $dF_T/d\varepsilon_f$ of the fibre ply is the same as that of the fibre/yarn, whereas the M_0 of the fibre ply is more than that of the fibre/yarn due to the addition of the matrix. Hence, the wave speed propagating in the fibre ply is slower than that in the fibre/yarn.

2.3.3 Effect of fibres

In ballistic impact events, the energy absorption capacity of composites is dominated by the mechanical properties of the fibres. It is commonly accepted that there are two fibre properties affecting the ballistic protection of composites. One property is the specific strain energy of fibres, which is related to the tensile strength and ductility of the fibre [176, 177]. Higher ballistic resistance of composites can be achieved by increasing the fibre toughness, rather than the tensile strength or failure strain alone. The other fibre property is the longitudinal wave speed propagating in the fibres, which is related to the Young's modulus and density of fibres [172]. Higher fibre elastic modulus and lower fibre density give rise to higher fibre wave speed, contributing to a wider range of energy transmissibility and composite deformation. Figure 2.14 shows a map of specific energy absorption as a function of longitudinal wave speed for different fibres in term of ballistic protection [178].

Cunniff [18] reported that the ballistic limit of fibre composites scales linearly with the Cunniff velocity c^* of the fibre filament and can be defined as follows:

$$c^* = \left(\frac{\sigma_f \epsilon_f}{2\rho_f} \sqrt{\frac{E_f}{\rho_f}} \right)^{1/3} \quad (2.6)$$

where σ_f is the tensile strength of fibres. Thus, the Cunniff velocity c^* is

governed by two material properties, i.e. specific strain energy $\frac{\sigma_f \epsilon_f}{2\rho_f}$ and

longitudinal wave speed $\sqrt{\frac{E_f}{\rho_f}}$ of fibres. The contours of the theoretical Cunniff

velocity have been plotted in Fig. 2.14. This approach provides guidance to determine fibre composites of high ballistic limits. However, it fails to predict the ballistic limit velocity of UHMWPE fibre composites.

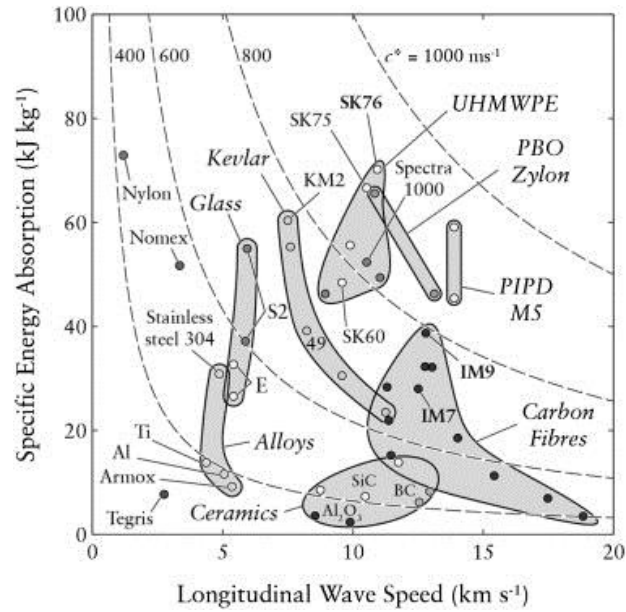


Fig. 2.14 A map showing specific energy absorption as a function of longitudinal wave speed of fibres and other high-performance materials [178]. The contours of Cunniff velocity c^* are also included in the map. ‘PBO’ and ‘PIPD’ in this figure represent Poly-p-phenylene benzobisoxazole and polyhydroquinone-diimidazopyridine, respectively.

2.3.4 Effect of matrix

Based on the review in Section 2.3.3, Cunniff velocity c^* only considers the effect of fibres on the ballistic resistance of composites, but does not provide an insight into the effect of the matrix. The matrix has the responsibility of bonding fibre reinforcements together and transferring stress between them [179]. It can also protect fibres against abrasion as well as adverse environmental impacts. Though the matrix itself is unable to dissipate a large amount of energy, it has an indirect effect on the energy absorption of fibre composites by influencing the number of broken fibres. Lee et al. [180] argued that, in ballistic impact events, the yarns in dry fabric fracture individually along the periphery of the projectile, whereas the yarns in fibre composites fracture under the constraint of the matrix which reduces the mobility of yarns. In addition, the properties of the matrix also influences the bond strength between fibres and matrix, further influencing the ballistic protection of composites [177]. The high-strength matrix enhances the bonding of the fibre-matrix interface which results in brittle failure and weak energy absorption capacity of composites during ballistic impact. The low-strength matrix leads to significant delamination between layers but better energy absorption capacity of composites. The medium-strength

matrix behaves best in composites that give rise to progressive failure under ballistic impact. The matrix of medium strength not only ensures excellent integrity of fibre composites but also contributes to the relatively high energy absorption capacity of composites.

Normally, matrices of most fibre composites, e.g. carbon fibre, glass fibre and aramid fibre composites, become stiff after curing. However, the matrices of a small portion of composites, such as UHMWPE fibre composites [181], are made from soft materials that have low stiffness and shear strength. Each layer of soft matrix composites can be folded with a high curvature [182], and fibres microbuckle without matrix failure. This behaviour is different from that of stiff matrix composites where fibre microbuckling occurs in combination with matrix fracture [86, 183, 184].

It has been proven that when compared to a soft matrix, a stiff matrix results in a smaller range of deformation and more significant stress concentration in composites, leading to less fibre failure [180]. Ruijter et al. [185] analysed the effect of matrix stiffness, at a range of 10^{-4} to 4 GPa, on the ballistic impact protection of Twaron[®] fabric composites via a series of experimental measurements. They found that the ballistic limit of the composites strongly depended on the matrix stiffness, and the highest ballistic limit was achieved when the matrix stiffness was in the range of 0.01 to 1 GPa. Beyond this stiffness range, the matrix restricted the deformation of fibres and was unable to provide enough adhesion for bonding the fibres together below this range. Karthikeyan et al. [178, 186] investigated the effect of shear strength on the ballistic response

of laminated composites, including cured and prepreg carbon fibre composites, and polyethylene fibre composites (Dyneema[®]) with two different matrices. They reported that the Cunniff velocity fails to characterise the ballistic resistance of fibre composites, and the ballistic limit of the composites increases with a decrease in shear strength of the matrix. The matrix with a lower shear strength was able to relieve a larger stress gradient for the cross-ply laminates through interlaminar shearing [187], thus a wider range of membrane stretching in each layer was achieved, ensuring higher impact force resistance.

Under high-velocity impact (the initial velocity of a projectile is greater than 10 m/s), the ballistic response of composites is governed by the stress wave propagation relation [188]. As the response time of stiff composites is short during ballistic impact, the localised damage in stiff composites is significant. However, due to the flexible contact between projectile and soft composites, the response time may increase and stress concentration may reduce. The failure mechanisms of the two types of composites are different [178, 189]. For stiff composites, the projectile first comminutes the fibres within the front face, then penetrates the composite plate. Significant bending of the plate around the impact site leads to the tensile fracture of fibres. For soft composites, the material fails progressively due to the tensile rupture of fibres; the sketch of this penetration mechanism is shown in Fig. 2.15.

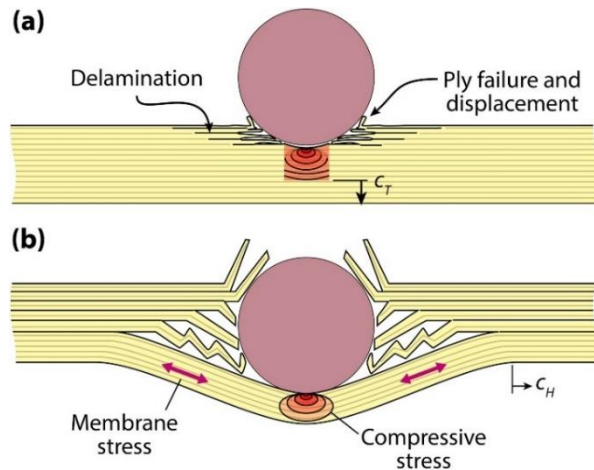


Fig. 2.15 The penetration mechanism of the edge clamped ultra high molecular-weight polyethylene (UHMWPE) fibre composite laminate [189].

2.3.5 Ballistic resistance of hybrid fibre composite laminates

Although composites with a soft matrix exhibit higher ballistic limits than those with stiff matrices, they have a limited ability to resist the out-of-plane bending force as well as in-plane compression. The concept of a hybrid material, which is the combination of two or more different materials and superimposes the properties of each material to be multifunctional in nature, was first proposed by Ashby and Brechet [117]. Figure 2.16 shows the possible outcomes of hybridizing two component materials, M_1 and M_2 . The hybrid design provides a property optimization that cannot be achieved with a single material, and is expected to retain the desirable attributes of both materials. Hybrid A, combining the best properties and diminishing the disadvantages of both components, is highly desired, e.g. steel coated by zinc has the capacity to resist loads as well as corrosion. Hybrid B, the arithmetic average of the properties of two constituent components, is most commonly obtained. The authors [117] argue

that the axial elastic modulus of unidirectional fibre composites is close to the rule of mixtures.

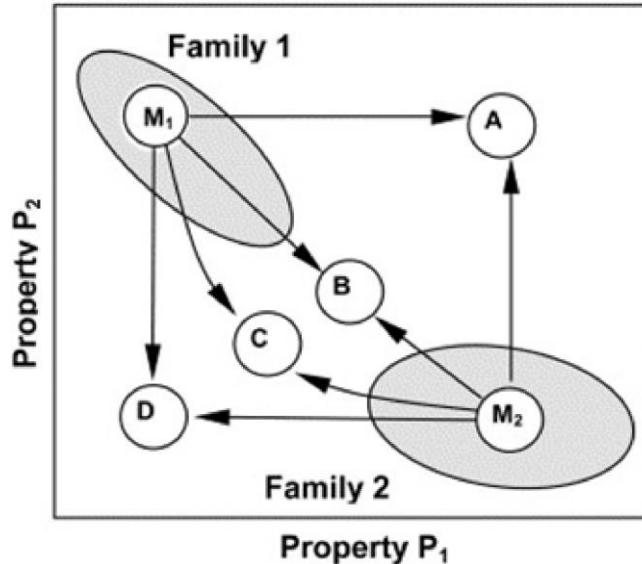


Fig. 2.16 The possible outcomes of hybridization based on two component materials [117]. M₁ and M₂ represent the original materials, A, B, C and D represent the possible outcomes after the hybridization of A and B.

Hybrid fibre composites are the combinations of two or more fibre reinforced composites. Fibres of different scales and properties can toughen the hybrid composite system, delaying and stabilizing the development of matrix cracks [190]. The quasi-static mechanical properties of the hybrid composites depend on many factors, e.g. fibre properties, matrix properties, volume fraction of fibres, ply-stacking orientation (see Section 2.3.6) and ply-stacking sequence (see Section 2.3.7). For example, kapok-glass hybrid fibre polymer composites exhibit higher flexural and compressive strengths than sisal/glass and kapok/sisal fibre composites. In addition, the inter-laminar shear strength of

kapok/glass hybrid composites decreases as the ratio of kapok fibres to glass fibres increases [191].

It has been demonstrated that hybrid composite laminates reinforced by two or more types of fibres can offer better ballistic performance than laminates reinforced by only one type of fibre. As reported by Pandya et al. [192], ballistic limit can be increased by adding E-glass fibre layers to carbon fibre composites when compared to single carbon fibre composites with the same thickness. Bandaru et al. [193] investigated the different combinations of fibre reinforced composites, namely glass fibre, carbon fibre and Kevlar fibre composites. They found that Kevlar composite laminate hybridized with carbon fibre layer possesses the better ballistic resistance than the other combinations, and the ballistic performance can be improved by increasing the toughness of composites. Similar results were reported by Dorey et al. [194]. They proved that carbon/Kevlar hybrid fibre composites had better ballistic resistance and higher residual strengths (i.e. tensile, flexural and inter-laminar shear strengths) than composites reinforced by carbon fibres or Kevlar fibres alone, though the quasi-static mechanical properties of the hybrid composites were not as good as those of the carbon fibre composites.

Except for the above investigations into thermoset matrix hybrid composites, thermoplastic matrix hybrid composites have also been studied in terms of ballistic resistance. The investigation into the penetration behaviour of the hybrid laminate, which is a combination of two different types of UHMWPE fibre composites with a soft matrix (Dyneema[®]), was conducted by O'Masta et

al. [189]. It was reported that the interaction between the two composite components was negligible for ballistic impact events, i.e. the ballistic resistance of the hybrid composites was dominated by the properties of the front-face and back-face composites independently before and after penetration of the front-face composites, respectively.

The existing hybrid fibre composite materials are mainly due to the hybridization of two types of fibre reinforcements while maintaining the same matrix properties. There are rare reports about hybrid fibre composites with two different types of matrices. Larsson et al. [195] gave an insight into ballistic protection and post-impact mechanical properties of the hybrid system combining carbon fibre composites with soft polyethylene fibre composites via a series of tests. They concluded that the choice of fibres is the primary focus in order to obtain expected characteristics of composites. Wang et al. [196] investigated the effect of a ductile matrix as well as a brittle matrix on the impact toughness of fibre composites using a low-velocity drop weight setup. They found that the ductile thermoplastic polyphenylene sulphide (PPS) matrix enhanced the impact toughness of composites compared to the brittle epoxy matrix. In addition, the weak interface between the PPS matrix laminate and epoxy matrix laminate resulted in debonding that dissipated considerable energy. As the energy absorbed by laminate debonding has not been quantified yet, it is a future topic of research within this field. Also, the failure modes as well as energy absorption capacity of the hybrid materials containing soft and stiff composites are still unclear. **We will address the issue in Chapter 5.**

2.3.6 Effect of ply-stacking orientation

Stacking orientation of unidirectional fibre plies in polymer composites plays an important role in resisting ballistic impact. Changing the layer stacking orientation is an effective way to improve the impact resistance while keeping the same areal density of composites. It should be noted that different stacking orientations result in different in-plane mechanical properties for composites [178, 197].

Within the family of stiff matrix composite laminates, quasi-isotropic $[(0^\circ/90^\circ)/(\pm 45^\circ)]_n$ fibre composites laminates exhibit higher peak force and smaller back face deformation than cross-ply $[0^\circ/90^\circ]_n$ and angle-ply $[\pm 45^\circ]_n$ laminates subject to low-velocity drop weight impact [198]. Moreover, lower angle mismatch between adjacent plies contributes towards less significant inter-laminar and localized damage in composites. In all composite laminates which do not exhibit a quasi-isotropic stacking architecture, the $[0^\circ/90^\circ]_n$ cross-ply laminates provide the best impact resistance [199].

For soft matrix composites, the effect of layer-up orientation ($[0^\circ/90^\circ]_n$ cross-ply, traditional $[(0^\circ/90^\circ)/(\pm 45^\circ)]_n$ quasi-isotropic and helicoidal quasi-isotropic) on the impact resistance of UHMWPE fibre composites, was investigated by Hazzard et al. [197] using the similar drop weight test setup. The helicoidal quasi-isotropic fibre orientation had smaller angle mismatch than the traditional quasi-isotropic fibre orientation, as shown in Fig. 2.17. They highlighted that the quasi-isotropic architectures reduce on average a 43% back face deflection compared to cross-ply architectures. However, the ballistic limit of the cross-ply

architectures was higher than those of the quasi-isotropic architectures [148]. The quasi-isotropic laminates involved a wider range of deformed area than the cross-ply laminates [200]. The deformation of the cross-ply laminates was governed by a large amount of in-plane shear, whereas the deformation of the quasi-isotropic laminates was dominated by a large amount of panel buckling that was initiated from the impact site. In addition, the angle mismatch of the quasi-isotropic laminates is insignificant in terms of impact resistance.

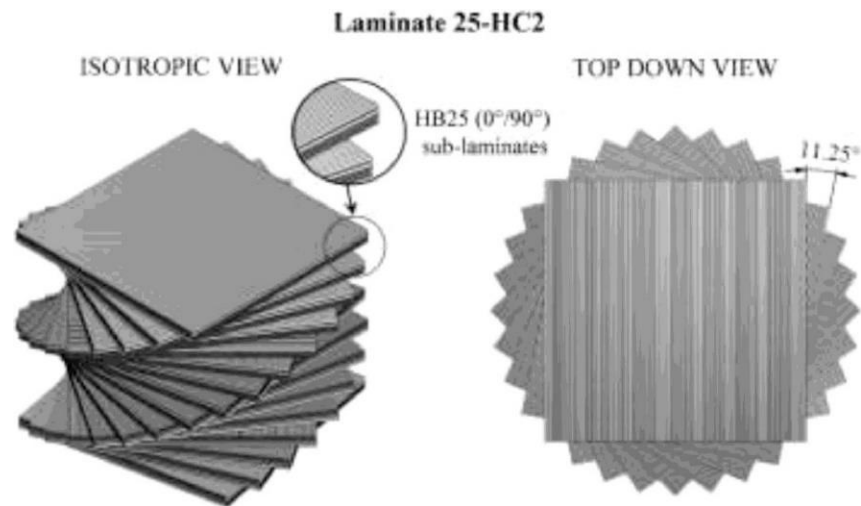


Fig. 2.17 A schematic of helicoidal quasi-isotropic stacking architecture with an angle mismatch of 11.25° [197].

2.3.7 Effect of ply-stacking sequence and laminate-stacking sequence

As there are distinct types of fibre composites in a hybrid composite laminate, it is necessary to determine which type of ply or laminate should be used as the front impact face. Similar to ply-stacking orientation as reviewed in Section 2.3.6, the optimization of ply-stacking sequences can also improve the ballistic protection of laminated composites effectively [201].

Regarding laminate-stacking sequence, no reference can be found for hybrid fibre composites combining stiff matrix and soft matrix composites. However, for hybrid composites only with a stiff matrix, the ballistic performance is improved by placing stiff fibre (say carbon fibre) laminate and tough fibre (say Kevlar fibre) laminate at the front face and rear face, respectively [193, 204]. For hybrid composites only with a soft matrix, the penetration resistance might benefit from the optimized stacking sequence of laminates, i.e. the laminate with higher compressive strength and lower impedance as a front face, and the laminate with higher tensile strength as a back face [189].

During ballistic impact, the stiff plate prevents ductile deformation and failure of the soft plate when the soft plate is located at the front face. This may lead to a plugging failure of the front soft plate rather than ductile failure. Hence, less plastic deformation occurs and a lower ballistic limit is achieved for this type of laminate-stacking sequence in hybrid composites [205, 206]. In addition, the front-face soft laminate in hybrid composites can be regarded as back supported by the back-face stiff plate. Attwood et al. [207] reported that both critical velocities to initiate failure and complete penetration of the back supported fibre composites were lower than that for free standing composites, as shown in Fig. 2.19. This is due to the fact that the interfacial pressure is determined by the relative velocity between projectile and composites, and a higher relative velocity gives rise to a higher pressure.

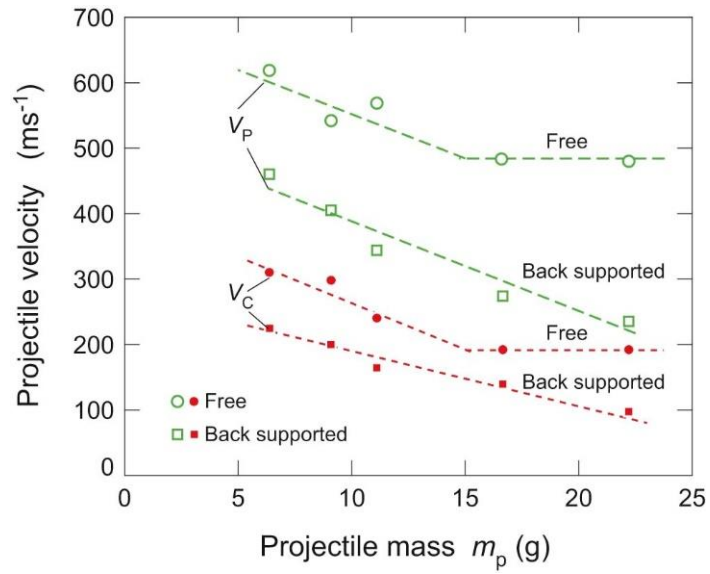


Fig. 2.19 Summary of the measured critical velocity v_c to initiate failure and ballistic limit v_p of the UHMWPE fibre composites for back supported and free standing cases [207].

Chapter 3

Compressive Response of AlSi10Mg Alloy Hierarchical Honeycombs

Abstract

Periodic honeycombs have been used for their high strength, low weight and multifunctionality. The quasi-static and dynamic compressive responses of three types of additively manufactured AlSi10Mg honeycomb structures, specifically a single-scale honeycomb and two hierarchical honeycombs with two and three levels of hierarchy, respectively, have been investigated using experimental measurement and finite element (FE) simulation. The validated FE simulation has been employed to investigate the effects of relative density of the honeycombs and the key experimental parameters. The following failure modes of the three types of honeycombs have been observed both under quasi-static and dynamic compression: (1) the single-scale honeycomb experienced a transition of failure mechanism from local plastic buckling of walls to local damage of the parent material without buckling with the increase of the relative density of the honeycomb; (2) the hierarchical honeycombs all failed with parent material damage without buckling at different relative densities. For both quasi-static and dynamic compression, the hierarchical honeycombs offer higher peak nominal wall stresses compared to the single-scale honeycomb at low relative density of $\bar{\rho} = 0.19$; the difference is diminished as relative density increases,

i.e. the three types of honeycombs can achieve similar peak wall stresses when $\bar{\rho} \geq 0.26$. Numerical results have suggested the hierarchical honeycombs can offer better energy absorption capacity than the single-scale honeycomb. The two-scale and three-scale hierarchical honeycombs achieved similar peak nominal wall stresses for both quasi-static and dynamic compression, which may suggest that the structural performance under out-of-plane compression is not sensitive to the hierarchical architecture. This work suggests that the structural advantage of hierarchical honeycombs can be utilised to develop high performance lightweight structural components.

3.1 Introduction

With the increase in terrorist attacks and regional conflicts, it is an urgent need to design high-performance honeycomb cores to improve the impact resistance of sandwich structures. The hierarchical honeycombs, as optimized structures based on traditional honeycombs in nature, exhibit exceptional out-of-plane mechanical performance [105, 106, 138, 208, 209]. Though only a limited amount of studies on the out-of-plane compressive response of hierarchical honeycombs have been done numerically under dynamic impact, experimental measurements are rarely available in the literature.

Honeycombs with simple topologies can be obtained via conventional manufacturing techniques [41]. However, conventional manufacturing approaches may encounter difficulty in manufacturing hierarchical honeycombs owing to their complex 3D geometries. The Selective Laser Melting (SLM)

manufacturing technique can be employed to overcome this difficulty. In addition, due to the anisotropic feature of SLM manufactured structures [210], an effective finite element methodology is also required to predict the compressive response of hierarchical honeycombs manufactured by the SLM manufacturing method.

The aim of this chapter is to gain insight into the behaviour of SLM manufactured metallic hierarchical honeycombs under static and high strain rate out-of-plane compressions, through both experimental measurements and numerical simulations. The failure modes of honeycombs with different relative densities are also characterized to identify the advantages of hierarchical honeycombs. The outcome will provide the basis for the development of high performance, SLM manufactured, hierarchical honeycomb core sandwich structures. The outline of the chapter is as follows. First, the geometries and manufacturing methodology for three types of honeycombs, and the mechanical properties of parent materials are presented. Second, the quasi-static and dynamic experimental protocols are explained, and the methodology for finite element simulation is also described. Finally, the experimental and simulation results are discussed, including the dynamic compressive strengths and failure modes of hierarchical honeycombs, and also the influence of key parameters on the compressive response of honeycombs.

3.2 Material and manufacturing

3.2.1 The honeycomb specimens

Three types of cylindrical honeycomb specimens were manufactured using Selective Laser Melting (SLM): single-scale, two-scale and three-scale. The schematics and photographs of the honeycombs are shown in Figs. 3.1 (a) and (b), respectively. They were made from AlSi10Mg alloy. Throughout this chapter, the global coordinates are defined with the 3-axis aligned with the out-of-plane direction of the honeycombs, and the 1-axis and 2-axis representing the in-plane directions of the honeycombs. Each specimen has an out-of-plane (3-axis direction) thickness of $H = 40$ mm and an in-plane (1-2 plane) maximum diameter of $D = 27$ mm. The single-scale honeycomb specimen consists of 7 identical curved hexagonal unit cells with average wall thickness 0.675 mm, radius of each curved side 4.8 mm and central angle 60° . The design is motivated by Bauer, et al. [211], which demonstrates that it can offer higher specific compressive strength than typical, straight-walled honeycomb geometry.

Hierarchical honeycombs have been reported to have good in-plane mechanical behaviour, as reviewed in Chapter 2. To examine their out-of-plane compressive behaviour, the two-scale and three-scale honeycombs were designed with in-plane hierarchical structures, i.e. combination of hexagons at two length scales for the two-scale honeycomb, and at three length scales for the three-scale honeycomb. The two-scale honeycomb consists of 7 large hexagons, each containing 6 smaller hexagons. The average wall thickness of the specimens is

0.66 mm, and the lengths of each side of the larger and smaller hexagons are 4.64 mm and 1.66 mm, respectively. The three-scale honeycomb consists of 7 large hexagons, each containing 6 medium-sized hexagons, which in turn contains 3 small hexagons. The average wall thickness of the sample is 0.55 mm, and the lengths of each side of the largest, medium-sized and smallest hexagons are 4.34 mm, 1.27 mm and 0.77 mm, respectively. The geometrical parameters of these honeycombs are mainly determined by the limitation of the manufacturing facility. The relative density $\bar{\rho}$ of the honeycombs is defined as $\bar{\rho} = \rho / \rho_0$, where ρ and ρ_0 denote the densities of the honeycombs and the AlSi10Mg alloy parent material, respectively. The measured relative densities of the honeycombs were 0.19, 0.26 and 0.35 for single-scale, two-scale and three-scale honeycombs, respectively.

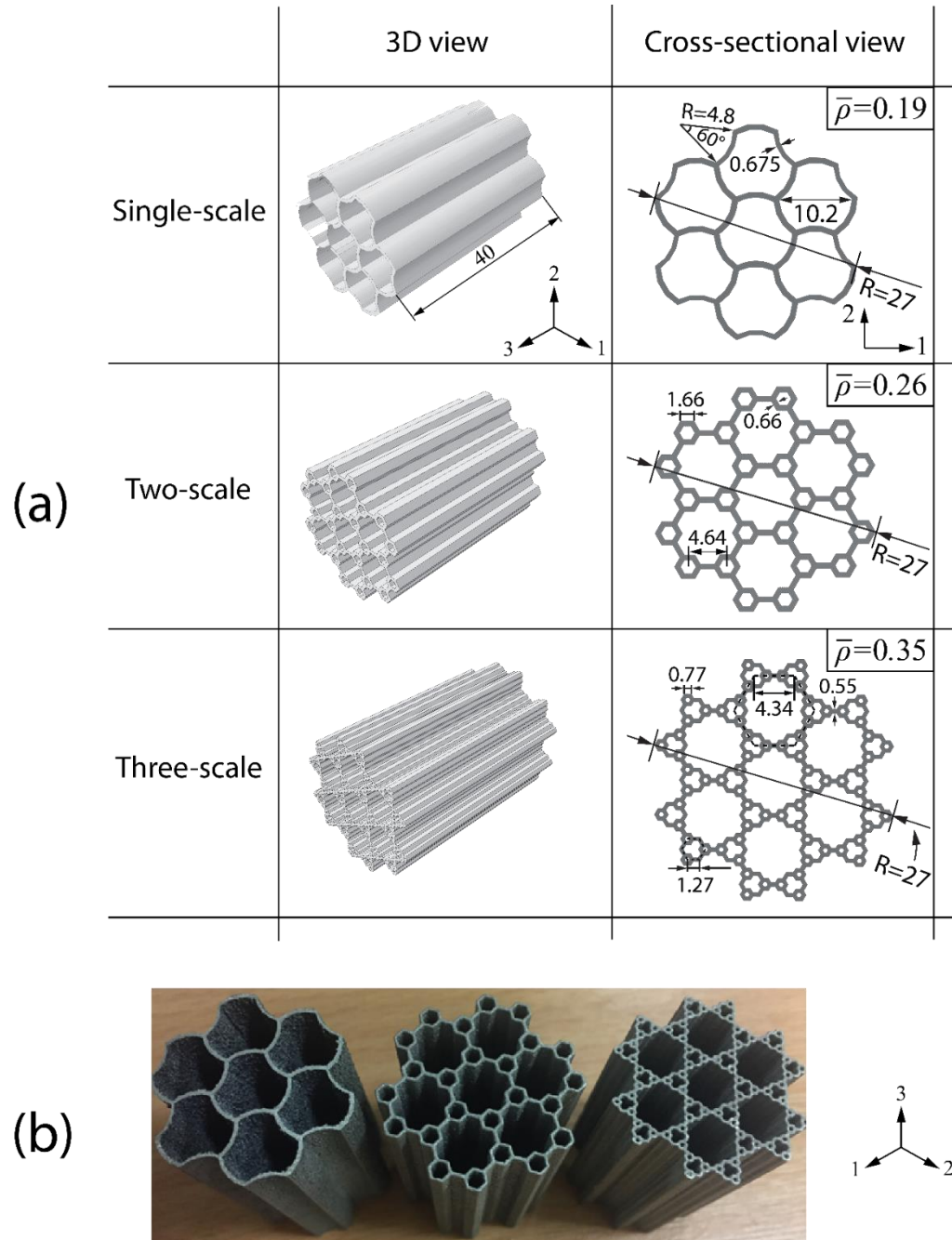


Fig. 3.1 (a) Sketch and (b) photograph of the Selective Laser Melting (SLM) manufactured single-scale, two-scale and three-scale honeycombs. All dimensions are in mm.

3.2.2 Manufacturing

A Renishaw AM250 SLM machine (Fig. 3.2 (a)) was used to fabricate the specimens. This machine has a build volume of $250 \times 250 \times 300 \text{ mm}^3$, and enables to provide fast additive manufacturing for metal components by melting the flexible fine metal powder such as AlSi10Mg, AlSi12, commercially pure titanium (cp-Ti), Ti-6Al-4V, Ti-6Al-7Nb, H13 tool steel, cobalt-chrome alloy and Inconel 718 alloy. The external powder hopper with valve interlock system allows additional powder to be added during fabrication. The hopper can also be removed for cleaning or be replaced by another hopper with different powder materials. Hence, flexible materials can be interchanged on the platform.

The fabricated specimens include dog-bone shaped coupons and the honeycombs. The principal chemical composition of the constituent material of AlSi10Mg powder (supplied by TLS Technik GmbH) contains Al 88.9 wt%, Si 10.7 wt%, Mg 0.5 wt%, and the powder particle size ranges from $15 \text{ }\mu\text{m}$ to $110 \text{ }\mu\text{m}$. The optimised manufacturing process described in [212, 213] was adopted to produce parent material with minimal porosity. The Renishaw AM250 SLM machine was equipped with an Yb fibre laser of power 200 W and wavelength 1070 nm. The laser scan strategy was chessboard and a scan speed of approximately 570 mm/s was achieved by employing $80 \text{ }\mu\text{m}$ point distance and $140 \text{ }\mu\text{s}$ exposure time. The hatch spacing was $130 \text{ }\mu\text{m}$. During processing, the AlSi10Mg powder was deposited in $25 \text{ }\mu\text{m}$ layers with the temperature of the build platform being held at $180 \text{ }^\circ\text{C}$. The specimens were manufactured under argon atmosphere with an oxygen content less than 0.09%. The microstructure

of the SLM manufactured AlSi10Mg alloy is shown in Fig. 3.2 (b) [214]. This SLM manufactured material with fine microstructure and characteristic melt pools is transformed into a coarser-grained material, where the Si has agglomerated into equiaxed particles. Both the honeycombs and dog-bone shaped coupons were manufactured with their 3-axis along the SLM build direction. The mechanical behaviour of the AlSi10Mg alloy parent material was characterised via coupon tensile tests, as described next.

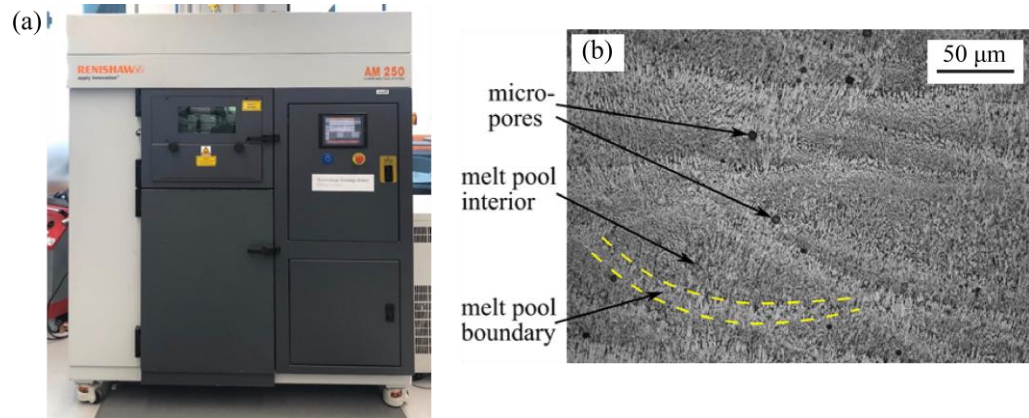


Fig. 3.2 (a) The Renishaw AM250 SLM machine used for manufacturing AlSi10Mg alloy dog-bone coupons and honeycombs, (b) the microstructure of the SLM manufactured AlSi10Mg alloy material [214].

3.2.3 Quasi-static tensile coupon tests of parent material

In order to characterise the mechanical behaviour of the AlSi10Mg alloy parent material, quasi-static uniaxial tensile tests were conducted using dog-bone shaped coupons and the method described by ASTM standard E8/E8M [215]. The SLM manufactured test coupons had dimensions of gauge length 45 mm and diameter 9 mm, as schematically shown in the insert of Fig. 3.3. The coupons

were manufactured with the longitudinal direction of the coupons aligned with either the 3-axis or 1-axis (2-axis). The uniaxial tensile stress was measured using an Instron 5581 screw-driven testing machine at a constant extension rate of 0.5 mm/min with three repeats. A single Stingray F146B Firewire Camera video gauge was used to measure the corresponding nominal strain. Figure 3.3 shows the measured nominal stress-strain relationship using the coupons with longitudinal direction aligned with either 3-axis or 1-axis (which was shown experimentally to be nearly identical to the 2-axis). Only one stress-strain curve in each loading direction is shown in this figure for clarity. The key tensile properties of the SLM manufactured AlSi10Mg alloy material both in 3-axis and 1-axis (or 2-axis) loading directions are summarized in Table 3.1. It indicates that the deviation is in the range of 10% for each tensile property, the repeatability of measurements can be therefore guaranteed. For both alignments, the coupons exhibit the same linear elastic behaviour of average Young's modulus $E_{\text{SLM}} = 69.3 \text{ GPa}$ and yield strength $\sigma_y^{\text{SLM}} = 160 \text{ MPa}$. However, the coupon aligned with the 1-axis (or 2-axis) has higher tensile strength and greater ductility than that aligned with the 3-axis. Similar anisotropy has been seen in previous work and ascribed to microstructural anisotropy stemming from the asymmetric heat flux during laser irradiation and cooling and from the preference for flaws to align in this direction [216].

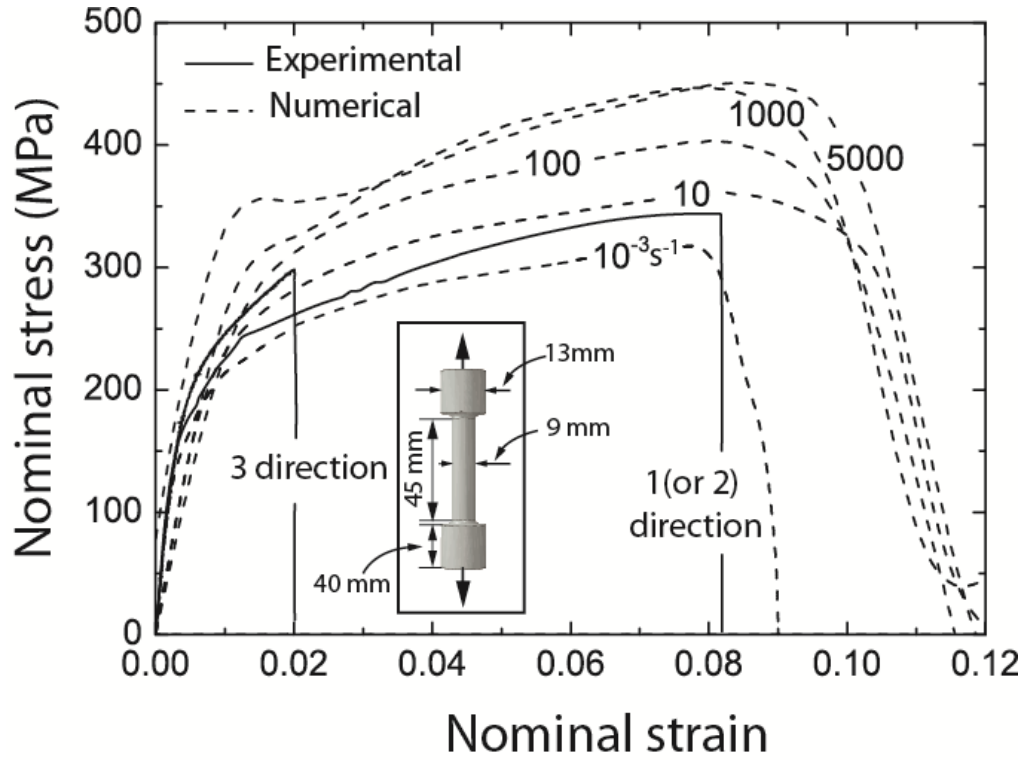


Fig. 3.3 The uniaxial tensile stress - strain relation of AlSi10Mg alloy at selected strain rates. The insert shows the geometry of the dog-bone coupon employed in the quasi-static test.

Table 3. 1 Tensile properties of the SLM manufactured AlSi10Mg alloy material in different loading directions.

Mechanical properties	Ultimate tensile strength (MPa)	Young's modulus (GPa)	Elongation (%)
1 (or 2) direction	345 ± 12	69.3 ± 5	8 ± 0.7
3 direction	298 ± 8	69.8 ± 4	2 ± 0.2

The experimental results shown in Fig. 3.3 are comparable to those of the SLM manufactured AlSi10Mg alloy reported by Kempen et al. [217]. The tensile

behaviour in the 1-axis or 2-axis direction was nearly identical to that of the cast AlSi10Mg alloy as reported by Manfredi et al. [218] and Joseph et al. [219]. In Section 3.4, the uniaxial tensile test results are used as the input of the constitutive model employed in the finite element simulations.

3.3 Experimental protocols for honeycombs under compression

3.3.1 Quasi-static compression testing

Quasi-static out-of-plane compression tests were conducted using an Instron® 5581 screw-driven testing machine with a constant displacement rate of 2 mm/min in the out-of-plane direction, see Fig. 3.4 (a). The compressive force F and the vertical displacement δ of the crosshead were both directly measured from the testing machine. The nominal compressive strain and stress of the honeycomb specimens were calculated as $\varepsilon = \delta / H$ and $\sigma = F / A_0$, respectively, where H is the original height of the honeycomb specimens and A_0 the original cross-sectional area of the honeycomb specimens, $A_0 = \pi D^2 / 4$. The averaged wall stress $\bar{\sigma}$ of the honeycomb specimens can be related to nominal compressive stress σ and relative density $\bar{\rho}$ via $\bar{\sigma} = \sigma / \bar{\rho}$. A Phantom Mercury HS V12.1 high-speed camera was used to record the compressive deformation histories of the honeycombs.

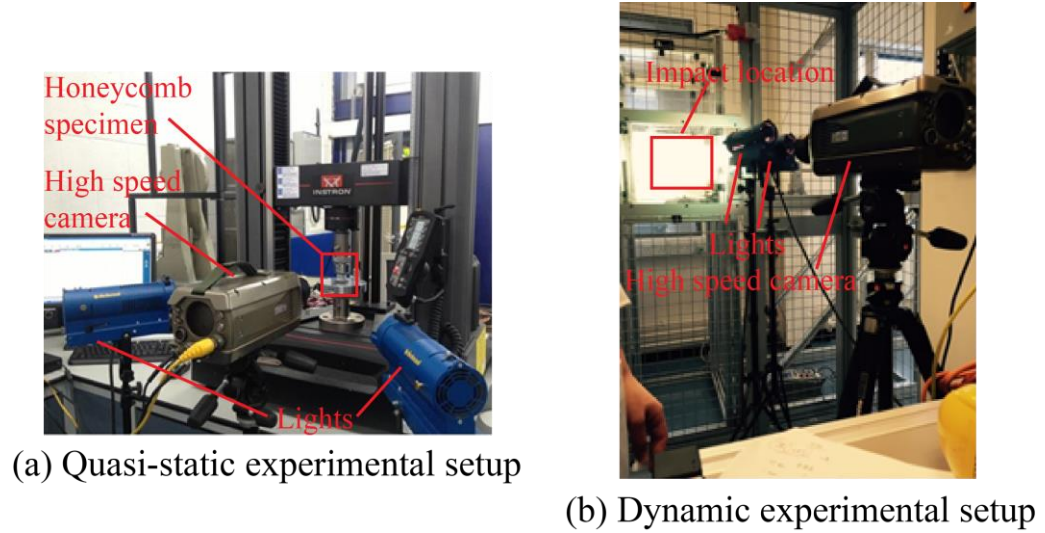


Fig. 3.4 (a) Quasi-static and (b) dynamic experimental setups for determining the compressive response of additively manufactured AlSi10Mg alloy honeycombs.

3.3.2 Dynamic compressive testing

Figure 3.4 (b) shows the photograph of the experimental setup under dynamic compression. The dynamic out-of-plane compressive response of the SLM manufactured honeycombs was measured via a set of direct impact tests with a strain-gauged Kolsky pressure bar setup [65, 220, 221], as shown in Fig. 3.5. Two types of impact test were employed: back face and front face impact. For back face impact, a striker was accelerated through the gun barrel to impact a sample adhered to the impact end of the Kolsky bar with a low strength adhesive material, see Fig. 3.5 (a). For front face impact, a sample adhered to a striker was fired from the gun barrel to impact on the Kolsky bar, see Fig. 3.5 (b). The two impact tests result in different plastic shock wave propagation within a sample with the directions of the plastic shock wave propagation being opposite. As

demonstrated in Section 3.7.1, the compressive strengths of honeycomb specimens achieved in both back face impact and front face impact are nearly identical for lower velocity impact ($v_0 \leq 20 \text{ ms}^{-1}$) and higher velocity impact ($v_0 \geq 80 \text{ ms}^{-1}$). The Kolsky bar was positioned 110 mm from the open end of the gas gun, and had a diameter identical to that of the strikers, $D_s = 27.5 \text{ mm}$, and a length of 1.8 m. Both the Kolsky bar and the strikers were made from M300 maraging steel with elastic modulus of $E_s = 210 \text{ GPa}$ and yield strength of $\sigma_s = 1900 \text{ MPa}$. The Kolsky bar was supported by four knife-edge friction-reducing Nylatron bearings and momentum was resisted at the distal end by an ACE MA 4757M self-adjusting shock absorber. Two diametrically opposite $120 \text{ } \Omega$ TML foil strain gauges of gauge length 1 mm in a half-Wheatstone bridge were located at the centre point. The stress history was recorded as a voltage change from the strain gauges, which was amplified by a Vishay 2310B signal conditioning amplifier system before being recorded on an Instek GDS-1052-U 50 MHz 2-channel Digital Oscilloscope. During signal capture, the two strain gauges on diametrically opposite sides allowed for a simple check of any bending in the Kolsky bar. Bending will produce sinusoidal oscillations with a π phase-difference between the two channels. If negligible bending was recorded during the testing, the results were accepted and the average value of the two gauges was taken.

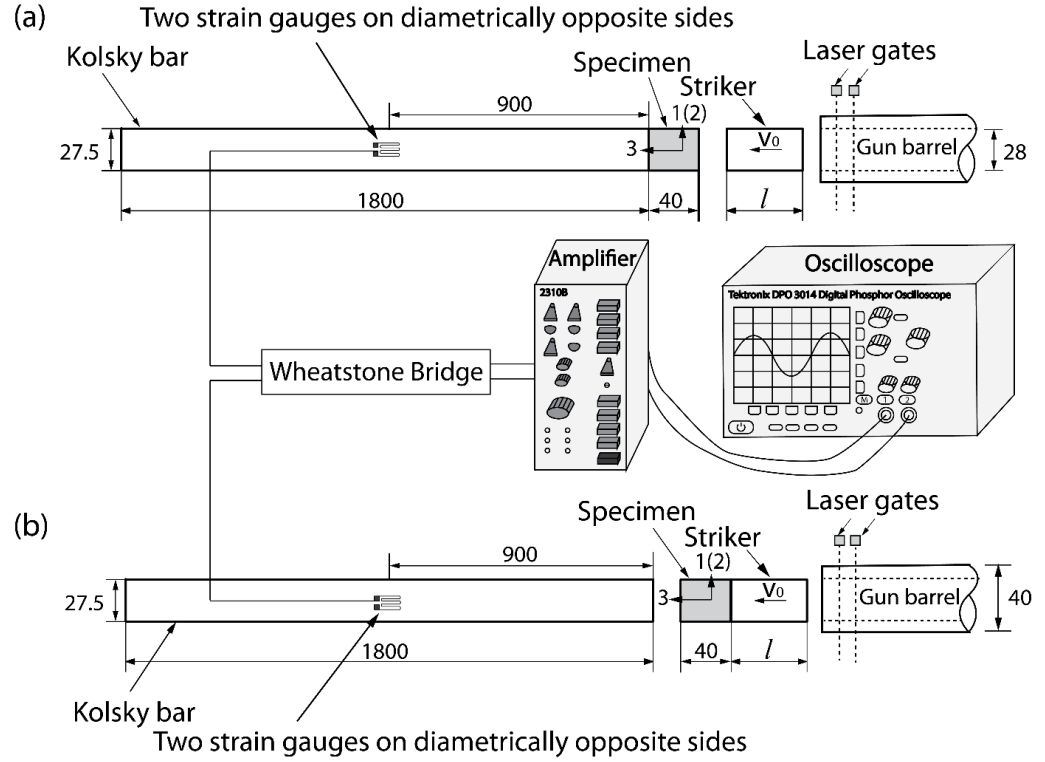


Fig. 3.5 Sketches of Kolsky bar setup employed in the experiment, (a) back face and (b) front face impact. All dimensions are in mm.

Three cylindrical strikers of different masses were employed in the impact tests in order to achieve different striker velocities: a small striker of length $l = 0.02$ m and mass $M = 0.0927$ kg was used at velocity range of $80 \leq v_0 \leq 120 \text{ ms}^{-1}$, an intermediate striker of length $l = 0.1$ m and mass $M = 0.463$ kg for velocity range $20 \leq v_0 \leq 80 \text{ ms}^{-1}$, and a larger striker of length $l = 0.5$ m and mass $M = 2.3$ kg for lower velocity range $2.5 \leq v_0 \leq 20 \text{ ms}^{-1}$. The effect of the striker mass on the compressive response of the honeycombs has been examined in Section 3.7.2. It is demonstrated that

(i) the striker is subjected to significant deceleration during the lower velocity impact events, e.g. $v_0 \leq 20 \text{ ms}^{-1}$, and the deceleration is negligible for the higher velocity impact events, e.g. $v_0 \geq 80 \text{ ms}^{-1}$, and (ii) striker mass has a small effect on the compressive response of honeycombs under the higher velocity impact. The striker was accelerated using a pressurised gas gun of barrel length 3.5 m, internal diameter of 28 mm and outer diameter of 40 mm. Either compressed air (for lower velocity) or pressurised nitrogen (for higher velocity) was used to propel the striker to velocities in the range $2.5 \leq v_0 \leq 120 \text{ ms}^{-1}$. The velocities of strikers with different masses related to the applied pressurised gas are summarized in Table 3.2. Striker velocity was measured using two laser gates located at the open end of the gas gun barrel and confirmed with the high speed camera. High-speed photography was also employed to measure the response of the honeycomb specimens; the frame rate was typically 70,000 fps and the exposure time was 8 μs . As indicated in Section 3.6.1, the force equilibrium in honeycomb specimen was achieved within the time scale of the dynamic compression.

Table 3. 2 Summary of the pressurised gas used in the tests.

Striker mass (kg)	Pressure (Bar)	Approximate velocity of striker (m/s)
2.3	2	10
2.3	5	20
0.463	25	80
0.0927	4	80
0.0927	10	120

Calibration of the Kolsky pressure bar was conducted via direct impact of a striker (without a specimen) to trigger a stress wave within the bar. Fig. 3.6 shows the measured time history of stress with a striker velocity of $v_0 = 4.1 \text{ ms}^{-1}$. The measurement is compared with the predicted stress based on 1D elastic wave theory, which states that the axial stress within the steel bar can be calculated as $\sigma_c = \rho_s c_s v_0 / 2 = 77.1 \text{ MPa}$ with ρ_s and c_s as the steel bar density and longitudinal elastic wave speed, respectively. The average stress throughout the calibration test was measured as 78.5 MPa, within 2% of the prediction. The longitudinal elastic wave speed, c_s , was measured experimentally as the time taken for the reflection of the compressive wave from the distal end of the Kolsky bar returning to the strain gauges as a tensile wave. It was measured as 4865 ms^{-1} , giving a time taken for reflection and thus complication of the stress measurement as $370 \text{ }\mu\text{s}$.

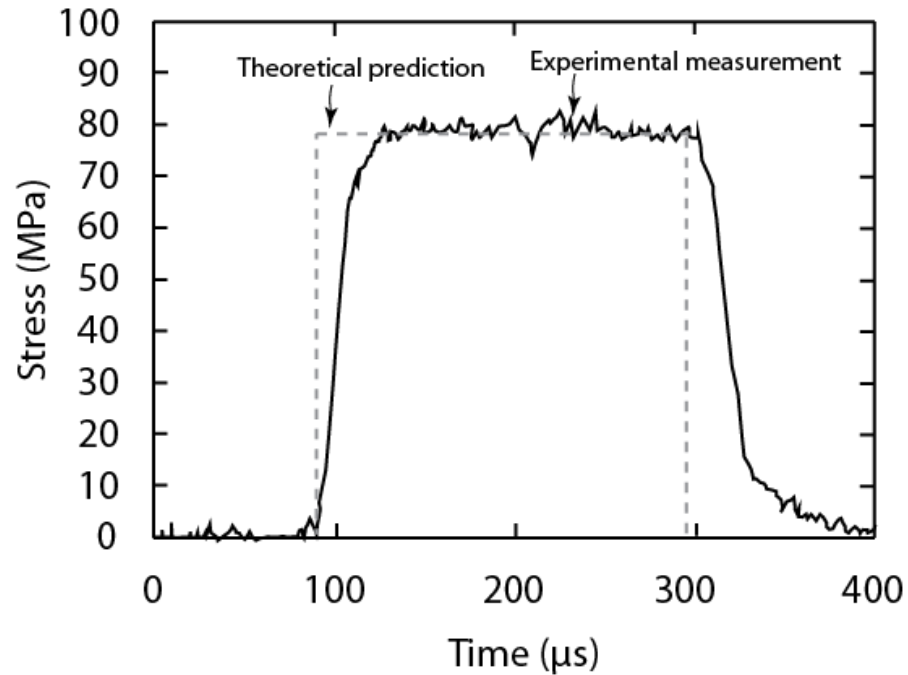


Fig. 3.6 Time history of stress measured by the Kolsky pressure bar setup during a calibration test.

3.4 Finite element simulation

3.4.1 The finite element model

Numerical simulation was conducted to simulate both the quasi-static and dynamic compressive response of the honeycombs in order to (i) verify the experimental measurements, and (ii) develop further understanding of the effects of the key experimental parameters. The explicit version of the commercially available finite-element (FE) package ABAQUS® was employed in the FE calculations. The webs of the honeycomb specimens were modelled with 8-node linear 3D solid elements (ABAQUS element C3D8R). Numerical study confirmed that a maximum element edge length of half the wall thickness was

required to achieve converged results which have been discussed in Section 3.5.1. The FE model of a honeycomb was sandwiched between two rigid plates (discretised with the 4-node rigid elements, R3D4) in the 3-axis direction: one of the rigid plates was fully clamped, and the other rigid plate was restricted to translation in the 3-axis direction.

For quasi-static compression, the movable rigid plate imposed compressive loading on the sample with a constant velocity. To ensure the simulation was quasi-static, the velocity was controlled so that the kinetic energy was under 5% of the total energy in the system. In the dynamic simulation, the movable rigid plate was associated with a point mass and an initial velocity that were identical to those of the strikers employed in the experiment. For front face impact, the honeycombs were tied to the movable rigid plate and moved with the rigid plate to impact on the clamped rigid surface. For back face impact, the honeycombs were tied to the clamped rigid plate and crushed by the movable rigid plate. High-speed photographs of the experiments showed that negligible sliding occurred at the interfaces between the honeycomb, the striker and Kolsky bar. Hence, the tie constraint is appropriate. For all calculations, a penalty contact approach was employed to simulate the interaction between all the surfaces, with friction coefficient 0.5. This was sufficient as tests showed that the simulation results were not sensitive to the value of the friction coefficient employed in the calculations.

3.4.2 The constitutive model and material parameters

The constitutive model for the parent material of the honeycombs, AlSi10Mg alloy, should include elasticity, rate dependent plasticity, and damage. The elastic response was modelled using a linear elasticity model for an isotropic solid with Young's modulus E_{SLM} and Poisson's ratio ν_{SLM} . E_{SLM} and ν_{SLM} were measured via a uniaxial coupon tensile test, see Section 3.2.3. For the quasi-static simulation, the J2 yield criterion in conjunction with isotropic hardening was employed to model plasticity of the material. The experimental data obtained from coupon uniaxial tension along both 3-axis and 1-axis/2-axis (Fig. 3.3) were used as the inputs to the constitutive model to specify the yield stress–plastic strain relationship. However, the data from 1-axis/2-axis uniaxial tension gave the best agreement between numerical simulations and experimental measurements for the quasi-static compressive response of honeycombs, see Section 3.7.4. Numerical studies of the honeycombs under high strain-rate compression suggested that the development of plasticity in the parent material was strain rate dependent. The following model was used to capture the rate dependency in the simulations.

$$k_1 = 1 + C_{SLM} \ln(\dot{\epsilon}_p / \dot{\epsilon}_o) \quad (3.1)$$

where C_{SLM} and $\dot{\epsilon}_o$ are a material constant and the reference strain rate for quasi-static testing, respectively; $\dot{\epsilon}_p$ is the von Mises equivalent plastic strain rate, and k_1 is the strength enhancement ratio of the yield stress at $\dot{\epsilon}_p$ to the yield

stress at $\dot{\varepsilon}_o$. In the simulations, $\dot{\varepsilon}_o$ was chosen to be the same as the strain rate used in quasi-static testing, i.e. $\dot{\varepsilon}_o = 10^{-3} \text{ s}^{-1}$. The value of C_{SLM} , determined to be 0.02, was obtained via calibration against dynamic testing of the honeycombs. The accuracy of this value can be explained as follow. In the quasi-static compression modelling, the finite element predictions in Section 3.5.1 were validated to have a good agreement with the experimental measurements by inputting the experimental data. Compared to the quasi-static compression modelling, the dynamic compression modelling only considered one more effect, i.e. strain rate effect where C_{SLM} was the key parameter. The finite element calculation indicated that the best fitting (under 5% deviation) can be achieved when $C_{\text{SLM}} = 0.02$. Moreover, Johnson and Cook [87] experimentally measured that the value of C_{SLM} was in the range of 0.06-0.6 for metal material, and was 0.10 and 0.15, respectively, for two types of aluminium material. Hence, the value of 0.02 is reasonable and accurate for AlSi10Mg alloy in this study.

Damage initiation in the AlSi10Mg was assumed to occur when the von Mises equivalent plastic strain reached a critical value, ε_c . After initiation of damage, a damage variable, d ($0 \leq d \leq 1.0$), was assumed to develop based on the following relation

$$\dot{d} = \frac{L_e \sigma_{y0}}{2G_f} \dot{\varepsilon}_p \quad (3.2)$$

where G_f is the fracture energy, L_e the characteristic element size and σ_{y0} the yield stress at the initiation of damage. The fracture energy G_f is defined as

$$G_f = \int_{\varepsilon_c}^{\varepsilon_{frac}} L_e \sigma_o d\varepsilon_p \quad (3.3)$$

where ε_p is the von Mises equivalent plastic strain and ε_{frac} is the equivalent plastic strain when failure occur [222]. The material parameters, ε_c and ε_{frac} , were obtained from the 1-axis/2-axis uniaxial tension of SLM manufactured coupons, see Section 3.2.3. σ_o is the yield stress of parent material. The damage variable was set to zero at the initiation of the damage, and reduced the yield stress of the material according to the relation $(1-d)\sigma_o$. When the value of d in an element reached the maximum value 1.0, the element was removed from the mesh. Even if not considering element deletion, the stiffness of the elements was very low when the value of damage variable reached 1.0. By numerically comparing the compressive stress-strain response of the honeycombs with and without considering element deletion, it showed that the element deletion has a negligible effect on the finite element calculation.

The material properties used for finite element simulations are shown in Table 3.3. Figure 3.3 shows the predicted 1-axis/2-axis tensile stress-strain relations at strain rates ranging from 10^{-3} s^{-1} to 5000 s^{-1} . The strain rate effect enhances the strength and increases the ultimate elongation of the parent material.

Table 3. 3 Material properties for the SLM manufactured AlSi10Mg alloy.

Property	E_{SLM}	V_{SLM}	ρ_0	C_{SLM}	$\dot{\epsilon}_o$	ϵ_{frac}	ϵ_c
Value	69.3 GPa	0.3	2.67 g.cm ⁻³	0.02	10 ⁻³ s ⁻¹	0.08	0.0075

3.5 Quasi-static compressive response of honeycombs

3.5.1 Experimental measurement and numerical prediction

Figures 3.7 (a)-(c) show representative stress–strain relations for the three types of honeycomb under quasi-static compression. The experimentally observed and numerically simulated failure modes are shown in Figs. 3.7 (d)-(f) at selected compressive strains post failure. The contours shown in the simulation results (Figs. 3.7 (d)-(f)) represent values of the damage variable d .

The single-scale honeycomb had an average compressive strength $\sigma_{\text{S-max}} = 51 \text{ MPa}$ at relative density $\bar{\rho} = 0.19$, which corresponds to a peak nominal wall stress (compressive strength/relative density) $\bar{\sigma}_{\text{max}} = 268 \text{ MPa}$.

Higher peak nominal wall stresses were achieved by the hierarchical honeycombs, $\bar{\sigma}_{\text{max}} = 358 \text{ MPa}$ for the two-scale honeycomb with compressive strength $\sigma_{\text{S-max}} = 93 \text{ MPa}$ at relative density $\bar{\rho} = 0.26$, and $\bar{\sigma}_{\text{max}} = 337 \text{ MPa}$ for the three-scale honeycomb with compressive strength $\sigma_{\text{S-max}} = 118 \text{ MPa}$ at relative density $\bar{\rho} = 0.35$. It is notable from this that both hierarchical

honeycombs showed similar peak nominal wall stresses that were significantly higher than seen with the single-scale honeycomb. The compressive strength versus density relations of the three types of honeycombs have been plotted in the map of Fig. 2.8 in Chapter 2. It is shown that the specific strengths of the two hierarchical honeycombs in this map are above those of the natural materials and engineering polymers, whereas the single-scale honeycomb is located in the range of specific strength of natural materials. This means that the two AlSi10Mg alloy hierarchical honeycombs are promising structures which fill the gap of high-performance structures.

The single-scale honeycomb failed by local plastic buckling of walls followed by damage close to the base. The finite element simulation successfully captured this failure mechanism. The peak compressive stress of the honeycomb was achieved at the onset of damage. Further development of damage within the honeycomb walls led to a significant decrease of the compressive stress (Fig. 3.7 (a)). The two-scale honeycomb failed with damage close to the bottom support, see Fig. 3.7 (e), and no wall buckling was observed throughout the experiment. The three-scale honeycomb specimen failed catastrophically through global plastic buckling, which may have been triggered by the damage of the parent material. Local plastic buckling was not observed in the experiment for either of the hierarchical honeycombs. This may be ascribed to the in-plane structures of the hierarchical honeycombs possessing higher structural stability.

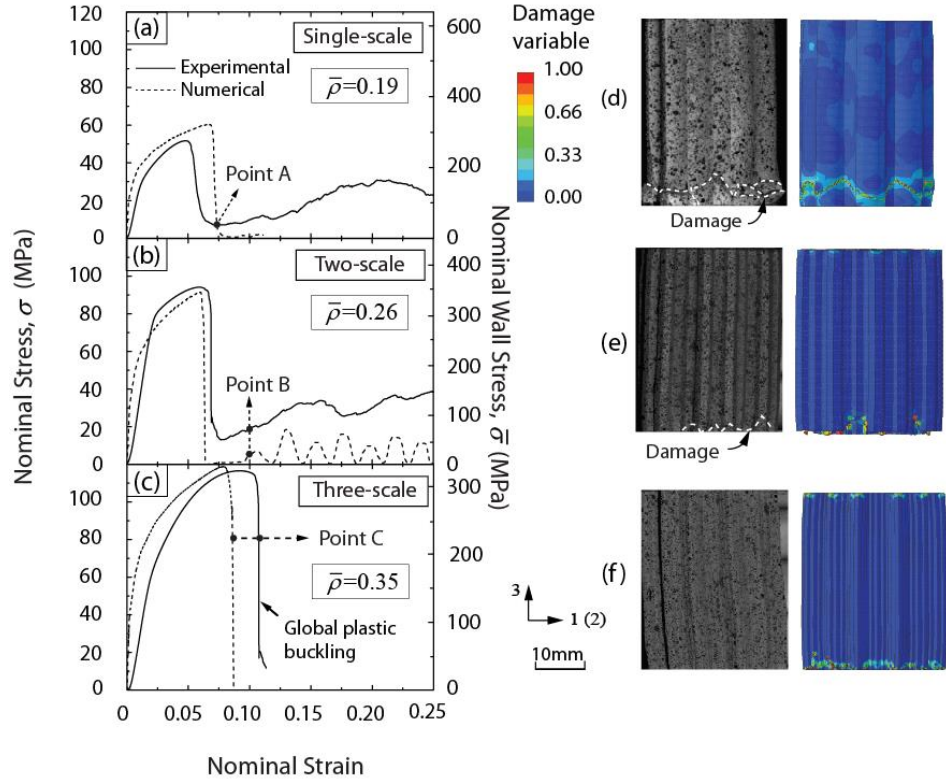


Fig. 3.7 Honeycombs under quasi-static compression. (a)-(c) Compressive stress-strain relations of the three types of honeycombs, and (d)-(f) experimentally measured (left) and FE predicted (right) damage mechanisms at Point A in (a), Point B in (b), and Point C in (c), respectively. The white dash lines in (e) and (f) show the damage locations of the single-scale and two-scale honeycombs, respectively.

The predicted compressive stress-strain relationships and failure mechanisms agree well with those obtained from the experiments for the single-scale and two-scale honeycombs. However, there is certain discrepancy in prediction of the global plastic buckling mode in comparison with the experimental measurements for the three-scale honeycomb, as shown in Fig. 3.7 (f). This discrepancy may be attributed to the asymmetrical flaws induced by damage of

the parent material, which was not accurately captured in the finite element simulations.

Figure 3.8 shows the effect of mesh size on the finite element predictions of the honeycombs, taking the two-scale honeycomb for example. It indicates that the compressive strength of the honeycomb with one element in wall thickness is lower than that with two elements in wall thickness. However, the effect of mesh size on the compressive response of the honeycomb is negligible when there are no less than 2 elements along web wall thickness.

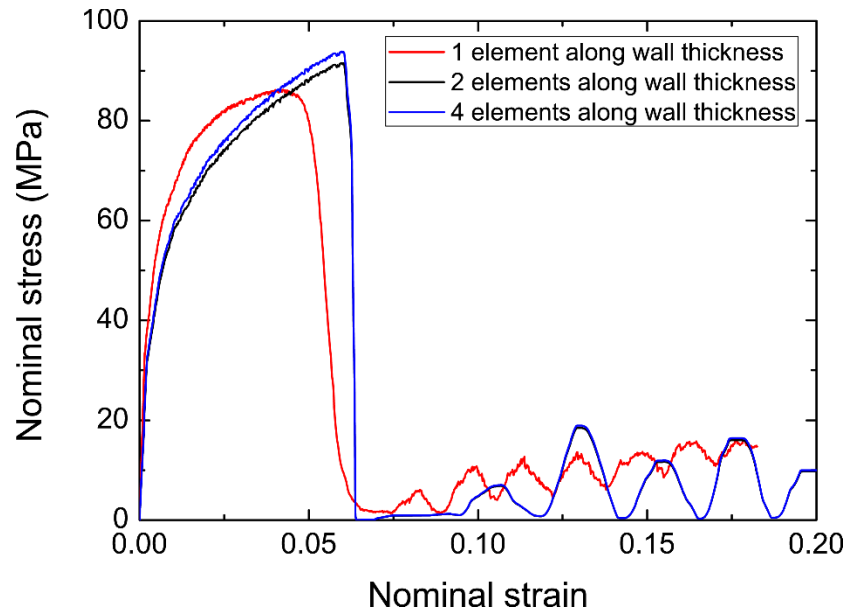


Fig. 3.8 The effect of mesh size on the compressive response of two-scale honeycomb

3.5.2 Effect of relative density on quasi-static compression

As mentioned in Section 3.2.1, the geometrical parameters of honeycomb samples were limited by the manufacturing resolution of the SLM manufacturing

facility, and the three types of honeycombs have different relative densities. To evaluate the effect of relative density, the verified FE simulation is employed to examine the quasi-static compressive response of the three types of honeycombs with identical density. The cross-sectional views of each type of honeycomb are presented in Figs. 3.1 and 3.8. The predicted quasi-static compressive stress-strain relations and the failure mechanisms of selected honeycombs are shown in Fig. 3.9. The failure mechanism of the single-scale honeycomb is sensitive to relative density, i.e. the failure mechanism changed from plastic buckling of walls at lower relative density ($\bar{\rho} = 0.19$) to the local damage of parent material without buckling at the bottom support at higher relative density ($\bar{\rho} \geq 0.26$). However, the failure mechanism of the two hierarchical honeycombs is not sensitive to relative density, i.e. parent material damage at the bottom support without buckling. This may be ascribed to the in-plane structures of the hierarchical honeycombs possessing higher structural stability. The nominal compressive strengths of both the two-scale and three-scale honeycombs are higher than that of the single-scale honeycomb at low relative density of $\bar{\rho} = 0.19$ owing to the different failure mechanisms. For higher relative density ($\bar{\rho} \geq 0.26$), the nominal compressive strengths of the three types of honeycombs are nearly identical as all of the honeycombs failed with parent material damage at the bottom support.

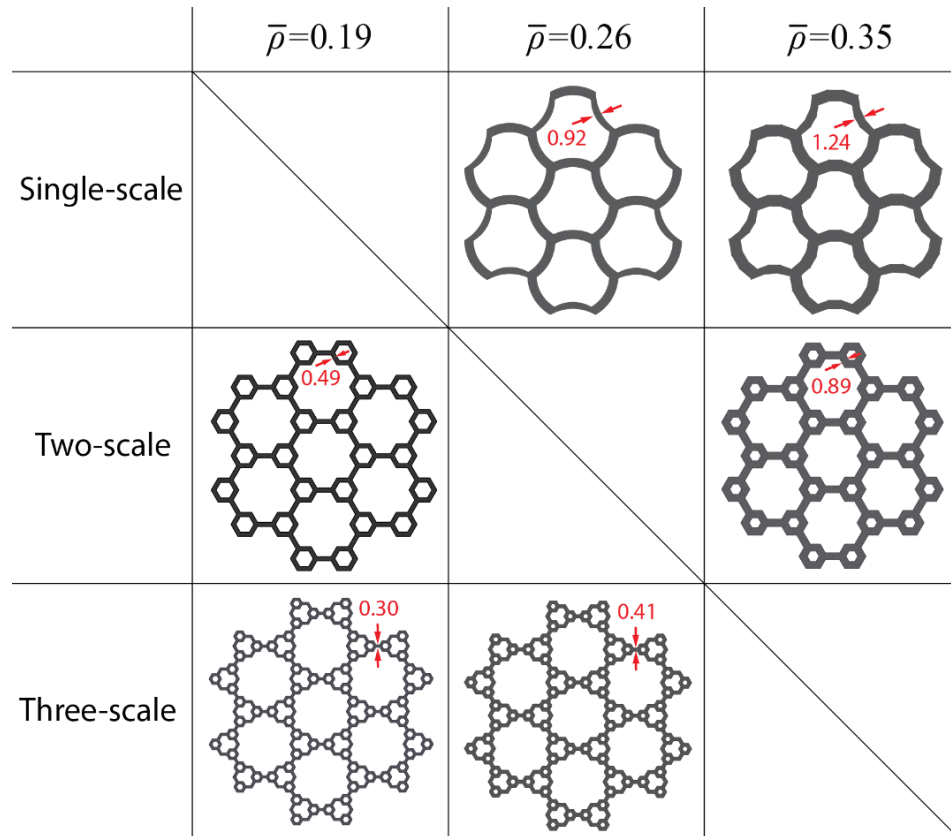


Fig. 3.9 The cross-sectional views of the single-scale, two-scale and three-scale honeycombs for finite element prediction. All dimensions are in mm.

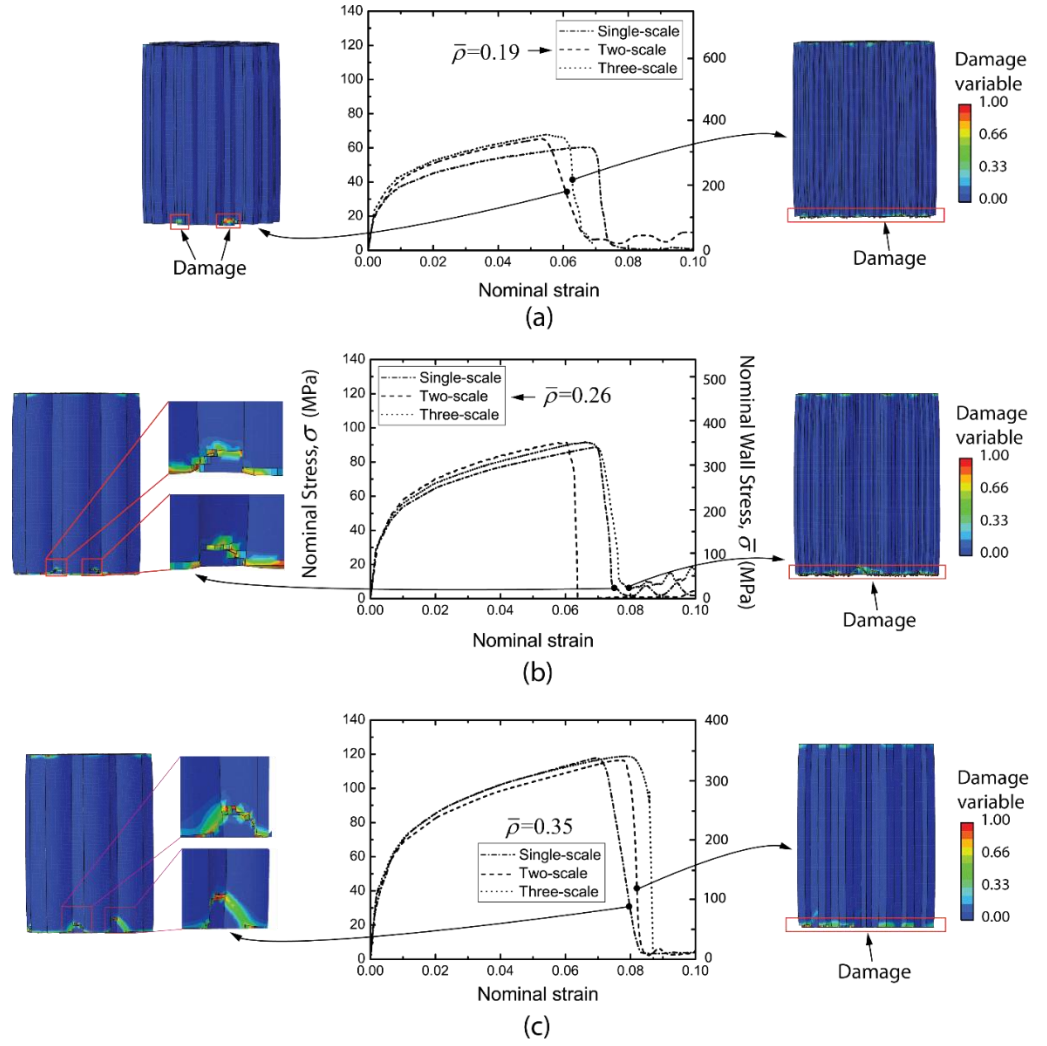


Fig. 3.10 Finite element predictions for honeycombs under quasi-static compression, including the compressive stress-strain relations and the damage mechanisms of the three types of honeycombs at relative density of (a) $\bar{\rho} = 0.19$, (b) $\bar{\rho} = 0.26$, (c) $\bar{\rho} = 0.35$. The damage mechanisms of honeycombs which have been shown in Fig. 3.7 are not included in this figure.

3.6 Dynamic compressive response of the honeycombs

3.6.1 Back face impact

In this section, we first examine the dynamic response of the honeycombs shown in Fig. 3.1. Figure 3.11 shows the nominal compressive stress of the honeycomb structures as a function of normalised time $v_0 t/H$ for three selected impact velocities in the back face impact test, with $t = 0$ corresponding to the beginning of the impact. As the Young's elastic modulus and density of the AlSi10Mg alloy parent material are measured as $E_{\text{SLM}} = 69.3 \text{ GPa}$ and $\rho_0 = 2670 \text{ kg.m}^{-3}$, respectively, the longitudinal elastic wave speed propagated in the honeycombs can be calculated through $c_{\text{SLM}} = \sqrt{\frac{E_{\text{SLM}}}{\rho_0}} = 5095 \text{ ms}^{-1}$. According to the experimental results shown in Fig. 3.11, the compressive strengths of the honeycombs were achieved at $t \approx 24 \mu\text{s}$ for impact velocity of $v_0 = 120 \text{ ms}^{-1}$. Hence, around three elastic-wave reflections took place in the honeycomb specimen of $H = 40 \text{ mm}$ before the peak strength of the honeycombs achieved. At lower impact velocities, i.e. $10 \leq v_0 \leq 80 \text{ ms}^{-1}$, there were more elastic-wave reflections because the time increased before achieving peak compressive stress of honeycombs. Thus, the force equilibrium has been achieved when measuring the compressive strength of honeycombs [223]. As shown in Section 3.7.1, the dynamic compressive strengths of honeycomb specimens are not sensitive to which of the two dynamic test methods investigated, i.e. the back face impact

and the front face impact. Hence, only the results from the back face impact test are presented here. Both the finite element simulations and experimental measurements are shown in the figure for comparison. As shown in Section 3.7.2, numerical simulations demonstrated that the striker decelerated significantly during lower velocity impact events, e.g. 10%-20% deceleration for $v_0 = 20 \text{ ms}^{-1}$, and the deceleration is negligible for higher velocity impact events, e.g. $v_0 \geq 80 \text{ ms}^{-1}$. Hence, the normalised time $v_0 t / H$ is equivalent to nominal compressive strain for the velocities $v_0 = 80 \text{ ms}^{-1}$ and $v_0 = 120 \text{ ms}^{-1}$ but not for the lower velocities $v_0 \leq 20 \text{ ms}^{-1}$. Compared with the quasi-static compressive response (Figs. 3.7 (a)-(c)), dynamic compression enhanced the compressive strengths of the honeycombs. In contrast to catastrophic failure under quasi-static compression, the dynamic compressive stresses decreased steadily after the peak values were achieved. The agreement for peak strengths of honeycombs between finite element simulations and experimental measurements is reasonably good, however, the element deletion technique employed in the numerical simulations altered the mass matrix when elements were removed from the FE meshes, potentially making the simulation results more oscillatory than the experimental measurements for post-failure response. In addition, the geometrical flaws induced by additively manufactured process may increase the discrepancy between experimental measurements and FE simulations, as the flaws were not modelled in the FE simulations.

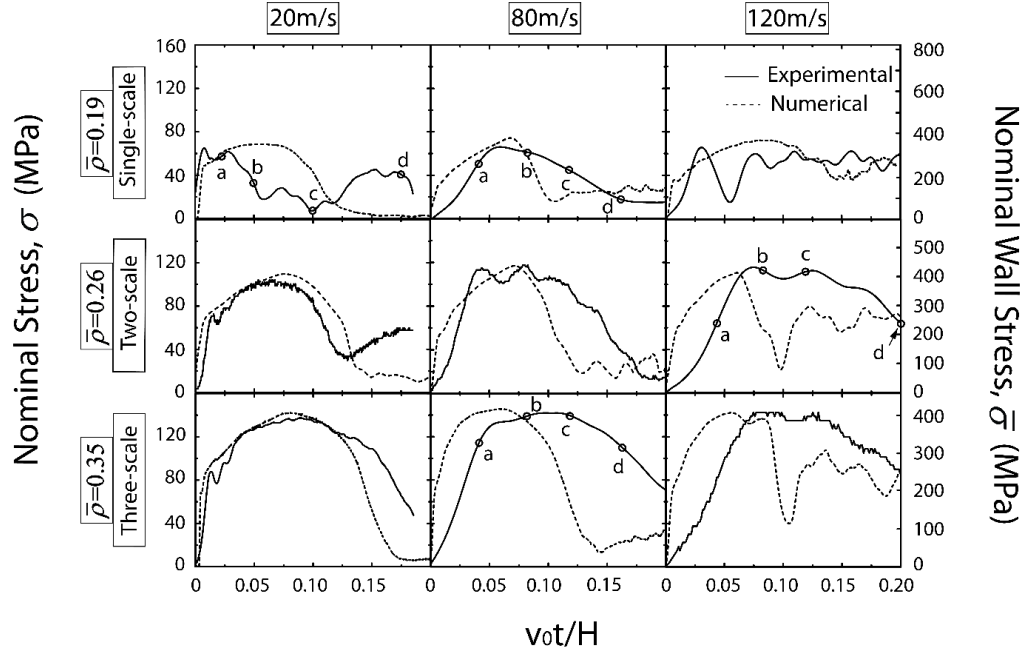


Fig. 3.11 Compressive stress as a function of normalised time $v_0 t / H$ obtained by the back face impact test at low ($v_0 = 20 \text{ ms}^{-1}$), medium ($v_0 = 80 \text{ ms}^{-1}$) and high velocities ($v_0 = 120 \text{ ms}^{-1}$). The hollow circle “○” marks the stresses at the selected time instants in Fig. 3.12 – Fig. 3.15.

The failure modes of the honeycombs are revealed from montages of high-speed photographic images recorded at selected time instants (Points a, b, c and d in Fig. 3.11) during the impact events, as shown in Figs. 3.11 through 3.14. In these figures, the high-speed photographic images are compared to FE predictions. Figures 3.11 and 3.12 show montages of single-scale honeycombs under the impact of the striker with $v_0 = 20 \text{ ms}^{-1}$ and $v_0 = 80 \text{ ms}^{-1}$, respectively. The failure mechanism of the honeycomb under dynamic impact is similar to that under quasi-static compression, i.e. the honeycomb failed with plastic buckling of walls followed by damage close to the end attached to the Kolsky bar, at

impact velocity of $v_0 = 20 \text{ ms}^{-1}$ (Fig. 3.12). However, at the velocity of $v_0 = 80 \text{ ms}^{-1}$ (Fig. 3.13), the plastic buckling damage in single-scale honeycomb was less significant owing to the micro inertial effects. Finite element simulations captured the failure mechanisms accurately, with element deletion activated when the peak stress was achieved ($d=1$).

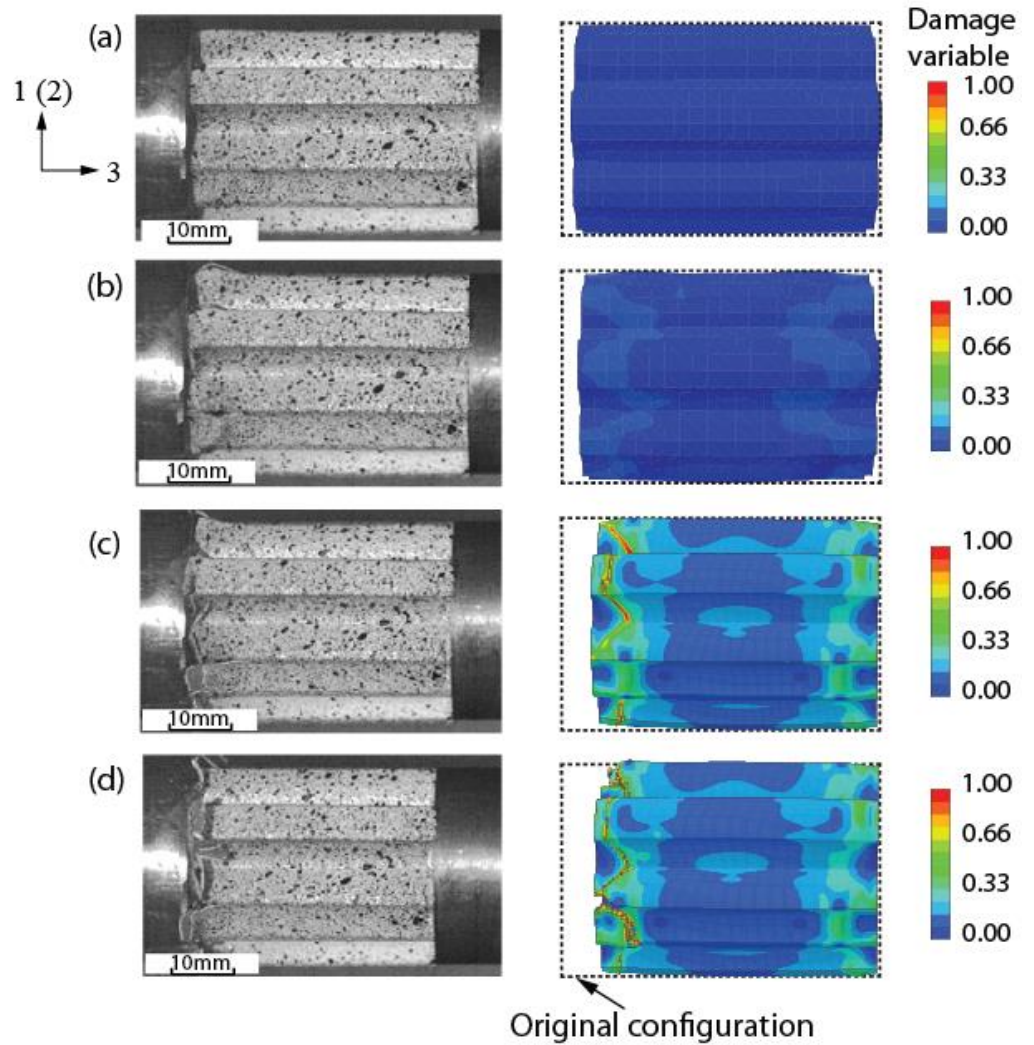


Fig. 3.12 Montage of the single-scale honeycomb under back face impact at the velocity of 20 ms^{-1} obtained from experiment and numerical simulations. Time $t=0$ corresponds to the time instant when the steel striker impacted on the

honeycomb. The images were taken at (a) $t=50$ us, (b) $t=100$ us, (c) $t=200$ us, (d) $t=350$ us, respectively.

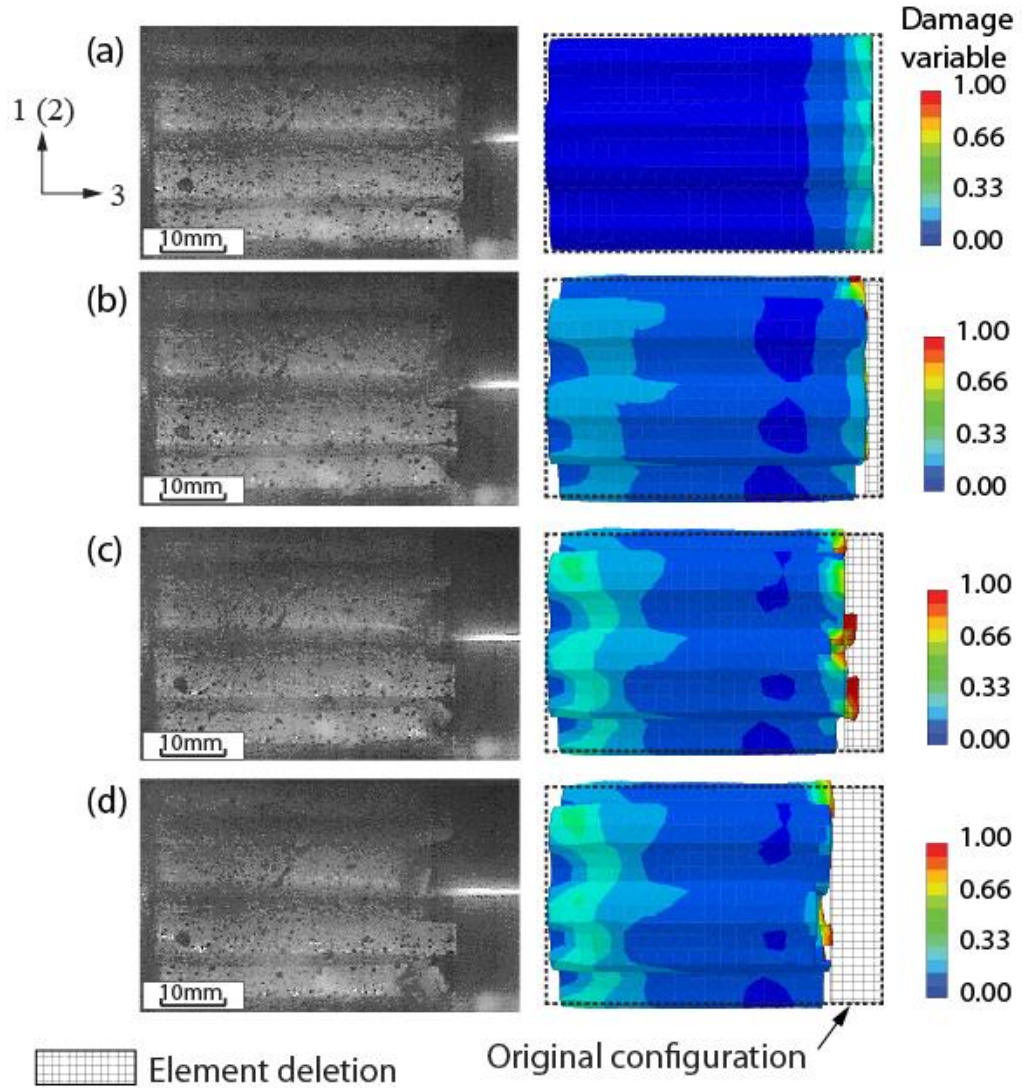


Fig. 3.13 Montage of the single-scale honeycomb under back face impact at the velocity of 80ms^{-1} obtained from experiment and numerical simulations. Time $t=0$ corresponds to the time instant when the steel striker impacted on the honeycomb. The images were taken at (a) $t=20$ us, (b) $t=40$ us, (c) $t=60$ us, (d) $t=80$ us, respectively.

As the response under the lower velocity impact ($v_0 = 20 \text{ ms}^{-1}$) is essentially quasi-static, Figs. 3.13 and 3.14 only show the montages of the two-scale honeycomb and the three-scale honeycomb under higher speed impact ($v_0 \geq 80 \text{ ms}^{-1}$), respectively. For both hierarchical honeycombs, the montages taken from experiments suggest the damage started to develop at the impacted end. The specimens failed with significant plastic deformation and cracking. No wall buckling was observed throughout the experiments on hierarchical honeycombs. The FE simulation captured the failure mechanism for the two-scale honeycomb specimen; the element deletion being activated at the impacted end. However, there is some discrepancy in prediction of the failure mechanism for the three-scale honeycomb sample; although the damage initially developed at the impacted end, the element deletion was first activated at the distal end of the specimen.

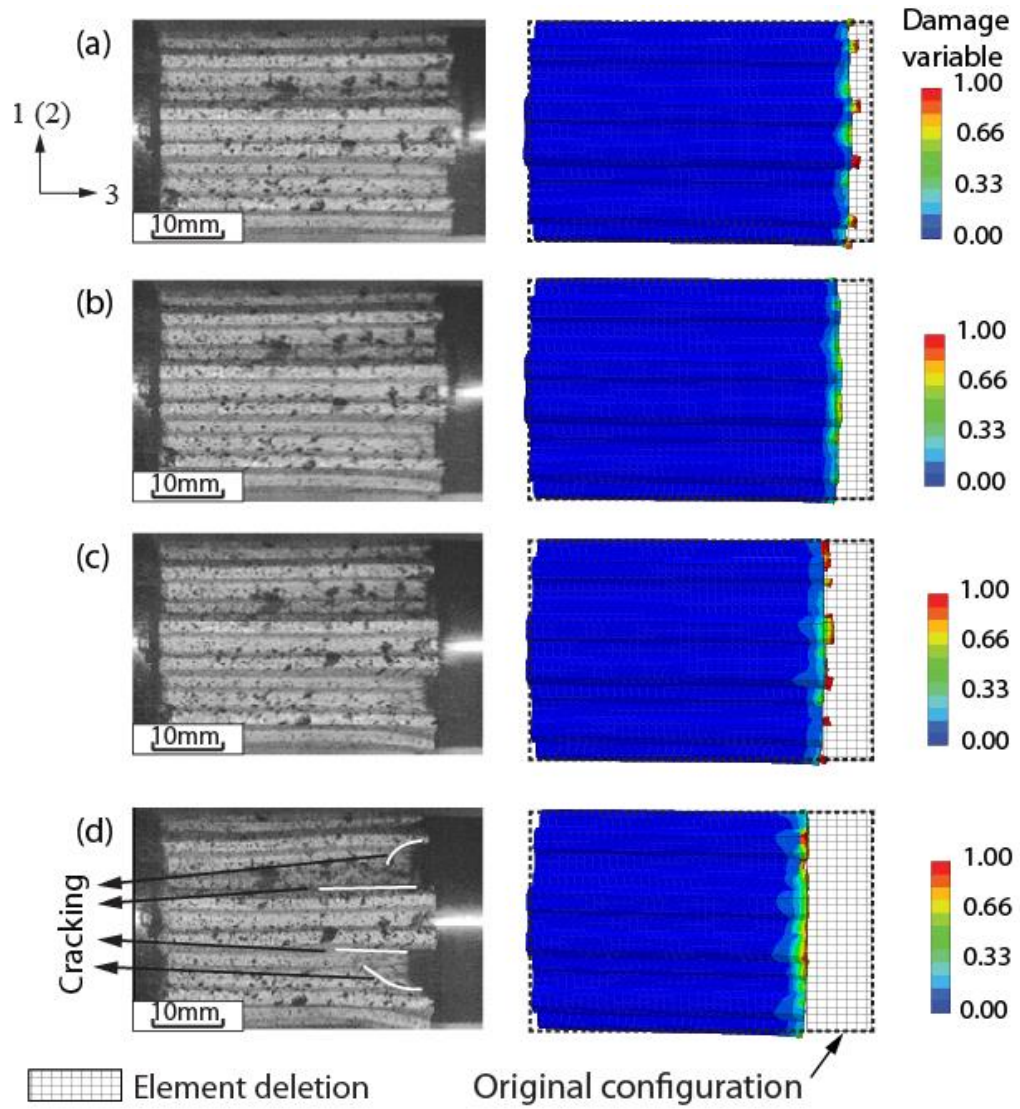


Fig. 3.14 Montage of the two-scale honeycomb under back face impact at the velocity of 120ms^{-1} obtained from experiment and numerical simulations. Time $t=0$ corresponds to the time instant when the steel striker impacted on the honeycomb. The images were taken at (a) $t=13.3\text{ us}$, (b) $t=26.7\text{ us}$, (c) $t=39.9\text{ us}$, (d) $t=66.5\text{ us}$, respectively.

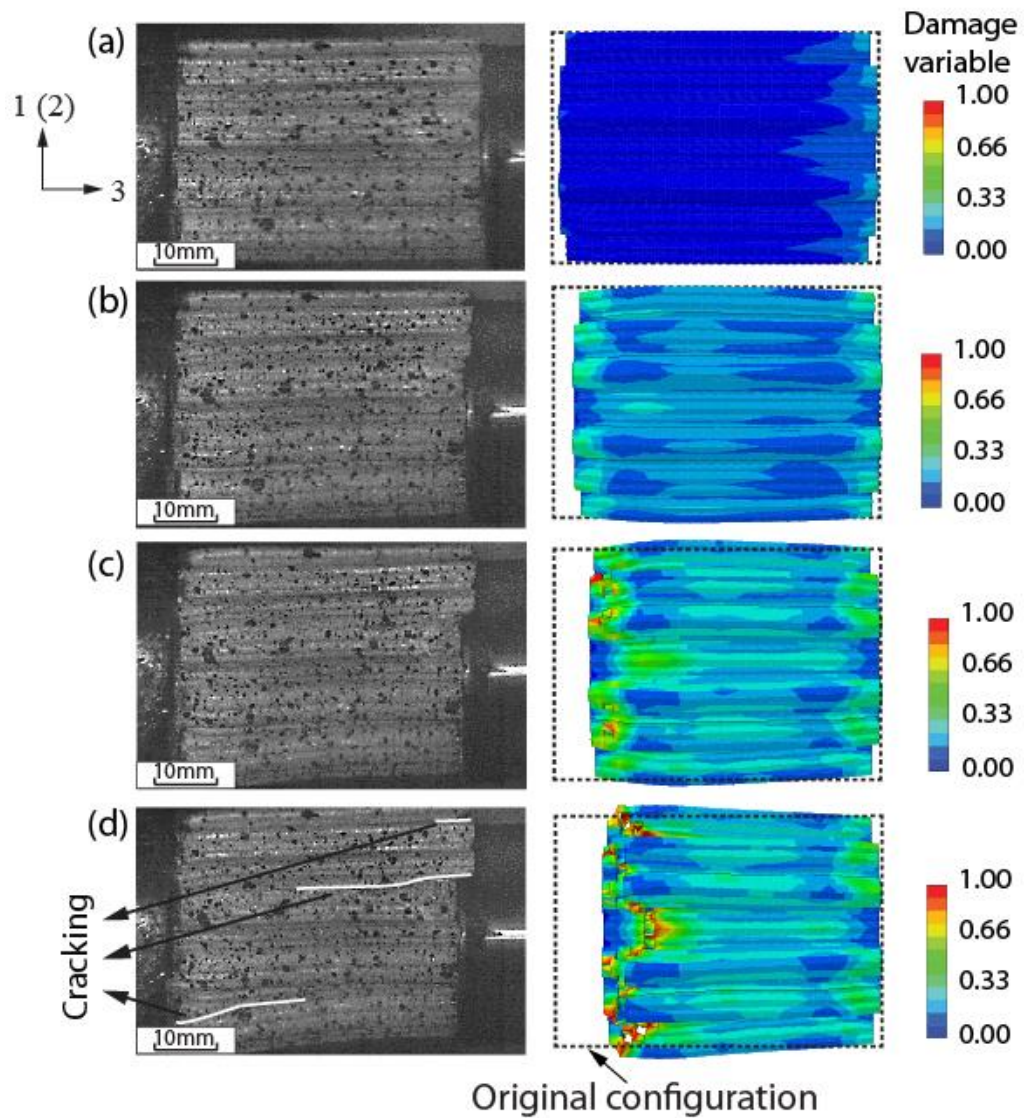


Fig. 3.15 Montage of the three-scale honeycomb under back face impact at the velocity of 80ms^{-1} obtained from experiment and numerical simulations. Time $t=0$ corresponds to the time instant when the steel striker impacted on the honeycomb. The images were taken at (a) $t=20\text{ us}$, (b) $t=40\text{ us}$, (c) $t=60\text{ us}$, (d) $t=80\text{ us}$, respectively.

To examine the effect of the relative density of the honeycomb structures, numerical simulations were conducted based on the geometries shown in Figs.

3.1 and 3.8. The outcomes are shown in Fig. 3.16 for peak wall stress $\bar{\sigma}_{\max}$ normalised by the quasi-static 1(2)-direction tensile strength σ_T of the AlSi10Mg parent material as a function of v_0/H , and Fig. 3.17 for the nominal compressive stress as a function of normalised time $v_0 t/H$. The measured normalised peak wall stress for selected samples as well as the rate dependency of the parent material predicted using Eq. (3.1) are also included in Fig. 3.16 for comparison. The finite element predictions are in good agreement with the experimental measurements. The two hierarchical honeycombs have similar peak wall stresses throughout the densities considered as the failure mechanism is governed by damage of the parent material (Fig. 3.16). The measured and predicted trends of the strength enhancement of the two hierarchical honeycombs are similar to that predicted using the rate dependent material model (Eq. (3.1)), indicating that the strength enhancements at higher impact velocities may mainly be governed by the strain rate sensitivity of the parent material. At low relative densities, i.e. $\bar{\rho} = 0.19$, the single-scale honeycomb failed with wall plastic buckling as the peak wall stress is significantly less than those of the two hierarchical honeycombs. With increase of relative density, say $\bar{\rho} \geq 0.26$, the failure mechanism of single-scale honeycomb is governed by damage of the parent material without wall plastic buckling. Hence, the difference in the peak wall stress is diminished, i.e. the three types of honeycombs have similar peak wall stresses when $\bar{\rho} \geq 0.26$. The time history of the dynamic response shown

in Fig.3.16 indicates that the two hierarchical honeycombs can absorb more energy than the single-scale honeycomb with identical relative density.

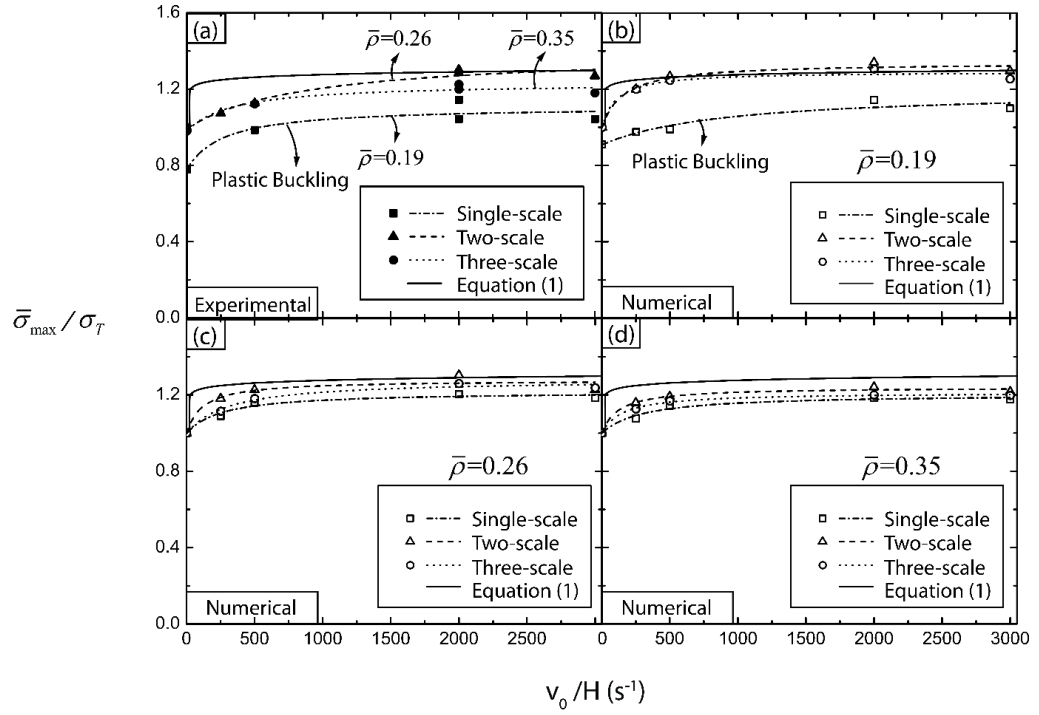


Fig. 3.16 The peak nominal wall stresses $\bar{\sigma}_{\max}$ of the honeycombs normalized by the quasi-static 1(2)-axis tensile strength σ_T of the AlSi10Mg alloy parent material as a function of v_0/H . The (a) experimental measurements and numerical predictions of the honeycombs at the relative density of (b) $\bar{\rho} = 0.19$, (c) $\bar{\rho} = 0.26$, (d) $\bar{\rho} = 0.35$ are presented.

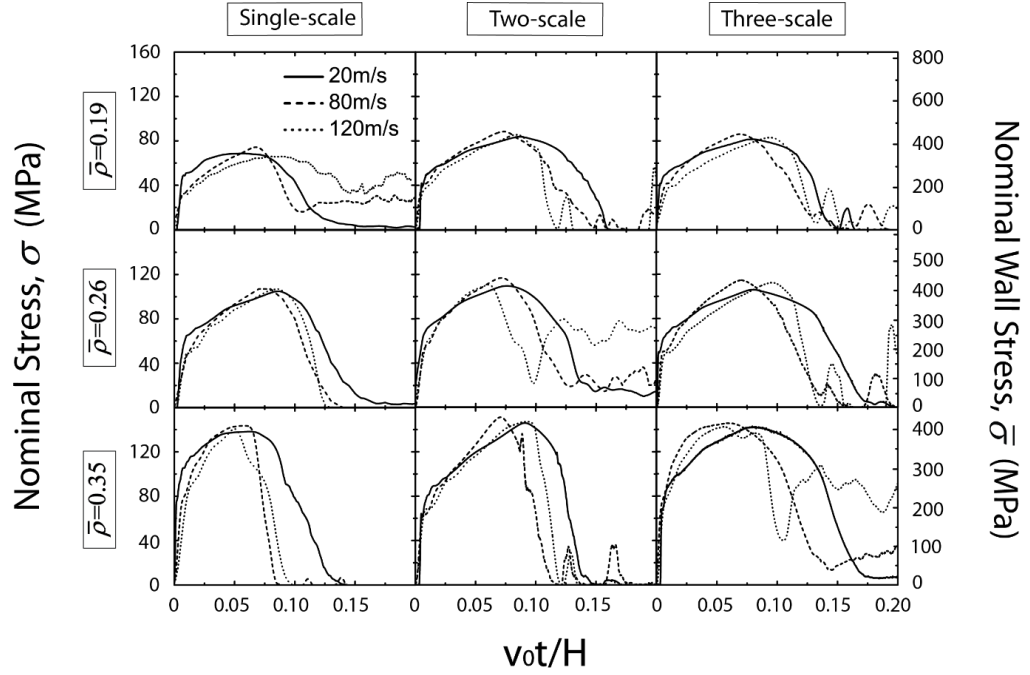


Fig. 3.17 Finite element predicted dynamic compressive responses of the three types of honeycombs at three different relative densities.

3.6.2 Effect of strain rate sensitivity of the parent material

As mentioned in Section 3.6.1, the strain rate dependency of the parent material is a key factor for dynamic strength enhancement of the honeycombs. To further understand this, Fig. 3.18 presents the predicted compressive responses of selected honeycombs with and without the parent material strain rate dependency for both back face and front face impact at low velocity impact ($v_0 = 20 \text{ ms}^{-1}$) and high velocity impact ($v_0 = 80 \text{ ms}^{-1}$). For low velocity impact ($v_0 = 20 \text{ ms}^{-1}$), the dynamic response is similar to that obtained under quasi-static compression, see analysis presented in Section 3.6.1. Hence, the effect of

the parent material strain rate dependency is not significant. However, for high velocity impact ($v_0 = 80 \text{ ms}^{-1}$), the effect becomes significant.

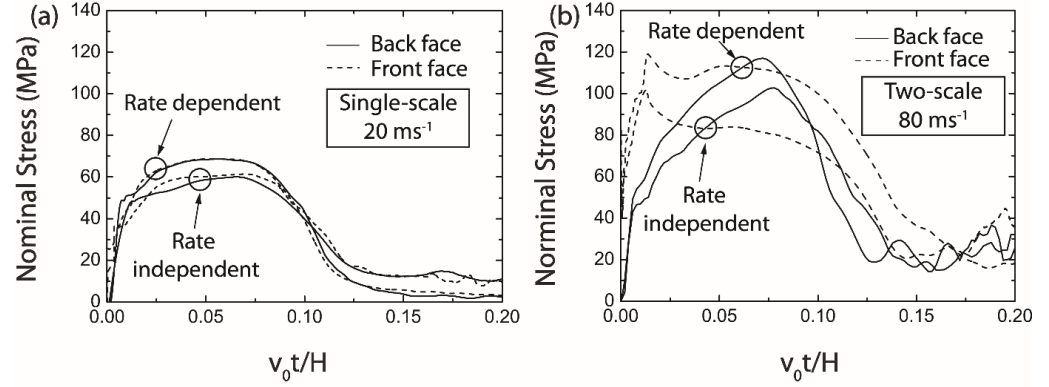


Fig. 3.18 Numerical study on the effect of strain rate sensitivity of the parent material. (a) The single-scale honeycomb impacted at the velocity 20 ms^{-1} and (b) the two-scale honeycomb impacted at the velocity 80 ms^{-1} .

3.7 Effect of key parameters on the compressive response of honeycombs

3.7.1 Effect of experimental method

The plastic shock wave propagation within honeycomb specimen resulting from the front face impact is different from that by the back face impact test. Hence, the dynamic compressive response of the honeycombs under front face impact is different from that under the back face impact test, as shown in Fig. 3.19 which includes four representative cases. However, the difference is not significant: the peak strengths achieved by both back face impact and front face impact are nearly identical at lower velocity impact ($v_0 = 20 \text{ ms}^{-1}$) as well as higher

velocity impact ($v_0 \geq 80 \text{ ms}^{-1}$). The finite element simulations were conducted for the selected cases, as shown in Fig. 3.19. The agreement between experimental measurement and numerical simulations is reasonably good.

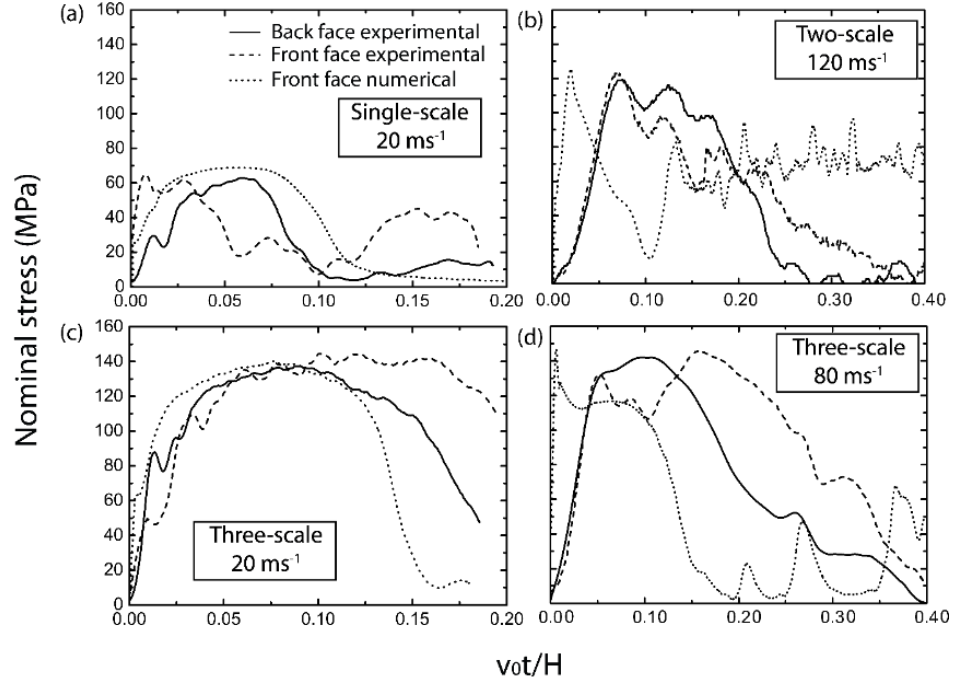


Fig. 3.19 Nominal compressive stress as a function of $v_0 t / H$ for selected honeycombs at selected striker velocities obtained by both back face and front face experimental measurements as well as FE simulations.

3.7.2 Effect of mass of striker

As mentioned in Section 3.3.2, strikers with different masses have been employed in the experiment to achieve different impact velocities. Fig. 3.20 shows FE predictions of the normalized striker velocity as a function of $v_0 t / H$ for the back face impact. The striker is subjected to significant deceleration in

the lower velocity impact events, e.g. $v_0 \leq 20 \text{ ms}^{-1}$. However, the deceleration is negligible for higher velocity impact events, e.g. $v_0 \geq 80 \text{ ms}^{-1}$. To examine the effect of striker mass in higher velocity impact events, Fig. 3.21 shows the measured and predicted compressive response of the three-scale honeycomb under the back face impact by two striker masses, $M = 0.0927 \text{ kg}$ and $M = 0.463 \text{ kg}$, respectively, at initial striker velocity $v_0 = 80 \text{ ms}^{-1}$. Both the experimental measurement and numerical prediction suggest striker mass has a small effect on the compressive response under the higher velocity impact.

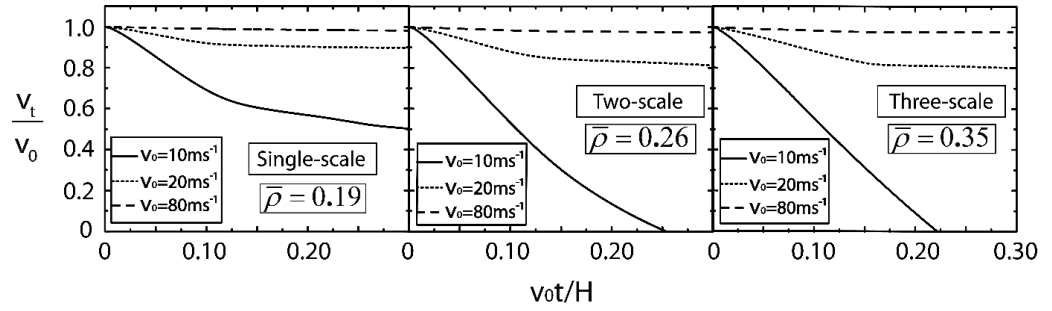


Fig. 3.20 FE predictions of the normalized striker velocity as a function of $v_0 t / H$ for the back face impact on honeycombs.

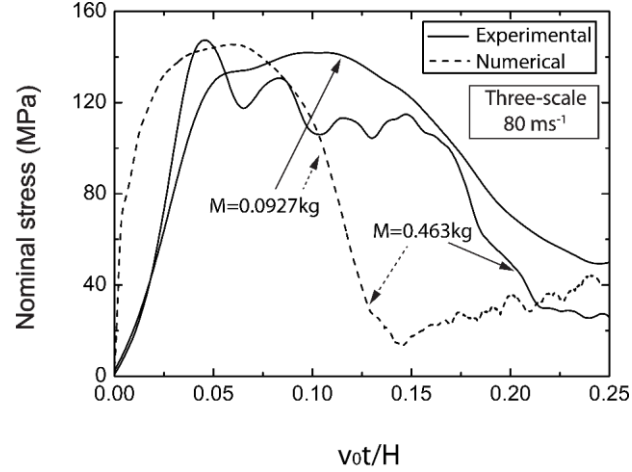


Fig. 3.21 Nominal compressive stress as a function of $v_0 t / H$ for the three-scale honeycomb under back face impact with striker velocity 80 ms^{-1} and striker mass $M = 0.0927 \text{ kg}$ and $M = 0.463 \text{ kg}$.

3.7.3 Effect of initial geometrical imperfections

Geometrical imperfections may play an important role in compressive response of honeycomb samples as it may have a significant influence on buckling behaviour. The effect of initial imperfections are examined via FE simulations. Quasi-static buckling eigenvalue analysis of the honeycombs was conducted. The first eigenmode was employed to introduce perturbation to the FE mesh of the honeycombs, with maximum perturbation 5% or 10% of the thickness of the honeycomb webs. The finite element predictions for quasi-static and dynamic compression are shown in Fig. 3.22 (a) and (b), respectively, for the single-scale honeycomb. It is shown that the effect of initial imperfections on the compressive response of the single-scale honeycomb is negligible as with and without initial imperfections result in almost identical compressive response.

The effect of initial imperfections on the hierarchical honeycombs has also been investigated. For brevity, only the two-scale honeycomb is presented in Fig. 3.22 (c) for quasi-static compression and Fig. 3.22 (d) for dynamic compression at $v_0 = 80 \text{ ms}^{-1}$. Similar to the single-scale honeycomb, the imperfections have a negligible effect on the compressive response of the hierarchical honeycomb. Therefore, it is concluded that the simulation results are not sensitive to initial imperfections in the honeycomb specimens.

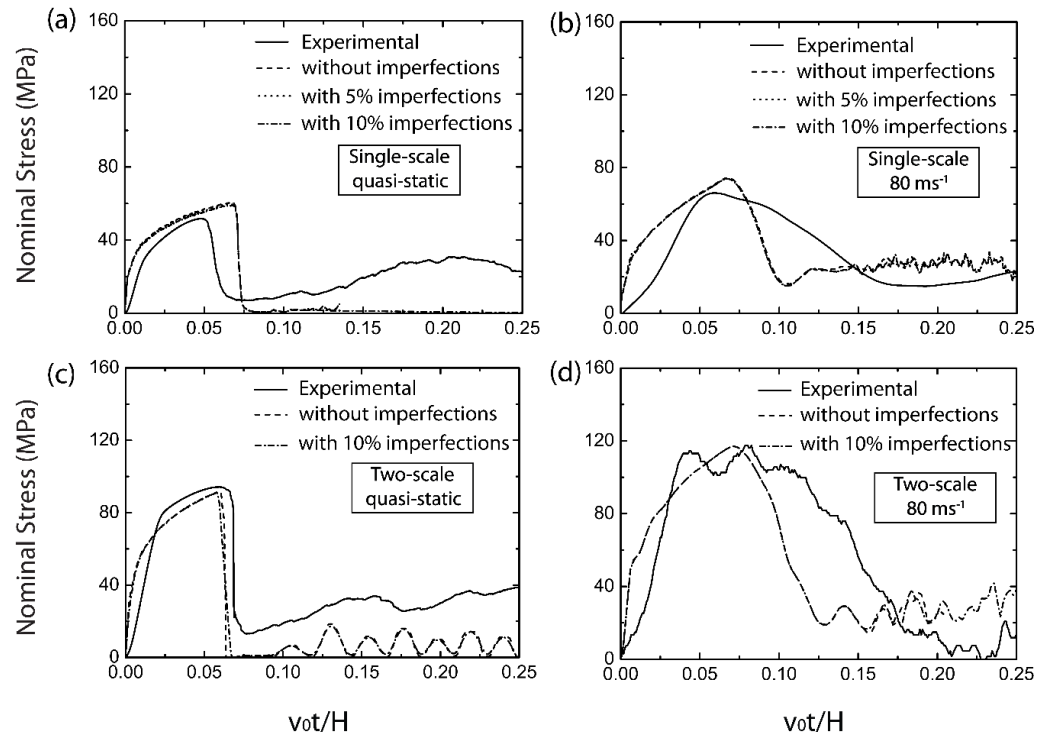


Fig. 3.22 FE predictions of the honeycombs with initial imperfections, the single-scale honeycomb for (a) quasi-static and (b) back face dynamic compression at the velocity 80 ms^{-1} , the two-scale honeycomb for (c) quasi-static and (d) back face dynamic compression at the velocity 80 ms^{-1} .

3.7.4 Quasi-static compressive responses of the honeycombs based on the 3-axis or 1-axis (2-axis) uniaxial tension test data

Due to the fabrication methodology, the SLM manufactured materials exhibit anisotropic behaviour. Hence, the mechanical properties of parent materials in different manufacturing directions may lead to the different simulation results when they are used as the input of the constitutive model. Figure 3.23 shows the comparison of the quasi-static out-of-plane compressive responses for the three types of honeycombs using the uniaxial tension test data in 3-axis and 1-axis (2-axis) directions. It is concluded that the compressive response of honeycombs obtained using 1-axis (2-axis) input have a better agreement with the experimental measurements than using 3-axis input.

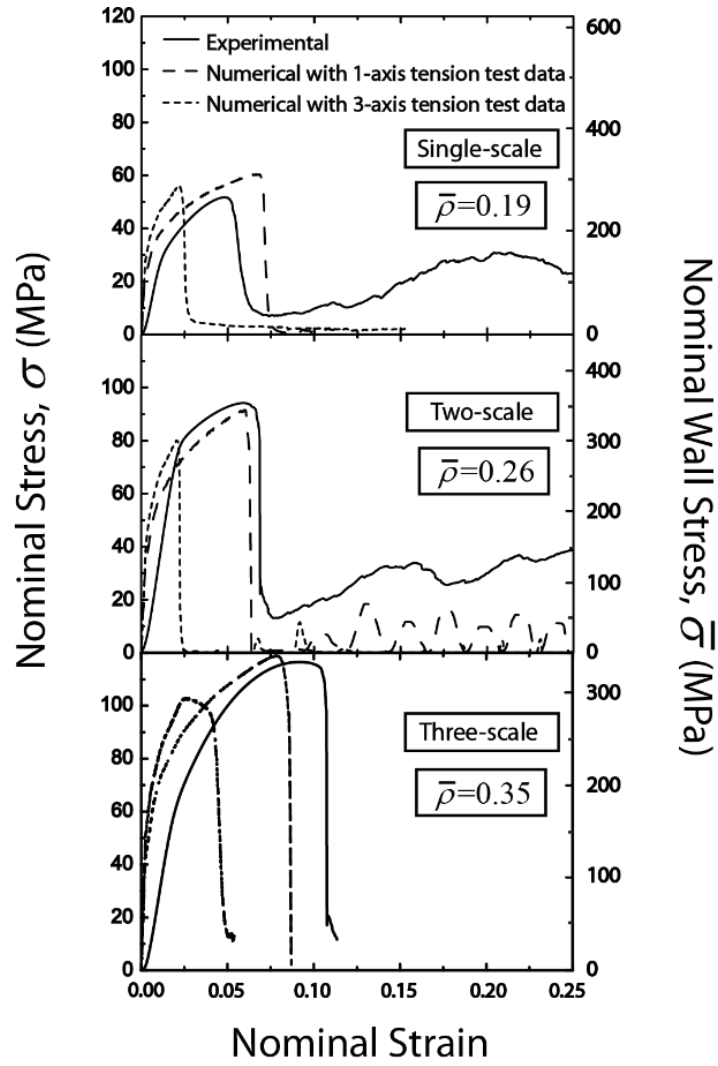


Fig. 3.23 Predicted quasi-static compressive responses of the honeycombs based on the 3-axis or 1-axis (2-axis) uniaxial tension test data of the AlSi10Mg alloy parent material.

3.8 Concluding Remarks

The out-of-plane quasi-static and high strain rate dynamic compressive responses of Selective Laser Melting (SLM) manufactured hierarchical

honeycombs have been reported. Three types of honeycombs, i.e. single-scale, two-scale and three-scale, were manufactured from an AlSi10Mg alloy. A Kolsky pressure bar was employed for the dynamic test with a striker velocity up to $v_0 = 120 \text{ ms}^{-1}$. Validated finite element (FE) simulations were conducted to facilitate interpretation of the experimental measurements. Different failure mechanisms among these honeycombs have been identified for quasi-static and dynamic compression, i.e. transition of the plastic buckling of walls to the local damage of the parent material without buckling for the single-scale honeycomb when the relative density of the honeycomb increased, and damage of the parent material without buckling for both the two-scale and three-scale honeycombs at different relative densities of the honeycombs. The strength enhancement of the hierarchical honeycombs under dynamic compression is dominated by the strain rate sensitivity of the parent material. The micro-inertial effects under higher velocity impact ($v_0/H \geq 500 \text{ s}^{-1}$) also enhance the dynamic compressive strength of the single-scale honeycomb. The two-scale and three-scale hierarchical honeycombs can offer higher peak nominal wall stresses compared to the single-scale honeycomb at the low relative density ($\bar{\rho} = 0.19$); The difference is diminished as relative density increases, i.e. the three types of honeycombs can achieve similar peak wall stresses when $\bar{\rho} \geq 0.26$. Numerical results have suggested the hierarchical honeycombs can offer better energy absorption capacity than the single-scale honeycomb. The two-scale and three-scale hierarchical honeycombs have achieved similar peak nominal wall stresses

for both quasi-static and dynamic compression, which may suggest that the structural performance under out-of-plane compression is not sensitive to the hierarchical architecture. The structural advantage of the hierarchical honeycombs can be utilised to develop high performance metallic lightweight structural components.

In order to capture the constitutive response of the SLM AlSi10Mg alloy, a uniaxial tension coupon test was conducted, which has shown that the parent material had anisotropic plasticity and damage. The constitutive model for the parent material employed in the simulations included elasticity, rate dependent plasticity and damage. However, the anisotropic plasticity and damage of the parent material was not included. FE simulations were seen, in general, to be in good agreement with experimental measurements. The failure modes of the honeycombs have been captured reasonably by FE predictions.

Chapter 4

Dynamic Compressive Response of Nomex Honeycombs

Abstract

In Chapter 3, the compressive response of AlSi10Mg alloy hierarchical honeycombs was investigated. In this chapter, the lightweight phenolic resin-impregnated aramid paper honeycombs, commercially known as Nomex[®] honeycombs, will be studied. Nomex honeycombs are promising cores for sandwich structures in aerospace applications due to their high ratios of stiffness and strength to density. The out-of-plane compressive properties of the Nomex honeycombs have been widely investigated under quasi-static and low strain rates (up to 300 s^{-1}). There is a need to understand the behaviour of this structure under higher strain rate compression. This will widen the applicability of these structures to more areas such as debris impact and other impacts which induce high strain rates. This chapter reports the out-of-plane compressive responses of Nomex honeycombs subject to quasi-static loading and high strain rate dynamic loading up to 1500 s^{-1} . The work involves experimental measurements and numerical modelling and validation. The compressive responses of the honeycombs were measured using a sensitive magnesium alloy Kolsky bar setup with front and back face impacts. The failure modes of the Nomex honeycombs were identified to be different under quasi-static and dynamic compressions. Under quasi-static compression, the honeycombs failed with local phenolic resin fracture after the elastic buckling of the honeycomb walls. For the dynamic

compression, the honeycombs failed with the stubbing of cell walls at the ends of specimens. A finite element (FE) numerical model was devised and validated with the experimental data. The FE model considered the strain rate effect of phenolic resin material. The model predictions were in good agreement with the experimental measurements and facilitated interpreting the out-of-plane compressive response of the Nomex honeycombs. It was shown that there was a linear compressive strength enhancement up to 30% from quasi-static to strain rate of 1500 s^{-1} . The strength enhancement was governed by two mechanisms: the strain rate effect of the phenolic resin and inertial stabilization of the honeycomb unit cell walls, where 61%-74% of the enhancement was contributed by the inertial stabilization of the unit cell walls. In addition, it was shown that the impact method and initial imperfections had negligible effect on the compressive response of the Nomex honeycombs.

4.1 Introduction

Due to terrorist attacks, wars and other uncontrollable factors, there is a great need to model impact from fragments, ballistic elements, debris and other projectiles that induce high strain rates. Hence, there is an urgent need to understand the performance of Nomex honeycombs under such high strain rates. The dynamic compressive response of Nomex honeycombs under strain rates higher than 300 s^{-1} has not yet been reported. Also, as neither the Pendulum impactor technique [114] nor drop weight measurements [111] with a load cell will be able to detect the compressive response of low-strength honeycombs under high strain rate impact, novel experimental methodology needs to be

developed for measuring the compressive response of Nomex honeycombs under high strain rates.

Although the studies on strength enhancement mechanisms of similar types of honeycomb structures have been performed, as reviewed in Section 2.2.4 of Chapter 2, there exists no related investigation on Nomex honeycombs under dynamic compression. Finite element simulation is an effective method to reproduce the compressive response and identify the enhancement mechanisms of Nomex honeycombs. Such simulations at high strain rates, however, have not yet been reported.

The aim of the present study is to experimentally investigate the out-of-plane dynamic compressive behaviour at high strain rates (up to 1500 s^{-1}) and develop a validated FE model of the Nomex honeycombs. The outline of this chapter is as follows. First, the configuration of the Nomex honeycomb specimen as well as the experimental protocols are described. Then the finite element simulation methodology for Nomex honeycombs under quasi-static and dynamic compressions is developed. Finally, the experimental measurements and finite element predictions are discussed to determine the compressive failure modes and the strength enhancement mechanisms of Nomex honeycombs.

4.2 Nomex honeycomb specimen

This study investigates the Nomex honeycomb specimen, with density and out-of-plane thickness of $\rho = 54 \text{ kgm}^{-3}$ and $H = 10 \text{ mm}$, respectively. The manufacturing process of the honeycombs is described as follow: the Nomex

aramid paper layers made from random aramid fibres are stacked on top of each other and adhered by strips of thermoset epoxy adhesive at intervals. The hexagonal unit cells are formed by expanding the honeycombs along the stacking direction of the paper layers. Finally, the expanded geometry is impregnated into phenolic resin until the specific density of the honeycombs achieved [224]. Figures 4.1 (a) and (b) show the three-dimensional geometry of the Nomex honeycombs and the in-plane structure of its hexagonal unit cell, respectively. The scanning electron microscopic (SEM) image of the wall joints between the unit cells is shown in Fig. 4.1 (c). The wall joints are defined as the wall intersections of three adjacent unit cells. In addition, the axes of 1, 2 and 3 represent the directions of width L_w , length L_L and out-of-plane thickness H of the Nomex honeycomb specimen, respectively. The cell walls of the Nomex honeycombs are three-layer structures, i.e. an aramid paper layer is sandwiched by two phenolic resin layers on each surface of the aramid paper layer. The thicknesses of the single aramid paper layer and phenolic resin layer are $t_f = 70 \mu\text{m}$ and $t_r = 12 \mu\text{m}$, respectively, which are determined by the SEM image analysis. The characteristic cell size of the honeycombs is defined as $L_c = \sqrt{3}l_c = 4.8 \text{ mm}$, with l_c as the edge length of the hexagonal unit cell, see Fig. 4.1 (b). The dimensionless relative density of the honeycombs can be defined as a function of cell wall thickness and edge length of the unit cell [8, 225]

$$\bar{\rho} = \frac{\rho}{\rho_w} = \frac{(l_c/2 + l_c + l_c/2)t_N}{(\sqrt{3}/2)l_c(l_c/2 + l_c/2 + l_c/2)} = \frac{8t_N}{3\sqrt{3}l_c} \quad (4.1)$$

where ρ_w is the density of the cell walls of the Nomex honeycombs. t_N ($t_N = t_f + 2t_r$) is the single-wall thickness of the unit cell geometry.

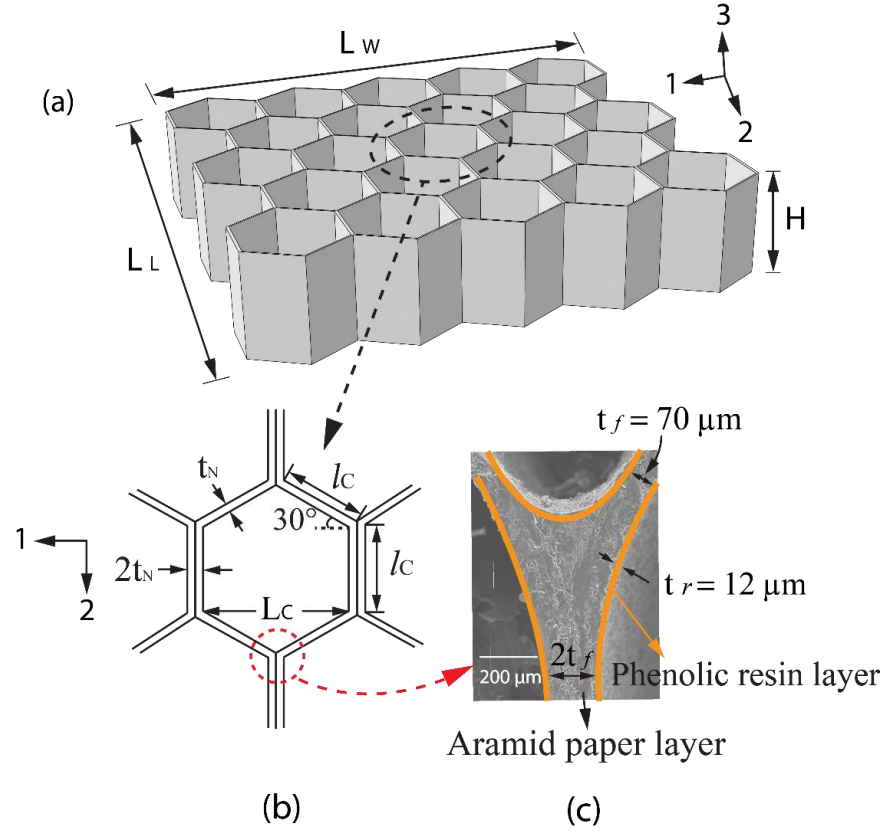


Fig. 4.1 (a) Three-dimensional sketch of the Nomex honeycombs and (b) the in-plane sketch of a unit cell. (c) The scanning electron microscopic (SEM) photograph at the wall joint.

4.3 Experimental protocols

4.3.1 Quasi-static compression testing

Figure 4.2 shows the quasi-static out-of-plane compression test setup for Nomex honeycombs. The quasi-static tests were conducted using an Instron® 5581

screw driven testing machine with a 50 KN load cell. Two Linear Variable Differential Transformers (LVDT) installed symmetrically were employed for measuring the transverse deformation δ of honeycomb specimen, and the transverse force F of the honeycombs was determined by the load cell. The sources of LVDT errors are mainly from the following three factors. First, the LVDT has linearity error. Second, the surface of specimen is not flat. Third, LVDT is not set straightly. In this study, the linearity error of the LVDTs used was $\pm 0.25\%$ of full range output, which can be neglected. The errors caused by the last two factors can be eliminated via applying pre-stress on the honeycombs and setting the LVDTs straightly. Hence, the errors of the LVDTs are negligible in this test, and the accuracy of the LVDTs is much higher than that of the crosshead.

To ensure the compression was quasi-static, the honeycomb specimens were compressed in 3 direction at a constant displacement rate of 0.5 mm/min. The Nomex honeycomb specimens of in-plane length $L_L = 65$ mm, width $L_W = 65$ mm and 175 unit cells are used. The nominal compressive stress and strain of the honeycomb specimens were taken as $\sigma = F / A_0$ and $\varepsilon = \delta / H$, respectively, with $A_0 = 65 \times 65 \text{ mm}^2$ as the original cross-sectional area of the honeycomb specimen. The average wall stress $\bar{\sigma}$ of the honeycombs can be defined in terms of nominal compressive stress σ and relative density $\bar{\rho}$, i.e.

$$\bar{\sigma} = \sigma / \bar{\rho}.$$

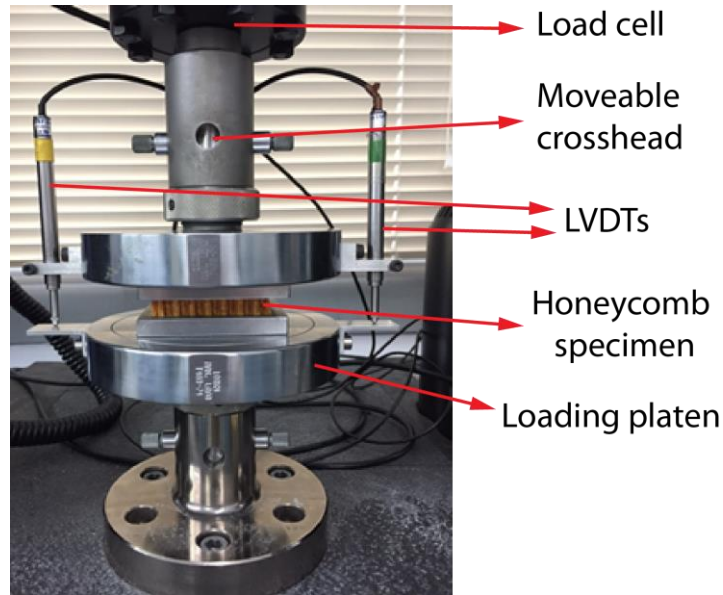


Fig. 4.2 Quasi-static experimental setup for determining the compressive response of Nomex honeycomb.

4.3.2 Dynamic compression testing

The honeycomb specimens of in-plane length $L_L = 18$ mm, width $L_W = 18$ mm and 14 unit cells were used for dynamic out-of-plane compression tests. The dynamic out-of-plane compressive characteristics of the Nomex honeycombs were investigated in a series of direct impact tests using a strain-gauged magnesium alloy Kolsky bar setup [33, 226] which was similar to the maraging steel Kolsky bar setup used in Chapter 3. The transient forces on the distal end and impacted end of the honeycomb specimens were measured using back face and front face impact tests, respectively. For the back face impact, a specimen attached to the impact end of the Kolsky bar was impacted centrally by a striker that was fired from a gun barrel, see Fig. 4.3 (a). For the front face impact, a specimen was adhered to the impact end of a striker that was fired from the gun

barrel and impacted on the Kolsky bar, see Fig. 4.3 (b). The sketch of the three-dimensional honeycomb specimen at the point of impact is shown in Fig. 4.3 (c). In order to be able to measure the low compressive force of the Nomex honeycomb specimen and improve the response sensitivity of the measurement apparatus, the Kolsky bar made from magnesium alloy [226] (grade AZ61A) with low elastic modulus of $E_m = 45$ GPa and compressive yield strength of $\sigma_m = 130$ MPa was employed. The mechanical properties of magnesium AZ61A alloy is summarized in Table 4.1. The Kolsky bar had a length of 1 m and a diameter of $D_m = 25.5$ mm. The Kolsky bar was in alignment with the gas gun and supported by four knife-edge friction-reducing Nylatron bearings. The impact end of the Kolsky bar was positioned 110 mm from the muzzle of the gas gun, and the bar was resisted at the distal end by an ACE MA 4757M self-adjusting shock absorber. The stress history of the specimen was measured by two diametrically opposite 120 Ω TML foil strain gauges, which were placed 200 mm from the impact end of the Kolsky bar, of gauge length 1 mm in a half-Wheatstone bridge. The stress history, recorded as a voltage change, was amplified by a Vishay 2310B signal conditioning amplifier system and then output onto an Instek DPO3014 100 MHz 4-channel Digital Oscilloscope.

Table 4.1 The mechanical properties of magnesium AZ61A alloy.

Properties	Value
Density	1800 kgm ⁻³
Poisson's ratio	0.35
Elastic modulus	45 GPa
Tensile strength	310 MPa
Compressive yield strength	130 MPa
Shear strength	140 MPa
Elongation at break	16%
Hardness, Brinell	60

Same as the striker used for impacting AlSi10Mg alloy hierarchical honeycombs, the strikers used to impact Nomex honeycombs were made from M300 maraging steel with elastic modulus of $E_s = 210$ GPa and yield strength of $\sigma_s = 1900$ MPa, and had a diameter of $D_s = 27.5$ mm. To ensure that the magnesium alloy Kolsky bar is elastically deformed under direct impact of the strikers (without specimen being placed between the striker and the Kolsky bar), the maximum impact velocity of the steel strikers, $v_{s-\max}$, can be calculated based on the elastic wave theory as follows:

$$v_{s-\max} = \frac{\sigma_m (A_s \rho_s c_s + A_m \rho_m c_m)}{A_m \rho_s c_s \rho_m c_m} \quad (4.2)$$

where $\rho_m = 1800 \text{ kgm}^{-3}$, $c_m = \sqrt{\frac{E_m}{\rho_m}}$ and A_m are the density, elastic wave

velocity and cross sectional area of the magnesium alloy bar, respectively;

$\rho_s = 7800 \text{ kgm}^{-3}$, $c_s = \sqrt{\frac{E_s}{\rho_s}}$ and A_s are the density, elastic wave velocity and

cross sectional area of the steel strikers, respectively.

It is calculated that the steel strikers of impact velocity more than 20 ms^{-1} can lead to the yield of the magnesium alloy Kolsky bar when there is no specimen between the striker and the Kolsky bar. In the present study, the initial velocity of the steel striker is no more than 15 ms^{-1} when impacting specimens. Two cylindrical strikers of different masses were employed in the impact tests in order to achieve the required striker velocities and provide constant velocity during the dynamic compression: a small striker of length 0.1 m and mass 0.463 kg was used for velocity range of $9 \leq v_0 \leq 15 \text{ ms}^{-1}$, and a larger striker of length 0.5 m and mass 2.3 kg was used for velocity range of $4.5 \leq v_0 \leq 9 \text{ ms}^{-1}$. The strikers were accelerated by a pressurised gas gun, in which strikers were propelled by compressed air. The gas gun had a barrel length of 3.5 m , outer diameter of 40 mm and internal diameter of 28 mm . The initial velocity of the striker was measured at the open end of the gun barrel via two laser gates and confirmed with a Phantom Mercury HS v12.1 high-speed camera. Typically, the frame rate and exposure time were $40,000 \text{ fps}$ and $20 \text{ }\mu\text{s}$, respectively. As analysed in Section 4.6.1, the force equilibrium in Nomex honeycomb specimen has been achieved during the time scale in the dynamic compression tests.

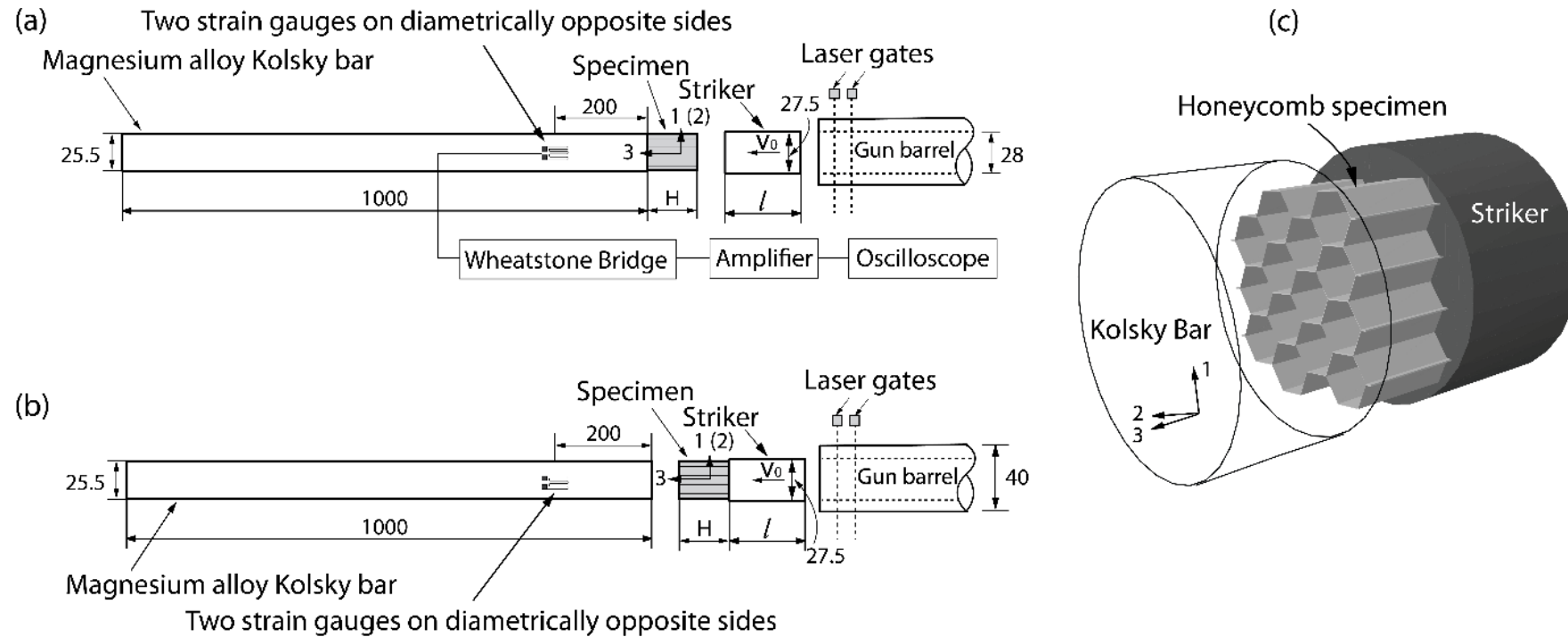


Fig. 4.3 Sketch of the Magnesium alloy Kolsky bar setup in (a) back face and (b) front face impact tests, and (c) the three-dimensional sketch at the impact point. All dimensions are in mm.

4.4 Finite element simulation

4.4.1 Finite element model

Numerical simulations were conducted to simulate the quasi-static and dynamic compressive responses of the Nomex honeycombs using the explicit solver of the commercial finite element package ABAQUS® [222]. The primary aims of the numerical investigation are:

- To develop an accurate three-dimensional finite element model to predict the compressive response of Nomex honeycomb structure under quasi-static and dynamic loading.
- To facilitate interpreting the role of the strain rate effect and inertial effect on enhancing the dynamic compressive strength of Nomex honeycomb structure.
- To understand the effects of the key parameters on the out-of-plane compressive response of the Nomex honeycombs.

Figure. 4.4 shows the finite element model of Nomex honeycombs. In order to capture the wall buckling and failure of the honeycomb specimen, the aramid paper layer and phenolic resin layer were modelled separately. Both the aramid paper layer and phenolic resin layer were modelled with 8-node 3D linear solid elements (C3D8R in ABAQUS notation) with reduced integration. Under uniaxial out-of-plane compression, the Nomex honeycombs mainly resisted force in loading direction, whereas the in-plane stress of the phenolic resin layers is low. Although there was only one element along each of the single aramid paper layer and phenolic resin layer thickness, the honeycombs of layers modelled with 8-node 3D solid elements, which had more nodes and degrees of

freedom in each element than each shell element, have had a good convergence. In addition, it takes huge time and memory if there are two or more elements along the layer thickness. Hence, the convergence of single layer mesh can be guaranteed. The interaction of the interfaces between the aramid fibre layer and the phenolic resin layers was modelled as tie in ABAQUS notation, i.e. there is no relative displacement between the aramid fibre layer and the phenolic resin layers. To achieve converged solution, a mesh sensitivity analysis was carried out which determined that the element size of the honeycombs needed to be less than 0.15 mm. The FE model of the honeycomb specimen was sandwiched by two rigid plates with 4-node discrete rigid elements (R3D4 in ABAQUS notation) in 3 direction. One of the rigid plates was fully constrained (all translational and rotational directions), and the other rigid plate was restricted to translate in 3 direction only.

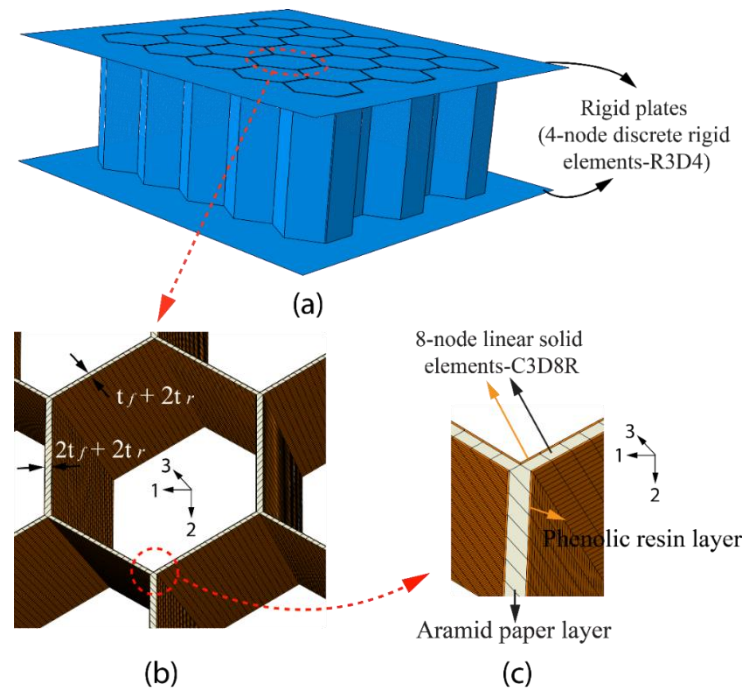


Fig. 4.4 Finite element (FE) model of (a) Nomex honeycombs sandwiched by two rigid plates, (b) a honeycomb unit cell and (c) wall joint.

For the quasi-static compression simulation, the movable rigid plate imposed loading on the honeycomb specimen with a constant velocity. To ensure the simulation was quasi-static, the kinetic energy was controlled to be under 5% of the total energy in the system. For the dynamic compression simulation, the movable rigid plate was associated with a mass point and an initial impact velocity that were identical to those of the strikers employed in the impact tests. In the back face impact, the honeycombs were tied to the fixed rigid plate and crushed by the movable rigid plate. In the front face impact, the honeycombs were tied to the movable rigid plate and moved together with the plate to impact on the fixed rigid plate. A general contact option with a friction coefficient of 0.05 was employed in all finite element calculations to simulate the interaction. A total of 134,000 elements were meshed for aramid paper layers, and 213,000 elements were meshed for phenolic resin layers.

4.4.2 Constitutive model for aramid paper layer

The constitutive model for the aramid paper layer included elasticity and rate independent plasticity. The elastic response of aramid paper layer was modelled using linear elasticity model for an isotropic solid with density $\rho_{ap} = 1075 \text{ kgm}^{-3}$, elastic modulus $E_{ap} = 2.36 \text{ GPa}$ and Poisson's ratio $\nu_{ap} = 0.3$. The J2 yield criterion in conjunction with isotropic hardening was used as the plasticity model of aramid paper layer.

There is a significant shortage of experimental study on the compressive behaviour of the aramid paper layer. Available research mainly focuses on the

tensile behaviour. In the present study, the compressive behaviour of the aramid paper layer is assumed to be identical to the tensile behaviour [72] . As the compressive strength of aramid fibre is normally lower than the ultimate tensile strength [227], the assumption may overestimate the compressive strength of the aramid paper layer. Figure 4.5 (a) shows the tensile responses of the aramid paper layer in 0° (paper roll direction), 90° (transverse direction) and 45° , respectively, reported by Roy et al. [120]. The tensile strengths of the aramid paper layer in the three directions were much lower than the compressive strength of the phenolic resin layers. Therefore, the mechanical properties of aramid paper layer have limited effect on the compressive response of Nomex honeycombs. The numerical simulation conducted in this study using the experimental data in 45° from Roy et al. [120] suggested this data gave the best fit for the experimental measurements of the Nomex honeycombs. Thus, the experimental data in 45° obtained by Roy et al. [120] was used as the input to the constitutive model to specify the yield stress-plastic strain relation of the aramid paper layer. Here, we assume that the aramid paper layer is strain rate independent. The effect of strain rate dependency of aramid paper layer on the dynamic compressive response of Nomex honeycombs will be discussed in Section 4.6.5.

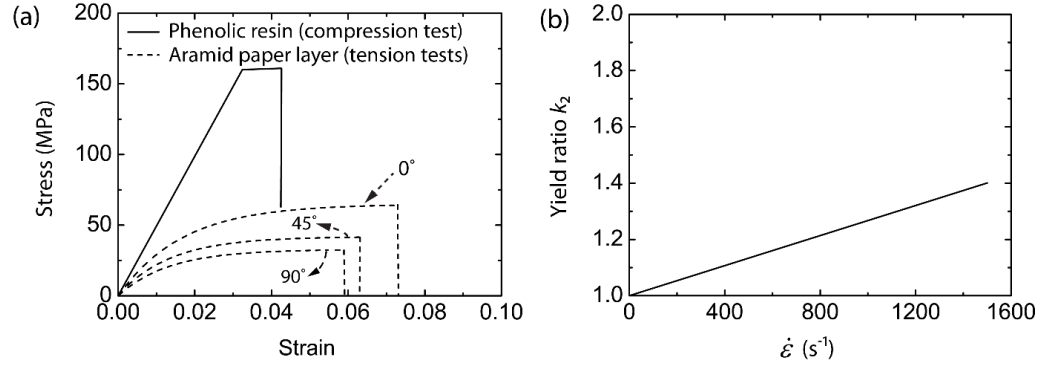


Fig. 4.5 (a) The stress-strain relations of aramid paper layer [121] and compressive response of phenolic resin layer [228]. (b) The yield ratio rate-dependent model of phenolic resin layer.

4.4.3 Constitutive model for phenolic resin

The constitutive model for the phenolic resin layer included elasticity and rate dependent plasticity [86]. Similar to the aramid paper layer, the elastic response of phenolic resin layer was modelled using linear elasticity model for an isotropic solid with density of $\rho_r = 1100 \text{ kg} \cdot \text{m}^{-3}$, elastic modulus of $E_r = 4.94 \text{ GPa}$ and Poisson's ratio of $\nu_r = 0.3$. The J2 yield criterion combined with isotropic hardening was employed to model the plasticity. The compressive behaviour of the phenolic resin can be modelled as elastic-perfectly plastic before failure [228], as shown in Fig. 4.5 (a). The experimental data reported by Kilchert [228] was used as the input to the constitutive model to define the yield stress-plastic strain relation of the phenolic resin. The following yield ratio rate-dependent model [229] was employed to capture the rate dependency of the phenolic resin material.

$$k_2 = \frac{\sigma_{rp}}{\sigma_{r0}} = C_N \dot{\epsilon}_p \quad (4.3)$$

where $\dot{\epsilon}_p$ is the von Mises equivalent plastic strain rate ; k_2 is the ratio of yield stress; σ_{r0} and σ_{rp} are the compressive yield stresses of phenolic resin layer under quasi-static compression and dynamic compression, respectively; C_N is the material constant that was obtained via calibration against dynamic testing of the Nomex honeycombs, and was determined to be $C_N = 9.33 \times 10^{-4} \text{ s}$. Based on Eq. (4.3), the ratio of yield stress k_2 as a function of strain rate $\dot{\epsilon}_p$ at strain rates ranging from quasi-static value to 1500 s^{-1} is shown in Fig. 4.5 (b).

4.5 Quasi-static compressive response of Nomex honeycombs

The experimentally measured and FE predicted out-of-plane quasi-static compressive responses of the Nomex honeycomb specimen are shown in Fig. 4.6 for nominal stress-strain curve. The FE predictions show a good agreement with the experimental measurements. The specimen showed a linear elastic mechanical behaviour before achieving the peak compressive stress and had an abrupt softening after achieving the peak stress, then displayed hardening followed by the densification at a nominal compressive strain of $\epsilon = 0.75$. The compressive strength of the Nomex honeycomb specimen was measured to be $\sigma_{S-\max} = 3.09 \text{ MPa}$ at relative density $\bar{\rho} = 0.051$, corresponding to the average peak wall stress $\bar{\sigma}_{\max} = 60.6 \text{ MPa}$. The compressive strength of the honeycomb

sample was achieved at compressive strain $\varepsilon = 0.03$. This is the strain that the compressive strength of the phenolic resin layer was achieved, see Fig. 4.5 (a). The compressive strength of phenolic resin was significantly higher than the strength of aramid paper layer. Hence, the compressive response of phenolic resin layer played a dominate role in the failure of the Nomex honeycombs under compression.

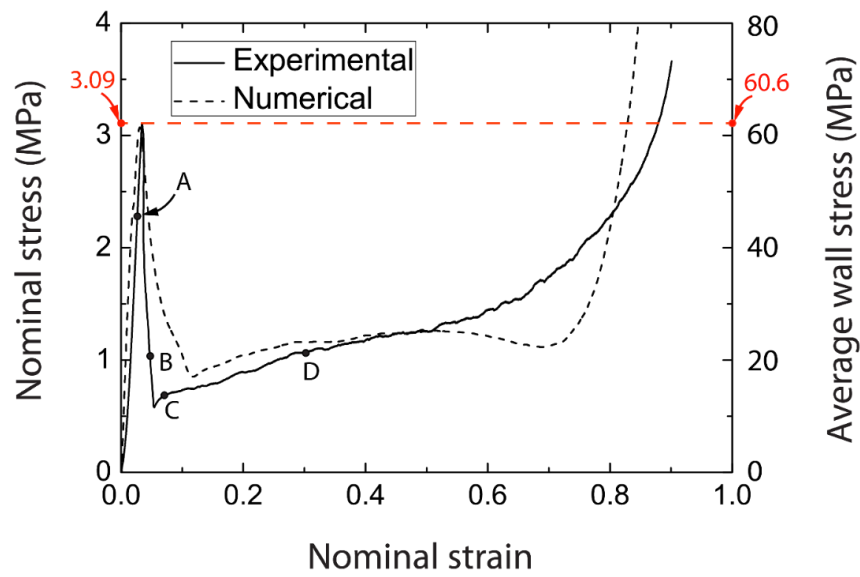


Fig. 4.6 Experimental measured and FE predicted stress-strain relationships of the Nomex honeycombs of density $\rho = 54 \text{ kg} \cdot \text{m}^{-3}$ and out-of-plane thickness $H=10 \text{ mm}$ under quasi-static compression.

The FE predicted contours of von Mises stress within the specimen at selected strain levels, both with and without showing the phenolic resin layer, are shown in Fig. 4.7. The selected strain levels can be related to Fig. 4.6 (Points A, B, C and D), which range from elastic behaviour to post peak compressive stress behaviour. The numerical simulation suggested that the Nomex honeycomb

walls first elastically buckled before achieving the compressive strength, as shown in Fig. 4.7 (a) at strain level A. At strain level B, the fracture of the phenolic resin layer was observed to be initiated at the mid-height area of the specimen. The fractured area was shown via the SEM image in Fig. 4.8 (a). For clarity, the three dimensional view of a unit cell taken from the middle of the specimen is shown in Fig. 4.7 (b). It can be seen that the stress at the junctions of the cell webs is higher than that in the middle of the cell webs owing to higher structural stability. At the hardening stage (strain levels C and D), the aramid paper layers of the specimen folded at the location of the fractured phenolic resin layer. The SEM images of the top view of the honeycomb unit cell at the strain level D (Fig. 4.8 (b)) suggested that there was no significant damage at the junctions of unit cell webs.

It should be noted, according to the manufacturing process, that the structure of Nomex honeycomb wall is similar to the typical sandwich structures: the weak aramid paper layer is the core of sandwich and the stiff phenolic resin layer is the face sheet of sandwich. Although the stiffness and strength of sandwich core is negligible relative to those of face sheets under in-plane compression, the core improves the stability of the face sheets and prevents the face sheet from premature buckling. The sandwich structures typically failed with face buckling, crushing and debonding, depending on the span length, face sheet thickness as well as core thickness [230, 231]. However, no debonding occurs [72, 120] between aramid paper layer and phenolic resin layer ascribed to the good integrity under out-of-plane compression.

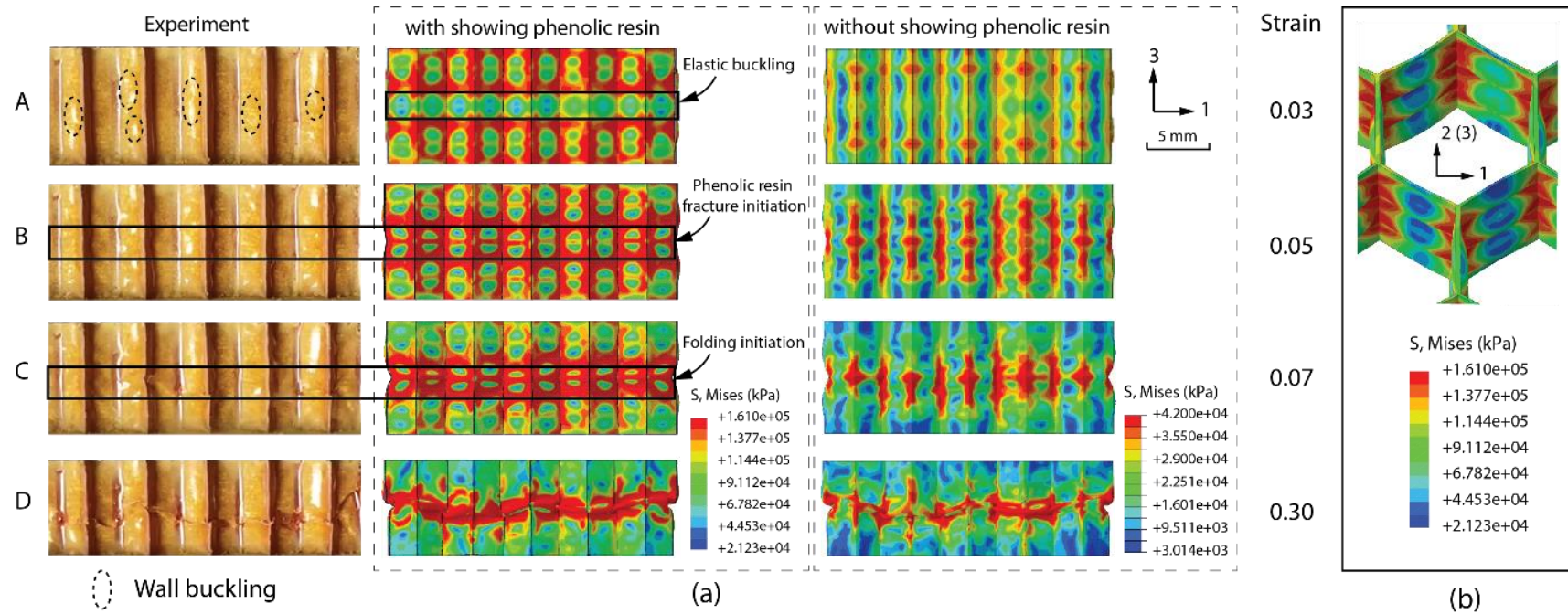


Fig. 4.7 (a) Montage of the Nomex honeycombs under quasi-static compression obtained from experimental measurements and numerical simulations, and (b) three-dimensional view of the unit cell taken from the middle of the FE honeycomb model at strain level B. The strain levels A-D refer to the Points A-D in Fig. 4.6.

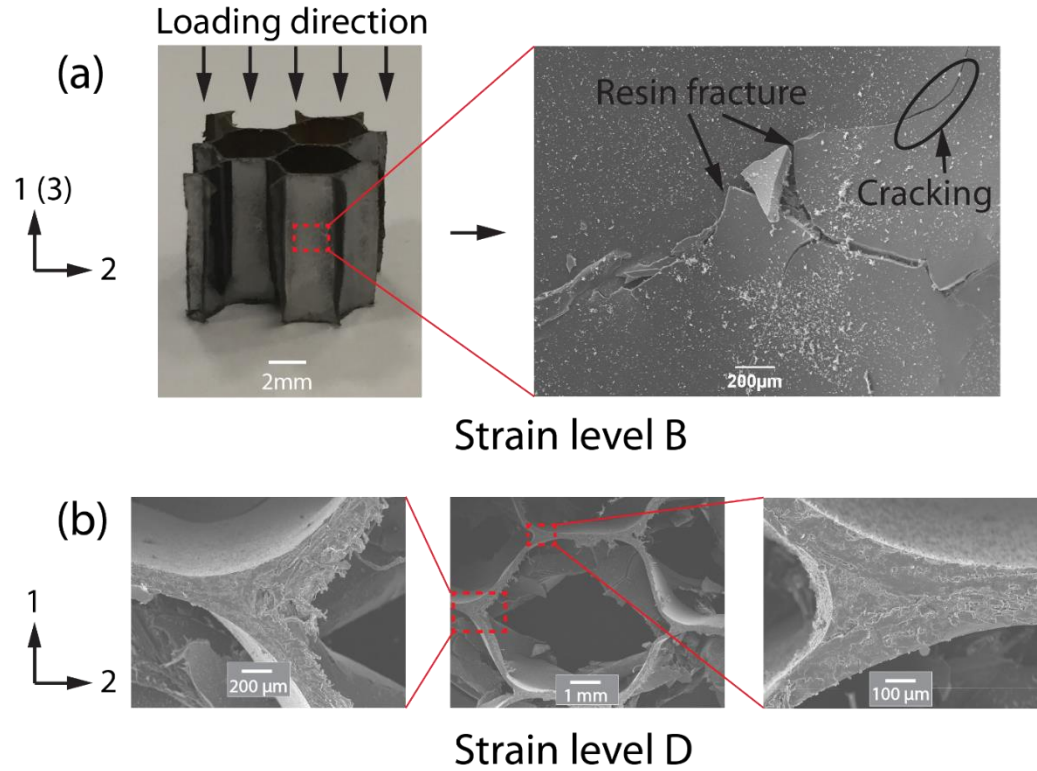


Fig. 4.8 Scanning electron microscopic (SEM) photographs of (a) the Nomex honeycomb wall at strain level B, and (b) top view of the honeycomb unit cell after quasi-static compression at strain level D, respectively. It is noted that the left image in (a) was taken by normal camera. The strain levels B and D refer to the Points B and D in Fig. 4.6, respectively.

4.6 Dynamic compressive response of Nomex honeycombs

4.6.1. Back face impact

The dynamic compressive response of the honeycomb specimen under back face impact is discussed next. The experimentally measured and FE predicted nominal compressive stresses versus the normalised time $v_0 t / H$ at four selected impact velocities are shown in Fig. 4.9. Both experimental measurement

and FE prediction confirmed that the strikers had constant velocity during the impact events. Hence, the compressive strain rates within the samples for the four selected impact velocities can be calculated as 150 s^{-1} (Fig. 4.9 (a)), 900 s^{-1} (Fig. 4.9 (b)), 1050 s^{-1} (Fig. 4.9 (c)) and 1500 s^{-1} (Fig. 4.9 (d)). To ensure the accuracy of the measured compressive response of the honeycomb specimen, it is necessary to confirm the force equilibrium during the dynamic impact events.

Using the elastic modulus and density of the aramid paper layer as well as the phenolic resin layer in Section 4.4.2 and Section 4.4.3, we determined the

longitudinal elastic wave speeds to be $c_{ap} = \sqrt{\frac{E_{ap}}{\rho_{ap}}} = 1482 \text{ ms}^{-1}$ and

$c_r = \sqrt{\frac{E_r}{\rho_r}} = 2119 \text{ ms}^{-1}$ for the aramid paper layer and phenolic resin layer,

respectively. The measured compressive strength of the specimen was achieved at $76 \mu\text{s} \leq t \leq 111 \mu\text{s}$ after impact. Hence, there were about 13 elastic wave reflections took place in the aramid paper layer and 19 elastic wave reflections took place in the phenolic resin layer when the compressive strength of the honeycombs achieved. Hence, it is concluded that the axial force equilibrium of the specimen was established when measuring the compressive strength.

As shown in Fig. 4.9, the dynamic compressive strengths under different strain rates are higher than that under quasi-static compression. Unlike the catastrophic failure under quasi-static compression, the dynamic compressive stress decreased smoothly after achieving the peak values. The compressive strengths of the honeycomb specimens obtained from the FE simulations agreed well with

the experimental measurements. Due to the response time of the Kolsky bar setup [221], the normalised time $v_0 t / H$ was different between experimental measurements and numerical simulations.

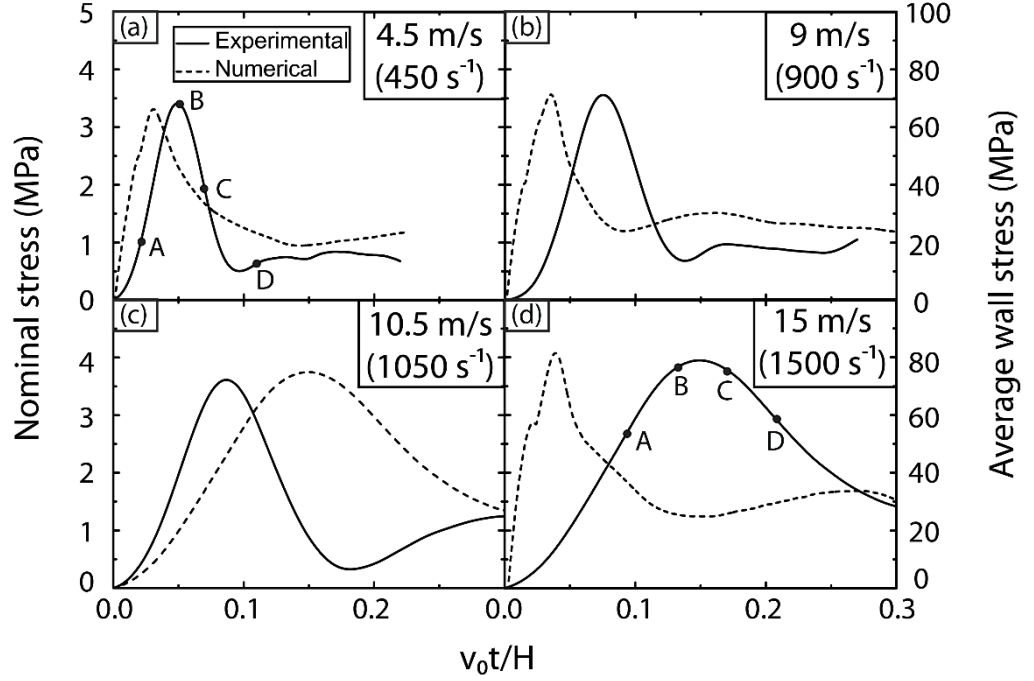


Fig. 4.9 Nominal compressive stress of Nomex honeycombs as a function of normalised time $v_0 t / H$ obtained from the back face impact tests at different strain rates of (a) 450 s⁻¹, (b) 900 s⁻¹, (c) 1050 s⁻¹ and (d) 1500 s⁻¹, respectively.

The montages of high-speed photographic images as well as the FE predictions at strain rates of 450 s⁻¹ and 1500 s⁻¹ are shown in Figs. 4.10 and 4.11, respectively, for selected time instants A, B, C, D (see Fig. 4.9) .

The walls of honeycomb specimen buckled before the peak compressive strength achieved in the impact events, as shown in Fig. 4.10 (a) and Fig. 4.11 (a). When the peak compressive strength achieved, the concentrated stress transferred to

the ends of the honeycomb specimens, as shown in Fig. 4.10 (b) and Fig. 4.11 (b). Then the unit cell walls stubbed against the faces of the Kolsky bar as well as the strikers. The folded locations of honeycomb walls were close to the ends of the specimen. The FE predictions showed that the maximum stress increased with the increase of impact velocity due to the strain rate sensitivity of the phenolic resin layer.

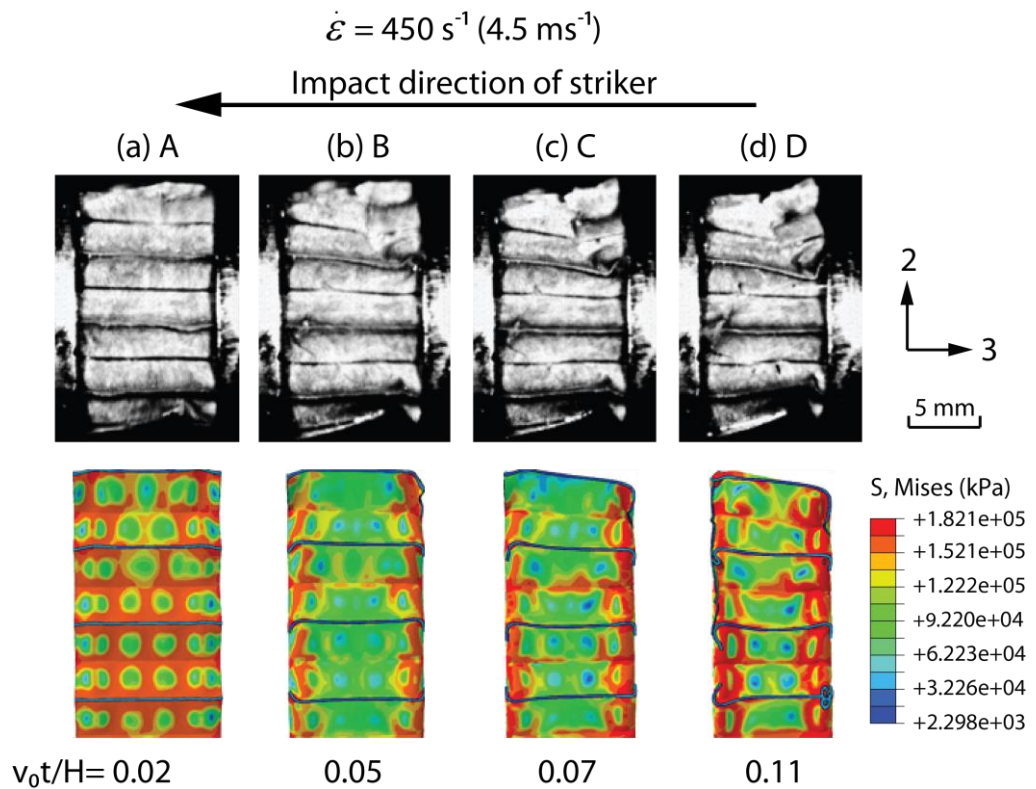


Fig. 4.10 Montage of high speed photographs showing the deformation patterns of the Nomex honeycombs under back face impact at strain rate of 450 s^{-1} obtained from experiment and numerical simulations. The time instants A-D refer to the Points A-D in Fig. 4.9 (a).

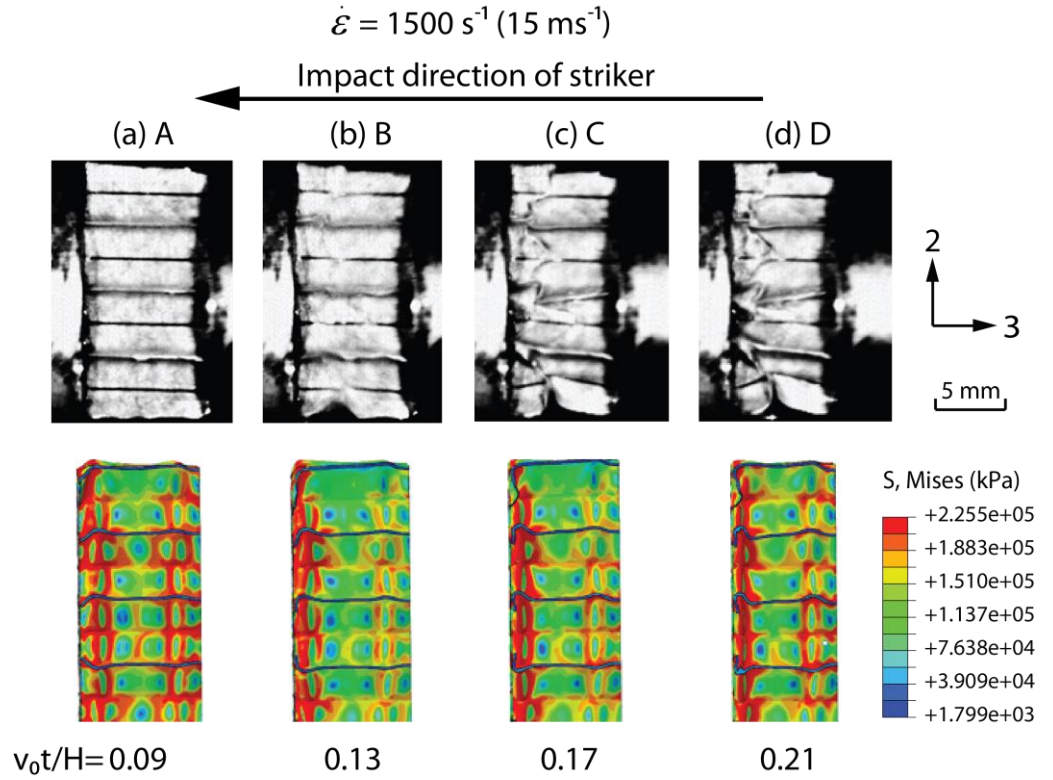


Fig. 4.11 Montage of high speed photographs showing the deformation patterns of the Nomex honeycombs under back face impact strain rate of 1500 s^{-1} obtained from experiment and numerical simulations. The time instants A-D refer to the Points A-D in Fig. 4.9 (d).

Figure 4.12 (a) shows the dependence of the dynamic peak compressive stress σ_{D-max} under back face impact normalised by the measured quasi-static peak compressive stress σ_{S-max} of honeycomb specimen upon the imposed strain rate $\dot{\epsilon}$. The peak compressive strengths of the honeycomb specimens increased linearly by approximately 30% from quasi-static to strain rate of 1500 s^{-1} . According to the FE calculations under dynamic compression, the strength enhancement is achieved from the inertial stabilization of the honeycomb cell

walls and the strain rate sensitivity of the phenolic resin layer. The FE model predicts the effects of these two enhancement mechanisms on the dynamic strength enhancement, as given in Fig. 4.12 (b). P_{ST} (%) and P_{IN} (%) are the percentages of strain rate effect of phenolic resin layer and inertial effect of unit cell walls in enhancing the dynamic compressive strength of the honeycombs, respectively. They are defined as

$$\begin{cases} P_{ST} = \frac{\sigma_{ST}}{\Delta\sigma_{EN}} \\ P_{IN} = \frac{\sigma_{IN}}{\Delta\sigma_{EN}} \end{cases} \quad (4.4)$$

where $\Delta\sigma_{EN}$ is the enhanced compressive strength of Nomex honeycombs compared to the quasi-static compressive strength, defined as $\Delta\sigma_{EN} = \sigma_{D-max} - \sigma_{S-max}$; σ_{ST} and σ_{IN} are the enhanced compressive strengths caused by the strain rate effect of phenolic resin layer and inertial effect of the unit cell walls, respectively.

The relationship between the two factors, P_{ST} and P_{IN} , is $P_{ST} + P_{IN} = 100\%$.

The effect of the two factors on enhancing the dynamic compressive strength of Nomex honeycombs can be evaluated with and without considering the strain rate effect of phenolic resin in the FE calculations. It indicates that the inertial stabilization of cell walls, providing 61%-74% enhancement, plays a more significant role than the strain rate effect of phenolic resin material in enhancing the dynamic compressive strength of the Nomex honeycombs.

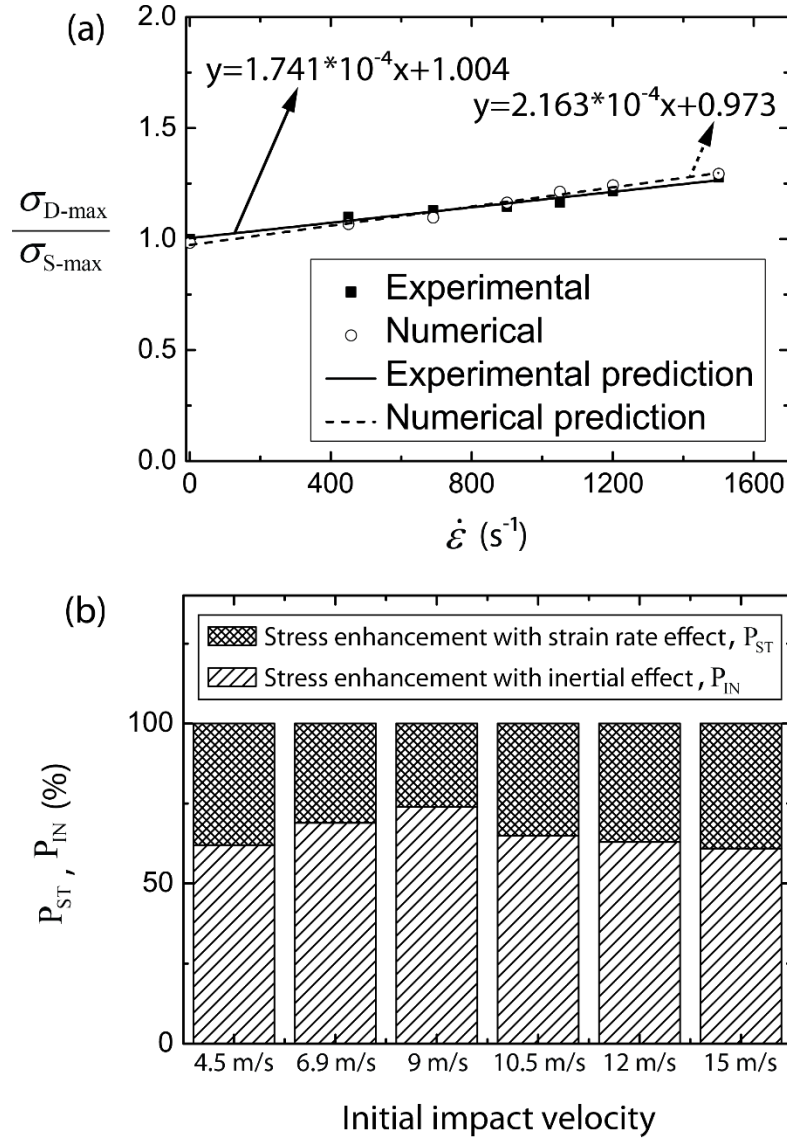


Fig. 4.12 (a) The dynamic peak compressive stress of the Nomex honeycombs under back face impact normalised by the experimentally measured quasi-static peak compressive stress as a function of strain rate $\dot{\epsilon}$, and (b) the contributions of two key factors, strain rate effect of phenolic resin and inertial stabilization of unit cell walls, to the compressive strength enhancement of the Nomex honeycombs under dynamic compression.

4.6.2 Effect of the experimental method

For the two impact configurations of back face and front face dynamic compressions, the plastic shock wave propagated oppositely within a honeycomb specimen. Hence, the dynamic compressive response of the honeycombs in back face impact configuration may be different from that in front face impact configuration. Figure 4.13 demonstrates that the compressive responses of the honeycombs with two impact methods are almost identical both at low impact velocity (Fig. 4.13 (a)) and high impact velocity (Fig. 4.13 (b)). The similar compressive responses under back face and front face compressions suggest that the specimens are in stress equilibrium over the deformation history. In addition, the finite element predictions conducted on the front face impact agreed well with the experimental measurements.

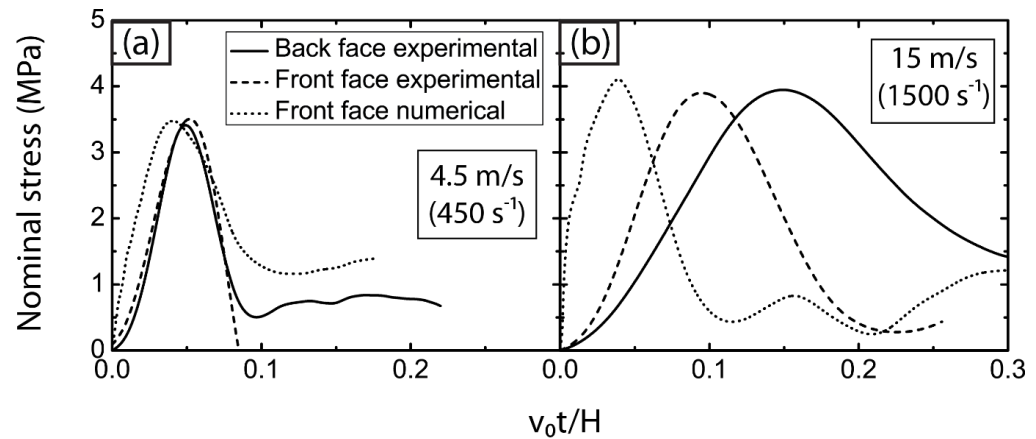


Fig. 4.13 Nominal compressive stress of the Nomex honeycombs as a function of $v_0 t / H$ at selected impact velocities obtained from back face and front face experimental measurements as well as FE simulations.

4.6.3 Effect of strain rate sensitivity

As discussed in Section 4.6.1, the strain rate sensitivity of the phenolic resin is one of the important factors in enhancing the compressive strength of the honeycomb specimen under dynamic compression. Figure 4.14 shows the comparison of the FE predicted dynamic compressive responses of the honeycomb specimens, with and without material rate dependency, under back face impact at strain rates of 450 s^{-1} and 1500 s^{-1} . Though the phenolic resin has mild strain rate sensitivity, the peak compressive strengths of the honeycombs in rate dependent cases are just about 3% and 10% higher than those in rate independent cases at strain rates of 450 s^{-1} (Fig. 4.14 (a)) and 1500 s^{-1} (Fig. 4.14 (b)), respectively. This is due to the fact that the phenolic resin layer was thin and the aramid paper layer made from random aramid fibre [224, 228] was treated as a rate independent material.

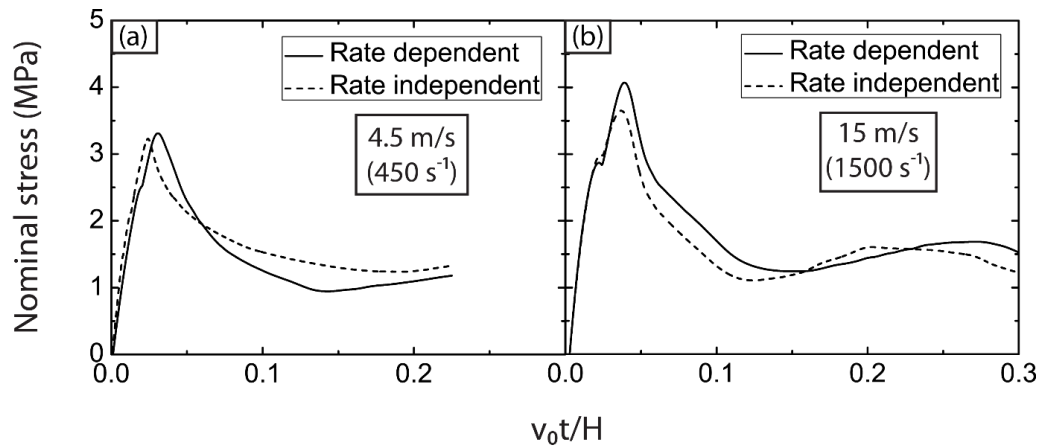


Fig. 4.14 FE study on the effect of strain rate sensitivity of the phenolic resin material at strain rates (a) 450 s^{-1} and (b) 1500 s^{-1} .

4.6.4 Effect of initial geometrical imperfections

In order to investigate the effect of the initial geometrical imperfections on the compressive response of the Nomex honeycombs, quasi-static buckling eigenvalue analysis of honeycombs was conducted via FE predictions to obtain the eigenmode. As the aramid paper layers had voids among random fibres [228] and were far thicker than the phenolic resin layers, we assumed the initial imperfections were mainly from the aramid paper layers. The effect of the magnitude of the initial imperfections on the compressive response of Nomex honeycombs was investigated, and only the lowest eigenmode was considered in the FE calculations. The lowest eigenmode was employed to introduce perturbation to the mesh of the aramid paper layer, with maximum imperfection amplitude 10% and 20% of the single-layer thickness of the aramid paper layer. Figure 4.15 shows the FE predictions for quasi-static and dynamic compressions. It suggests that the initial imperfections slightly decrease the peak compressive strength of honeycomb specimen but have a limited effect on the compressive response. Hence, the FE predicted compressive responses of the Nomex honeycombs are insensitive to the initial imperfections of amplitudes in the range 10%-20%.

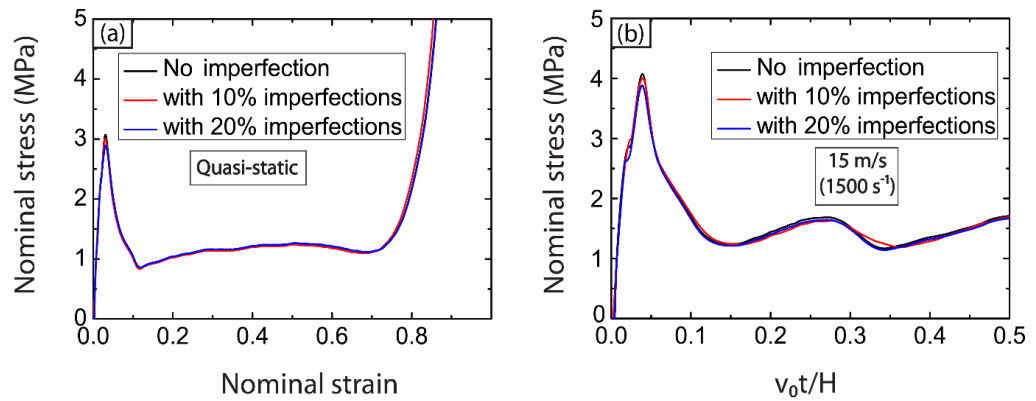


Fig. 4.15 FE predictions of the Nomex honeycombs with initial imperfections under (a) quasi-static compression and (b) back face impact at strain rate 1500 s^{-1} .

4.6.5 Effect of strain rate independency of aramid paper layer

As discussed in Section 4.5, the compressive strain for the compressive strength of Nomex honeycombs was identical to that for the compressive strength of the phenolic resin layer, whereas the aramid paper layer didn't reach the peak strength of the material when the honeycombs failed. Hence, the failure of the aramid paper layer was governed by the failure of the phenolic resin layer. Moreover, the strength of the aramid paper layer used in the present FE prediction is significantly lower than the strength of the phenolic resin layer. Hence, the strain rate effect of the aramid paper layer on enhancing the compressive strength of Nomex honeycombs was weak. Warrior et al. [184] reported that the failure of random fibre reinforced composite was governed by the matrix failure under high strain rate compression. Park et al. [86] also reported that the strain rate dependency of the matrix contributed to the strain

rate sensitivity of the carbon fibre composite square honeycombs. Thus the strain rate sensitivity of the phenolic resin layer played the dominate role in the strength enhancement contributed by the strain rate effect of material, and it was reasonable to assume that the aramid paper layer was strain rate independent.

4.7 Conclusion remarks

The out-of-plane compressive responses of the Nomex honeycombs of density 54 kg.m^{-3} and out-of-plane thickness 10 mm at strain rates ranging from quasi-static value to 1500 s^{-1} have been investigated. A series of dynamic impact tests were conducted with a magnesium alloy Kolsky bar setup. Finite element (FE) simulations were validated and used for facilitating the interpretation of the experimental measurements. The aramid paper layer and phenolic resin layer were modelled separately with different constitutive models.

Under quasi-static compression, the honeycomb specimen failed with catastrophic local fracture of phenolic resin layer after the elastic buckling of the honeycomb walls, which was followed by the aramid fibre layer folding at the location of the phenolic resin fracture. In addition, there was no significant damage at the wall joints as corroborated by the SEM image analysis. The compressive loading of the honeycombs before failure was principally carried by the coated phenolic resin layer. However, the aramid paper layer contributed to the high flexural rigidity of honeycomb walls that avoided the premature buckling of phenolic resin layer.

In the dynamic compression events, the honeycombs failed with stubbing of the cell walls at the ends of the specimens. Over the range of the strain rates applied from quasi-static to 1500 s^{-1} , the peak compressive strength of the honeycombs increased linearly by approximately 30%. The FE simulations demonstrated that two mechanisms enhanced the out-of-plane dynamic compressive strength: strain rate effect of the phenolic resin material and inertial stabilization effect of the honeycomb walls. The inertial stabilization of unit cell walls, contributing 61%-74% to the compressive strength enhancement of the Nomex honeycombs, played a more significant role. In addition, similar compressive responses of the honeycombs were obtained from two different impact tests, back face impact and front face impact.

Validated finite element simulation captured the experimental measurements reasonably. It demonstrated that the dynamic impact method as well as initial geometrical imperfections were insensitive to the out-of-plane compressive response of the Nomex honeycombs.

Chapter 5

Ballistic Resistance of Hybrid Carbon Fibre Laminate Beams

Abstract

In Chapter 3 and Chapter 4, the out-of-plane compressive responses of different honeycomb cores have been investigated. The current chapter will present the ballistic impact response of hybrid fibre composite beams that can be used as the face sheets of sandwich structures. The hybrid composites combining stiff composites with soft composites are developed to improve the ballistic impact resistance of fibre composite beams while maintaining good quasi-static loading bearing capacity. The failure modes and energy absorption capacity of the stiff/soft hybrid beams have been investigated experimentally under ballistic impact at a projectile velocity range of $50 \text{ ms}^{-1} \leq v_0 \leq 300 \text{ ms}^{-1}$, and were compared with those of the stiff and soft composite beams with identical areal mass. Both the monolithic and sandwich beams have been studied on the ballistic resistance. For each type of monolithic beams, i.e. stiff, soft and hybrid monolithic beams, three categories of failure modes have been identified: minor damage with rebound of projectile at low impact velocity, fracture of beam at medium impact velocity and perforation of beam at high impact velocity. The critical velocity of hybrid monolithic beam was similar to that of soft monolithic beam for the same failure mode, and higher than that of stiff monolithic beam.

This was attributed to the flexible matrix that dispersed the applied stress and increased the wave propagation time within the composites. For the sandwich beams with stiff, soft and hybrid face sheets, the failure modes were similar to those of the monolithic beams. Among the monolithic beams, the hybrid and soft monolithic beams exhibited better energy absorption capacity than the stiff monolithic beams. As for the sandwich beams, the hybrid-face sandwich beams absorbed more kinetic energy of projectile than the soft-face sandwich beams at higher projectile velocity, and the stiff-face sandwich beams behaved worst in energy absorption. The beams failed with fully fracture had better energy absorption capacity than those failed with perforation as more fibres fractured. The advantages of the stiff/soft hybrid construction include: (i) at lower impact velocity, the soft composite part survived with negligible damage under impact; (ii) due to the buffer effect of the soft part at the front face, stress within the stiff part of the hybrid monolithic/sandwich beams can have a more uniform distribution than that of the stiff monolithic/sandwich beams. The current investigation provides a new concept for designing the high-performance fibre composites against ballistic impact.

5.1 Introduction

Fibre reinforced composites have received increasing attention in military and civilian applications due to their outstanding mechanical properties. It has been demonstrated that lightweight structures made from fibre composites possess excellent performance to resist ballistic impact when the composites laminate is in $[0^\circ/90^\circ]$ cross-ply lay-up [18, 232]. The hybrid fibre reinforced composites,

proposed based on the concept of hybridization, are promising choices against ballistic impact. As discussed in the literature review, the existing hybrid fibre composites mainly focus on the hybridization of different types of fibre reinforcements, whereas only one type of matrix is used in hybrid composites, i.e. stiff or soft matrix. This results in similar failure modes for the different fibre composite parts in hybrid composites under ballistic impact. It also leads to high stiffness but poor ballistic resistance for hybrid composites with solely a stiff matrix [194], or high ballistic resistance but poor stiffness for hybrid composites with solely a soft matrix [189]. However, limited investigations have been conducted on hybrid composites which combine stiff composites and soft composites. The fibre composites hybridizing stiff /soft matrices within single composites which may achieve good ballistic resistance from soft parts as well as good quasi-static loading bearing capacity from stiff parts. As the failure modes of these two types of fibre composites are different, the understanding of the interaction between these two composites has not been well established. Although Larsson et al. [195] gave an insight into the ballistic performance of the hybrid composites which combined stiff carbon fibre composites with soft polyethylene fibre composites, the failure modes as well as energy absorption capacity of the hybrid material containing soft and stiff composites are still unclear.

Sandwich structures with fibre composite face sheets and a honeycomb core are multi-functional lightweight structures due to their excellent bending resistance and energy absorption capacity [8, 15, 233]. In order to improve the ballistic

resistance of sandwich structures, Gustin et al. [234] proposed a hybrid fibre composite sandwich structure. They reported that replacing carbon fibre composites with hybrid Kevlar/carbon fibre composites as face sheets, improved the energy absorption capacity of sandwich structures. However, the data on the ballistic performance of hybrid sandwich structures is still limited.

This chapter aims to experimentally investigate the ballistic impact response of a novel hybrid composite beam with stiff composites and soft composites, including the failure modes, energy absorption capacity and the interaction between the different composite parts. The outline of this chapter is as follows. First, the experimental materials and manufacturing process of different types of fibre composite beams are described, and the mechanical properties of the constituent materials are investigated. Then the methodology for the ballistic impact on hybrid fibre composite beams is developed. Finally, the advantages of the hybrid fibre reinforced composites are characterised by comparing the experimental measurements between stiff, soft and hybrid composite beams.

5.2 Materials and manufacturing

5.2.1 Materials

The laminated composite sheets, used as the monolithic beams and face sheets of sandwich beams, were reinforced by Pyrofil TR50S 15K carbon fibres (diameter is 7 μm). The thickness of each unidirectional fibre layer was 0.1 mm. The slow IN2 epoxy infusion resin and EF80 flexible epoxy resin, both supplied by Easy Composites Ltd, were used as the matrix materials for manufacturing

different types of fibre composites. Both of them are two part (resin and hardener) epoxy resin system. The IN2 epoxy resin with low mixed viscosity (200-450 mPa·s) is able to infuse through fibre reinforcements quickly, and becomes hard and brittle after full cure. Hence, it is suitable for manufacturing resin infusion composites. As for the EF80 flexible epoxy resin, it exhibits higher mixed viscosity (500-1200 mPa·s) than the IN2 epoxy resin. In addition, it has the capacity of maintaining flexibility after full cure, and is therefore suitable for the applications where the flexibility of fibre reinforced composite parts is required. Throughout the chapter, the fibre composites with IN2 epoxy infusion resin are termed stiff composites and the ones with EF80 flexible epoxy resin are termed soft composites.

The cores used in the sandwich beams are the Nomex honeycombs that are same as the ones investigated in Chapter 4, i.e. the density and out-of-plane thickness of the Nomex honeycomb core were $\rho = 54 \text{ kgm}^{-3}$ and $H = 10 \text{ mm}$, respectively. The in-plane sketch of the Nomex honeycomb core has been shown in Fig. 5.1 (a).

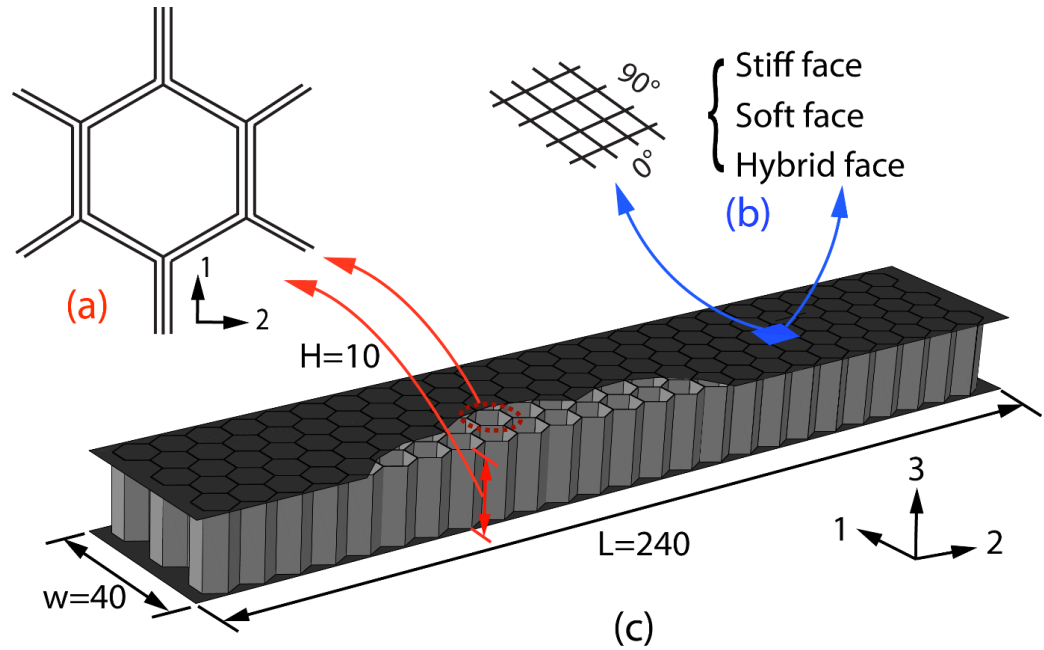


Fig. 5.1 (a) The in-plane sketch of the honeycomb core unit cell in sandwich beams, (b) the layer-up orientation of the laminated fibre composites and the types of face sheets. The sketch of the assembled sandwich beam is shown in (c). The co-ordinate systems associated with the beam and core are included in the figure. All dimensions are in mm.

5.2.2 Manufacturing

In this study, both the stiff and soft fibre reinforced composite panels were manufactured using a vacuum assisted resin transfer moulding (VA-RTM) system. Figures 5.2 (a) and (b) show the photographs of this system before and after assembly, respectively. The sketches for the top and bottom plates of the mild steel mould have been shown in Appendix Fig. A1 and Fig. A2, respectively, and the sketch of picture frame that is used for determining the

thickness of fibre laminate has been shown in Appendix Fig. A3. The unidirectional dry fibre layers were arranged in a $[0^\circ/90^\circ]_n$ lay-up inside the steel mould, i.e. orthogonally stacking, as shown in Fig. 5.1 (b) and Fig. 5.2 (a). The steel mould had one outlet port located at the centre and four inlet ports located at the four corners, both of diameter 2.5 mm. The O rings were inserted into the grooves of top and bottom plates to ensure good air tightness of steel mould. Eight bolts at the edges of the mould were tightened to provide sufficient seal. Degassing of resin and gas tightness checking of VA-RTM system were conducted before resin injection. A vacuum pump connected with the outlet port created a vacuum environment in the mould to infuse the resin through the dry fibre layers. For soft matrix, the compressed air of pressure 8 bars within a catch-pot was imposed to facilitate the infusion of liquid resin. The ratios of resin to hardener by weight were 100 : 30 and 100 : 145 for manufacturing stiff composite panels and soft composite panels, respectively. The infused composite panels were then cured for 7 h at 65 °C. To reduce the flaws caused by cutting dry fibre layers, approximately 10 mm was removed from each edge of the panels after demoulding.

The vacuum assisted resin transfer moulding (VA-RTM) is a mature method for manufacturing fibre reinforced composites. It has been widely used in laboratory and industry fabrication. The degassing of resin has been conducted before resin injection and the system was sealed well during the resin injection. There were few bubbles only occurred at the edges which have been removed before testing. Hence, the high-quality fibre composite specimens can be obtained.

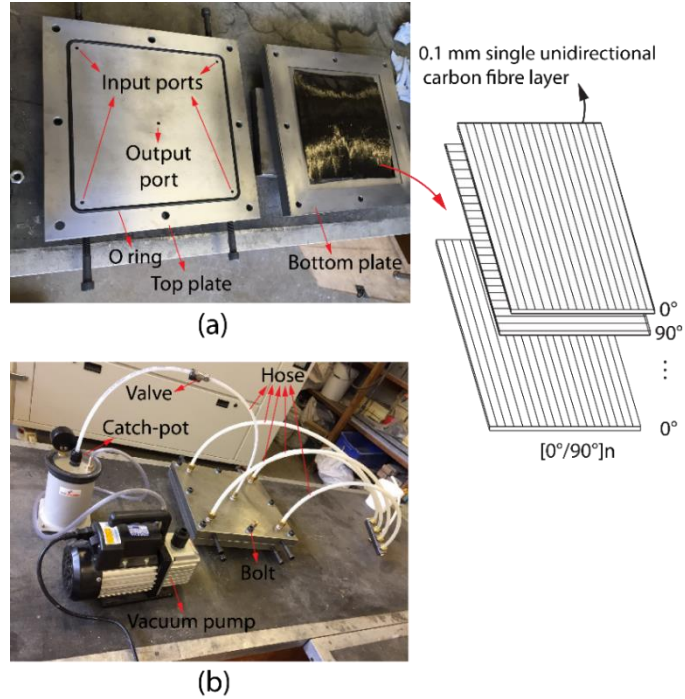


Fig. 5.2 The vacuum assisted resin transfer moulding system (VA-RTM) (a) before and (b) after assembly. The sketch in (a) shows the unidirectional carbon fibre layers with orthogonal stacking.







Figure 5.1 (c) shows the sketch of a Nomex honeycomb core sandwich beam specimen used for ballistic impact. Throughout this chapter, the global coordinates are defined with the 3-axis aligned with the out-of-plane direction of beams, and with the 1-axis and 2-axis representing the in-plane directions of beams. Different types of face sheets used in sandwich beam specimens are listed in Fig. 5.1 (b). All the face sheets and monolithic beams of total length $L = 240$ mm and width $w = 40$ mm were cut from the cured laminated panels using a diamond saw, and the Nomex honeycomb core was cut by a sharp blade to be the same dimension as the laminated beams. The details of monolithic fibre composite beams (i.e. stiff monolithic beam, soft monolithic beam and hybrid

monolithic beam) and sandwich beams (i.e. stiff-face sandwich beam, soft-face sandwich beam and hybrid-face sandwich beam) are summarized in Table 5.1. According to this Table, the stiff and soft composite beams of different thicknesses were used to assemble to form six types of beams with similar areal mass. n in the $[0^\circ/90^\circ]_n$ lay-up architecture is determined to be 10, 5, 4 and 2, respectively, corresponding to the panel thickness of $t = 3.9$ mm, 1.9 mm, 1.6 mm and 0.8 mm, respectively. The thicknesses of the stiff and soft monolithic beams were both $t = 3.9$ mm, and the thickness of each face sheet of the stiff-face and soft-face sandwich beams were both $t = 1.6$ mm. For the hybrid beams which comprised of stiff and soft composite parts with equal thickness, the thicknesses of each composite part of the hybrid monolithic beam and hybrid-face sandwich beam were $t = 1.9$ mm and $t = 0.8$ mm, respectively. Hence, the number of fibre layer in sandwich beams was 4 less than that in monolithic beams. The fibre volume fraction and density of each laminated composite part were approximately 50% and $\rho = 1380 \text{ kgm}^{-3}$, respectively.

Some additional steps were taken for assembling beams. The stiff and soft composite parts of hybrid monolithic beams, and the face sheets of hybrid-face sandwich beams were glued together, respectively, using the Loctite EA 9461[®] epoxy adhesive. This epoxy resin is a thixotropic, two component epoxy adhesive coupling high peel strength and excellent shear strength. The face sheets and honeycomb cores of sandwich beams were glued together also using

the Loctite EA 9461[®] epoxy adhesive. In hybrid-face sandwich beams, the part contacted with the each side of the Nomex honeycomb core was stiff part and soft part, respectively, as sketched in Table 1. In addition, to ensure the ends of the sandwich beams can be end-clamped sufficiently, the Nomex honeycomb core was filled with fast IN 2 epoxy resin, supplied by Easy Composites Ltd, over the clamped portion of each length 40 mm. The assembled hybrid monolithic beams and sandwich beams were then cured in the oven for 5 h at 60 °C with 25 KN transverse loading applied on the beams to achieve better bonding. The areal mass of the epoxy adhesive per layer was measured to be 0.14 kgm⁻², and all the assembled composite beams had similar areal mass in the range of 5.12 - 5.40 kgm⁻².

Table 5.1 Constituent details of the monolithic and sandwich beams.

	Monolithic beams			Sandwich beams		
Composite sheets	Stiff	Soft	Hybrid	Stiff face sheet	Soft face sheet	Hybrid face sheet
Sketch of beams						
Number of layers for sheet	20	20	10*2	8*2	8*2	4*4
Areal density of face sheets (kg/m ²)	5.38	5.38	5.30	4.30	4.30	4.30
Areal mass of honeycomb core(kg/m ²)	0	0	0	0.54	0.54	0.54
Areal mass of glue (kg/m ²)	0	0	0.14	0.28	0.28	0.56
Total areal mass of beams (kg/m ²)	5.38	5.38	5.44	5.12	5.12	5.40

5.3 Mechanical properties of constituent materials

The quasi-static uniaxial tensile and compressive responses of the fibre reinforced composites, and the quasi-static out-of-plane compressive response of Nomex honeycomb core were measured using an Instron screw-driven testing machine at an applied nominal strain rate 10^{-3} s^{-1} . There were five repeats for each type of test.

The tension and compression tests on the stiff and soft fibre composite materials were conducted using the methods described by the EN ISO 527-4 and ASTM D3410/B, respectively. The aluminium tabs were adhered to the clamped ends of the rectangular specimens for friction gripping during test. The uniaxial forces of the specimens were determined by the load cell of the screw-driven testing machine, and the uniaxial strain of the specimens were measured by a single Stingray F-146B Firewire camera video gauge. In tension, the stiff and soft laminates both in $[0^\circ/90^\circ]$ and $\pm 45^\circ$ orientations were tested. However, only the compressive response of the stiff laminate in $[0^\circ/90^\circ]$ orientation was measured as the compressive response of the soft laminate in $[0^\circ/90^\circ]$ orientations was too weak to be measured using the standard method. The specimens had a gauge length of 50 mm for tension test, whereas had a gauge length of 12 mm for compression test in order to prevent Euler buckling.

Figure 5.3 (a) shows the measured nominal tensile and compressive stress versus strain relations of the composite laminates in $[0^\circ/90^\circ]$ orientations. In the tension tests, the stiff and soft composite laminates displayed identical linear elastic

responses, with the tensile strength of 535 MPa and elastic modulus of 34 GPa. It was observed that the stiff and soft composite laminates had the same failure mechanism in tension, i.e. tensile fracture of fibre reinforcements. In the compressive tests, the stiff composites displayed elastic-brittle response, with the compressive strength was 221 MPa at nominal strain of 0.011.

In contrast, as the tensile response of the laminates in $\pm 45^\circ$ orientations was governed by the shear of matrix, the laminates in this orientation were more ductile and had lower strengths than those in $[0^\circ/90^\circ]$ orientations, see Fig. 5.3 (b). The stiff composites exhibit elastic-plastic hardening response with the tensile strength of 187 MPa and nominal failure strain of 0.225. However, the soft composites have significantly lower tensile strength and higher nominal failure strain, which are 36 MPa and 0.36, respectively in $\pm 45^\circ$ orientations. The slight hardening response of the soft composites after initial yield is governed by the fibre rotation towards the tensile axis [178]. In addition, both the stiff and soft composites in $\pm 45^\circ$ orientations failed with matrix cracking without fibre rupture.

For the Nomex honeycomb core, the out-of-plane compressive responses under quasi-static and dynamic loading have been investigated, see Chapter 4 for details. The measured quasi-static compressive stress versus strain curve of the Nomex honeycomb core is plotted in Fig. 5.3 (c) again for clarity.

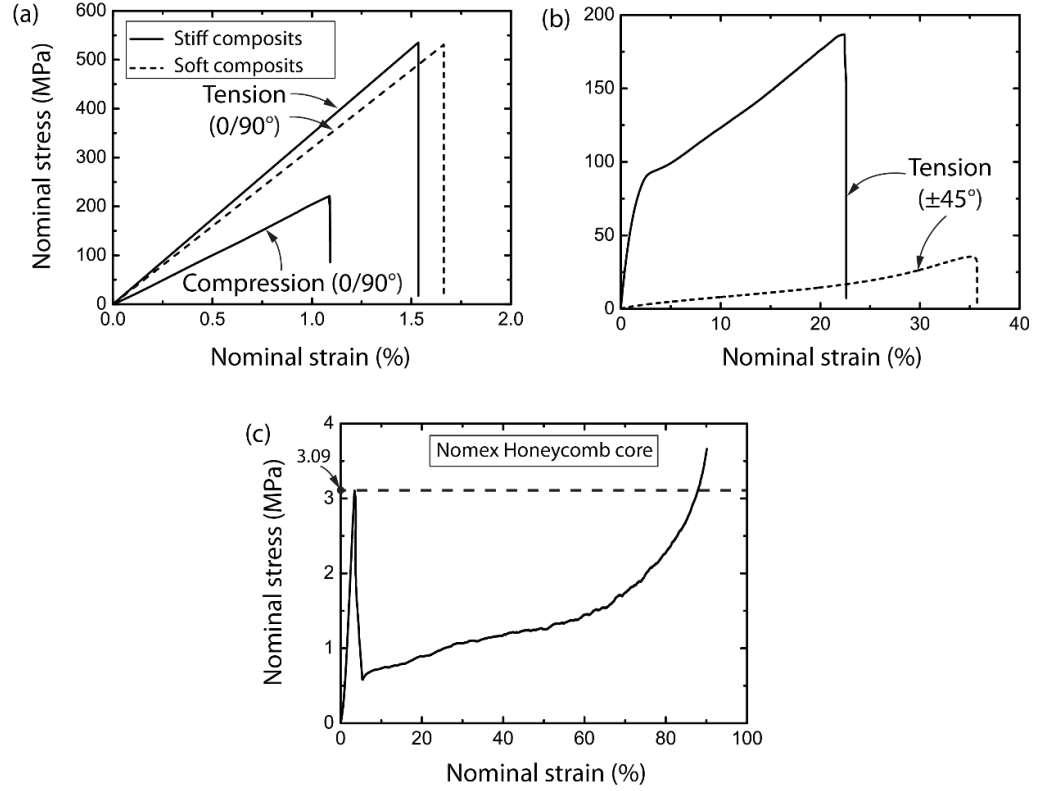


Fig. 5.3 Quasi-static stress-strain relationships of the stiff and soft fibre composites under uniaxial compression and tension tests for (a) 0°/90° and (b) ±45° lay-up architecture. The measured quasi-static out-of-plane compressive response of the Nomex honeycomb core of density $\rho = 54 \text{ kg} \cdot \text{m}^{-3}$ is shown in (c).

5.4 Ballistic impact test protocol

Ballistic impact tests were conducted to investigate the failure modes and energy absorption capacity of the monolithic and sandwich composite beams, and find out the advantages of the hybrid beams. The sketch of the experimental setup developed by Turner et al. [153] is shown in Fig. 5.4. A steel fixture with four M6 bolts at each end was used for fully clamping the beams. The free span

lengths of the beams were 170 mm and the front faces of beams were positioned 200 mm from the muzzle of the gas gun. The gas gun of barrel length 3.5 m, outer diameter 16 mm and internal diameter 13 mm was employed for accelerating a non-deforming steel spherical projectile of diameter $d = 12.7$ mm and mass $M = 8.3$ g. Either compressed air or pressurised liquid nitrogen was used to propel the projectile to various velocities in the range of $50 \text{ ms}^{-1} \leq v_0 \leq 300 \text{ ms}^{-1}$, producing the initial kinetic energy of projectile in the range of $10.4 \text{ J} \leq E_{k_0} \leq 373.5 \text{ J}$. Figure 5.5 indicates the relation of initial projectile velocity versus the applied gas pressure. The initial velocity of projectile was measured using two laser gates located at the open end of the gas gun barrel and confirmed with a Phantom Mercury HS v 12.1 high speed camera. The high speed camera was also used to capture the failure modes of beams and residual velocity of projectile during ballistic impact. Typically, the frame rate and exposure time were 38,000 fps and 10 μs , respectively, and the resolution was 320×344. It should be noted that we suppose the soft composite parts, which are in hybrid monolithic and hybrid-face sandwich beams, act as a cushion that avoids the direct stiff contact between non-deforming projectile and stiff composite part. Based on this assumption, we set the projectile firstly impact the soft composites part of the hybrid beams.

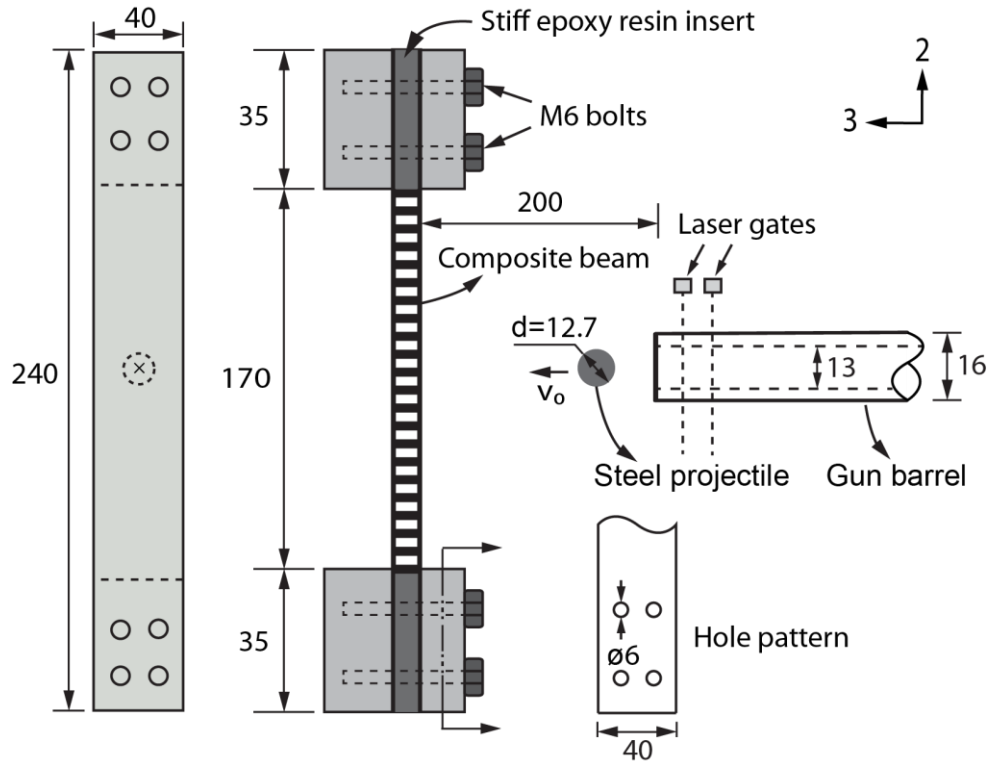


Fig. 5.4 Sketch of the experimental setup for ballistic impact on monolithic and sandwich beams. All dimensions are in mm.

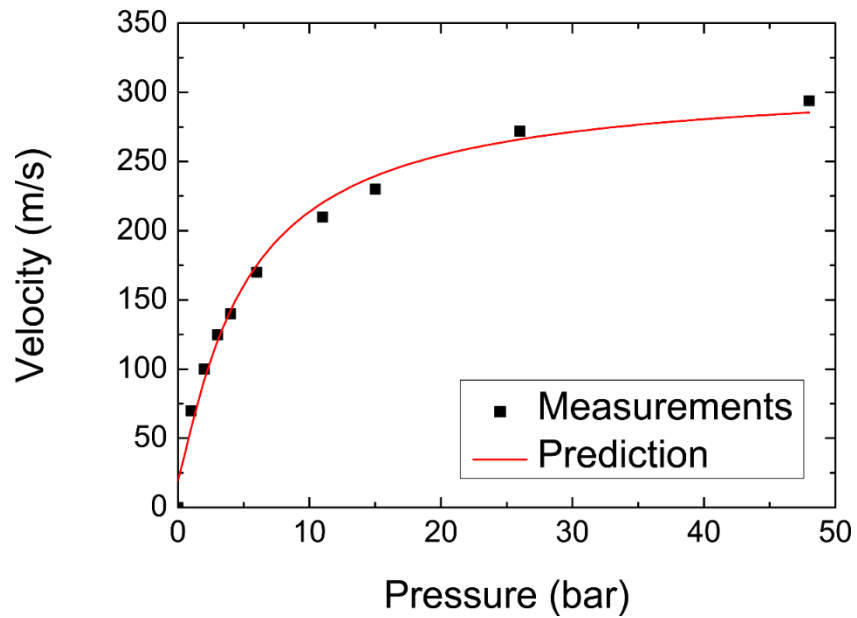


Fig. 5.5 The initial projectile velocity as a function of applied gas pressure.

5.5 Ballistic impact responses of beams

The experimental measurements for the six types of composite beams have been summarized in Table 5.2, including the initial projectile velocity, residual projectile velocity, kinetic energy of projectile transmitted to beams, and failure modes of beams.

Table 5.2 A summary of the experimental measurements for six types of composite beams.

Beams	Initial velocity, v_0 (m/s)	Residual velocity, v_r (m/s)	Kinetic energy transmitted to beams, ΔE_{abs} (J)	Failure modes
Stiff monolithic beam	56	-16	11.95	Rebound
	67	-18	17.28	Three-point fracture
	100	69	21.74	Three-point fracture
	133	111	22.28	Perforation
	160	136	26.75	Perforation
Soft monolithic beam	72	-6	20.19	Rebound
	96	26	35.44	One-point fracture
	140	85	51.36	One-point fracture
	207	153	80.67	Three-point fracture
	258	220	75.37	Perforation

Hybrid monolithic beam	72	-8	21.25	Rebound
	100	40	34.86	One-point fracture
	145	86	56.56	One-point fracture
	198	153	65.55	One-point fracture
	272	246	55.90	Perforation
Stiff-face sandwich beam	72	-14	21.70	Rebound
	107	61	32.07	Back face fracture
	145	124	23.44	Back face perforation
Soft-face sandwich beam	72	-8	21.25	Rebound
	107	43	39.84	Back face fracture
	145	148	38.85	Back face fracture
Hybrid-face sandwich beam	75	0	23.34	Projectile trapped
	100	42	34.18	Back face fracture
	143	98	45.01	Back face fracture

5.5.1 Impact responses of monolithic beams

In this section, the responses of three types of monolithic composite beams under a series of ballistic impact tests were investigated, and the failure modes of these beams at various velocities are identified. The fracture mode discussed below is defined as the complete fracture of beams, and the perforation mode as the beams

perforated without complete fracture. The critical velocity between two failure modes was calculated as the average value of the maximum velocity that triggered the low-velocity failure mode and the minimum velocity that triggered the high-velocity failure mode. Take the stiff monolithic beam for example, the measured maximum velocity for rebound mode was 56 ms^{-1} , and the measured minimum velocity for fracture mode was 67 ms^{-1} . Hence, the critical velocity between the rebound and fracture modes of the stiff monolithic beam was 61.5 ms^{-1} .

5.5.1.1 Stiff monolithic beam

The back-face deflections of the stiff monolithic beams before failure as a function of time at selected impact velocities are plotted in Fig. 5.6. The montages of high-speed photographic images for three different failure modes are shown in Fig. 5.7 and discussed below

Rebound ($v_0 \leq 61.5 \text{ ms}^{-1}$): The spherical projectile is rebounded by the deformed beam at impact velocity of 56 ms^{-1} , as shown in Fig. 5.7 (a).

Three-point fracture ($61.5 \text{ ms}^{-1} < v_0 \leq 116.5 \text{ ms}^{-1}$): The beams fail with fibre fracture at three positions in this range of impact velocity. Figure 5.7 (b) shows that the fracture in the middle develops from the back face of the beam, thus the fracture mechanism is stretch governed. The fracture at the clamped ends is also stretch governed, as indicated in the photograph of Fig. 5.6. At impact velocity of 67 ms^{-1} , the fracture mainly focuses on the middle of the beam while a part of

fracture also occurs at the clamped ends (Fig. 5.6). At higher impact velocity of 100 ms^{-1} , the beam fully fractures at three points, i.e. middle and two clamped ends. The back-face deflection of the beam before fracture decreases with the increase of impact velocity.

Perforation ($v_0 > 116.5 \text{ ms}^{-1}$): The beams fail with perforation when the initial impact velocity of projectile reaches to the perforation limit. As reported by Karthikeyan et al. [178], the projectile with high kinetic energy first comminutes the fibres at the impacted point, and then results in the local bending of back face. The significant bending of the back face leads to the tensile fracture of fibres (Fig. 5.7 (c)) and consequently the perforation of beam. The back face view of the perforated beam is diamond-shape damage at the impact point, as shown in Fig. 5.7 (c). The beams have been perforated before a large deflection achieves.

The failure modes and critical velocities of the stiff monolithic beams are similar to those of the three-dimensional woven carbon fibre resin composites [153].

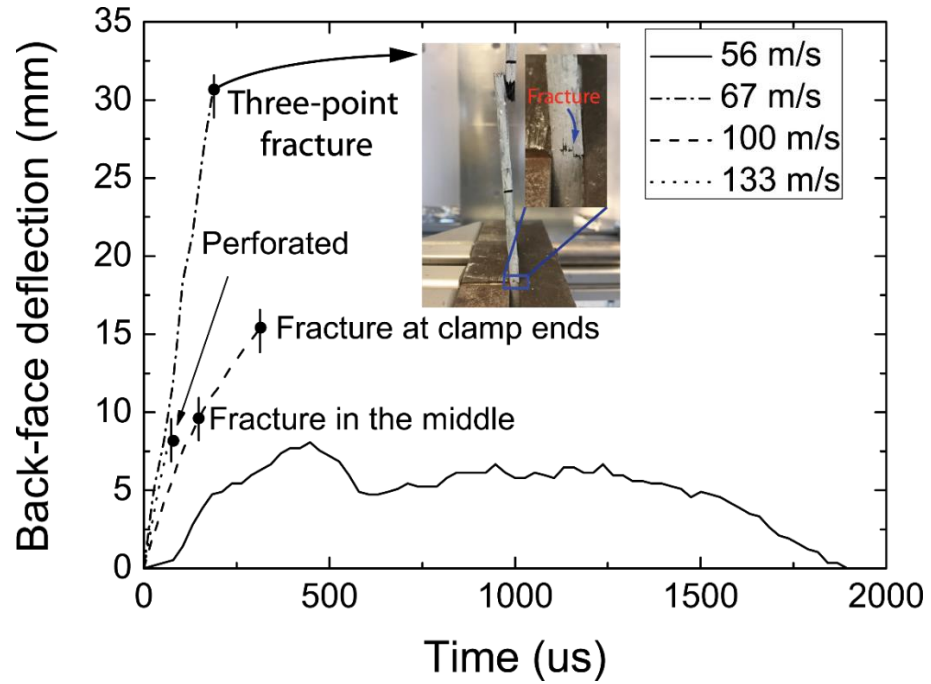


Fig. 5.6 The history of back face deflection of the stiff monolithic beams at selected impact velocities. Time $t=0$ corresponds to the time instant when the projectile impacted on the beams. The photographic image shows the part fracture of clamped end when the impact velocity was 67 ms^{-1} .

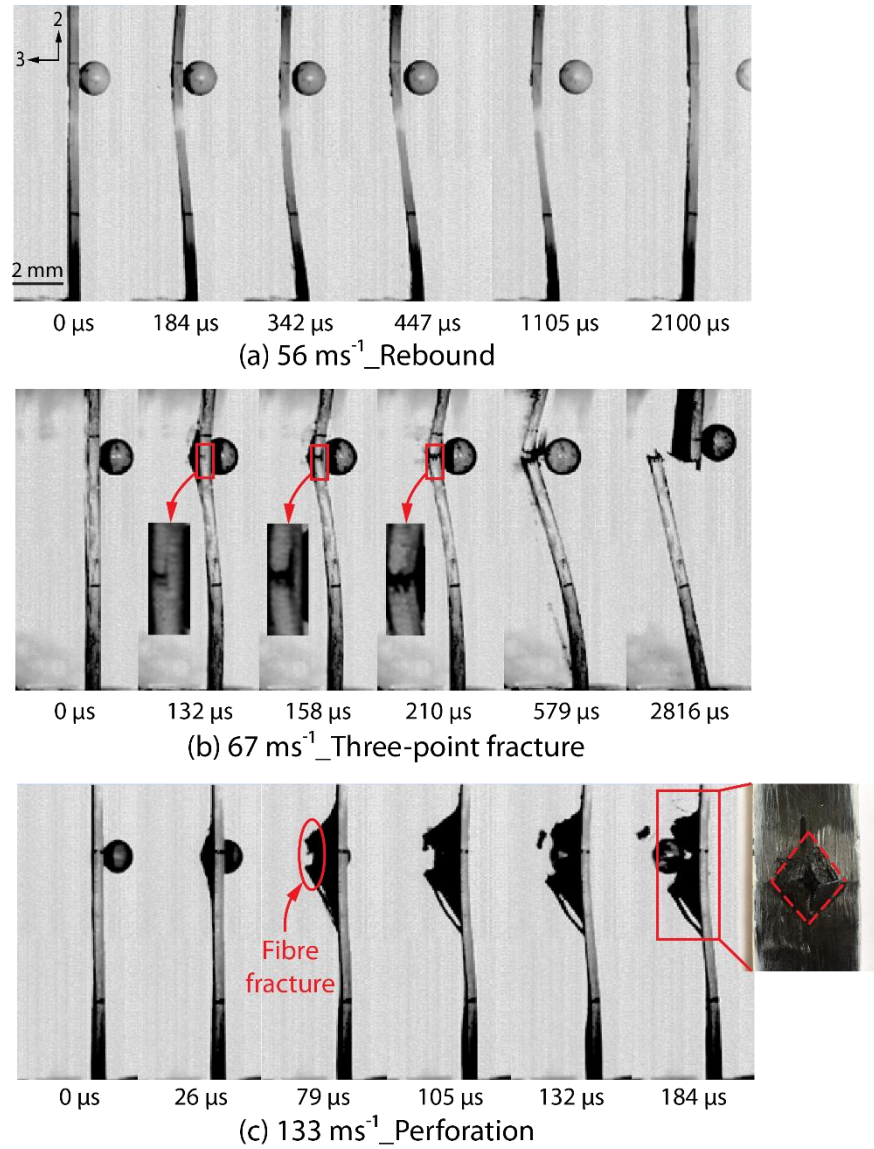


Fig. 5.7 Montage of the high speed photographs of the stiff monolithic beams under ballistic impact. Three different failure modes of the beams are shown in the figure. The back face view of the beam failed with perforation at the impact point is also shown in (c).

5.5.1.2 *Soft monolithic beam*

The back-face deflections of soft monolithic beams before failure as a function of time history at selected impact velocities are plotted in Fig. 5.8, and the montages of high-speed photographic images for three different failure modes are shown in Fig. 5.9. As the beam has a long response history at low impact velocity of 72 ms^{-1} , the response history at this velocity (Fig. 5.8 (a)) is separated from others at higher velocities (Fig. 5.8 (b)) for clarity. The ballistic behaviour is described as follow

Rebound ($v_0 \leq 84 \text{ ms}^{-1}$): At the velocity of 72 ms^{-1} , the projectile is rebounded along with a part of beam fracture in the width direction, as shown in Fig. 5.9 (a).

One-point fracture ($84 \text{ ms}^{-1} < v_0 \leq 232.5 \text{ ms}^{-1}$): In this range of applied projectile velocity, the soft monolithic beam only fractures in the middle. This is different from the three-point fracture mode of the stiff monolithic beam. As shown in Figs. 5.9 (b) and (c), the beam is first partly perforated by the projectile and then fully fractures in the middle. Fibre fracture along with matrix cracking develops from the back face of the beam due to the significant bending at the impact point.

Perforation ($v_0 > 232.5 \text{ ms}^{-1}$): The beam is perforated without full fracture when the impact velocity is high enough, as shown in Fig. 5.9. The back-face deflection history of the beam for this failure mode is not plotted in Fig. 5.8 as the deflection is negligible before perforation.

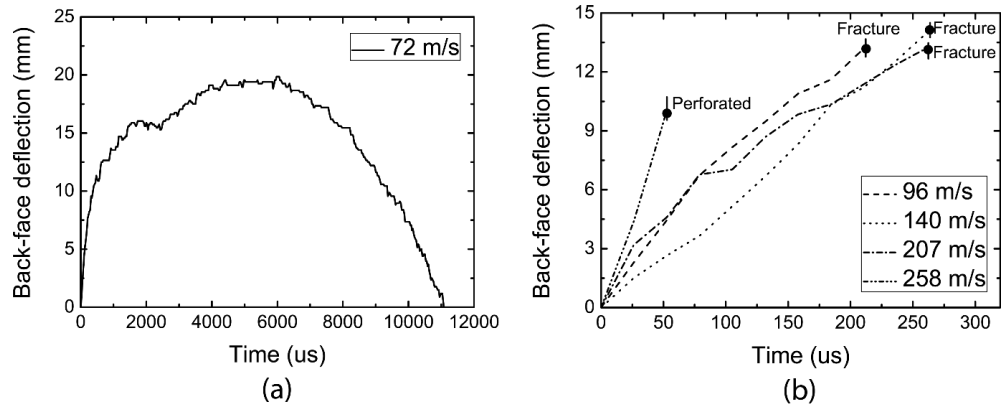


Fig. 5.8 The history of back face deflection of the soft monolithic beams at (a) impact velocities of 72 ms^{-1} and (b) higher impact velocities. Time $t=0$ corresponds to the time instant when the projectile impacts on the beams.

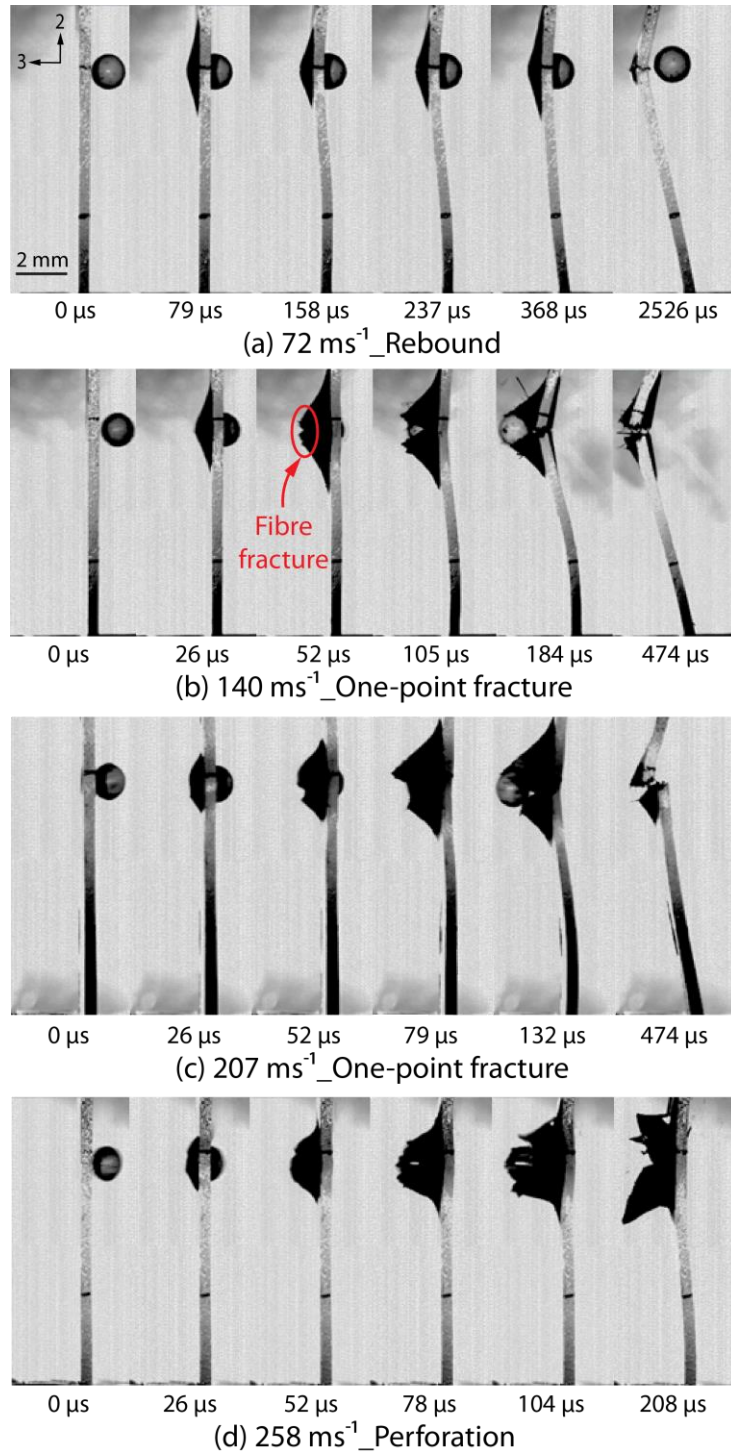


Fig. 5.9 Montage of the high speed photographs of the soft monolithic beams under ballistic impact. Three different failure modes of the beams are shown in the figure.

5.5.1.3 Hybrid monolithic beam

For the hybrid monolithic beam, the debonding occurs between the stiff and soft composite parts during ballistic impact. The back-face deflections of both stiff part and soft part before failure as a function of time are plotted in Fig. 5.10. As discussed in Section 5.4, the projectile impacts the soft part firstly, then the stiff part in the back of the beam. The montages of high-speed photographic images for three different failure modes are shown in Fig. 5.11.

Rebound ($v_0 \leq 86 \text{ ms}^{-1}$): The projectile was rebounded by the beam under low velocity impact, see Fig. 5.11 (a). Although the stiff composite part at the back face fractures, there is only slight cracking on the impacted surface of the soft composite part, as the micro photographs shown in Fig. 5.11 (a). The hybrid monolithic beam can therefore still resisting load after impact. Under the same impact velocity, however, the stiff and soft monolithic beams have fractured fully and partly, respectively, as discussed in Sections 5.5.1.1 and 5.5.1.2.

One-point fracture ($86 \text{ ms}^{-1} < v_0 \leq 235 \text{ ms}^{-1}$): Both the stiff and soft parts failed with beam fracture in the middle, and the debonding developed from the impact point to the clamped ends. During the ballistic impact, the fibre fracture is observed at the back face of the stiff part, see Fig. 5.11 (b).

Perforation ($v_0 \geq 235 \text{ ms}^{-1}$): When the impact velocity is high enough, the projectile perforates the beam with a negligible deflection. As shown in Fig. 5.11 (c), the debonding is not observed before perforation, but develops after that. It

is concluded that the debonding is due to the wave propagation rather than the different stiffness of the stiff part and soft part. Unlike the stiff monolithic beam in Fig. 5.7 (c), the back face view of the perforated beam at the impact point is circle-shape damage. This is due to the transition effect of soft composites at the front face, which results in more uniform stress distribution of the stiff composite sheet around the projectile.

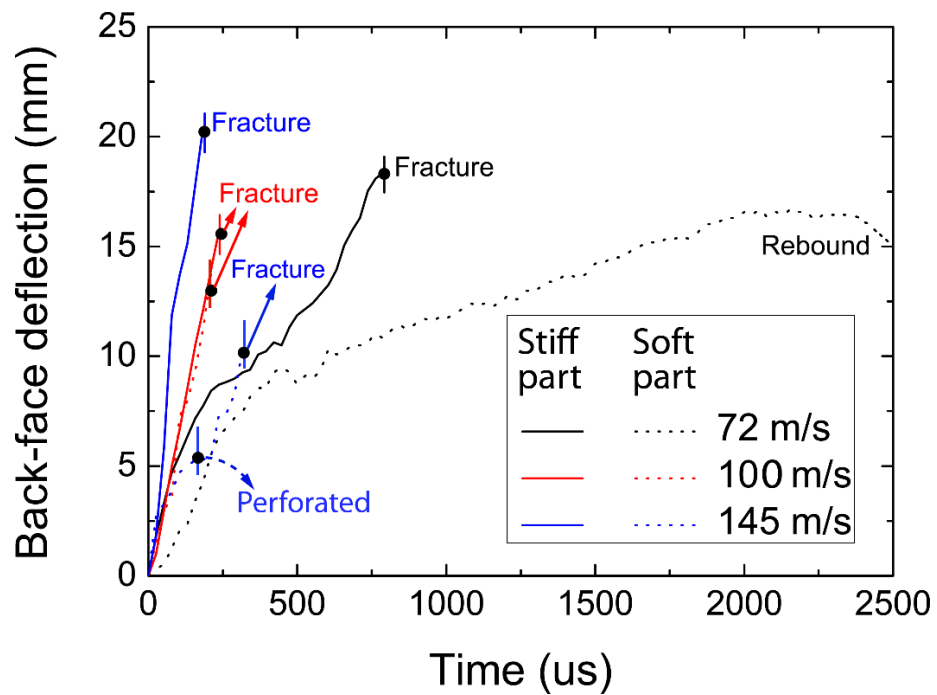


Fig. 5.10 The back face deflection history of the stiff part and soft part in hybrid monolithic beams at selected impact velocities. Time $t=0$ corresponds to the time instant when the projectile impacted on the beams.

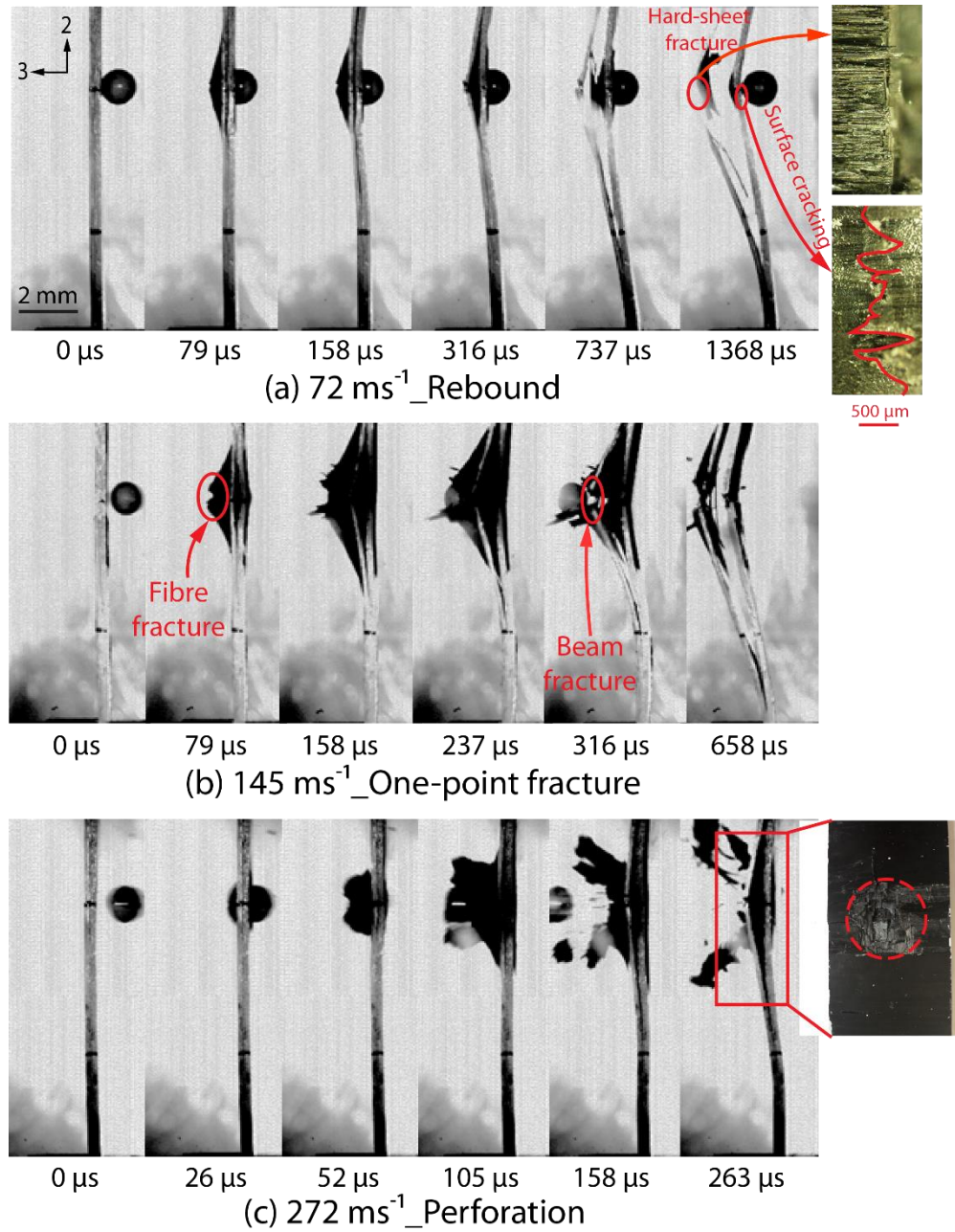


Fig. 5.11 Montage of the high speed photographs of the hybrid monolithic beams under ballistic impact. Three different damage modes of the beams are shown in the figure. (a) also shows the micro damage of the stiff composites and soft composites after impact, and (c) also shows the back face view of the beam failed with perforation at the impact point.

5.5.1.4 Discussion

Figure 5.12 shows the comparison of critical velocities with respect to the failure modes of stiff, soft and hybrid monolithic beams. The soft and hybrid monolithic beams have similar critical velocities regarding to the same failure mode, and both higher than the stiff monolithic beams, particularly for the failure mode of perforation.

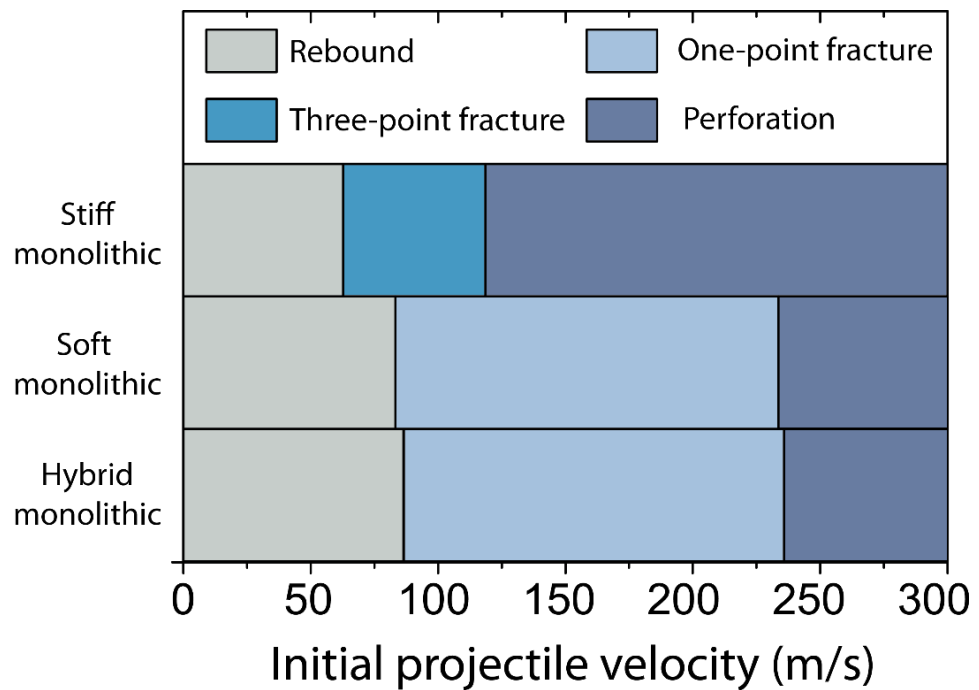


Fig. 5.12 The different ranges of impact velocity regarding to the different damage modes of the stiff, soft and hybrid monolithic beams.

The difference in critical velocities between the stiff and soft monolithic beams can be explained as follow. The flexible and ductile EF80 epoxy matrix makes the soft monolithic beam more deformable and less brittle than the stiff composite beam, which contributes to longer interaction time between the

projectile and composite beam. Hence, the plastic wave can keep propagating in the soft monolithic beam for the failure mode of fracture, even though the projectile has perforated the beam. With the increase of impact velocity, the interaction time and wave propagation time become shorter, the beam finally fails with perforation when the perforation limit velocity reaches. Compared to the soft monolithic beam, the wave propagation time in stiff monolithic beam is shorter due to the stiffer interaction, and the projectile impacts on stiff monolithic beam is more likely to give rise to stress concentration. Thus, the stiff monolithic beam can be perforated at lower impact velocity than the soft monolithic beam. Throughout the impacts on stiff and soft monolithic beams, there is no damage in terms of delamination observed in the plies.

Compared to the soft monolithic beam, the hybrid monolithic beam provides higher stiffness. The debonding between the stiff and soft parts of the hybrid monolithic beam can always be observed in the range of applied velocities, i.e. $72 \text{ ms}^{-1} < v_0 \leq 272 \text{ ms}^{-1}$. Due to the high viscosity of the epoxy adhesive, the adhesive was unable to be degassed or vacuum infused, which resulted in more imperfections introduced in the adhesive. Hence, the debonding between the stiff and soft parts is easier to occur during impact. Based on the above analysis to the perforation mode of hybrid monolithic beams, the development of debonding is mainly governed by the wave propagation time in the beam, which is inversely scale with the initial velocity of projectile. Hence, at low and medium velocities, the long interaction time between the projectile and beam results in long wave propagation time and significant debonding (Figs. 5.11 (a) and (b)).

5.5.2 Impact responses of sandwich beams

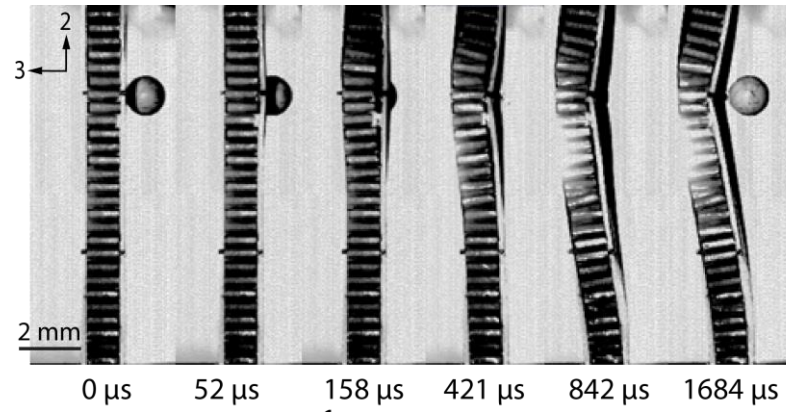
The responses of sandwich beams with three types of face sheets, i.e. stiff face, soft face and hybrid face, respectively, under ballistic impact are investigated. The montages of high-speed photographic images at three impact velocity levels are shown in Fig. 5.13, Fig. 5.15 and Fig. 5.16.

At low impact velocity of approximately 73 ms^{-1} , the projectiles are rebounded by the stiff-face and soft-face sandwich beams, as shown in Figs. 5.13 (a) and (b). However, the projectile penetrates the front face sheet of the hybrid-face sandwich beam and reaches to the back face sheet, leading to the debonding between back face sheet and honeycomb core, and finally trapped into the beam (Fig. 5.13 (c)). This may due to the fact that the initial kinetic energy of the projectile ($v_0 = 75 \text{ ms}^{-1}$) for hybrid-face sandwich beam is 7.8% higher than those of the projectiles ($v_0 = 72 \text{ ms}^{-1}$) for stiff-face and soft-face sandwich beams. In addition, there is debonding around the impact point occurred between front face sheet and honeycomb core of the soft-face sandwich beam owing to the flexibility of soft composite sheet. As stated in Section 5.2.2, though the number of fibre layer in sandwich beams is 4 less than that in monolithic beams, all the sandwich beams are able to resist the projectiles and behave better than the stiff and soft monolithic beams at this low velocity level. Figure 5.14 shows the back-face deflections of monolithic and sandwich beams as a function of time at initial projectile velocity of approximately 73 ms^{-1} . For clarity, only the deformation response of the soft composite part in hybrid monolithic beam

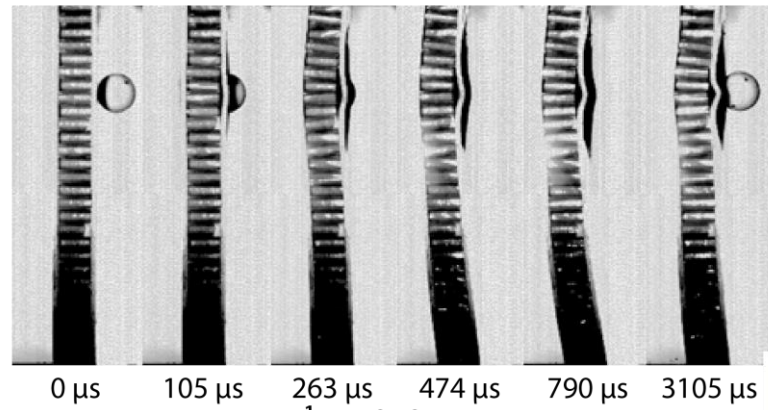
before the fracture of stiff composite part is plotted. It indicates that the projectiles are rebounded by all the beams except for the stiff monolithic beam. The stiff monolithic beam fails with fully fracture, and the maximum deflection is 31 mm that is significantly higher than those (no more than 20 mm) of other beams. The sandwich beams normally have smaller deflections than the monolithic beams due to the higher stiffness.

At medium impact velocity of around 105 ms^{-1} , the front face sheets of all sandwich beams are perforated and the back face sheets fully fracture during impact, as shown in Fig. 5.15. The debonding between back face sheet and honeycomb core is also observed in all sandwich beams. Similar to the hybrid monolithic beam, the sheet-sheet debonding occurs in the back face sheet of the hybrid-face sandwich beam, see Fig. 5.15 (c).

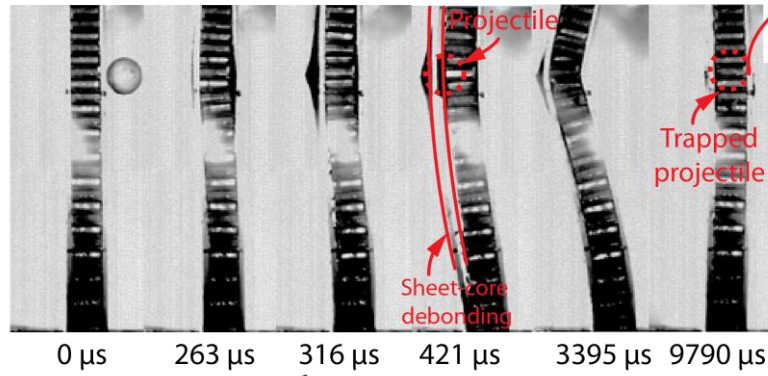
Figure 5.16 shows the montages of high-speed photographic images at higher impact velocity of around 144 ms^{-1} . For the stiff-face sandwich beam, both the front face sheet and back face sheet are perforated without full fracture. The explanation to this is identical to that to the stiff monolithic beam, i.e. owing to the short interaction time between projectile and stiff composites. For the soft-face as well as hybrid-face sandwich beams, the failure modes are similar to those under the impact velocity of around 105 ms^{-1} .



(a) 72 ms^{-1} _Stiff-face sandwich



(b) 72 ms^{-1} _Soft-face sandwich



(c) 75 ms^{-1} _Hybrid-face sandwich

Fig. 5.13 Montage of the high speed photographs of the (a) stiff-face, (b) soft-face and (c) hybrid-face sandwich beams impacted by the spherical projectile at velocity around 73 ms^{-1} . The two red curves in (c) represent the edges of back face sheet and honeycomb core, and the front face view of hybrid-face sandwich beam at impact point are also shown in (c).

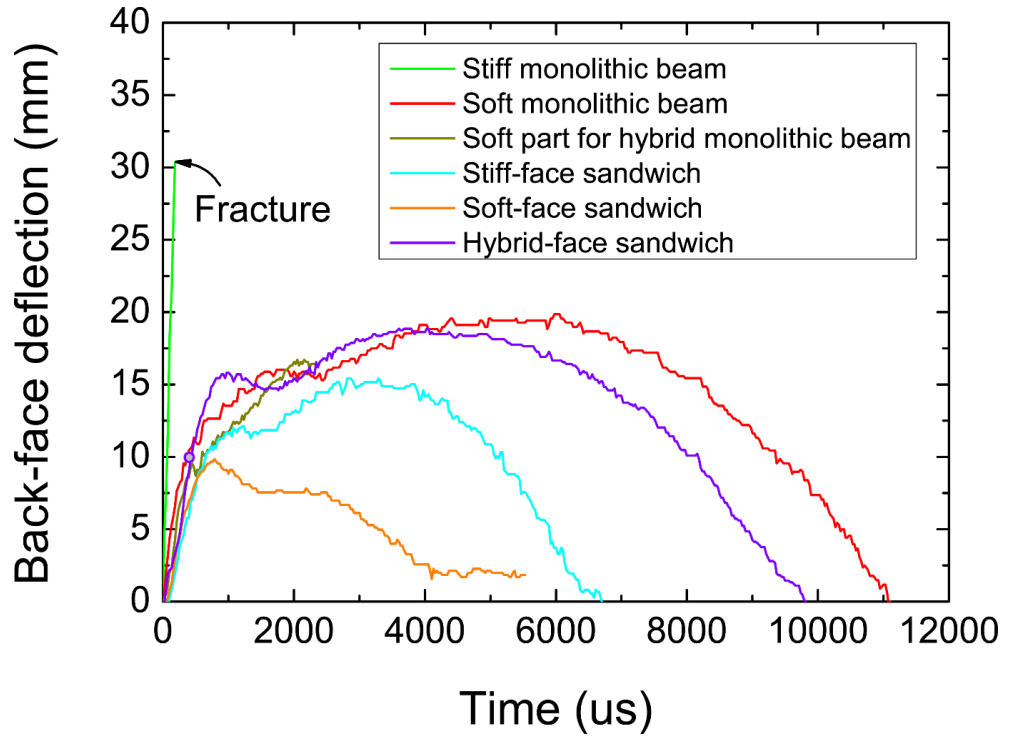


Fig. 5.14 Back-face deflection history of monolithic and sandwich beams at impact velocity of around 73 ms^{-1} . It should be noted that the stiff monolithic beam and hybrid-face sandwich beam are impacted at the velocity of 67 ms^{-1} and 75 ms^{-1} , respectively.

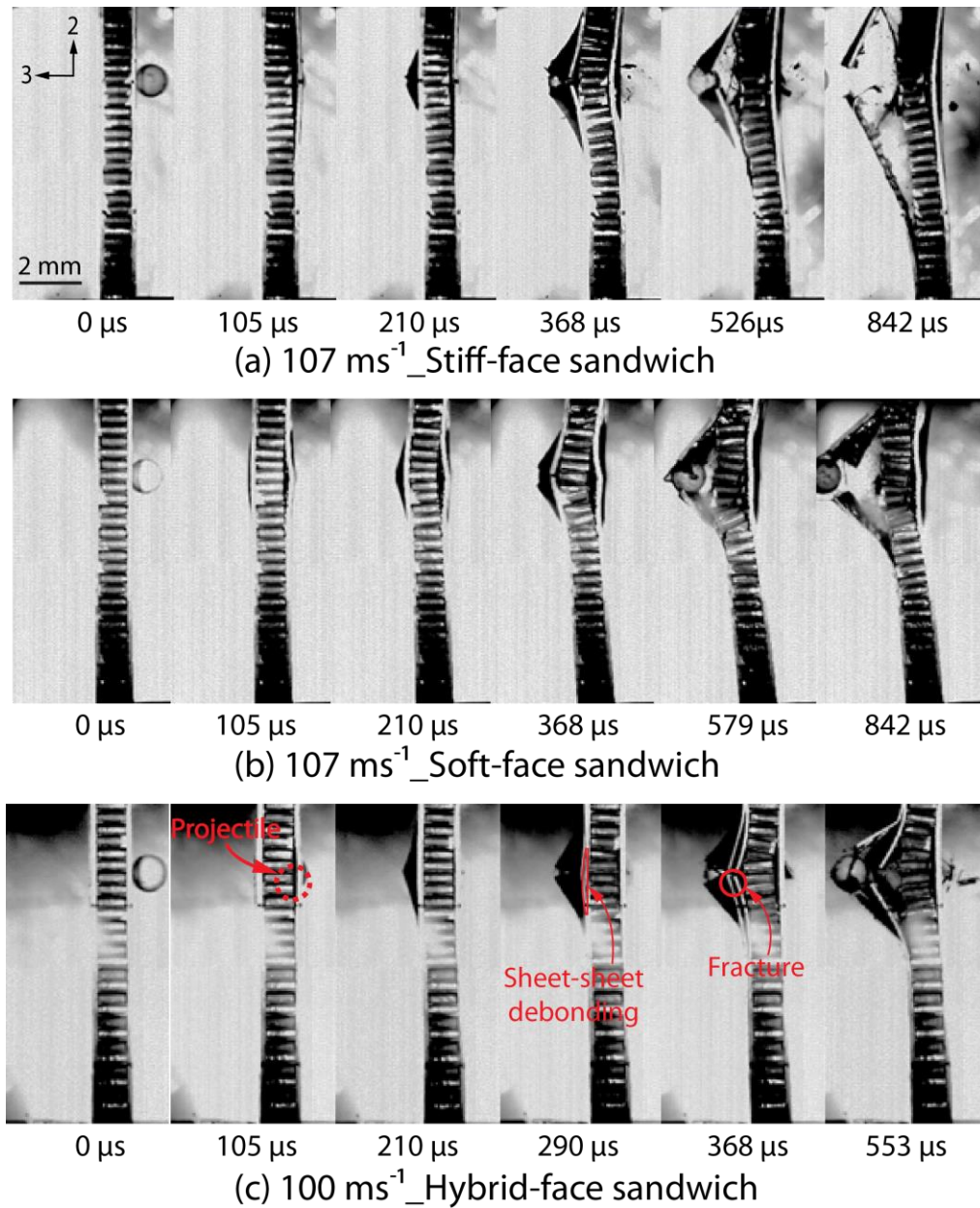


Fig. 5.15 Montage of the high speed photographs of the (a) stiff-face, (b) soft-face and (c) hybrid-face sandwich beams impacted by the projectile at velocity around 105 ms⁻¹.

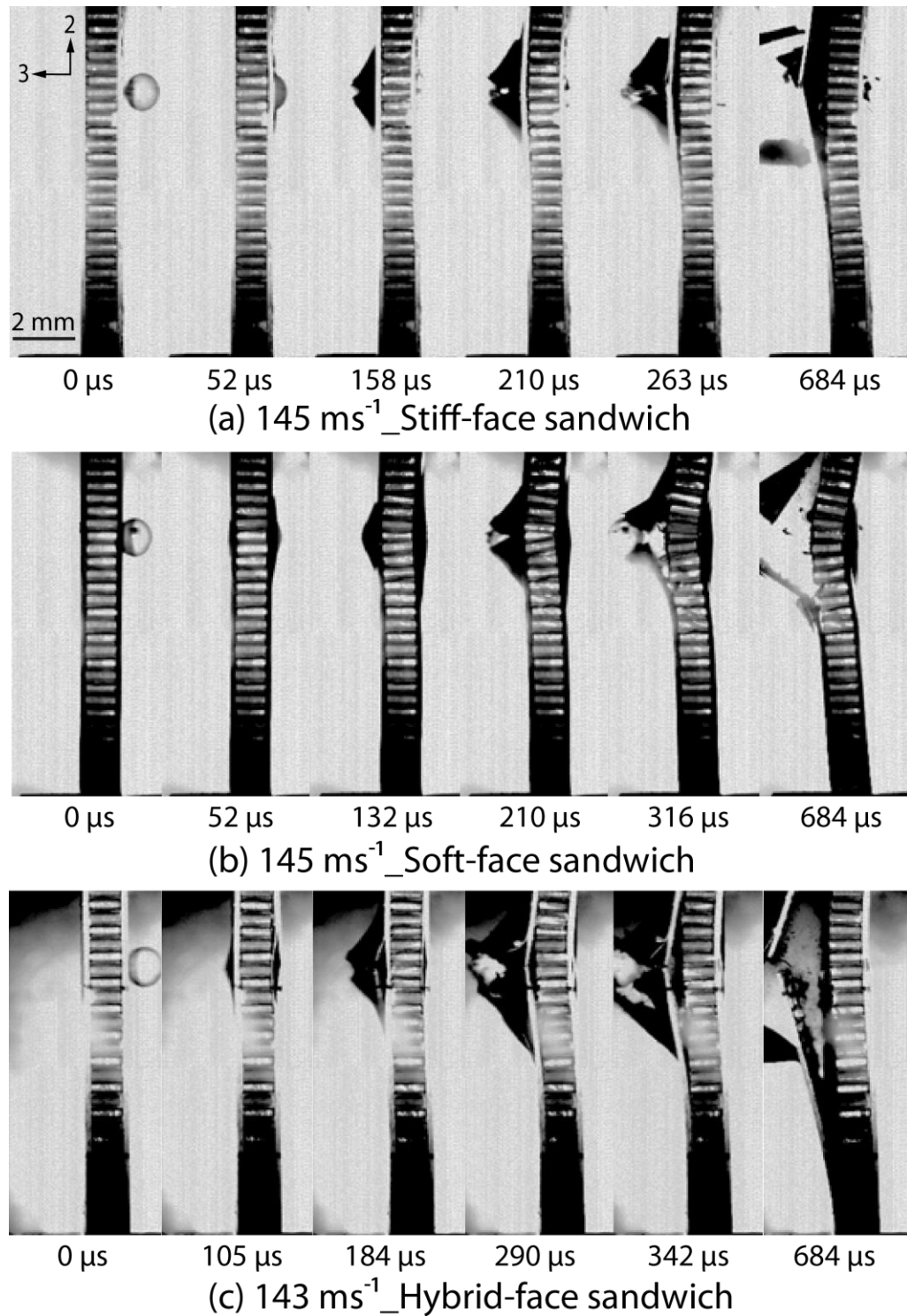


Fig. 5.16 Montage of the high speed photographs of the (a) stiff-face, (b) soft-face and (c) hybrid-face sandwich beams impacted by the projectile at velocity around 144 ms⁻¹.

5.5.3 Ballistic resistance of beams characterised by the initial-residual velocity relation of the projectile

Figure 5.17 shows the initial projectile velocity v_0 as a function of residual projectile velocity v_r . Here, v_r is assumed to be 0 when the projectile is trapped into the beam. The ballistic impact resistance of the beams can be reflected by the slopes and intercepts of the fitting lines, i.e. higher slope and intercept correspond to better impact resistance of beams. This figure indicates that the lowest intercept and slope of fitting lines are from the stiff monolithic beam and stiff-face sandwich beam, respectively. In addition, the slopes of the stiff, soft and hybrid monolithic beams are higher than those of the corresponding stiff-face, soft-face and hybrid-face sandwich beams, respectively. This is because the number of fibre layer for monolithic beams is more than that for sandwich beams in order to achieve identical areal mass, and carbon fibre laminated composites play a far more significant role than the Nomex honeycomb core in resisting ballistic impact.

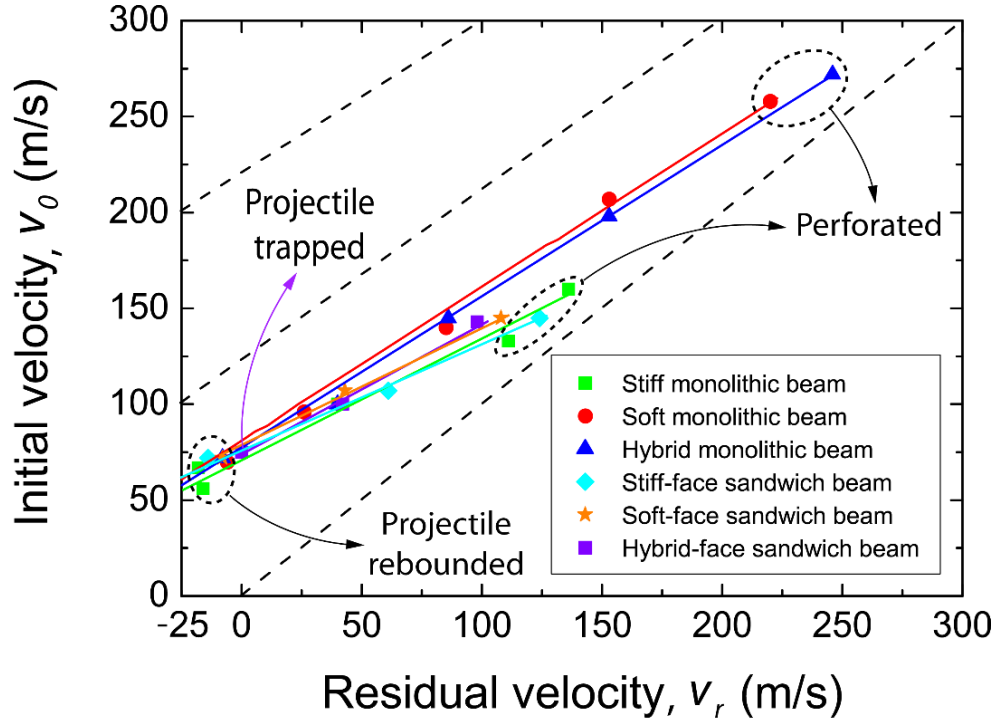


Fig. 5.17 Initial projectile velocity v_o as a function of residual projectile velocity v_r . The projectile embedded in the hybrid-face sandwich beam has been highlighted in Fig. 5.13 (c). The straight dash lines are reference lines. The impact direction of projectile is along 3-axis of the coordinate system.

5.5.4 Energy absorption capacity of beams

The kinetic energy of the projectile transmitted to the beams can be calculated as follow

$$\Delta E_{abs} = E_{k_o} - E_{k_r} = \frac{1}{2} M (v_o^2 - v_r^2) \quad (5.1)$$

where E_{k_o} and E_{k_r} are the initial and residual kinetic energy of projectile, respectively. ΔE_{abs} is the energy transmitted from the projectile to fibre

composite beams. This transmitted energy converted to the kinetic energy of beams and energy absorbed by beams. Based on Fig. 5.17, the kinetic energy of projectile transmitted to beams as a function of initial kinetic energy of projectile is summarized in Fig. 5.18. The initial kinetic energy of projectile is in the range of $13 \text{ J} \leq E_{k_0} \leq 307 \text{ J}$. Due to the different architectures, the monolithic and sandwich beams may acquire different kinetic energy during the impact events. Assuming that the kinetic energy acquired is identical for the beams with the same architecture, i.e. monolithic or sandwich, during impact. Hence, the energy absorbed by beams with the same architecture can be compared using the kinetic energy of projectile transmitted to beams.

For the monolithic beams, the soft and hybrid monolithic beams have the best energy absorption capacity, whereas the soft monolithic beam behaves better in energy absorption than the hybrid monolithic beam when the initial projectile velocity is higher than 160 ms^{-1} , as highlighted in Fig. 5.18. The stiff monolithic beam behaves worst in energy absorption. For the sandwich beams, as the failure mode of the soft-face sandwich beams is same in the impact velocity range of $107 \text{ ms}^{-1} < v_0 \leq 145 \text{ ms}^{-1}$, the energy absorption capacity of these beams reaches a plateau. However, within this velocity range, the energy absorbed by hybrid-face sandwich beams still increasing. The hybrid-face sandwich beam has better energy absorption capacity than soft-face sandwich beam at impact velocity of 145 ms^{-1} . This may due to the interaction between the soft and hard parts of hybrid face sheets. The other reason may be the debonding between back face sheet and honeycomb core, which absorbs a part of kinetic energy of projectile.

Except for the soft-face and hybrid-face sandwich beams, the measured maximum initial kinetic energy of projectile regarding to the mode of fracture is marked in Fig. 5.18 using an upward dash arrow. This kinetic energy can be regarded as the critical value that results in the transition of failure modes from fracture to perforation. It indicates that the energy absorption capacity of these beams normally decreases during the transition of these two failure modes. It can be explained as follow. Along the width direction of the beams, there are less fibres fracture for the failure mode of perforation than those for the failure mode of fracture. As the energy absorption capacity of composites is proportional to the failed fibres [180], the beams failed with perforation therefore absorb less kinetic energy of projectile than the beams failed with fracture. However, there is a slight increase for the energy absorbed by the stiff monolithic beam during the transition of failure modes. This is due to the fact that the stiff monolithic beam failed with perforation has wider range of fibre deformation and damage (e.g. fracture and comminution) than that failed with fracture. It can be demonstrated by comparing the high-speed photographic images in Figs. 5.7 (b) and (c), and also by Karthikeyan et al. [178]. This explanation is not suitable for the stiff-sheet sandwich beams as the beam failed with fracture of back face sheet also has significant fibre deformation and damage, as shown in Fig. 5.15 (a).

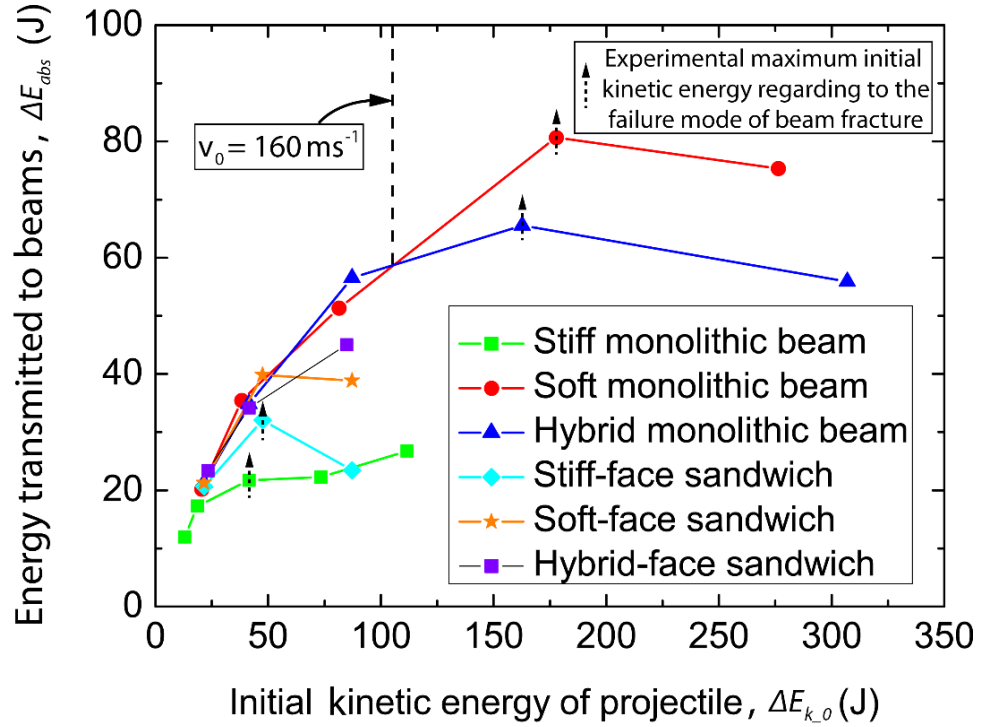


Fig. 5.18 Kinetic energy of projectile absorbed by the beams as a function of initial kinetic energy of projectile.

5.5.5 The effect of epoxy adhesive

Except for the failure of carbon fibre reinforcements, the epoxy adhesive also failed due to the debonding between stiff and soft composite parts as well as face sheet and honeycomb core. There are more debondings observed in hybrid monolithic and hybrid-face sandwich beams than the other types of beams. In the present study, the tensile strength of the adhesive is 30 MPa [235], much lower than that of the carbon fibre. Russell et al. [32] numerically demonstrated that no more than 5% of the initial kinetic energy of projectile is dissipated by the delamination of fibre layers in the soft impact events. Kirthikeyan and Russel [187] reported that the ballistic limit of the pre-delaminated fibre laminate was

10% higher than that of the laminate with same areal mass but without pre-delamination. This was due to the benefit of delamination that promoted an earlier transition from fibre fracture to stretching. The debonding, between the stiff and soft composite parts of hybrid beams, governed by the low-strength adhesive can also be regarded as ‘pre-delamination’. Hence, the weak adhesive interface may play an important role in indirectly dissipating impact energy of a projectile.

5.6 Concluding remarks

The ballistic responses of six types of carbon fibre composite beams, i.e. three monolithic beams and three sandwich beams, have been investigated to identify the advantages of hybrid beams. For each type of monolithic beam, three distinct failure modes, which were minor damage with projectile rebound, fracture and perforation, respectively, have been identified. The failure modes of fracture and perforation were mainly governed by the fracture of fibre reinforcements, and the development of these two damage modes depended on the wave propagation time in beams. The hybrid and soft monolithic beam had similar critical velocities for each failure mode, and both higher than the stiff monolithic beam. In addition, the hybrid monolithic beam had benefits under low velocity impact as the failure only occurred in the stiff composite part of beam and the soft part could still resisting loading. The back face damage mode of the hybrid monolithic beam that failed with perforation was different from that of stiff monolithic beam ascribed to the buffer effect of the soft composite part at the front face. For the stiff-sheet, soft-sheet and hybrid-sheet sandwich beams, the

failure modes were similar to those of the corresponding monolithic beams, i.e. the projectiles were rebounded by or trapped into sandwich beams at low impact velocity, and the back face sheet fully fractured and were perforated at medium and high impact velocities, respectively.

The energy absorption capacity of the monolithic and sandwich beams have also been studied. For the monolithic beams, the energy absorption capacity of the hybrid and soft monolithic beams were better than that of the stiff monolithic beams, whereas the stiff monolithic and stiff-face sandwich beams behaved worst. In addition, as more fibre reinforcements fractured, the beams failed with fracture had better energy absorption capacity than those failed with perforation. For the sandwich beams, the hybrid-face sandwich beams exhibited better energy absorption capacity than the soft-face sandwich beams at high impact velocity.

The weak adhesive interface between the stiff and soft composite parts in hybrid monolithic/sandwich beams may have a positive effect on the energy absorption capacity of beams. The strength and flexibility of adhesive may influence the development of debonding, their effects on the ballistic impact resistance of hybrid laminated composites is a future topic.

Chapter 6

Conclusions and Future Works

This thesis aims to investigate the dynamic response of high-performance components, i.e. honeycomb cores and fibre composite face sheets in sandwich structures. The objectives include: (i) to characterise the out-of-plane compressive response of hierarchical honeycombs under dynamic impact and identify the advantages of hierarchical honeycombs relative to normal honeycombs; (ii) to examine the dynamic compressive response of Nomex fibre composite honeycombs at high strain rates; (iii) to develop novel hybrid fibre composites for improving the ballistic resistance of beams. To achieve these objectives, the related work has been presented in Chapter 3 through to Chapter 5, and the conclusions are summarized below. Afterwards, the future works are discussed based on the conclusions of the current study.

6.1 Conclusions

6.1.1 Compressive response of additively manufactured AlSi10Mg alloy hierarchical honeycomb structures

The quasi-static and dynamic out-of-plane compressive performance of the Selective Laser Melting (SLM) manufactured AlSi10Mg alloy hierarchical honeycomb has been investigated via experiments and finite element simulations. The dynamic compression tests were conducted using a steel Kolsky bar setup. To identify the advantages of hierarchical honeycombs, the compressive

response of three types of honeycombs with different in-plane configurations and relative densities, i.e. single-scale, two-scale and three-scale honeycombs of relative density $0.19 \leq \bar{\rho} \leq 0.35$, were compared.

- i. The failure mechanisms of these metallic honeycombs were characterised to be different under quasi-static compression. With the increase in relative density of honeycombs, the failure mechanism of single-scale honeycomb changed from plastic buckling of walls to local damage of parent materials without buckling. However, the two-scale and three-scale honeycombs failed with the damage of the parent material in the same range of relative densities.
- ii. Due to the different failure mechanisms, the two hierarchical honeycombs offered higher peak nominal wall stresses than the single-scale honeycomb at a low relative density ($\bar{\rho} = 0.19$). The difference was diminished when the relative density of honeycombs increased, i.e. the single-scale honeycomb can achieve similar peak wall stress in comparison to hierarchical honeycombs. In addition, a similar peak wall stress achieved by two-scale and three-scale honeycombs may suggest that the structural performance under out-of-plane compression is not sensitive to hierarchical architecture.
- iii. The dynamic compressive strength enhancement of the honeycombs was governed by the strain rate sensitivity of the parent material. The hierarchical honeycombs exhibited better energy absorption capacity than the single-scale honeycomb under dynamic compression.

- iv. The developed finite element (FE) simulation methodology can predict the compressive response of the SLM manufactured honeycombs reasonably well. The effects of the impact method as well as initial geometrical imperfections on the compressive performance of honeycombs were both predicted to be negligible.

6.1.2 Dynamic compressive response of Nomex honeycombs

The out-of-plane compressive responses of Nomex honeycombs under quasi-static loading and high strain rates up to 1500 s^{-1} were measured via experiments, and predicted by validating finite element calculations. In order to detect the low stress of Nomex honeycombs, dynamic compression tests were performed using the sensitive magnesium alloy Kolsky bar setup.

- i. Different failure modes of Nomex honeycombs were achieved under quasi-static and dynamic compression. For quasi-static compression, the Nomex honeycombs failed with local phenolic resin fracture after the elastic buckling of honeycomb walls. However, for dynamic compression, the honeycombs failed with the stubbing of cell walls at the ends of specimens.
- ii. The Nomex honeycombs exhibited a linear compressive strength enhancement up to 30% from a quasi-static state up to a strain rate of 1500 s^{-1} . The strength enhancement was governed by two mechanisms: the strain rate effect of the phenolic resin and inertial stabilization of honeycomb unit cell walls. The inertial stabilization of unit cell walls which contributed 61%-74% to the strength enhancement, played a more significant role.

- iii. The validated finite element simulation, which modelled an aramid paper layer and phenolic resin layer separately, had a good agreement with experimental measurements. Predictions indicated that the impact method and the initial geometrical imperfections were insensitive to the out-of-plane compressive response of Nomex honeycombs.

6.1.3 Dynamic response of hybrid carbon fibre laminate beams under ballistic impact

The fibre composites hybridizing stiff composites and soft composites are developed to improve the dynamic performance of composite beams under ballistic impact. The ballistic impact responses of six types of carbon fibre composite beams, three monolithic beams and three sandwich beams at a projectile velocity range of $50 \text{ ms}^{-1} \leq v_0 \leq 300 \text{ ms}^{-1}$, have been characterised to identify the advantages of stiff/soft hybrid composite beams.

- i. Three different failure modes were observed for each type of monolithic beam at different projectile velocities, i.e. minor damage with rebound of projectile at low impact velocity, fracture of beam at medium impact velocity and perforation of beam at high impact velocity. For the sandwich beams with stiff, soft and hybrid face sheets, the failure modes were similar to those of the corresponding monolithic beams, i.e. the projectiles were rebounded or embedded into the sandwich beams at low impact velocity, and the back face sheet completely fractured and were perforated at medium and high impact velocities.

- ii. For monolithic beams, the hybrid and soft monolithic beams exhibited better energy absorption capacity than the stiff monolithic beams. As for sandwich beams, the hybrid-face sandwich beams absorbed more kinetic energy from the projectile than the soft-face sandwich beams at higher projectile velocity, and the stiff-face sandwich beams behaved the most poorly in terms of energy absorption. As more fibres were fractured during ballistic impact, the beams failed with full fracture absorbed more kinetic energy than those failed due to perforation.
- iii. The advantages of the developed stiff/soft hybrid composite beam are obvious. Under low velocity impact, the stiff part fractured whereas the soft composite part survived with negligible damage. Hence, the hybrid beams can still resist loading after low-velocity impact. In addition, owing to the buffer effect of the soft part at the front face, the stress within the stiff part of hybrid monolithic/sandwich beams can be distributed more uniformly than that of the stiff monolithic/sandwich beams.
- iv. In hybrid monolithic and sandwich beams, the weak adhesive interface between stiff and soft composite parts may play an important role in improving the energy absorption capacity of beams indirectly.

6.2 Future work

6.2.1 Compressive response of additively manufactured hierarchical honeycombs

i. Investigation of high-performance structures

Additive manufacturing methodology is promising for fabricating accurate and complex structural components which cannot be achieved via traditional manufacturing methods. More high-performance structures should be investigated for specific applications in the future. For example, the debonding between sandwich core and face sheets is easy to develop under dynamic impact. The adhesion between core and face sheets can be improved using additive manufacturing methods that ensure the good integrity of sandwich structures.

ii. The effect of hierarchical order

Chapter 3 only investigated the compressive response of two types of hierarchical honeycombs, i.e. two-scale and three-scale honeycombs. The effect of higher hierarchical order on the mechanical properties of honeycombs is an avenue for further research. Moreover, the honeycombs were only fabricated along the out-of-plane direction in this study whereas the compressive response of honeycombs fabricated along in-plane direction should also be investigated.

iii. Effect of relative density on failure mode

Due to the limitation of the manufacturing facility employed in this study, the relative densities of the SLM manufactured honeycombs were in the range of

$0.19 \leq \bar{\rho} \leq 0.35$. The high relative density may result in the same failure mechanism for hierarchical honeycombs, i.e. parent material damage. As we know, the honeycombs that failed with parent material were capable of resisting higher stress than those that failed with buckling. It is still unclear if hierarchical honeycombs fail with elastic or plastic buckling of cell walls when the relative density is low enough. Hence, in order to avoid wall buckling (if it exists), it is important to determine the critical relative density of hierarchical honeycombs between the failure mechanisms of wall buckling and parent material damage.

iv. Anisotropic model for finite element simulation

The homogeneous finite element model was used to predict the compressive response of additively manufactured honeycombs. However, the flaws between the stacking layers, stemming from the asymmetric heat flux during laser irradiation and cooling, were not considered. A further study is required using the anisotropic model to predict the mechanical response of additively manufactured structures. Also, the flaws between layers are more likely to give rise to damage. Hence, the additive manufactured technique should also be improved.

6.2.2 Dynamic compressive response of Nomex honeycombs

i. Optimization of in-plane topology

Under quasi-static out-of-plane compression, Nomex honeycomb walls gave rise to elastic buckling before the catastrophic local fracture of the phenolic resin.

Hence some measures such as optimizing the in-plane topology or the wall thickness ratio of phenolic resin layer to aramid paper layer, should be taken to prevent the walls from buckling.

ii. Compressive response under higher strain rate impact

In the present study, the magnesium alloy Kolsky bar and maraging steel striker were used to investigate the dynamic compressive response of Nomex honeycombs. In case of the yield of the magnesium alloy bar, the maximum imposed strain rate on the Nomex honeycombs was 1500 s^{-1} . However, the compressive response of Nomex honeycombs under higher strain rate loading is still needed to be studied.

iii. Mesoscopic model for finite element simulation

In the finite element simulation of Nomex honeycombs, the aramid paper layer was modelled as homogeneous. However, the aramid paper layer was made from random aramid fibre, as stated in Chapter 4. The mesoscopic model of aramid paper layer is desired to be modelled for further investigation.

6.2.3 Ballistic impact on hybrid fibre composites

i. The effect of projectile shape

In ballistic impact events, only a spherical projectile was used to impact the composite materials. The effect of other projectile nose shapes (e.g. conical, hemispherical and blunt) on the ballistic resistance of composites, in particular stiff/soft hybrid composites, still needs to be further investigated.

ii. Multi-hit impact

Rare protective systems are designed for resisting single impact in a specific period, they are mostly subject to multiple impacts at different sites. For example, there are on average 156 damage sites observed on the Discovery's space transportation system flights [236]. Hence, the investigation of a multi-hit impact on hybrid composites should be conducted to determine the damage characterisation of materials. In order to widen the applicability of hybrid composites, the response of hybrid composites impacted by other types of dynamic loading such as ballast impact, also needs to be understood.

iii. Effect of adhesive

Although the weak adhesive interface in stiff/soft hybrid composites absorbs a negligible amount of impact energy of a projectile during debonding, it may indirectly dissipate a large amount of impact energy. The effect of adhesive strength and flexibility on debonding and impact resistance of hybrid composite beams, is still unclear.

Published work

Chapter 3 has been published in Composite Structures and an International Conference on Composites/Nano Engineering (ICCE-25).

Yuwu Zhang, Tao Liu, Huan Ren, Ian Maskery, Ian Ashcroft. Dynamic compressive response of additively manufactured AlSi10Mg alloy hierarchical honeycomb structures. Composite Structure. 2018; 195: 45-59. DOI: [10.1016/j.compstruct.2018.04.021](https://doi.org/10.1016/j.compstruct.2018.04.021).

Yuwu Zhang, Tao Liu, Huan Ren, Ian Maskery, Ian Ashcroft. Experimental and finite-element investigations on the dynamic compressive characteristics of aluminium alloy based honeycomb structures. 25th Annual International Conference on Composites/Nano Engineering. Rome, Italy.

Chapter 4 has been published in Composite Parts B: Engineering.

Yuwu Zhang, Tao Liu, Walid Tizani. Experimental and numerical analysis of dynamic compressive response of Nomex honeycombs. Composites Part B: Engineering. 2018; 148: 27-39. DOI: [10.1016/j.compositesb.2018.04.025](https://doi.org/10.1016/j.compositesb.2018.04.025).

Chapter 5 has been submitted to the International Journal of Impact Engineering entitled ‘Dynamic response of hybrid carbon fibre laminate beams under ballistic impact’.

References

- [1] Jacinto AC, Ambrosini RD, Danesi RF. Experimental and computational analysis of plates under air blast loading. *International Journal of Impact Engineering*. 2001;25:927-47.
- [2] Jackson M, Shukla A. Performance of sandwich composites subjected to sequential impact and air blast loading. *Composites Part B: Engineering*. 2011;42:155-66.
- [3] Liang Y, Spuskanyuk AV, Flores SE, Hayhurst DR, Hutchinson JW, McMeeking RM, et al. The response of metallic sandwich panels to water blast. *Journal of Applied Mechanics*. 2007;74:81-99.
- [4] Wei Z, Dharmasena KP, Wadley HNG, Evans AG. Analysis and interpretation of a test for characterizing the response of sandwich panels to water blast. *International Journal of Impact Engineering*. 2007;34:1602-18.
- [5] Liu T, Fleck NA, Wadley HNG, Deshpande VS. The impact of sand slugs against beams and plates: Coupled discrete particle/finite element simulations. *Journal of the Mechanics and Physics of Solids*. 2013;61:1798-821.
- [6] Liu T, Wadley HNG, Deshpande VS. Dynamic compression of foam supported plates impacted by high velocity soil. *International Journal of Impact Engineering*. 2014;63:88-105.
- [7] Lu G, Yu TX. *Energy absorption of structures and materials*. Cambridge: Woodhead Publishing Ltd, 2003.
- [8] Gibson LJ, Ashby MF. *Cellular solids: structure and properties*. Cambridge, UK: Cambridge University Press, 1997.
- [9] D. RD, A. FN, S. DV. The response of clamped sandwich beams subjected to shock loading. *International Journal of Impact Engineering*. 2006;32:968-87.
- [10] Fleck NA, Deshpande VS. The Resistance of Clamped Sandwich Beams to Shock Loading. *Journal of Applied Mechanics*. 2004;71:386-401.
- [11] Xin FX, Lu TJ. Sound radiation of orthogonally rib-stiffened sandwich structures with cavity absorption. *Composites Science and Technology*. 2010;70:2198-206.

- [12] Kawasaki T, Kawai S. Thermal insulation properties of wood-based sandwich panel for use as structural insulated walls and floors. *Journal of Wood Science*. 2006;52:75-83.
- [13] Li Z, Crocker MJ. A review on vibration damping in sandwich composite structures. *International Journal of Acoustics and Vibration*. 2005;10:159-69.
- [14] Deshpande V, Fleck N. One-dimensional response of sandwich plates to underwater shock loading. *Journal of the Mechanics and Physics of Solids*. 2005;53:2347-83.
- [15] Wadley H. Fabrication and structural performance of periodic cellular metal sandwich structures. *Composites Science and Technology*. 2003;63:2331-43.
- [16] Tagarielli VL, Deshpande VS, Fleck NA. The dynamic response of composite sandwich beams to transverse impact. *International Journal of Solids and Structures*. 2007;44:2442-57.
- [17] Fleck NA, Deshpande VS, Ashby MF. Micro-architected materials: past, present and future. *Proceedings of the Royal Society A: Mathematical, Physical and Engineering Sciences*. 2010;466:2495-516.
- [18] Cunniff PM. Dimensionless Parameters for Optimization of Textile-Based Body Armor Systems. *Proceedings of the 18th International Symposium on Ballistics*. San Antonio 1999. p. 1303-10.
- [19] Zhou H, Fan T, Li X, Zhang D, Guo Q, Ogawa H. Biomimetic photocatalyst system derived from the natural prototype in leaves for efficient visible-light-driven catalysis. *Journal of Materials Chemistry*. 2009;19:2695-703.
- [20] Liu K, Jiang L. Bio-inspired design of multiscale structures for function integration. *Nano Today*. 2011;6:155-75.
- [21] Marmorstein AD, Bonilha VL, Chiflet S, Neill JM, Rodriguez-Boulan E. The polarity of the plasma membrane protein RET-PE2 in retinal pigment epithelium is developmentally regulated. *Journal of Cell Science*. 1996;109:3025-34.
- [22] Lecuit T, Lenne PF. Cell surface mechanics and the control of cell shape, tissue patterns and morphogenesis. *Nature Reviews: Molecular Cell Biology*. 2007;8:633-44.

- [23] Mackenzie DM. Proving the perfection of the honeycomb. *Science*. 1999;285:1338-9.
- [24] George J, Onodera J, Miyata T. Biodegradable honeycomb collagen scaffold for dermal tissue engineering. *Journal of Biomedical Materials Research*. 2008;87:1103-11.
- [25] Liu T, Deng ZC, Lu TJ. Bi-functional optimization of actively cooled, pressurized hollow sandwich cylinders with prismatic cores. *Journal of the Mechanics and Physics of Solids*. 2007;55:2565-602.
- [26] Wang D-M, Wang J, Liao Q-H. Investigation of mechanical property for paper honeycomb sandwich composite under different temperature and relative humidity. *Journal of Reinforced Plastics and Composites*. 2013;32:987-97.
- [27] Wang D, Bai Z. Mechanical property of paper honeycomb structure under dynamic compression. *Materials & Design*. 2015;77:59-64.
- [28] Hutchinson JW, Xue Z. Metal sandwich plates optimized for pressure impulses. *International Journal of Mechanical Sciences*. 2005;47:545-69.
- [29] Guo X, Cai X, Zhu L, Zhang L, Yang H. Preparation and properties of SiC honeycomb ceramics by pressureless sintering technology. *Journal of Advanced Ceramics*. 2014;3:83-8.
- [30] Ramavath P, Biswas P, Ravi N, Johnson R, Harkin-Jones E. Prediction and validation of buckling stress (σ_{cr}) of the ceramic honeycomb cell walls under quasi-static compression. *Cogent Engineering*. 2016;3:1-7.
- [31] Russell BP, Deshpande VS, Wadley HNG. Quasi-static deformation and failure modes of composite square honeycombs. *Journal of Mechanics of Materials and Structures*. 2008;3:1315-40.
- [32] Russell BP, Liu T, Fleck NA, Deshpande VS. The soft impact of composite sandwich beams with a square-honeycomb core. *International Journal of Impact Engineering*. 2012;48:65-81.
- [33] Tagarielli VL, Deshpande VS, Fleck NA. The high strain rate response of PVC foams and end-grain balsa wood. *Composites Part B: Engineering*. 2008;39:83-91.

- [34] Deshpande VS, Fleck NA. High strain rate compressive behaviour of aluminium alloy foams. *International Journal of Impact Engineering*. 1999;24:277-98.
- [35] Ashby MF, Evans AG, Fleck NA, Gibson LJ, Hutchinson JW, Wadley HNG. *Metal foams: a design guide*: Boston MA: Butterworth-Heinemann, 2000.
- [36] Luyten J, Mullens S, Cooymans J, De Wilde AM, Thijs I, Kemps R. Different methods to synthesize ceramic foams. *Journal of the European Ceramic Society*. 2009;29:829-32.
- [37] Peng HX, Fan Z, Evans JRG, Busfield JJC. Microstructure of ceramic foams. *Journal of the European Ceramic Society*. 1999;20:807-13.
- [38] Gibson LJ, Ashby MF, F.R.S. The mechanics of three-dimensional cellular materials. *Proceedings of the Royal Society A: Mathematical, Physical and Engineering Sciences*. 1982;382:43-59.
- [39] Gibson LJ, Ashby MF, F.R.S., Schajer JGS, Robertson CI. The mechanics of two-dimensional cellular materials. *Proceedings of the Royal Society A: Mathematical, Physical and Engineering Sciences*. 1982;382:25-42.
- [40] Elnasri I, Pattofatto S, Zhao H, Tsitsiris H, Hild F, Girard Y. Shock enhancement of cellular structures under impact loading: Part I Experiments. *Journal of the Mechanics and Physics of Solids*. 2007;55:2652-71.
- [41] Wadley HN. Multifunctional periodic cellular metals. *Philos Trans A Math Phys Eng Sci*. 2006;364:31-68.
- [42] Kooistra G. Compressive behavior of age hardenable tetrahedral lattice truss structures made from aluminium. *Acta Materialia*. 2004;52:4229-37.
- [43] Zok FW, Waltner SA, Wei Z, Rathbun HJ, McMeeking RM, Evans AG. A protocol for characterizing the structural performance of metallic sandwich panels: application to pyramidal truss cores. *International Journal of Solids and Structures*. 2004;41:6249-71.
- [44] Wicks N, Hutchinson JW. Optimal truss plates. *International Journal of Solids and Structures*. 2000;38:5165-83.
- [45] Kim T, Hodson HP, Lu TJ. Fluid-flow and endwall heat-transfer characteristics of an ultralight lattice-frame material. *International Journal of Heat and Mass Transfer*. 2004;47:1129-40.

- [46] Gu S, Lu TJ, Evans AG. On the design of two-dimensional cellular metals for combined heat dissipation and structural load capacity. *International Journal of Heat and Mass Transfer*. 44:2163-75.
- [47] Côté F, Deshpande VS, Fleck NA, Evans AG. The compressive and shear responses of corrugated and diamond lattice materials. *International Journal of Solids and Structures*. 2006;43:6220-42.
- [48] Mori LF, Lee S, Xue ZY, Vaziri A, Queheillalt DT, Dharmasena KP, et al. Deformation and fracture modes of sandwich structures subjected to underwater impulsive loads. *Journal of Mechanics of Materials and Structures*. 2007;2:1981-2006.
- [49] Xue Z, Hutchinson JW. A comparative study of impulse-resistant metal sandwich plates. *International Journal of Impact Engineering*. 2004;30:1283-305.
- [50] Dharmasena KP, Queheillalt DT, Wadley HNG, Dudt P, Chen Y, Knight D, et al. Dynamic compression of metallic sandwich structures during planar impulsive loading in water. *European Journal of Mechanics - A/Solids*. 2010;29:56-67.
- [51] Jang W-Y, Kyriakides S. On the crushing of aluminum open-cell foams: Part I. Experiments. *International Journal of Solids and Structures*. 2009;46:617-34.
- [52] Jang W-Y, Kyriakides S. On the crushing of aluminum open-cell foams: Part II analysis. *International Journal of Solids and Structures*. 2009;46:635-50.
- [53] Wang AJ, McDowell DL. In-Plane Stiffness and Yield Strength of Periodic Metal Honeycombs. *Journal of Engineering Materials and Technology*. 2004;126:137-56.
- [54] Fan HL, Jin FN, Fang DN. Mechanical properties of hierarchical cellular materials. Part I: Analysis. *Composites Science and Technology*. 2008;68:3380-7.
- [55] Papka SD, Kyriakides S. Experiments and full-scale numerical simulations of in-plane crushing of a honeycomb. *Acta Materialia*. 1998;46:2765-76.
- [56] Li Z, Gao Q, Yang S, Wang L, Tang J. Comparative study of the in-plane uniaxial and biaxial crushing of hexagonal, re-entrant, and mixed honeycombs. *Journal of Sandwich Structures & Materials*. 2018:1-23.

- [57] Ruana D, Lua G, Wang B, Yu TX. In-plane dynamic crushing of honeycombs—a finite element study. *International Journal of Impact Engineering*. 2003;28:161-82.
- [58] Ajdari A, Nayeb-Hashemi H, Vaziri A. Dynamic crushing and energy absorption of regular, irregular and functionally graded cellular structures. *International Journal of Solids and Structures*. 2011;48:506-16.
- [59] Deshpande VS, Ashby MF, Fleck NA. Foam topology-bending versus stretching dominated architectures. *Acta Materialia*. 2001;49:1035-40.
- [60] V.S. Deshpande MFA, N.A. Fleck. Foam topology bending versus strain stretching dominated architectures. *Acta Materialia*. 2001;49:1035-40.
- [61] Fleck NA, Qiu X. The damage tolerance of elastic–brittle, two-dimensional isotropic lattices. *Journal of the Mechanics and Physics of Solids*. 2007;55:562-88.
- [62] Haghpanah B, Oftadeh R, Papadopoulos J, Vaziri A. Self-similar hierarchical honeycombs. *Proceedings of the Royal Society A: Mathematical, Physical and Engineering Sciences*. 2013;469:1-19.
- [63] Khan MK, Baig T, Mirza S. Experimental investigation of in-plane and out-of-plane crushing of aluminum honeycomb. *Materials Science and Engineering: A*. 2012;539:135-42.
- [64] Wilbert A, Jang WY, Kyriakides S, Floccari JF. Buckling and progressive crushing of laterally loaded honeycomb. *International Journal of Solids and Structures*. 2011;48:803-16.
- [65] Radford DD, McShane GJ, Deshpande VS, Fleck NA. Dynamic Compressive Response of Stainless-Steel Square Honeycombs. *Journal of Applied Mechanics*. 2007;74:658-67.
- [66] Hales TC. The Honeycomb Conjecture. *Discrete & Computational Geometry*. 2001;25:1-22.
- [67] Zuhri MYM, Guan ZW, Cantwell WJ. The mechanical properties of natural fibre based honeycomb core materials. *Composites Part B: Engineering*. 2014;58:1-9.
- [68] Kim B, Christensen RM. Basic two-dimensional core types for sandwich structures. *International Journal of Mechanical Sciences*. 2000;42:657-76.

- [69] Yamashita M, Gotoh M. Impact behavior of honeycomb structures with various cell specifications—numerical simulation and experiment. *International Journal of Impact Engineering*. 2005;32:618-30.
- [70] Zhang Y, Lu M, Wang CH, Sun G, Li G. Out-of-plane crashworthiness of bio-inspired self-similar regular hierarchical honeycombs. *Composite Structures*. 2016;144:1-13.
- [71] Côté F, Deshpande VS, Fleck NA, Evans AG. The out-of-plane compressive behavior of metallic honeycombs. *Materials Science and Engineering: A*. 2004;380:272-80.
- [72] Liu L, Wang H, Guan Z. Experimental and numerical study on the mechanical response of Nomex honeycomb core under transverse loading. *Composite Structures*. 2015;121:304-14.
- [73] Hu LL, Cai DY, Wu GP, He XL, Yu TX. Influence of internal pressure on the out-of-plane dynamic behavior of circular-celled honeycombs. *International Journal of Impact Engineering*. 2017;104:64-74.
- [74] Feng H, Liu L, Zhao Q. Experimental and numerical investigation of the effect of entrapped air on the mechanical response of Nomex honeycomb under flatwise compression. *Composite Structures*. 2017;182:617-27.
- [75] Zhao H, Gary G. Crushing behaviour of aluminium honeycombs under impact loading. *International Journal of Impact Engineering*. 1998;21:827-36.
- [76] Tao Y, Chen M, Chen H, Pei Y, Fang D. Strain rate effect on the out-of-plane dynamic compressive behavior of metallic honeycombs: Experiment and theory. *Composite Structures*. 2015;132:644-51.
- [77] Wadley HNG, Dharmasena KP, Queheillalt DT, Chen Y, Dudt P, Knight D, et al. Dynamic compression of square honeycomb structures during underwater impulsive loading. *Journal of Mechanics of Materials and Structures*. 2007;2:2025-48.
- [78] Xu S, Beynon JH, Ruan D, Lu G. Experimental study of the out-of-plane dynamic compression of hexagonal honeycombs. *Composite Structures*. 2012;94:2326-36.

- [79] Baker WE, Togami TC, Weydert JC. Static and dynamic properties of high-density metal honeycombs. *International Journal of Impact Engineering*. 1998;21:149-63.
- [80] Zhao H, Elnasri I, Abdennadher S. An experimental study on the behaviour under impact loading of metallic cellular materials. *International Journal of Mechanical Sciences*. 2005;47:757-74.
- [81] Harrigan JJ, Reid SR, Peng C. Inertia effects in impact energy absorbing materials and structures. *International Journal of Impact Engineering*. 1999;22:955-79.
- [82] Su XY, Yu TX, Reid SR. Inertia-sensitive impact energy-absorbing structures. Part II: effect of strain rate. *International Journal of Impact Engineering*. 1995;16:673-89.
- [83] Su XY, Yu TX, Reid SR. Inertia-sensitive impact energy-absorption structures. Part I: effect of inertia and elasticity. *International Journal of Impact Engineering*. 1995;16:651-72.
- [84] Tao Y, Chen M, Pei Y, Fang D. Strain rate effect on mechanical behavior of metallic honeycombs under out-of-plane dynamic compression. *Journal of Applied Mechanics*. 2015;82:021007-1-6.
- [85] Xue Z, Hutchinson JW. Crush dynamics of square honeycomb sandwich cores. *International Journal for Numerical Methods in Engineering*. 2006;65:2221-45.
- [86] Park S, Russell BP, Deshpande VS, Fleck NA. Dynamic compressive response of composite square honeycombs. *Composites Part A: Applied Science and Manufacturing*. 2012;43:527-36.
- [87] Johnson GR, Cook WH. A constitutive model and data for metals subjected to large strains, high strain rates and high temperatures. *Proceedings of the Seventh International Symposium on Ballistics*. The Hague, The Netherlands 1983. p. 541-647.
- [88] Li L, Flores-Johnson EA, Shen L, Proust G, Chen Z. Effects of heat treatment and strain rate on the microstructure and mechanical properties of 6061 Al alloy. *International Journal of Damage Mechanics*. 2015;25:26-41.

- [89] Lemanski SL, Petrinic N, Nurick GN. Experimental Characterisation of Aluminium 6082 at Varying Temperature and Strain Rate. *Strain*. 2013;49:147-57.
- [90] Oosterkamp LD, Ivankovic A, Venizelos G. High strain rate properties of selected aluminium alloys. *Materials Science and Engineering: A*. 2000;278:225-35.
- [91] Picu RC, Vincze G, Ozturk F, Gracio JJ, Barlat F, Maniatty AM. Strain rate sensitivity of the commercial aluminum alloy AA5182-O. *Materials Science and Engineering: A*. 2005;390:334-43.
- [92] Chen Y, Clausen AH, Hopperstad OS, Langseth M. Stress–strain behaviour of aluminium alloys at a wide range of strain rates. *International Journal of Solids and Structures*. 2009;46:3825-35.
- [93] Clausen AH, Børvik T, Hopperstad OS, Benallal A. Flow and fracture characteristics of aluminium alloy AA5083–H116 as function of strain rate, temperature and triaxiality. *Materials Science and Engineering: A*. 2004;364:260-72.
- [94] Cadoni E, Dotta M, Forni D, Bianchi S, Kaufmann H. Strain rate effects on mechanical properties in tension of aluminium alloys used in armour applications. *DYMAT 2012 - 10th International Conference on the Mechanical and Physical Behaviour of Materials under Dynamic Loading*. Freiburg, Germany 2012.
- [95] Ajdari A, Jahromi BH, Papadopoulos J, Nayeb-Hashemi H, Vaziri A. Hierarchical honeycombs with tailorable properties. *International Journal of Solids and Structures*. 2012;49:1413-9.
- [96] Chen Y, Li T, Jia Z, Scarpa F, Yao C-W, Wang L. 3D printed hierarchical honeycombs with shape integrity under large compressive deformations. *Materials & Design*. 2018;137:226-34.
- [97] Aizenberg J, Weaver JC, Thanawala MS, Sundar VC, Morse DE, Fratzl P. Skeleton of euplectella sp.: structural hierarchy from the nanoscale to the macroscale. *Science*. 2005;309:275-8.
- [98] Oftadeh R, Haghpanah B, Vella D, Boudaoud A, Vaziri A. Optimal fractal-like hierarchical honeycombs. *Physical Review Letters*. 2014;113:104301.

- [99] Zhao L, Zheng Q, Fan H, Jin F. Hierarchical composite honeycombs. *Materials & Design*. 2012;40:124-9.
- [100] Mousanezhad D, Ebrahimi H, Haghpahan B, Ghosh R, Ajdari A, Hamouda AMS, et al. Spiderweb honeycombs. *International Journal of Solids and Structures*. 2015;66:218-27.
- [101] Lakes R. Materials with structural hierarchy. *Nature*. 1993;361:511-5.
- [102] Yi T. Mechanical properties of a hierarchical honeycomb with sandwich walls. *Proceedings of the Institution of Mechanical Engineers, Part C: Journal of Mechanical Engineering Science*. 2016;230:2765-75.
- [103] Kooistra GW, Deshpande V, Wadley HNG. Hierarchical corrugated core sandwich panel concepts. *Journal of Applied Mechanics*. 2007;74:259-68.
- [104] Fratzl P, Weinkamer R. Nature's hierarchical materials. *Progress in Materials Science*. 2007;52:1263-334.
- [105] Hao P, Du J. Energy absorption characteristics of bio-inspired honeycomb column thin-walled structure under impact loading. *J Mech Behav Biomed Mater*. 2018;79:301-8.
- [106] Sun G, Jiang H, Fang J, Li G, Li Q. Crashworthiness of vertex based hierarchical honeycombs in out-of-plane impact. *Materials & Design*. 2016;110:705-19.
- [107] Bourbigot S, Flambard X. Heat resistance and flammability of high performance fibres: A review. *Fire and Materials*. 2002;26:155-68.
- [108] Zhou J, Yao Z, Chen Y, Wei D, Wu Y, Xu T. Mechanical and thermal properties of graphene oxide/phenolic resin composite. *Polymer Composites*. 2013;34:1245-9.
- [109] Shafizadeh JE, Seferis JC. Characterization of phenolic resin for composite honeycomb applications. *ICCM-12. Pairs1999*.
- [110] Kandola BK, Krishnan L, Deli D, Ebdon JR. Blends of unsaturated polyester and phenolic resins for application as fire-resistant matrices in fibre-reinforced composites. Part 2: Effects of resin structure, compatibility and composition on fire performance. *Polymer Degradation and Stability*. 2015;113:154-67.

- [111] Heimbs S, Schmeer S, Middendorf P, Maier M. Strain rate effects in phenolic composites and phenolic-impregnated honeycomb structures. *Composites Science and Technology*. 2007;67:2827-37.
- [112] Aktay L, Johnson AF, Kröplin B-H. Numerical modelling of honeycomb core crush behaviour. *Engineering Fracture Mechanics*. 2008;75:2616-30.
- [113] Seemann R, Krause D. Numerical modelling of Nomex honeycomb cores for detailed analyses of sandwich panel joints. 11th World Congress on Computational Mechanics. Barcelona, Spain 2014.
- [114] Anagnostopoulos K, Kim H. Phenomenological investigation of Nomex core damage mechanics in honeycomb sandwich panels under transverse impact and quasi-static loading. 31st Annual Technical Conference of the American Society for Composites. Virginia, USA 2016.
- [115] Asprone D, Auricchio F, Menna C, Morganti S, Prota A, Reali A. Statistical finite element analysis of the buckling behavior of honeycomb structures. *Composite Structures*. 2013;105:240-55.
- [116] Zhang J, Ashby MF. The out-of-plane properties of honeycombs. *International Journal of Mechanical Sciences*. 1991;34:475-89.
- [117] Ashby MF, Bréchet YJM. Designing hybrid materials. *Acta Materialia*. 2003;51:5801-21.
- [118] Russell BP, Liu T, Fleck NA, Deshpande VS. Quasi-Static Three-Point Bending of Carbon Fiber Sandwich Beams With Square Honeycomb Cores. *Journal of Applied Mechanics*. 2011;78:031008.
- [119] Marasco AI, Cartié DDR, Partridge IK, Rezai A. Mechanical properties balance in novel Z-pinned sandwich panels: Out-of-plane properties. *Composites Part A: Applied Science and Manufacturing*. 2006;37:295-302.
- [120] Roy R, Park S-J, Kweon J-H, Choi J-H. Characterization of Nomex honeycomb core constituent material mechanical properties. *Composite Structures*. 2014;117:255-66.
- [121] Foo CC, Chai GB, Seah LK. Mechanical properties of Nomex material and Nomex honeycomb structure. *Composite Structures*. 2007;80:588-94.

- [122] Liu L, Meng P, Wang H, Guan Z. The flatwise compressive properties of Nomex honeycomb core with debonding imperfections in the double cell wall. *Composites Part B: Engineering*. 2015;76:122-32.
- [123] Keshavanarayana S, Thotakuri MV. Off-axis compression behaviour of honeycomb core in WT-plane. *International Journal of Crashworthiness*. 2009;14:173-81.
- [124] Bitzer TN. *Honeycomb technology*. London: Chapman & Hall 1997.
- [125] Dharmasena KP, Wadley HNG, Xue Z, Hutchinson JW. Mechanical response of metallic honeycomb sandwich panel structures to high-intensity dynamic loading. *International Journal of Impact Engineering*. 2008;35:1063-74.
- [126] Park S, Russell BP, Deshpande VS, Fleck NA. Dynamic compressive response of composite square honeycombs. 18th International Conference on Composites Materials (ICCM). Jeju, Korea 2011.
- [127] Hull CW. Apparatus for production of three-dimensional objects by stereolithography. Google Patent 1986.
- [128] Yap CY, Chua CK, Dong ZL, Liu ZH, Zhang DQ, Loh LE, et al. Review of selective laser melting: Materials and applications. *Applied Physics Reviews*. 2015;2:041101.
- [129] Kruth JP, Wang X, Laoui T, Froyen L. Lasers and materials in selective laser sintering. *Assembly Automation*. 2003;23:357-71.
- [130] Simonelli M, Tuck C, Aboulkhair NT, Maskery I, Ashcroft I, Wildman RD, et al. A Study on the Laser Spatter and the Oxidation Reactions During Selective Laser Melting of 316L Stainless Steel, Al-Si10-Mg, and Ti-6Al-4V. *Metallurgical and Materials Transactions A*. 2015;46:3842-51.
- [131] Sood AK, Ohdar RK, Mahapatra SS. Parametric appraisal of mechanical property of fused deposition modelling processed parts. *Materials & Design*. 2010;31:287-95.
- [132] Chacón JM, Caminero MA, García-Plaza E, Núñez PJ. Additive manufacturing of PLA structures using fused deposition modelling: Effect of process parameters on mechanical properties and their optimal selection. *Materials & Design*. 2017;124:143-57.

- [133] Sirringhaus H, Kawase T, Friend RH, Shimoda T, Inbasekaran M, Wu W, et al. High-resolution inkjet printing of all-polymer transistor circuits. *Science*. 2000;290:2123-6.
- [134] Liu Y, Cui T, Varshney K. All-polymer capacitor fabricated with inkjet printing technique. *Solid-State Electronics*. 2003;47:1543-8.
- [135] Bosscher P, Williams RL, Bryson LS, Castro-Lacouture D. Cable-suspended robotic contour crafting system. *Automation in Construction*. 2007;17:45-55.
- [136] Carroll BE, Palmer TA, Beese AM. Anisotropic tensile behavior of Ti–6Al–4V components fabricated with directed energy deposition additive manufacturing. *Acta Materialia*. 2015;87:309-20.
- [137] Chantarapanich N, Laohaprapanon A, Wisutmethangoon S, Jiamwatthanachai P, Chalermkarnnon P, Sucharitpwatskul S, et al. Fabrication of three-dimensional honeycomb structure for aeronautical applications using selective laser melting-a preliminary investigation. *Rapid Prototyping Journal*. 2014;20:551-8.
- [138] Fang J, Sun G, Qiu N, Pang T, Li S, Li Q. On hierarchical honeycombs under out-of-plane crushing. *International Journal of Solids and Structures*. 2018;135:1-13.
- [139] Rehme O, Emmelmann C. Selective laser melting of honeycombs with negative poisson's ratio. *Journal of Laser Micro Nanoengineering*. 2009;4:128-34.
- [140] Travitzky N, Bonet A, Dermeik B, Fey T, Filbert-Demut I, Schlier L, et al. Additive Manufacturing of Ceramic-Based Materials. *Advanced Engineering Materials*. 2014;16:729-54.
- [141] Sing SL, Yeong WY, Wiria FE, Tay BY, Zhao Z, Zhao L, et al. Direct selective laser sintering and melting of ceramics: a review. *Rapid Prototyping Journal*. 2017;23:611-23.
- [142] Lee H, Lim CHJ, Low MJ, Tham N, Murukeshan VM, Kim Y-J. Lasers in additive manufacturing: A review. *International Journal of Precision Engineering and Manufacturing-Green Technology*. 2017;4:307-22.

- [143] Compton BG, Lewis JA. 3D-printing of lightweight cellular composites. *Adv Mater.* 2014;26:5930-5.
- [144] Wang X, Jiang M, Zhou Z, Gou J, Hui D. 3D printing of polymer matrix composites: A review and prospective. *Composites Part B: Engineering.* 2017;110:442-58.
- [145] Ngo TD, Kashani A, Imbalzano G, Nguyen KTQ, Hui D. Additive manufacturing (3D printing): A review of materials, methods, applications and challenges. *Composites Part B: Engineering.* 2018;143:172-96.
- [146] Naik NK, Shrirao P, Reddy BCK. Ballistic impact behaviour of woven fabric composites: Formulation. *International Journal of Impact Engineering.* 2006;32:1521-52.
- [147] Mohan S, Velu S. Ballistic impact behaviour of unidirectional fibre reinforced composites. *International Journal of Impact Engineering.* 2014;63:164-76.
- [148] Karthikeyan K, Kazemahvazi S, Russell BP. Optimal fibre architecture of soft-matrix ballistic laminates. *International Journal of Impact Engineering.* 2016;88:227-37.
- [149] Roylance D. Stress wave propagation in fibres: Effect of crossovers. *Fibre Science and Technology.* 1980;13:385-95.
- [150] Mouritz AP, Bannister MK, Falzon PJ, Leong KH. Review of applications for advanced three-dimensional fibre textile composites. *Composites Part A: Applied Science and Manufacturing.* 1999;30:1445-61.
- [151] Tan VBC, Khoo KJL. Perforation of flexible laminates by projectiles of different geometry. *International Journal of Impact Engineering.* 2005;31:793-810.
- [152] Shim VPW, Tan VBC, Tay TE. Modelling deformation and damage characteristics of woven fabric under small projectile impact. *International Journal of Impact Engineering.* 1995;16:585-605.
- [153] Turner P, Liu T, Zeng X, Brown K. Three-dimensional woven carbon fibre polymer composite beams and plates under ballistic impact. *Composite Structures.* 2018;185:483-95.

- [154] Turner P. Deformation and collapse of orthogonal 3D woven composites: quasi-static and impact loading: The University of Nottingham, 2016.
- [155] Ye L, Daghyani HR. Characteristics of woven fibre fabric reinforced composites in forming process. *Composites Part A: Applied Science and Manufacturing*. 1997;28:869-74.
- [156] Russell BP, Karthikeyan K, Deshpande VS, Fleck NA. The high strain rate response of Ultra High Molecular-weight Polyethylene: From fibre to laminate. *International Journal of Impact Engineering*. 2013;60:1-9.
- [157] Kwon J, Choi J, Huh H, Lee J. Evaluation of the effect of the strain rate on the tensile properties of carbon–epoxy composite laminates. *Journal of Composite Materials*. 2016;51:3197-210.
- [158] Herraiez M, Fernandez A, Lopes CS, Gonzalez C. Strength and toughness of structural fibres for composite material reinforcement. *Philos Trans A Math Phys Eng Sci*. 2016;374:20150274.
- [159] Reis JML, Coelho JLV, Monteiro AH, da Costa Mattos HS. Tensile behavior of glass/epoxy laminates at varying strain rates and temperatures. *Composites Part B: Engineering*. 2012;43:2041-6.
- [160] Cheng M, Chen W, Weerasooriya T. Mechanical Properties of Kevlar® KM2 Single Fiber. *Journal of Engineering Materials and Technology*. 2005;127:197-203.
- [161] Gilat A, Goldberg RK, Roberts G. Experimental study of strain rate sensitivity of carbon fibre-epoxy composite. *Composites Science and Technology*. 2002;62:1469-76.
- [162] Zhou Y, Jiang D, Xia Y. Tensile mechanical behavior of T300 and M40J fibre bundles at different strain rate. *Journal of Materials Science*. 2001;36:919-22.
- [163] Zhou Y, Wang Y, Xia Y, Jeelani S. Tensile behavior of carbon fiber bundles at different strain rates. *Materials Letters*. 2010;64:246-8.
- [164] Naito K. Effect of Strain Rate on Tensile Properties of Carbon Fiber Epoxy-Impregnated Bundle Composite. *Journal of Materials Engineering and Performance*. 2013;23:708-14.

- [165] Daniel IM, LaBedz RH, Liber T. New method for testing composites at very high strain rates. *Experimental Mechanics*. 1980;21:71-7.
- [166] Gilat A, Goldberg RK, Roberts GD. Strain rate sensitivity of epoxy resin in tensile and shear loading. *Journal of Aerospace Engineering*. 2005;20:1-33.
- [167] Wang Z, Xia Y. Experimental evaluation of the strength distribution of fibers under high strain rates by bimodal Weibull distribution. *Composites Science and Technology*. 1997;57:1599-607.
- [168] Wang Y, Xia Y. The effects of strain rate on the mechanical behaviour of kevlar fibre bundles- an experimental and theoretical study. *Composites Part A: Applied Science and Manufacturing*. 1998;29A:1411-5.
- [169] Koh CP, Shim VPW, Tan VBC, Tan BL. Response of a high-strength flexible laminate to dynamic tension. *International Journal of Impact Engineering*. 2008;35:559-68.
- [170] Koh ACP, Shim VPW, Tan VBC. Dynamic behaviour of UHMWPE yarns and addressing impedance mismatch effects of specimen clamps. *International Journal of Impact Engineering*. 2010;37:324-32.
- [171] Smith JC, McCrackin FL, Schiefer HF. Stress-strain relationships in yarns subjected to rapid impact loading. *Textile Research Journal*. 1958;28:288-302.
- [172] Song B, Park H, Lu WY, Chen W. Transverse Impact Response of a Linear Elastic Ballistic Fiber Yarn. *Journal of Applied Mechanics*. 2011;78:051023-1-9.
- [173] Carr DJ. Failure mechanisms of yarns subjected to ballistic impact. *Journal of Materials Science Letters*. 1999;18:585-8.
- [174] Chocron S, Kirchdoerfer T, King N, Freitas CJ. Modeling of Fabric Impact With High Speed Imaging and Nickel-Chromium Wires Validation. *Journal of Applied Mechanics*. 2011;78:051007-1-13.
- [175] Chocron S, King N, Bigger R, Walker JD, Heisserer U, van der Werff H. Impacts and Waves in Dyneema®HB80 Strips and Laminates. *Journal of Applied Mechanics*. 2013;80:1-10.
- [176] Zee RH, Hsieh CY. Energy loss partitioning during ballistic impact of polymer composites. *Polymer Composites*. 1993;14:265-71.

- [177] Bader MG, Bailey JE, Bell I. The effect of fibre-matrix interface strength on the impact and fracture properties of carbon-fibre-reinforced epoxy resin composites. *Journal of Physics D: Applied Physics*. 1973;6:572-90.
- [178] Karthikeyan K, Russell BP, Fleck NA, Wadley HNG, Deshpande VS. The effect of shear strength on the ballistic response of laminated composite plates. *European Journal of Mechanics - A/Solids*. 2013;42:35-53.
- [179] Congress US. Advanced materials by design. Washington, DC1988.
- [180] B.L. Lee, Walsh TF, Won ST, Patts HM. Penetration failure mechanisms of armor-grade fiber composites under impact. *Journal of Composite Materials*. 2001;35:1605-33.
- [181] Attwood JP, Khaderi SN, Karthikeyan K, Fleck NA, O'Masta MR, Wadley HNG, et al. The out-of-plane compressive response of Dyneema® composites. *Journal of the Mechanics and Physics of Solids*. 2014;70:200-26.
- [182] Jimenez FL. Mechanics of thin carbon fiber composites with a silicone matrix. Pasadena, California: California Institute of Technology, 2011.
- [183] Fleck NA. Compressive failure of fibre composites. *Advances in Applied Mechanics*. 1997;33:43-117.
- [184] Warrior NA, Fernie R, Jones IA. High strain rate tensile and compressive testing of braided composite materials. 2003 SEM Annual Conference & Exposition on Experimental and Applied mechanics. Charlotte, North Carolina2003.
- [185] de Ruijter C, van der Zwaag S, Stolze R, Dingemans TJ. Liquid crystalline matrix polymers for aramid ballistic composites. *Polymer Composites*. 2010;31:612-9.
- [186] Yu B, Karthikeyan K, Deshpande VS, Fleck NA. Perforation resistance of CFRP beams to quasi-static and ballistic loading: The role of matrix strength. *International Journal of Impact Engineering*. 2017;108:389-401.
- [187] Karthikeyan K, Russell BP. Polyethylene ballistic laminates: Failure mechanics and interface effect. *Materials & Design*. 2014;63:115-25.
- [188] Agrawal S, Singh KK, Sarkar PK. Impact damage on fibre-reinforced polymer matrix composite – A review. *Journal of Composite Materials*. 2013;48:317-32.

- [189] O'Masta MR, Crayton DH, Deshpande VS, Wadley HNG. Mechanisms of penetration in polyethylene reinforced cross-ply laminates. *International Journal of Impact Engineering*. 2015;86:249-64.
- [190] McColl IR, Morley JG. Crack growth in hybrid fibrous composites. *Journal of Materials Science*. 1977;12:1165-75.
- [191] Venkata Reddy G, Shobha Rani T, Chowdoji Rao K, Venkata Naidu S. Flexural, Compressive, and Interlaminar Shear Strength Properties of Kapok/Glass Composites. *Journal of Reinforced Plastics and Composites*. 2008;28:1665-77.
- [192] Pandya KS, Pothnis JR, Ravikumar G, Naik NK. Ballistic impact behavior of hybrid composites. *Materials & Design*. 2013;44:128-35.
- [193] Bandaru AK, Vetiyatil L, Ahmad S. The effect of hybridization on the ballistic impact behavior of hybrid composite armors. *Composites Part B: Engineering*. 2015;76:300-19.
- [194] Dorey G, Sidey GR, Hutchings J. Impact properties of carbon fibre/Kevlar 49 fibre hybrid composites. *Composites*. 1978;25-32.
- [195] Larsson F, Svensson L. Carbon, polyethylene and PBO hybrid fibre composites for structural lightweight armour. *Composites Part B: Engineering*. 2002;33:221-31.
- [196] Wang CJ, Jang BZ, Panus J, Valaire BT. Impact behavior of hybrid-fiber and hybrid-matrix composites. *Journal of Reinforced Plastics and Composites*. 1991;10:356-78.
- [197] Hazzard MK, Hallett S, Curtis PT, Iannucci L, Trask RS. Effect of fibre orientation on the low velocity impact response of thin Dyneema® composite laminates. *International Journal of Impact Engineering*. 2017;100:35-45.
- [198] Caminero MA, García-Moreno I, Rodríguez GP. Damage resistance of carbon fibre reinforced epoxy laminates subjected to low velocity impact: Effects of laminate thickness and ply-stacking sequence. *Polymer Testing*. 2017;63:530-41.
- [199] Belingardi G, Vadori R. Influence of the laminate thickness in low velocity impact behavior of composite material plate. *Composite Structures*. 2003;61:27-38.

- [200] Vargas-Gonzalez LR, Gurganus JC. Hybridized composite architecture for mitigation of non-penetrating ballistic trauma. *International Journal of Impact Engineering*. 2015;86:295-306.
- [201] Onal L, Adanur S. Effect of Stacking Sequence on the Mechanical Properties of Glass–Carbon Hybrid Composites before and after Impact. *Journal of Industrial Textiles*. 2016;31:255-71.
- [202] Bandaru AK, Ahmad S, Bhatnagar N. Ballistic performance of hybrid thermoplastic composite armors reinforced with Kevlar and basalt fabrics. *Composites Part A: Applied Science and Manufacturing*. 2017;97:151-65.
- [203] Amico SC, Angrizani CC, Drummond ML. Influence of the Stacking Sequence on the Mechanical Properties of Glass/Sisal Hybrid Composites. *Journal of Reinforced Plastics and Composites*. 2008;29:179-89.
- [204] Muhi RJ, Najim F, de Moura MFSF. The effect of hybridization on the GFRP behavior under high velocity impact. *Composites Part B: Engineering*. 2009;40:798-803.
- [205] O'Masta MR, Deshpande VS, Wadley HNG. Mechanisms of projectile penetration in Dyneema® encapsulated aluminum structures. *International Journal of Impact Engineering*. 2014;74:16-35.
- [206] Karthikeyan K. Dynamic response of polyethylene composites: University of Cambridge, 2013.
- [207] Attwood JP, Russell BP, Wadley HNG, Deshpande VS. Mechanisms of the penetration of ultra-high molecular weight polyethylene composite beams. *International Journal of Impact Engineering*. 2016;93:153-65.
- [208] Sun F, Lai C, Fan H, Fang D. Crushing mechanism of hierarchical lattice structure. *Mechanics of Materials*. 2016;97:164-83.
- [209] Zheng J, Zhao L, Fan H. Energy absorption mechanisms of hierarchical woven lattice composites. *Composites Part B: Engineering*. 2012;43:1516-22.
- [210] Kunze K, Etter T, Grässlin J, Shklover V. Texture, anisotropy in microstructure and mechanical properties of IN738LC alloy processed by selective laser melting (SLM). *Materials Science and Engineering: A*. 2015;620:213-22.

- [211] Bauer J, Hengsbach S, Tesari I, Schwaiger R, Kraft O. High-strength cellular ceramic composites with 3D microarchitecture. *Proceedings of the National Academy of Sciences of the United States of America*. 2014;111:2453-8.
- [212] Aboulkhair NT, Maskery I, Tuck C, Ashcroft I, Everitt NM. Improving the fatigue behaviour of a selectively laser melted aluminium alloy: Influence of heat treatment and surface quality. *Materials & Design*. 2016;104:174-82.
- [213] Aboulkhair NT, Everitt NM, Ashcroft I, Tuck C. Reducing porosity in AlSi10Mg parts processed by selective laser melting. *Additive Manufacturing*. 2014;1-4:77-86.
- [214] Maskery I, Aboulkhair NT, Aremu AO, Tuck CJ, Ashcroft IA, Wildman RD, et al. A mechanical property evaluation of graded density Al-Si10-Mg lattice structures manufactured by selective laser melting. *Materials Science and Engineering: A*. 2016;670:264-74.
- [215] ASTM. E8/E8M-13a Standard Test Method for Tension Testing of Metallic Materials. West Conshohocken: American Society for Testing and Materials ASTM: Book of standard volume 0301; 2013.
- [216] Maskery I, Aboulkhair NT, Corfield MR, Tuck C, Clare AT, Leach RK, et al. Quantification and characterisation of porosity in selectively laser melted Al-Si10-Mg using X-ray computed tomography. *Materials Characterization*. 2016;111:193-204.
- [217] Kempen K, Thijs L, Van Humbeeck J, Kruth JP. Mechanical Properties of AlSi10Mg Produced by Selective Laser Melting. *Physics Procedia*. 2012;39:439-46.
- [218] Manfredi D, Calignano F, Krishnan M, Canali R, Ambrosio E, Atzeni E. From Powders to Dense Metal Parts: Characterization of a Commercial AlSiMg Alloy Processed through Direct Metal Laser Sintering. *Materials*. 2013;6:856-69.
- [219] S. Joseph SK. A systematic investigation of fracture mechanisms in Al-Si based eutectic alloy—Effect of Si modification. *Materials Science & Engineering A*. 2013;588:111-24.

- [220] Kolsky H. An Investigation of the Mechanical Properties of Materials at very High Rates of Loading. *Proceedings of the Physical Society Section B*. 1949;62:676-700.
- [221] Liu T, Turner P. Dynamic compressive response of wrapped carbon fibre composite corrugated cores. *Composite Structures*. 2016.
- [222] ABAQUS. ABAUQS analysis user's manual, Version 6.14, ABAQUS, Inc. 2014.
- [223] Benjamin P. Russell, Adam Malcom, Haydn N. G. Wadley, Deshpande VS. Dynamic Compressive Response of Composite Corrugated Cores. *Journal of Mechanics of Materials and Structures*. 2010;5:477-93.
- [224] Abrate S, Castanié B, Rajapakse YDS. *Dynamic Failure of Composite and Sandwich Structures*. New York: Springer, 2012.
- [225] Penado FE. Effective Elastic Properties of Honeycomb Core with Fiber-Reinforced Composite Cells. *Open Journal of Composite Materials*. 2013;03:89-96.
- [226] Park S, Uth T, Fleck NA, Wadley HNG, Deshpande VS. Sand column impact onto a Kolsky pressure bar. *International Journal of Impact Engineering*. 2013;62:229-42.
- [227] W J, Jr D, Newell JA. Characterization of structural changes in thermally enhanced Kevlar-29 fiber. *Journal of Applied Polymer Science*. 2003;91:417-24.
- [228] Kilchert SV. Nonlinear finite element modelling of degradation and failure in folded core composite sandwich structures: University of Stuttgart, 2013.
- [229] NagarajaRao N, Lohrmann M, Tall L. Effect of strain rate on the yield stress of structural steel. *ASTM Journal of Materials*. 1966;1:1684-737.
- [230] Fan HL, Meng FH, Yang W. Sandwich panels with Kagome lattice cores reinforced by carbon fibers. *Composite Structures*. 2007;81:533-9.
- [231] Xiong J, Zhang M, Stocchi A, Hu H, Ma L, Wu L, et al. Mechanical behaviors of carbon fiber composite sandwich columns with three dimensional honeycomb cores under in-plane compression. *Composites Part B: Engineering*. 2014;60:350-8.
- [232] Cheeseman BA, Bogetti TA. Ballistic impact into fabric and compliant composite laminates. *Composite Structures*. 2003;61:161-73.

- [233] Reyes Villanueva G, Cantwell WJ. The high velocity impact response of composite and FML-reinforced sandwich structures. *Composites Science and Technology*. 2004;64:35-54.
- [234] Gustin J, Joneson A, Mahinfalah M, Stone J. Low velocity impact of combination Kevlar/carbon fiber sandwich composites. *Composite Structures*. 2005;69:396-406.
- [235] Loctite. <http://www.loctite.co.uk/loctite-4087.htm?nodeid=8802629156865> 2018.
- [236] Walker JD. From Columbia to Discovery: Understanding the impact threat to the space shuttle. *International Journal of Impact Engineering*. 2009;36:303-17.

Appendix

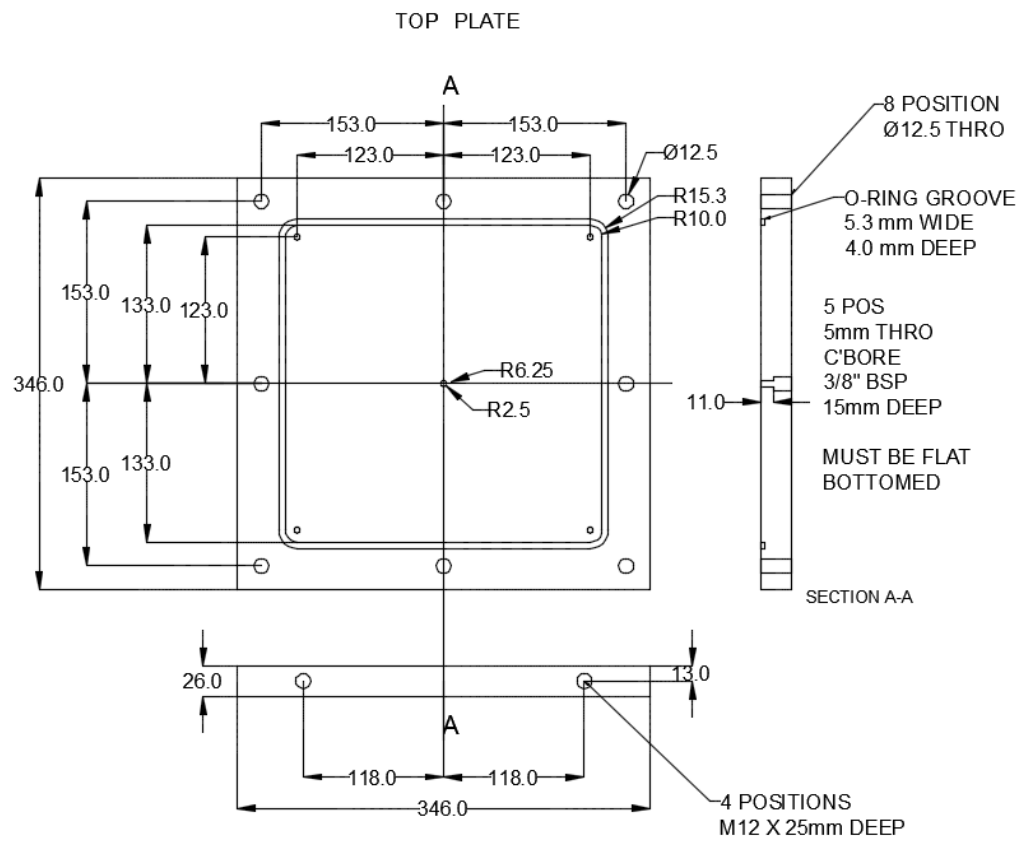


Fig. A1 Sketch showing the dimensions of top plate of mild steel mould. All dimensions are in mm.

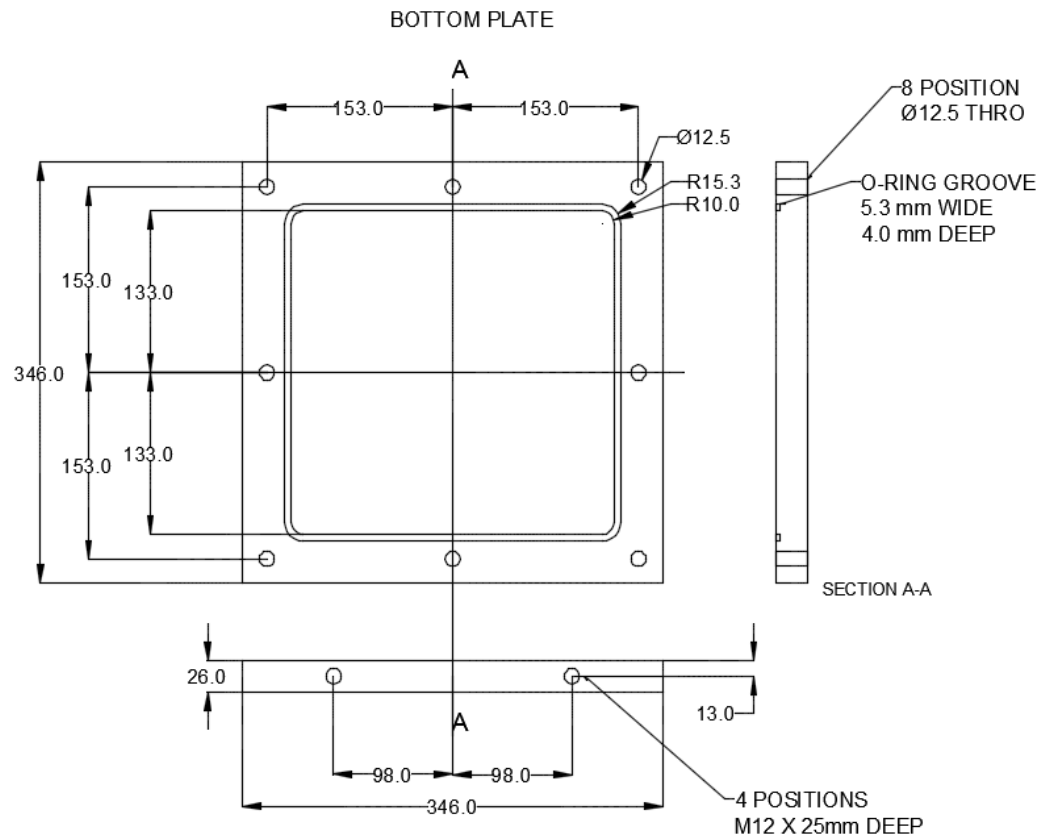


Fig. A2 Sketch showing the dimensions of bottom plate of mild steel mould.

All dimensions are in mm.

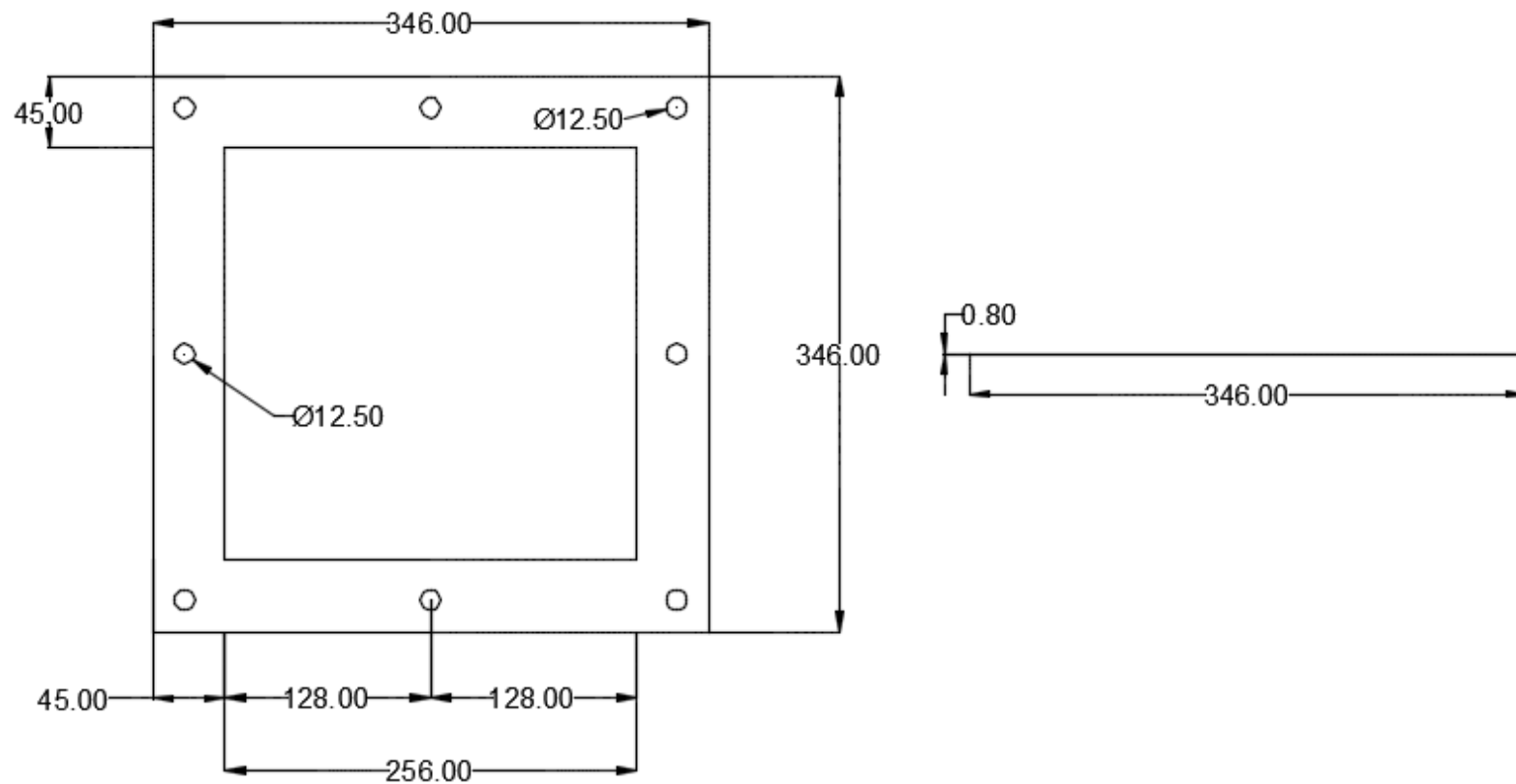


Fig. A3 Sketch showing the dimensions of picture frame in vacuum assisted resin transfer moulding (VA-RTM) system. All dimensions are in mm.